CODEFORMATION PROCESSING OF MECHANICALLY-DISSIMILAR METAL/INTERMETALLIC COMPOSITES

by

Judson Sloan Marte

Dissertation submitted to the Faculty of the

Virginia Polytechnic Institute and State University

in partial fulfillment of the requirements for the degree of

DOCTOR OF PHILOSOPHY

in

Materials Engineering Science

APPROVED:

S. L. Kampe, Chairman	
W.T. Reynolds, MSE	**A. O. Aning, MSE/EF**
L. Christodoulou, MSE	**C.R. Crowe, MSE**
G. Wilkes, MESc Program Director	**R.H. Sturges, ME/ISE**

January 1999
Blacksburg, Virginia

Key Words: Codeformation, Metal Matrix Composites, Intermetallic Matrix Composites, Extrusion, Powder Metallurgy, Reaction Synthesis

Codeformation Processing of Mechanically-Dissimilar Metal/Intermetallic Composites

by

Judson S. Marte

Committee Chairman: Stephen L. Kampe
Materials Science and Engineering
(ABSTRACT)

A systematic and scientific approach has been applied to the study of codeformation processing. A series of composites having mechanically-dissimilar phases were developed in which the high temperature flow behavior of the reinforcement material could be varied independent of the matrix. This was accomplished through the use of a series of intermetallic matrix composites (IMCs) as discontinuous reinforcements in an otherwise conventional metal matrix composite.

The IMCs are produced using an in-situ reaction synthesis technique, called the XD™ process. The temperature of the exothermic synthesis reaction, called the adiabatic temperature, has been calculated and shown to increase with increasing volume percentage of TiB_2 reinforcement. Further, this temperature has been shown to effect the size and spacing of the TiB_2, microstructural features which are often used in discontinuous composite strength models.

Study of the high temperature flow behavior of the components of the metal/IMC composite is critical to the development of an understanding of codeformation. A series of compression tests performed at 1000° to 1200°C and strain-rates of 10^{-3} and 10^{-4} sec^{-1}. Peak flow stresses were used to evaluate the influence of material properties and process conditions. These data were incorporated into phenomenologically-based constitutive equations that have been used to predict the flow behavior. It has been determined that plastic deformation of the IMCs occurs readily, and is largely TiB_2 independent, at temperatures approaching the melting point of the intermetallic matrices.

Ti-6Al-4V/IMC powder blends were extruded at high temperatures to achieve commensurately deformed microstructures. The results of codeformation processing were analyzed in terms of the plastic strain of the IMC particulates. IMC particle deformation was shown to increase with increasing IMC particle size, volume percentage of IMC, extrusion temperature, homologous temperature, extrusion strain-rate, and decreasing TiB_2 reinforcement within the IMCs.

A series of finite element models were developed to simulate codeformation processing via the extrusion of a discontinuously-reinforced composite. The results were evaluated through comparison between average equivalent strain in matrix and reinforcement elements. These results show that codeformation should increase with increasing volume percentage of IMC, homologous temperature, volume percentage of IMC, and decreasing IMC particle size. With the exception of the particle size, these results correlate to those of the experimental extrusion analysis.

Acknowledgments

The author wishes to extend his deepest thanks to his advisor, Dr. Steve Kampe, for his direction and encouragement. He would also like to extend his thanks to Drs. Alex Aning, Robert Crowe, Leo Christodoulou, William Reynolds, and Robert Sturges for their participation in this study and the author's dissertation review committee.

Financial support for this work was provided through an SBIR grant sponsored by Drs. Tony Zahrah and Phil Parrish of MATSYS, Inc. and Dr. Steve Fishman at the Office of Naval Research. In addition, the author would like to thank: Drs. Richard Dashwood, Peter Lee, Julie Christodoulou, and Richard Thackray; Mrs. Melvin Andrews and Edwin Eardley; and Mss. Emma (Jane) Minay, and Kate Harris of the Materials Department at Imperial College of Science, Technology, and Medicine for the various bits of assistance and inspiration they provided.

Special thanks are due to the faculty, staff, and students of the Materials Science and Engineering Department who were very helpful, especially: Jan Doran, Amy Hill, Dr. Ronald Gordon, Raphael Martin, Thobeka Pete, Levon Fattal, James Clarke, and the many others whom I've had the privilege to interact with during the past six years.

Finally, the work performed herein would not have happenned without the encouragement and confidence provided by the author's family: Charles, Edith, Ryan, Spencer, and my wife-to-be Michelle.

List of Figures

List of Tables

List of Equations

1. An Introduction to Codeformation Processing

Codeformation processing uses plastic strain to densify, bond, or create desired microstructural features in a material. To date, codeformation processes have largely been developed through experience combined with trial-and-error methods.

Conventional manufacturing methodologies rely on the principles of codeformation processing. Co-rolling and pack-rolling of metal foils involves layering several sheets of a single type of metal to produce thinner foils. This practice is used in the aluminum industry to increase productivity. In another example, pack-rolling provides the increased thermal mass needed for the rolling of nickel-base foils. Sheathing and cladding are processes in which a metal is bonded, via deformation processing, with a second metal. This type of technique is also used to reduce metal filament diameters through extrusion, drawing and rolling. Still another example exists in the processing of metal powders which are canned prior to extrusion, to provide an environmental barrier, and in some cases, a high temperature lubricant.

The ability to codeform any composite is believed to lie in the relative flow behavior of its components. The flow stress is a function of the imposed deformation conditions, i.e., the strain, strain-rate and temperature. However, the delineation of the flow stress is complicated by the interaction of these conditions. For example, increasing the strain-rate can give rise to temperature increases as a result of adiabatic heating, which in turn, affects the amount of strain, and in a more general sense, the relative flow stress. This can be further convoluted by problems associated with the dynamic changes in interfacial (i.e., chemical and thermodynamic) character between components.

In nearly all the examples given above, the composition and processing conditions are fixed and relatively unique to the specific system. Thus, a systematic study to independently evaluate the influence of materials properties, such as flow stress and thermochemical stability, would serve to advance our understanding of how mechanically-dissimilar materials can be commensurately deformed.

1.1. Objectives

The objective of the current research is to develop a systematic, scientific methodology for the study of codeformation processing. The methodology will be demonstrated experimentally through the processing of a composite material consisting of mechanically-dissimilar components. The methodology will also demonstrate the ability to simulate such processes through finite element modelling.

1.2. Approach

The approach this study has taken will utilize a material system in which the relative plastic flow behavior can be controlled through compositional manipulation. A composite material is ideally suited to this task, especially if one can independently alter the flow stress of one phase without affecting the other. A metal matrix composite (MMC) will be utilized for this purpose. In the MMC, the relative deformation of a conventional metallic alloy will be assessed with respect to a second component (i.e., reinforcement) comprised of a discontinuously-reinforced intermetallic matrix composite (DR-IMC). The DR-IMCs consist of an atomically-ordered alloy reinforced by a dispersion of fine ceramic particulate. As a component in a study of codeformation, the DR-IMC can be considered to be isotropic and treatable as a continuum with respect to its macroscopic flow behavior. However, the actual flow properties are broadly variable through microscopic variations in constituency and composition. Thus, it is possible to create "families" of IMCs with widely varying flow properties as model components for the study of codeformation processing. The control and flexibility of the flow behavior of DR-IMCs make them well suited to be used as the "reinforcing" phase in the codeformation processed composite. Thus, systematic variation of both the IMC "reinforcement" and process conditions enables a wide range of relative flow behavior to be examined and quantified.

Successful codeformation of the composite implies that the two components (i.e., metal and DR-IMC) will commensurately deform, creating a composite with the desired microstructural features. A powder-based process will be used in which the blended metal/IMC powder will be codeformed to produce a densified composite similar to an *in-*

situ deformation processed (DP) composite. A schematic of this powder-based codeformation by means of extrusion is shown in Figure 1.

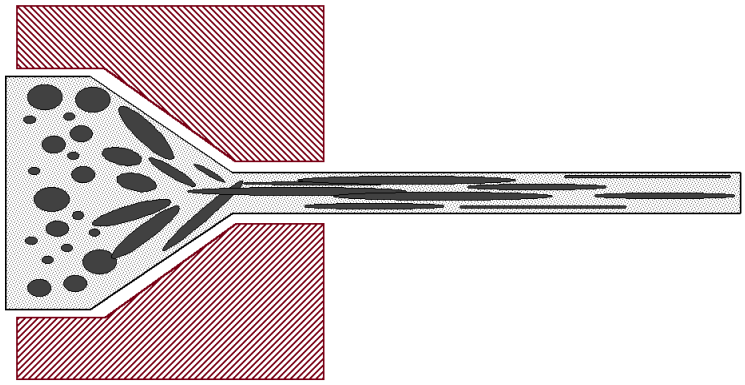

Figure 1: A schematic representation of codeformation processing via extrusion. The blended mechanically-dissimilar powders (on the left) are commensurately deformed to become an in-situ deformation processed composite.

In order for this to be possible, several general pre-requisites must be fulfilled. First, IMCs must be selected which are solid, deformable, and stable at high temperatures. Second, the IMC must be thermochemically stable within the metal matrix at temperatures high enough to allow ductility within both the metal and the IMC. Third, the relative flow stresses of the metal and the IMC must be roughly equivalent at the processing temperature, thereby allowing efficient load transfer from one phase onto the other, achieving commensurate deformation. With these prerequisites in mind, the $\alpha + \beta$ titanium alloy, Ti-6Al-4V, was selected as the metal matrix. This matrix will be reinforced by a titanium aluminide intermetallic matrix composite, which was itself reinforced with titanium diboride particulates. Titanium aluminide matrix composites were selected because of their stability within the Ti-6Al-4V matrix, their relatively low melting temperatures, and their comparable, but still controllable, flow stresses.

The extent of the codeformation will be assessed in terms of the evolution of a specific reinforcement morphology. Several parameters will be systematically varied to determine their influence on the codeformation behavior of the metal/IMC composite (M/IMC). This codeformation will be evaluated in terms of the relative flow behavior of the Ti-6Al-4V and IMC components. The flow behavior is controlled by the volume percentage of IMC in the M/IMC composite, the IMC matrix composition, the amount of dispersed ceramic reinforcement within the IMC, and the microstructural features of that ceramic reinforcement (i.e., size, spacing, and aspect ratio.) Additionally, the thermomechanical codeformation process parameters (temperature, strain-rate) will have an effect on the relative flow behavior. Both the material and process parameters will be systematically varied to evaluate their influence on the codeformation behavior of the M/IMC composite. The results of the experimental study of codeformation will then be used to develop a finite element model (FEM) to simulate the process.

Several specific goals must be achieved to meet the broad objectives outlined in the approach above:

1. characterize how the flow behavior of the IMC relies on temperature, strain-rate, composition, and volume percentage of dispersed ceramic reinforcement;
2. understand how processing history affects the microstructure, and hence, flow behavior of the IMC (e.g., size and interparticle spacing of the ceramic reinforcement);
3. develop a strategy to quantify the codeformation of the IMC “reinforcement” component, in terms of its deformed morphology; and
4. develop a finite element model to simulate the process and predict the microstructural changes resulting from codeformation.

1.3. Format of this Dissertation

The dissertation will address each objective as a stand-alone section of the issue and combine the analysis in a discussion of the final results. The sections and a brief description of each are:

- Literature Review: The scientific literature available and its influence on the current study will be assessed. This will include a survey of the literature on codeformation-based processes, reaction synthesis, constitutive equation development, and the modelling of codeformation processes.
- Synthesis: The production of intermetallic matrix composites which are used as the reinforcing phase in the metal/IMC composite will be detailed. As will be shown, the deformation behavior of the IMC relies upon certain details of the synthesis event.
- Characterization of Flow Behavior: The high temperature flow behavior of the components of the metal/IMC composite is the subject of this chapter. The influence of material properties and process conditions will be assessed and incorporated into phenomenologically-based constitutive equations which can be used to predict the flow behavior.
- Extrusion: A description of the codeformation event will be described. The effect of component flow behavior and process parameters will be assessed through a quantitative analysis of deformed IMC morphology. This analysis will serve as the foundation for the correlation of relative component flow behavior to codeformability.
- Modelling and Process Simulation: This section combines the aspects of the previous chapters into the development of a finite element model. The model will be shown to be capable of qualitatively predicting the commensurate component deformability in codeformation processed mechanically-dissimilar composites.
- Summary: This final chapter provides a summary of the research and conclusions reached. It will also detail recommendations for future analyses of codeformation processes.

2. Literature Review

A review of the current understanding of deformation processing, IMC synthesis, and finite element modelling is provided to furnish a basis for the current research.

2.1. Deformation-based Processes

Codeformation processing finds its foundation in conventional metalworking technologies. A survey of the literature on this subject, therefore, is fundamental to understanding the motivation for the systematic study of codeformation.

2.1.1. Extrusion

The literature on deformation-based processes is substantial. Kalpakjian[1,2] provides a very thorough, albeit basic, description of bulk deformation processes. His texts offer a great introduction to the terminology and is accompanied by numerous examples.

Hosford and Caddell[3] provide a very thorough explanation of the mechanics behind deformation processes, as well as a brief introduction to constitutive equations. Of interest to this study are the details of adiabatic heat generated during extrusion processes. Adiabatic heating can cause thermal softening as the temperature rises during deformation. This phenomenon results in localization of flow in narrow bands. If one region deforms more than another, the subsequent increase in temperature may lower the flow stress in that region, causing more concentration of flow and more local heating in this region. This could lead to incipient melting of localized areas. Localized flow gradients are inherent to the processing of mechanically-dissimilar materials, therefore adiabatic heating of a degree which might cause incipient melting is a concern. A precaution which the current study must observe is that the extrusion temperature used be kept low enough that no incipient melting occur. The high homologous temperatures at which the metal/IMC composites are being processed make this concern especially important.

2.1.2. Codeformation Processes

Codeformation processing has been performed using a morphological *in-situ* processing technique. During morphological *in-situ* processes, the composite's microstructure is formed through non-conventional processing of an otherwise "conventional" alloy in which the primary effect of the processing is seen in the shape and orientation of the reinforcement phase. This result is of primary interest to the current study.

Spitzig, Trybus, and Verhoeven[4] presented a useful study of deformation-processed composites in which they examined the codeformation of Cu-Nb composites. In this work they described four basic requirements for codeformation processing to occur. The first requirement is that the phases of the desired compositions be produced. That is to say, the phases should be present during the deformation process and not introduced afterward. The second requirement is that the minor phase be uniformly distributed throughout the matrix. Third, the matrix/reinforcement boundaries must be free of oxide films and contamination, to promote strong interfaces. Finally, he states that both phases must be sufficiently ductile and have relatively similar flow stresses so that large total deformation strains may be obtained. Additionally, it was stated that commensurate deformation of minor and matrix phases via extrusion will produce aligned filaments of the minor phase regardless of its initial shape. This is important to the current study because it verifies that irregularly shaped reinforcement particles can evolve into an aligned, fibrous reinforcement through conventional powder metallurgical (P/M) techniques. The study also noted, however, that larger spherical particles failed to form a filamentary structure, while smaller irregular particles did. As will be noted later, this trend was not observed for the series of metal/IMC composites examined in the present study.

Perhaps the most thorough analysis of codeformation is presented by Avitzur[5]. His text presents examples of the production of multifilament rod and the co-rolling and stamping of modern coins from bimetallic sheets. He also provides an exhaustive list of the equations used to calculate the relative extrusion pressure for a bimetallic rod consisting of core material different from the sheathing material. Specifically, he describes the extrusion pressure required to codeform bimetallic rods in terms of flow stress of the core

material and the flow stress of the sleeve material. He states that if the core is significantly harder than the sleeve (i.e., the flow stress of the core is higher than that of the sleeve), it will resisit deformation, undergo a smaller reduction in area, elongate less, and fracture. He presents guidelines to prevent core fracture in terms of the ratio of the flow stresses (i.e., σ_{0S}/σ_{0C}) and the relative core radius (i.e., R_i/R_0). In the case of a core which is stronger than the sleeve (i.e., $\sigma_{0S}/\sigma_{0C} < 1$), he shows that as the relative core radius decreases, the ability of the deformation to occur without fracture increases. This is important to this study as it may have implications on the fracture or cavitation observed in the IMC component of some codeformed composites.

Roberts[6] discloses a codeformation technique which can be utilized for the production of sub-50 micrometer wire filaments through extrusion, rolling, or wire-drawing. Although, the primary goal of his work was to produce extremely fine metal filaments with cross-sectional areas that are nearly constant. He does describe the processing of some bimetallic filamentary composites. The examples of codeformation processes he provides are specific to certain materials systems (e.g., steel/Monel, steel/copper). This work reinforces the need for a systematic and scientific study which provides guidelines for generic systems and processes in terms of certain materials properties, e.g., modulii, recrystallization temperature, strain-rate sensitivity, etc. One general trend Roberts does point out is that, through the use of lower matrix to reinforcement volume ratios, it is possible to achieve a higher degree of deformation. This matrix to reinforcement volume ratio is one of the processing variables this study will be examining.

2.1.2.1. Codeformation processing of discontinuous IMC-reinforced composites

The present research has attempted to use the high-temperature deformability characteristics of an IMC-reinforcement to achieve *in-situ* elongation within a metal matrix. Previous to this study, deformability was partially demonstrated by the works of Pete and Martin[7, 8], where extrusions of IMC-reinforced titanium matrix composites were produced at elevated temperatures (1066°C). The extrusions produced did not exhibit fully commensurate deformation between matrix and the intermetallic matrix composite. It was concluded that the titanium matrices (Commercially Pure Ti and Ti-6Al-4V) did

not impart enough stress onto the IMC particles to deform them under the experimental process conditions.

The primary objective of the current study is to address this problem in a more fundamental manner by measuring flow behavior of the IMC as a function of temperature, strain-rate and composition such that the processing conditions can be more efficiently determined. It is expected that, if the homologous temperature (i.e., T/T_{melt}) of the reinforcing phase could be increased (e.g., through appropriate intermetallic alloy selection), then the titanium alloy matrix would transmit enough stress to effectively codeform the IMC.

The results found in the literature suggest that codeformation processing is a plausible means of producing a discontinuous IMC-reinforced composite. The studies presented here also show that attention must be paid to the relative volume percentages and flow stresses of the matrix and reinforcement components if codeformation is to be successful.

2.2. Model Systems for Codeformation

The properties of the metal/IMC components will have considerable influence on codeformation processing. The properties of intermetallic alloys, specifically titanium aluminides, and their composites have direct effect on the flow behavior and chemical stability of the composite during and after processing. This review serves to acquaint the reader with the synthesis and properties of these materials.

2.2.1. Intermetallic Alloys

Intermetallic based alloys and intermetallic matrix composites (IMCs) have been the focus of numerous studies for their potential as low-density alternatives to the heavier nickel- and iron-based superalloys in high temperature applications[9, 10, 11, 12, 13, 14, 15, 16, 17, 18, 19, 20].

These studies generally serve to highlight the many attractive properties of intermetallic alloys, notably their resistance to high temperature deformation, while attempting to address their major shortcoming of relatively low ductilities at low to moderate temperatures. The deformation of intermetallics evolves, in large part, due to their

crystallographic order and the thermodynamic constraints this imposes on dislocation motion and atomic diffusion. Deformation in ordered structures generally occurs with the movement of superdislocations within a relatively few specific slip systems. The ordered structure also reduces diffusion rates, since atomic motion tends to occur in pairs to likewise maintain the crystallographic order. Several studies have linked these atomic scale features to the excellent elevated temperature strength retention and creep behavior, since resistance to both dislocation- and diffusion-based deformation mechanisms are simultaneously addressed. [21, 22]

The influence of crystallographic order on the deformation characteristics of intermetallic alloys tends to decrease as the temperature at which deformation occurs increases. While strength and ductility tend to be relatively insensitive to temperature over a reasonably broad range, intermetallics will evetually tend to exhibit a distinct brittle-to-ductile temperature (BDT). Depending on the specific system, the abrupt increase in tensile ductility (approaching values comparable to disordered alloys) with the concommitant decrease in strength has been attributed to a loss of long and/or short range order[23], to the activation of additional slip-systems[24], and/or to an increasing influence of conventional thermally-activated diffusional-assisted deformation.[23] Indeed, many studies have demonstrated that intermetallics are readily processable by conventional means at temperatures in excess of their respective BDT.[25, 26, 27, 28, 29]

2.2.1.1. Titanium Aluminides

The Ti-Al system contains three stable intermetallic compounds, Ti_3Al (α_2), TiAl (γ), and Al_3Ti (τ), as shown in the phase diagram presented in Figure 2. Much research has been focused on either Ti_3Al (α_2), TiAl (γ) or a TiAl-rich combination of the two (i.e., "near-γ") because of the potential for nearest-term application of these systems. The Al_3Ti compound has, in general, been viewed with skepticism because of its severe brittleness at ambient temperatures, even relative to Ti_3Al and TiAl. Many investigations of titanium aluminides have been conducted in an attempt to overcome their lack of room temperature ductility.[30, 31, 32, 33, 34]. Monolithic titanium aluminides have a BDT of approximately 800°-1000°C, depending on the specific system.

Processing above these temperatures, then, circumvents potential ductility limitations, allowing for the incorporation of titanium aluminides into conventional deformation processes.

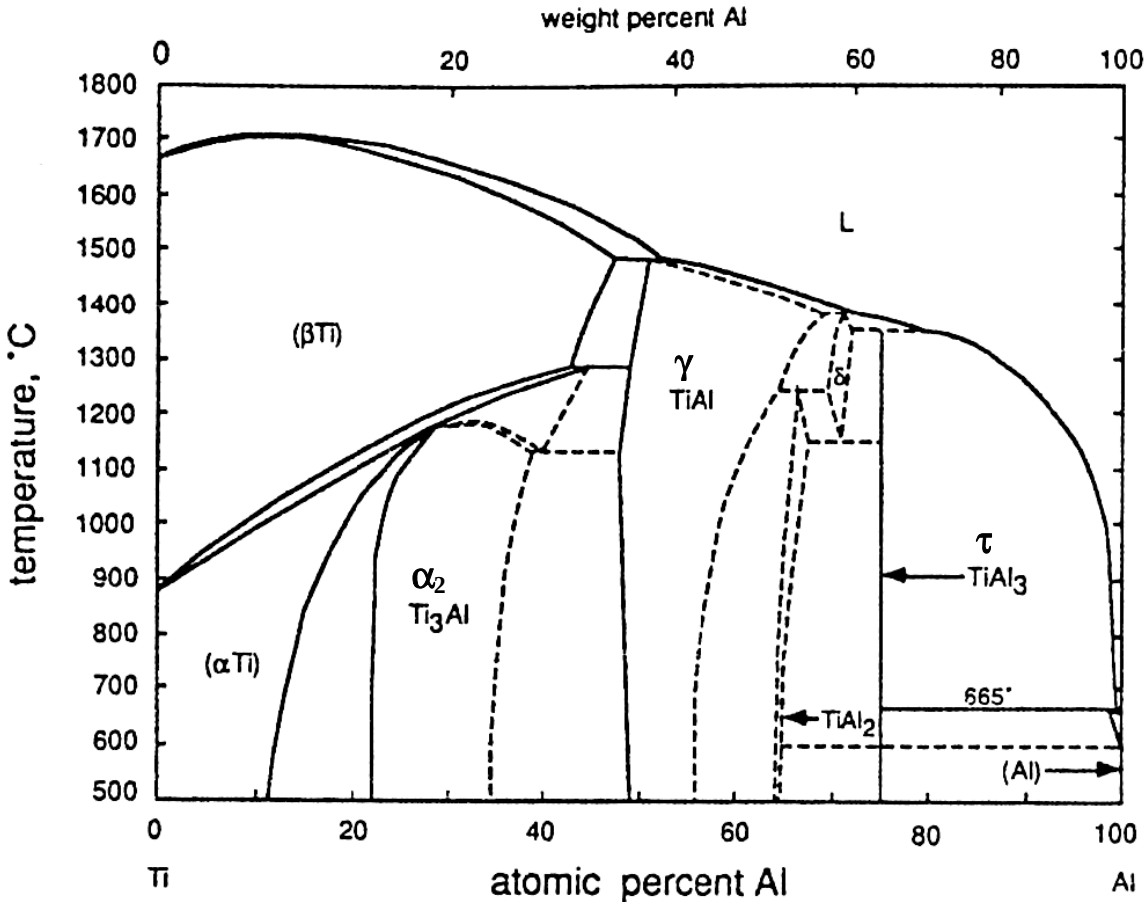

Figure 2: The titanium aluminum phase diagram, showing the three stable ordered intermetallic phases: Ti_3Al, TiAl, and Al_3Ti.[20]

2.2.1.2. Titanium Aluminide Matrix Composites

The IMCs employed in the current study are titanium aluminide matrix composites reinforced with high loadings of TiB_2. This class of IMCs was selected for its deformability at elevated temperatures (i.e., above 1000°C) and ceramic-like room temperature mechanical properties. VanMeter, *et.al*, presented a comparison of the elastic modulii and hardness of several TiAl-matrix IMCs to those of SiC and Al_2O_3.[35] This data is shown in Table I.

Table I: A Comparison of the elastic modulii of titanium aluminide matrix composites to SiC and Al_2O_3.[34]

Material	*Elastic Modulus (GPa)*	*Knoop Hardness (1kg) GPa*	*Reference*
Ti-46Al + 40 v% TiB_2	290	9.0	29
Ti-46Al + 50 v% TiB_2	305	9.5	29
Al_2O_3	303	11	36
SiC	393	25	30

There has been speculation that the room temperature strength of these composites is derived in part from the presence of the discontinuous reinforcement. Strong correlations between strengthening and reinforcement size and distribution have been made.[37] Models relating the strengthening potency to the size and spacing of discontinuously-reinforced composites are well-developed.[38, 39] The present study has sought to form a correlation between the presence of TiB_2 and elevated temperature flow behavior. In this regard, the influence synthesis conditions have on composite microstructural development would provide a means of relating IMC strength to synthesis.

The composites used in the current study are produced using a reaction synthesis technique known as exothermic dispersion (XD) synthesis. This technique makes use of the exothermic heats of formation to provide the activation energy for the formation of a ceramic particulate reinforcement directly within a metallic solvent, the latter eventually representing the intermetallic matrix component of the discontinuously reinforced composite. The reaction temperature achieved during synthesis scales with the volume percentage of the highly exothermic reinforcing component (i.e., TiB_2), and will be shown to have strong correlation to the particulate microstructural features of interest. Martin attempted to correlate the calculated reaction temperature to the size of TiB_2 particulate in a previous study.[40] This correlation is extended and improved in the current study.

One of the most-cited advantages of XD synthesis is the formation of clean and thermodynamically-stable matrix/reinforcement interfaces that necessarily evolve during the process.[41] The thermochemical stability of these interfaces is a matter of some

concern when elevated processing tempeartures are employed. However, this stability has been confirmed for temperatures and systems similar to those used in the current study.[42]

2.2.2. Ti-6Al-4V

Ti-6Al-4V is the most widely used of the α+β titanium alloys. This alloy was selected for its high specific strength[43], excellent deformability[44], and compatability with titanium aluminides. Of primary importance to the present study is the alloy's high temperature flow behavior and chemical stability. Elevated temperature flow behavior is available from a variety of sources.[45, 46] A plot of the flow stress as a function of the temperature and strain-rate is shown in Figure 3. Normally, this alloy is wrought at temperatures of 400 to 900°C. The slight difference between the temperatures and strain-rates used to generate the data in the literature and that required by the current study will be addressed in later chapters.

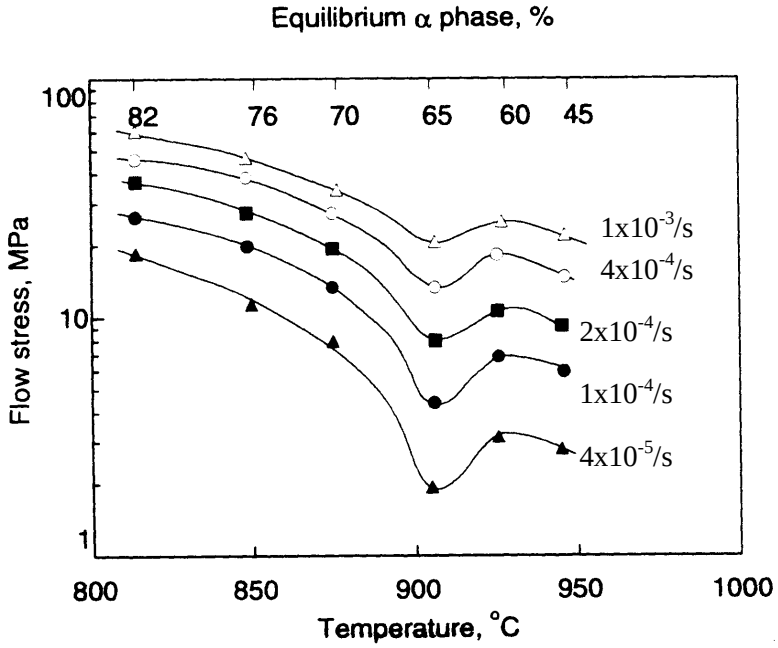

Figure 3: The flow stress as a function of temperature and strain-rate for Ti-6Al-4V.[47]

The stability of titanium aluminide composites in titanium alloys were studied by Pete[48] and Martin.[49] Electron microscopy performed in these studies found that little or no

reaction layer was formed at the Ti-6Al-4V/IMC interface as opposed to significant reaction layer formation found in samples reinforced with commercially-pure (C.P.) titanium. This has lead to speculation that the stability of the alloy/IMC interfaces are due to the presence of the body centered cubic beta phase in the titanium alloy.[50]

2.3. Modelling Deformation-based Processing

One of the reasons for developing of a systematic study of codeformation is to provide a capability to predict composite microstructures which result, in terms of the shape of a dispersed component. This capability will be incorporated into a finite element model of the codeformation process, thereby reducing the need for trial-and-error experiments.

2.3.1. Constitutive Equations

The modelling of deformation processes normally involves the evolution of a constitutive equation determined by systematically varying the process parameters. The process conditions can then be applied to the phenomenologically-derived constitutive equation to predict material behavior. The constitutive equations used in the current research describe the flow stress of a material in terms of the material properties, temperature, strain, and strain-rate. These basic equations are ultimately used to describe the flow stress of a material "element" in a finite element model (FEM).

The first "scientific" approach to studying the effects of strain-rate and temperature on deformation characteristics was performed by Zener and Hollomon in 1943[51]. Their research investigated the deformation of steels in an effort to incorporate the effects of strain-rate and temperature into one parameter. The result was that an isothermal stress-strain relation could be described with only 2 variables: the later-named Zener-Hollomon parameter and the strain. Using these two variables, the stresses at a given strain, plotted as a function of the Zener-Hollomon parameter, will fall onto a common curve. The accuracy of this method lies in the determination of the deformation activation energy, Q, which is often assumed to be a constant material property. The Zener-Hollomon parameter and the constitutive equation developed are:

$$Z = \dot{\varepsilon} \cdot \exp\left[\frac{Q}{RT}\right] \qquad \text{(Equation 1)}$$

$$\sigma = A \cdot Z^m = A \cdot \dot{\varepsilon}^m \cdot \exp\left[\frac{mQ}{RT}\right] \qquad \text{(Equation 2)}$$

where Z is the Zener-Hollomon parameter, $\dot{\varepsilon}$ is the strain-rate, Q is the activation energy required for deformation, R is the ideal gas constant, T is the absolute temperature, m is the strain-rate sensitivity, and A is a proportionality constant. One flaw of the Zener-Hollomon parameter, however, is that the assumption of a material constant Q does not hold true over large ranges of temperature[52] or strain-rate.[53] This necessitates the determination of both the strain-rate sensitivity, m, and an activation energy, Q, for process-specific ranges of temperature and strain-rate. The current study utilizes the flow stress equation (Equation 2) to predict flow stresses. The constitutive equations developed have been used to develop flow stress maps. These maps have been used as an aid in the determination of extrusion parameters, specifically metal/IMC composition, temperature and ram speed.

2.3.2. Finite Element Modelling

The development of flow stress maps are later incorporated into a finite element model (FEM) of the codeformation process. Finite element analysis (FEA) or finite element modelling (FEM) is used in many fields of engineering. As its name implies, finite element analysis breaks a problem into a matrix of interdependent equations which, when solved simultaneously within the boundary conditions, provide an accurate representation of the solution. Although normally used as a tool for stress analysis, finite element models can be developed to aid in the prediction of the results of deformation processes, as well.

The finite element method can be separated into 5 steps.[54] The first is the discretization of the problem. In most software packages this is performed through the “meshing” of the workpiece. In the case of the present study, meshing is the discretization of the geometry of the composite billet into smaller sections, known as elements. Each element consists of “nodes” which represent points of mobility within the mesh. The next step

involves the selection of the constitutive equation, similar to those described above. The third and fourth steps are the assembly of a matrix which interrelates the properties of each point of freedom on an element (i.e., each node) with every other node within the mesh, and the simultaneous solution of those equations. The finite element software normally performs these tasks; solving for the displacement of each node on each element. In most models this also includes solutions for secondary variables, such as temperature, and stress at each node. The fifth step is the interpretation of the results. In the current study, a model has been developed to predict the strains resulting from the codeformation processing of a composite consisting of mechanically dissimilar phases.

The finite element model developed to simulate the extrusion of a metal/IMC billet uses relative flow stresses in the metal and IMC components to describe the overall codeformation behavior of the composite. To this end, a description of the assumptions used in the finite element modelling of deformation processes is needed.

Finite element modelling of metal-forming processes has been addressed for many monolithic metals[55, 56, 57]. In the analysis of metal-forming processes, the plastic strains normally are much greater in magnitude than the elastic strains; therefore the idealization of a rigid-plastic or rigid-viscoplastic behavior is acceptable.

Material variables of importance to the deformation processing of a metal are the strain and heat-treatment history, the ductility, and the flow stress of the metal. The strain and heat treatment history of the metal is important when these variables affect the flow behavior of the material, e.g., strain aging and work hardening. These factors also influence the ductility of the metal, which itself becomes a factor if strain-induced fracture is possible. The flow stress describes the overall manner in which a material will deform under specific conditions (i.e., temperature, strain and strain-rate.) In many cases, the flow stress of the material becomes the most important factor in the analysis.

The flow stress of a material is dependent upon dislocation motion, and on longer time scales, atomic diffusion.[58] These processes, in turn, are dependent upon the chemical compositon of the material, its microstructure, the density of previously accumulated dislocations, and the process variables of temperature and deformation rate. At elevated

temperatures, dislocation annihilation and atomic diffusion are rapid and therefore, the effect of accumulated strain is negligible and can be ignored in the analysis.

Of paramount importance in the analysis of a deformation process is the accumulation of deformation, or strain. Finite element analysis is performed by assuming that the strain-rates are the values at the center of an element; the velocities of the nodal points of the element are known, as are the coordinates of the element centers and the nodes. A point at which the effective strain is zero is selected at the boundary entrance to the deformation zone. By interpolation from surrounding nodal points, the components of the velocity and the strain-rate are calculated for this point. The components of the velocity are incrementally added to the coordinates of this point to determine its new position. The effective strain at the new point can then be determined by multiplying the strain-rate by the time increment. This is added to the effective strain of the point and the procedure is repeated, incrementally, until the point exits the deformation zone. After the point exits the deformation zone, its velocity and strain are assumed to remain constant. In this manner, all strain is accumulated in the deformation zone, as defined by the finite element model.[59]

Of particular interest to this study is the model produced by Zahrah and colleagues.[60] The model developed is an axisymmetric finite element model consisting of a combination of four-noded axisymmetric elements, contact elements, and rigid surface. A schematic of the model is shown as Figure 4. The axisymmetric elements, shown in red, represent the workpiece. The blue contact elements account for the interaction of the workpiece and the die, which is represented by the black rigid elements. The model simulates an extrusion process, having an extrusion ratio of 10 to 1. This model was designed such that a certain volume fraction of the elements could be randomly placed within the mesh and defined as “reinforcement” elements, having material properties other than the “matrix” elements.

This series of finite element model simulations will be the framework for finite element models pursued in the current study. The present study will alter the Zahrah model to more accurately simulate the extrusion conditions, specifically die ratio and ram speed,

imposed during experimental extrusion trials. Additionally, flow stress ratios reflecting the those observed for experimental extrusion conditions will be incorporated into the model.

Figure 4: Zahrah's Finite element model used to simulate the extrusion of a multiphase billet.[61]

2.4. Summary

- The literature on deformation-based processes is substantial, and includes descriptions of strain-rate calculations and adiabatic heating which are important in the determination of processing variables, specifically temperature and extrusion ram speed.

- Spitzig, *et.al.*, described four basic requirements for the development of morphological in-situ composites via codeformation. Studies of bimetallic composites augmented two important factors which are studied more intensely in the present study: relative flow stresses and volume percentages of each component.

- Studies performed by Martin and Pete[62,63] on IMC reinforced titanium matrix composites failed to achieve a significant degree of codeformation. This is likely due to the low extrusion temperatures utilized.
- It has been shown that these IMCs have strengths comparable to structural ceramics at room temperature, but are deformable using conventional metalworking techniques above the BDT of the intermetallic matrix.
- Previous studies of the synthesis of the IMC "reinforcement" have shown that titanium aluminide matrix composites can be made with high loadings of titanium diboride reinforcements, and that those reinforcements are stable at temperatures above the BDT.
- The reaction temperature achieved during synthesis has a considerable influence on the flow behavior of the IMC, as it influences both the size and spacing of the ceramic reinforcement within the IMC.
- Zener and Hollomon showed that the flow stress of a material is influenced by the temperature, strain, and strain-rate. The equation proposed will be utilized in modelling the flow behavior of the components of the composite, as a function of the temperature and strain-rate. This will later be influential in the determination of flow stress ratios of the Ti-6Al-4V matrix to the IMC "reinforcement."
- Finite element modeling has shown the ability to qualitatively predict the degree of commensurate deformation in a discontinuously-reinforced composite. Zahrah and colleagues have developed a finite element model simulation of the extrusion of such a composite. This model will be used as the framework in the development of a quantitative predictive tool in the codeformation processing of metal/IMC composites.

2.5. References

[1] S. Kalpakjian, *Manufacturing Engineering and Technology - 3rd edition*, Addison Wesley Longmann, Inc. Menlo Park, CA, 1995.

[2] S. Kalpakjian, *Manufacturing Processes for Engineering Materials - 3rd edition*, Addison Wesley Longmann, Inc. Menlo Park, CA, 1997.

[3] W.F. Hosford & R.M. Caddell, *Metal Forming Mechanics and Metallurgy-2nd edition*, PTR Prentice Hall, Englewood Cliffs, NJ, 1993.

[4] W.A. Spitzig, C.L. Trybus, & J.D. Verhoeven, "Deformation Processed Metal/Metal Composites" in *Metal Matrix Composites: Processing and Interfaces*, ed. R.K. Everett and R.J. Arsenault, Boston : Academic Press, 1991, pp. 151-179.

[5] B. Avitzur, *Handbook of Metal Forming Processes*, Wiley-Interscience, New York, 1983.

[6] J.A. Roberts & P.R. Roberts, U.S. Patent # 3,698,863, *Fibrous Metal Filaments*, October 1972.

[7] R. Martin, *Synthesis and Processing of Intermetallic Matrix Composites as Reinforcements in Metallic Matrices*, Master's Thesis, VA Tech, September 1994., p. 25.

[8] T. Pete, *Deformation Processed IMC-Reinforced Metal Matrix Composites*, Master's Thesis, Virginia Polytechnic Institute and State University, Fall 1994.

[9] S.L. Kampe, *Final Technical Report to ONR contract # N00014-93-1-0539*, 1994.

[10] K. Sharvan Kumar, *ISIJ International* vol. 31, no. 10, pp.1249-59, 1991.

[11] S.L. Kampe, P.Sadler, L. Christodoulou & D.E. Larsen, *Metall. Trans. A*, vol. 25A, pp.2181-97, 1994.

[12] K.S. Kumar and J.D. Whittenberger, *.Mat Sci Tech*, vol. 8, pp.317-30, 1992.

[13] J.M. Kampe, *SBIR Proposal #94-104.08 5082 A*, (1994).

[14] J.C. Beddoes, W. Wallace & M.C. Mahlerbe, *Mater Man Proc.* vol. 7, no. 4, pp.527-59, 1992.

[15] D.M. Dimiduk, D.B. Miracle, Y-W. Kim & M.G. Mendiratta, *ISIJ International*, pp.1223-34, 1991.

[16] C.R. Kachelmyer & A. Varma, *Mat Res Soc Symp Proc*, vol. 350, pp. 33-9, 1994.

[17] D.E. Alman, J.A. Hawk, C.P. Dogan, M. Ziomek-Moroz & A.V. Petty, Jr., *Mat Res Soc Symp Proc*, vol. 350, pp. 25-31, 1994.

[18] M.E. Hyman, C. McCullough, J.J. Valencia, C.G. Levi & R. Mehrabian, *Met Trans A*, vol. 20A, pp. 1847-59, 1989.

[19] F.H. Froes, C. Suryanarayana & D. Eliezer, *ISIJ International*, vol. , pp. 1235-48, 1991.

[20] F.H. Froes, C. Suryanarayana & D. Eliezer, *J Mat Sci*, vol. 27, pp. 5113-40, 1992.

[21] A.B. Pandey, R.S. Mishra & Y.R. Mahajan, *Mat Sci & Eng*, vol A189, pp. 95-104, 1994.

[22] *Binary Alloy Phase Diagrams*, edited by T.B. Massalski, ASM, Metals Park, Ohio, vol. 1, p. 104, 1986.

[23] M.B. Winnicka & R.A. Varin, *Metall. Trans A*, vol 24A, pp. 935-46, 1993.

[24] C.M. Sabinash, S.M.L. Sastry, & K.L. Jerina, *Scripta Met. Mat.*, vol. 32, no. 9, pp. 1381-6, 1995.

[25] M.L. Adams, S.L. Kampe, A.R. Harmon, & L. Christodoulou, unknown, unknown, pp. 439-48, unknown.

[26] K.G. Anand, D. Zhao, J.J. Valencia, & S.J. Wolff, *in Model-based Design of Materials and Processes*, ed. E.S. Russell, D.M. Elzey, & D.G. Backman, TMS, Warrendale, PA, pp. 57-71, 1992.

[27] C.M. Sabinash, S.M.L. Sastry, & K.L. Jerina, *Mat. Sci. Eng. A*, Vol A192/A193, pp. 837-47, 1995.

[28] M. Matsuo, *ISIJ Internat'l*, Vol 31, No 10, pp. 1212-22

[29] C.M. Sabinash, S.M.L. Sastry, & K.L. Jerina, *Scripta Met. Mat.*, vol. 32, no. 9, pp. 1381-6, 1995.

[30] L. Wu, D. Pope & V. Vitek, *Scr Met*, vol. 24, pp.2187-90, 1990.

[31] K.S. Kumar and J.R. Pickens, *Scr Met*, vol. 22, pp. 1015-18, 1988.

[32] S. Zhang, J.P. Nic, W.M. Milligan & D.E. Mikkola, *Scr Met*, vol. 24, pp.1441-6, 1990.

[33] X. Chen, X. Wu, W.L. Fang, S. Chen & G. Hu, *Mat Sci Eng*, vol. A153, pp. 370-6, 1992.

[34] X. Chen, X. Wu, S. Chen & G. Hu, *Scr Met*, vol. 26, pp.1775-8, 1992.

[35] M.L. VanMeter, S.L. Kampe, & L. Christodoulou, *Scripta Mater.*, Vol 34, No 8, pp. 1251-6, 1996.

[36] Data for AD-94, from Coors Ceramic Company Publication Std 990, Golden, CO, 1989.

[37] S.L. Kampe, P.Sadler, L. Christodoulou & D.E. Larsen, *Met. Trans A*, vol. 25A, pp.2181-97, 1994.

[38] *Mechanical Metallurgy*, ed. M.A. Meyers & K.K. Chawla, Prentice-Hall, New Jersey, p. 409, 1984.

[39] J.W. Martin, *Micromechanisms in Particle-Hardened Alloys*, Cambridge University Press, Cambridge, UK, p. 63, 1980.

[40] R. Martin, *Synthesis and Processing of Intermetallic Matrix Composites as Reinforcements in Metallic Matrices*, Master's Thesis, VA Tech, September 1994., p. 105-10.

[41] O.P. Poola, C. Cordier, P. Pirouz, and A.H. Heuer: *in Interfaces in Metal-Ceramic Matrix Composites*, TMS, Warrendale, PA 1990, pp. 465-473.

[42] M. Saqib, I. Weiss, G.M. Mehrotra, E. Clevenger, A.G. Jackson, & H.A. Lipsitt, *Metall. Trnas. A*, Vol 22A, No 8, pp. 1721-8, 1991.

[43] *Structure and Properties of Engineering Alloys*, p. 41.

[44] *Atlas of Formability: Ti-6Al-4V ELI*, National Center for Excellence in Metalworking Technology, Johnstown, PA, 1993.

[45] *Atlas of Formability: Ti-6Al-4V ELI*, National Center for Excellence in Metalworking Technology, Johnstown, PA, 1993.

[46] *Titanium Alloys: Material Properties Handbook*, ed. R. Boyer, G. Welsch, & E.W. Collings, pp. 592-4, 1994.

[47] C.H. Hamilton, *Superplastic Forming*, ASM International, Warrendale, PA, pp. 13-22, 1985.

[48] T. Pete, *Deformation Processed IMC-Reinforced Metal Matrix Composites*, Master's Thesis, Virginia Polytechnic Institute and State University, Fall 1994.

[49] R. Martin, *Synthesis and Processing of Intermetallic Matrix Composites as Reinforcements in Metallic Matrices*, Master's Thesis, VA Tech, September 1994., p. 111.

[50] S.L. Kampe, private communication, December 1998.

[51] C. Zener & J.H. Hollomon, *Effect of Strain Rate Upon Plastic Flow of Steel*, J. Appl. Physics, vol. 15, no. 1, pp. 22-32, 1944.

[52] W.F. Hosford & R.M. Caddell, *Metal Forming Mechanics and Metallurgy-2nd edition*, PTR Prentice Hall, Englewood Cliffs, NJ, 1993.

[53] G.T. Kridli, A.S. El-Grizawy, & R.Lederich, *Mat. Sci. Eng. A*, Vol. A244, pp. 224-32, 1998.

[54] Class notes: Materials Modelling - FEM by Peter D. Lee, Imperial College of Science, Technology and Medicine, 1997.

[55] *Numerical Modelling of Material Deformation Processes*, eds. P. Hartley, I. Pillinger, and C. Sturgess, Springer-Verlag Publishing, Berlin, Germany, 1992.

[56] S. Kobayashi, S-I., Oh, & T. Altan, *Metal Forming and the Finite ELement Method*, Oxford University Press, New York, 1989.

[57] C.R. Boër, N. Rebelo, H. Rydstad, G. Schröder, *Process Modelling of Metal-Forming and Thermomechanical Treatment*, Springer-Verlag Publishing, Berlin Germany, 1985.

[58] M.F. Ashby, *Phil. Mag.*, vol. 21, no., 2, pp. 399-424, 1970.

[59] S. Kobayashi, S-I., Oh, & T. Altan, *Metal Forming and the Finite ELement Method*, Oxford University Press, New York, p. 175, 1989.

[60] T. Zahrah, *Development of Intelligent Processing Methodology for Intermetallic Matrix Composites*, Progress Report N00014-96-C-0427, ONR, MATSYS, Inc., 1998.

[61] ibid, p.18.

[62] R. Martin, *Synthesis and Processing of Intermetallic Matrix Composites as Reinforcements in Metallic Matrices*, Master's Thesis, VA Tech, September 1994.

[63] T. Pete, *Deformation Processed IMC-Reinforced Metal Matrix Composites*, Master's Thesis, Virginia Polytechnic Institute and State University, Fall 1994.

3. Reaction Synthesis

Variations in the composition of the intermetallic matrix composites (IMCs) used as the "reinforcement" in the metal/IMC composites represent an important independent variable in the present study of codeformation behavior. Synthesis of the IMCs has been effected as a part of this study through the use of a variant of the XD process, a reaction-synthesis-based technique in which ceramic particulate is chemically synthesized in situ within an intermetallic matrix. This chapter serves to familiarize the reader with this processing technique as it pertains to the microstructural features which evolve and the influence these features have on the systematic variation of the IMC's deformation behavior.

3.1. Introduction

Reaction synthesis refers to a processing technique in which the exothermic thermodynamic heats of formation provide the activation energy for the formation of certain compounds. The process is a derivative of the broad technology known as self-propagating high temperature synthesis (SHS), and shares a common mechanistic base with numerous other processes which seek to exploit the exothermicity of a participating chemical reaction to provide kinetic advantage. Notable examples of the latter include pressureless and pressure-assisted reactive sintering, reactive hot isostatic pressing, combustion milling, and reactive casting.[61]

A particularly useful variation of the principles of reactive processing has been its application for the synthesis of in situ-derived metal or intermetallic matrix composites.[62] In this regard, the evolution of a ceramic particulate reinforcement occurs directly within a metallic solvent, the latter eventually representing the metallic or intermetallic component of the discontinuously reinforced composite. The technique differs from conventional SHS-based methodologies in that the metallic matrix often serves as a non-stoichiometric liquidous solvent (e.g., a diluent) which serves to facilitate the particulate-forming exothermic (i.e., thermodynamically favored) reaction. Used in this way, the technique offers several practical and theoretical advantages that influence both

processability and ultimate performance of the composite, largely as a consequence of the clean and thermodynamically-stable matrix/reinforcement interfaces that necessarily evolve during the process.[63]

While clean interfaces and thermodynamic stability are most frequently cited as support for in-situ processing strategies, ultimate performance will also rely heavily on the details of the size, shape, and microstructural stability of the evolved reinforcement. For example, strengthening potency of discontinuously-reinforced composites tend to scale inversely with interparticle spacing according to traditional Orowan or enhanced matrix work-hardening models.[64, 65] As an independent variable of composite behavior, interparticle spacing incorporates both reinforcement size and volume spacing. Thus, a methodology that can relate processing details to reinforcement size can provide a direct link between processing and performance.

This study examines the influence of solvent temperature on the size of the particulate that is formed in-situ within various intermetallic matrices. In this regard, it is reasonable to assume that the size and shape of the particulate reinforcement that evolves will depend on the temperature at the time of, and/or immediately subsequent to, the nucleation of the particulate within the metallic matrix. In such systems, the temperature that the solvent attains will be determined primarily by the heat derived from the compound-forming reactions that occur during synthesis. Thus, the temperature of the solvent will rely upon not only on the relative exothermicity of the participating reactions, but also on the relative volume fraction of resulting particulate versus the matrix components.

Specifically, composites based upon two titanium aluminide intermetallic compounds, $Ti_{54}Al_{46}$ and Al_3Ti, have been synthesized with relatively high volume percentages (i.e., 30-50 volume percent (v%) dispersed TiB_2. Titanium aluminide intermetallics are of interest because of their relatively low density and high strength, particularly at moderately high (e.g., 600-900°C) temperatures. In this work, the influence of temperature will be assessed through the calculation of the adiabatic temperature of reaction, T_{ad}, a qualitatively-faithful measure of the net heat generated by a particular

composite formulation during reaction synthesis processing. T_{ad} is calculated by considering the changes in enthalpy (ΔH) of the reactants and products as a function of temperature. The calculation of adiabatic temperature rests on the assumption that the heat generated during the reaction is used to raise the temperature of the final product.[66] Thus it is a theoretical maximum temperature the reaction can reach, since it assumes no heat losses to the surroundings.

3.2. Experimental Approach

Composites were produced by blending elemental powders of titanium, aluminum, and boron (Atlantic Equipment Engineers, Micron Metals, Inc.), appropriately formulated to create Al_3Ti and $Ti_{54}Al_{46}$ each with 30, 40, and 50 vol% TiB_2, as specified in Table II. The formulations were cold compacted and reacted in an argon-rich environment using induction heating. The as-reacted synthesized titanium aluminide composite sponge was communitively reduced to powder form and subsequently densified using hot isostatic pressing (HIP) at 1300°C and 205 MPa for two hours.

Table II: Formulations for Al_3Ti- and $Ti_{52}Al_{48}$-based intermetallic matrix composites reinforced with 30, 40, and 50 volume % TiB_2.

	Weight Percentage		
IMC Formulation	***Aluminum***	***Titanium***	***Boron (amorphous)***
Al_3Ti + 30 vol% TiB_2	39.93	48.73	11.33
Al_3Ti + 40 vol% TiB_2	33.21	52.13	14.66
Al_3Ti + 50 vol% TiB_2	26.88	55.33	17.79
$Ti_{54}A_{46}$ + 30 vol% TiB_2	21.54	68.02	10.44
$Ti_{54}A_{46}$ + 40 vol% TiB_2	18.16	68.15	13.69
$Ti_{54}A_{46}$ + 50 vol% TiB_2	14.88	68.29	16.83

Following densification, conventional metallographic procedures were utilized to create planar sections to facilitate direct TiB_2 particle size and interparticle spacing measurements. In the latter regard, the major and minor diameter on the planar section were measured, and reported as a spherical-equivalent diameter. Volume fraction TiB_2 reinforcement was experimentally determined using point counting techniques. This information and the particle size can be used to calculate an edge-to-edge using equation 3:

$$\lambda_{edge-edge} = 1.225 \cdot \bar{r}_{measured} \cdot \sqrt{\frac{2 \cdot \pi}{3 \cdot f_{measured}}} - 1.63 \cdot \bar{r}_{measured} \qquad \text{(Equation 3)}$$

where $\lambda_{edge\text{-}edge}$ is the edge-to-edge spacing, $\bar{r}_{measured}$ is the measured, average TiB_2 particle radius, and $f_{measured}$ is the measured volume fraction of TiB_2 particulate.

For each composite formulation, an adiabatic temperature has been calculated by equating the enthalpy changes that occur upon heating of the elemental reactants to those which occur upon the subsequent cooling of the products. The calculations require a knowledge of the heat capacity as a function of temperature for each reactant and product, as well as the enthalpy for any phase transitions which occur within the active temperature range.

Several assumptions were required to complete the necessary matrix of thermodynamic data for the adiabatic temperature calculations. The enthalpy of the titanium aluminide compounds in liquid form has be estimated using the approximation:[67]

$$\Delta H = C_p \cdot \Delta T = 33.74 \cdot N \cdot \Delta T \left(\frac{J}{mol} \right) \qquad \text{(Equation 4)}$$

where N is the number of atoms in a "molecule" of the molten compound (4 and 2 for Al_3Ti and TiAl, respectively). The latent heat of fusion, ΔH_f, was also estimated using known values of the entropy of fusion:

$$\Delta H_f = \Delta S_m \cdot T_m \qquad \text{(Equation 5)}$$

Finally, temperature-dependent heat capacities for the amorphous boron used in this study were extrapolated to temperatures beyond its 2300K melting temperature. The thermodynamic data utilized in the adiabatic temperature calculations have been incorporated into Appendix A.

3.3. Results

3.3.1. Microstructural Analysis

The phase constituency of the composites was verified using x-ray diffraction. Representative x-ray diffraction patterns and the peak designations for the $Ti_{52}Al_{48}$- and Al_3Ti- matrix composites are shown in Figure 5. The $Ti_{54}Al_{46}$-based IMCs exhibit both Ti_3Al and TiAl peaks in addition to the TiB_2 peaks. The Al_3Ti-based IMCs show the Al_3Ti peaks and some evidence of TiAl peaks, indicating a slightly aluminum lean composition.

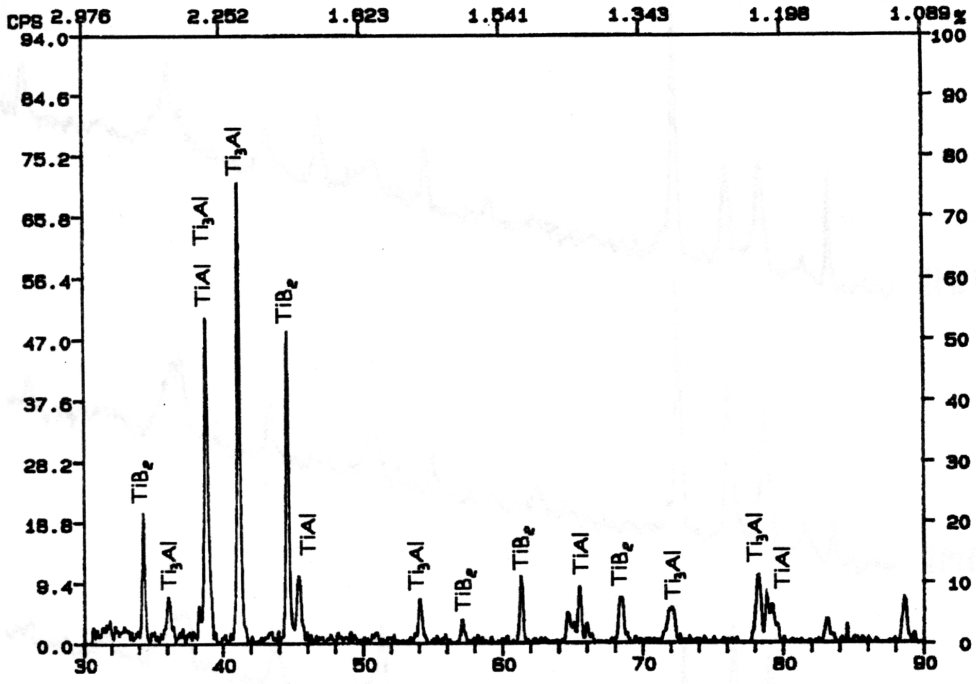

(a)

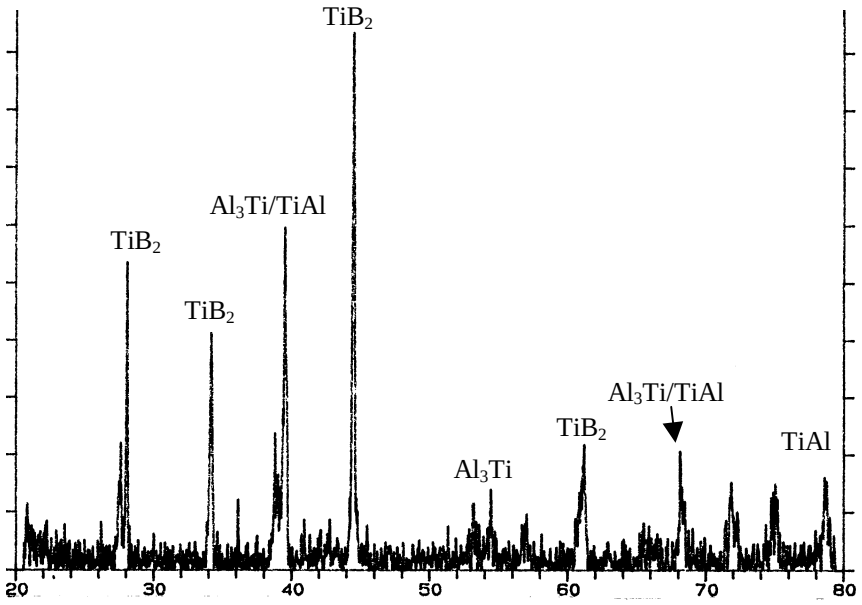

(b)

Figure 5: X-ray diffraction patterns for (a) $Ti_{54}Al_{46}$-[68], and (b) Al_3Ti-matrix composites reinforced with 40 vol% TiB_2.

In every case the presence of TiB_2 is evident throughout the structure as a uniform distribution of faceted prism-shaped crystals. Figure 6 shows a representative micrograph illustrating the presence of both the faceted TiB_2 crystals and the laminar structure of the $Ti_{54}Al_{46}$ matrix, resulting from the α_2 (Ti_3Al) and γ (TiAl) phases present at this composition. The micrograph shown was taken from the inside of an exposed pore wall in the as-synthesized $Ti_{54}Al_{46}$ matrix reinforced with 50 volume % TiB_2.

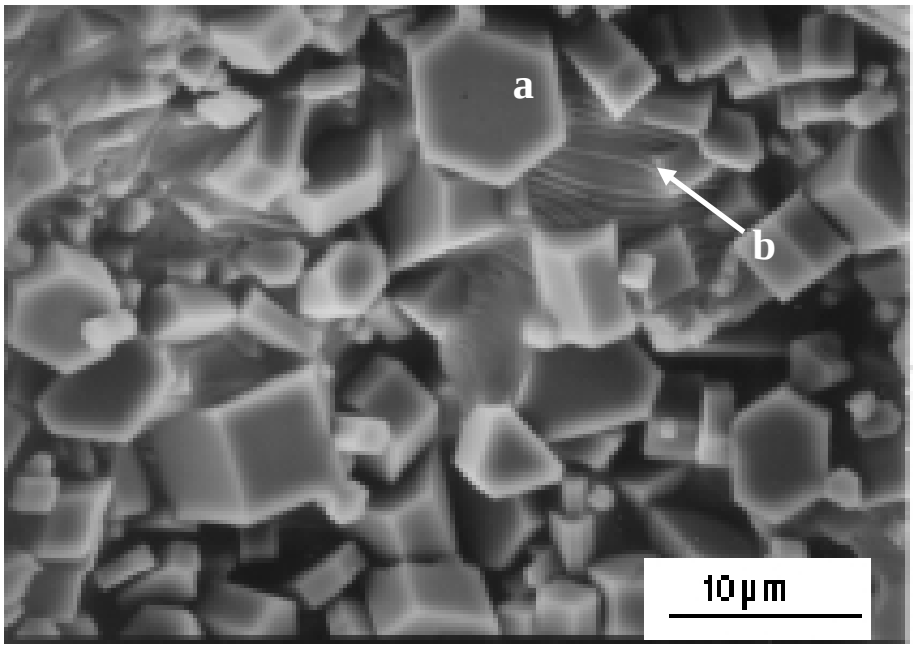

Figure 6: As-synthesized near-γ TiAl reinforced with 50 volume % TiB_2. This scanning electron micrograph was taken from the inside of a pore wall. Both the (a) faceted TiB_2 crystals are visible as well as the (b) laminar structure of the near-γ TiAl matrix.

Figure 7 illustrates an example of the as-reacted and densified composite microstructures which have been produced; in this instance, for the Al_3Ti + 40 vol% TiB_2 and $Ti_{54}Al_{46}$ + 40 vol% TiB_2 composites. The average measured sphere-equivalent TiB_2 diameters and the volume fraction of TiB_2 particulate, and the as-calculated edge-to-edge interparticle spacing are summarized in Table III for each of the variants examined. As shown, there tends to be a general increase in TiB_2 size as its volume percentage in the formulation increases. Interparticle spacing, which simultaneously incorporates both size and volume percentage effects within the microstructure, is shown to generally decrease as the formulated TiB_2 volume percent increases.

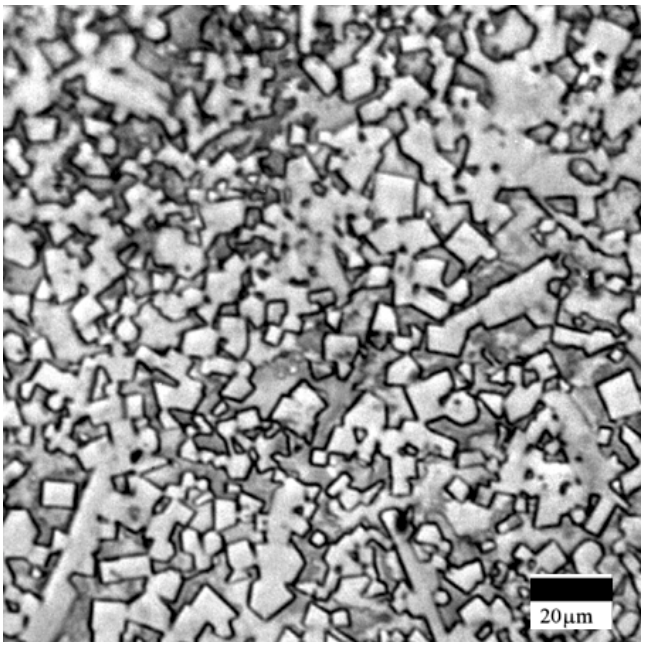

(a)

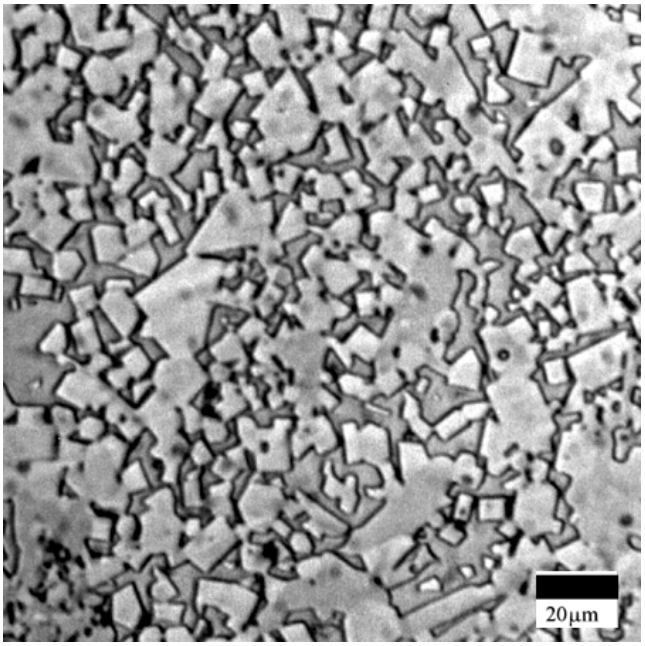

(b)

Figure 7: Representative micrographs of the densified titanium aluminide matrix composites produced by exothermic dispersion synthesis processing: a) Al_3Ti + 40 vol% TiB_2 and b) $Ti_{54}Al_{46}$ + 40 vol% TiB_2.

Table III: Experimentally-measured values of sphere-equivalent diameter and interparticle spacing for the two composite matrices.

IMC Composition	*Particle Diameter** *(μm)*	*Volume fraction of TiB_2 particles†*	*Interparticle Spacing‡ (μm)*
Al_3Ti + 30 vol% TiB_2	1.8 ± 0.2	0.32 ± 0.03	1.4 ± 0.5
Al_3Ti + 40 vol% TiB_2	2.9 ± 0.3	0.42 ± 0.04	1.7 ± 0.4
Al_3Ti + 50 vol% TiB_2	2.6 ± 0.2	0.51 ± 0.03	1.1 ± 0.2
$Ti_{54}Al_{46}$ + 30 vol% TiB_2	1.6 ± 0.2	0.3	1.0 ± 0.1
$Ti_{54}Al_{46}$ + 40 vol% TiB_2	2.4 ± 0.3	0.4	1.0 ± 0.1
$Ti_{54}Al_{46}$ + 50 vol% TiB_2	2.6 ± 0.4	0.5	0.5 ± 0.1

* As-measured equivalent spherical diameter

† As-measured using point counting techniques for Al_3Ti-based IMCs, nominal for $Ti_{54}Al_{46}$-based IMCs.

‡ As calculated using Equation 4:

$$\lambda_{edge-edge} = 1.225 \cdot \bar{r}_{measured} \cdot \sqrt{\frac{2 \cdot \pi}{3 \cdot f_{measured}}} - 1.63 \cdot \bar{r}_{measured}$$

3.3.2. Adiabatic Temperature Calculations

Figure 8 illustrates, in graphical form, the basis for the adiabatic temperature calculation, for the specific cases of Al_3Ti + 40 vol % TiB_2 and $Ti_{54}Al_{46}$ + 40 vol% TiB_2. These "enthalpy loops" include and show components due to the heat capacities of the reactants (elemental titanium, aluminum. and amorphous boron), the enthalpies associated with any phase transitions that the reactants experience upon heating, and the heat capacities and enthalpies-of-solidification for the products (Al_3Ti, TiAl, and TiB_2). The calculations lead to values for both an adiabatic temperature and for the net enthalpy of the reaction.

Figure 9 shows the calculated adiabatic temperature as a function of formulated volume percent of TiB_2 within the Al_3Ti and $Ti_{54}Al_{46}$ matrices. As shown in Figure 9a, the adiabatic temperature is predicted to increase rapidly between TiB_2 percentages of approximately 10 and 50 volume %.

Figure 9b illustrates adiabatic temperature predictions for the $Ti_{54}Al_{46}$ matrix composites. These data predict that the adiabatic temperature is strongly dependent on formulation for TiB_2 volume percentages between 20 and 70 vol%.

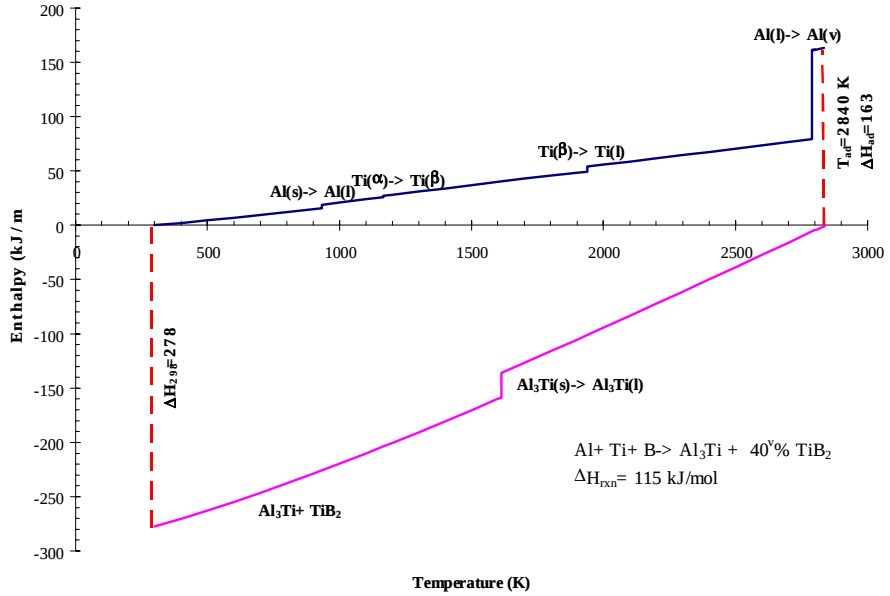

(a)

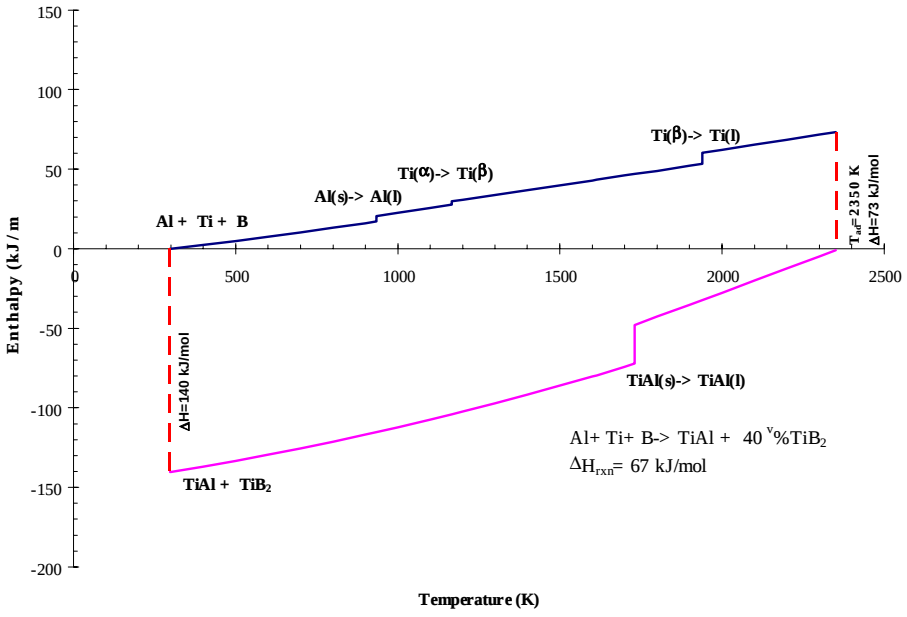

(b)

Figure 8: An "enthalpy loop" which illustrates the basis for the adiabatic temperature calculation; in these instances, for a.) Al_3Ti + 40 vol% TiB_2 and b) $Ti_{54}Al_{46}$ + 40 vol% TiB_2 composite calculations. The adiabatic temperature is that temperature which equates the total enthalpy of the products (e.g., on heating) to that of the reactants (e.g., on cooling).

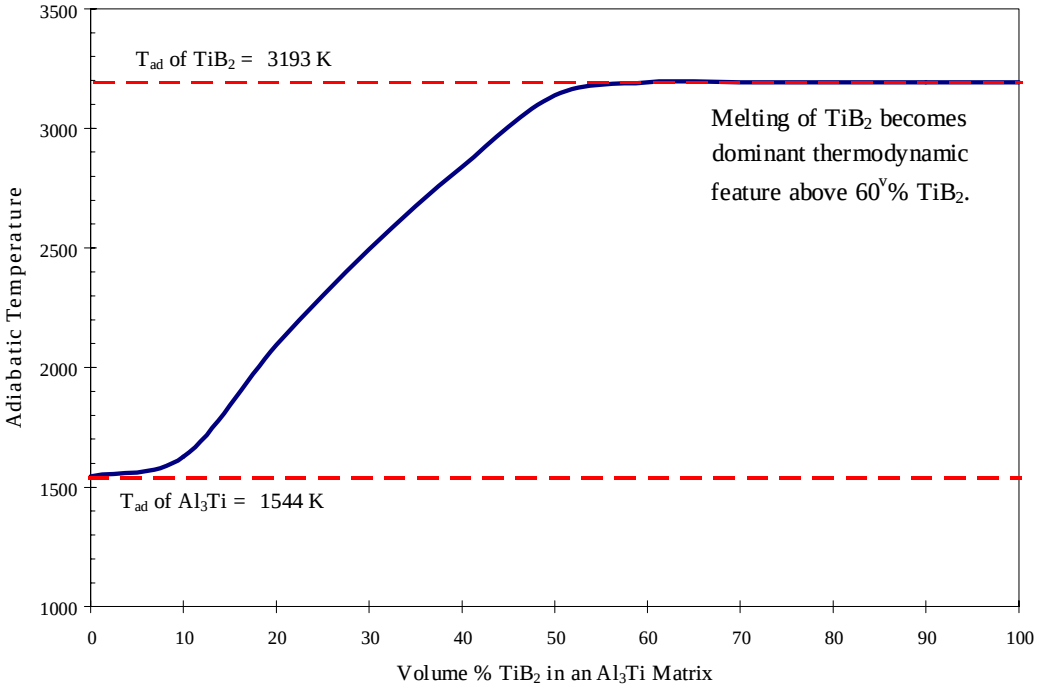

(a)

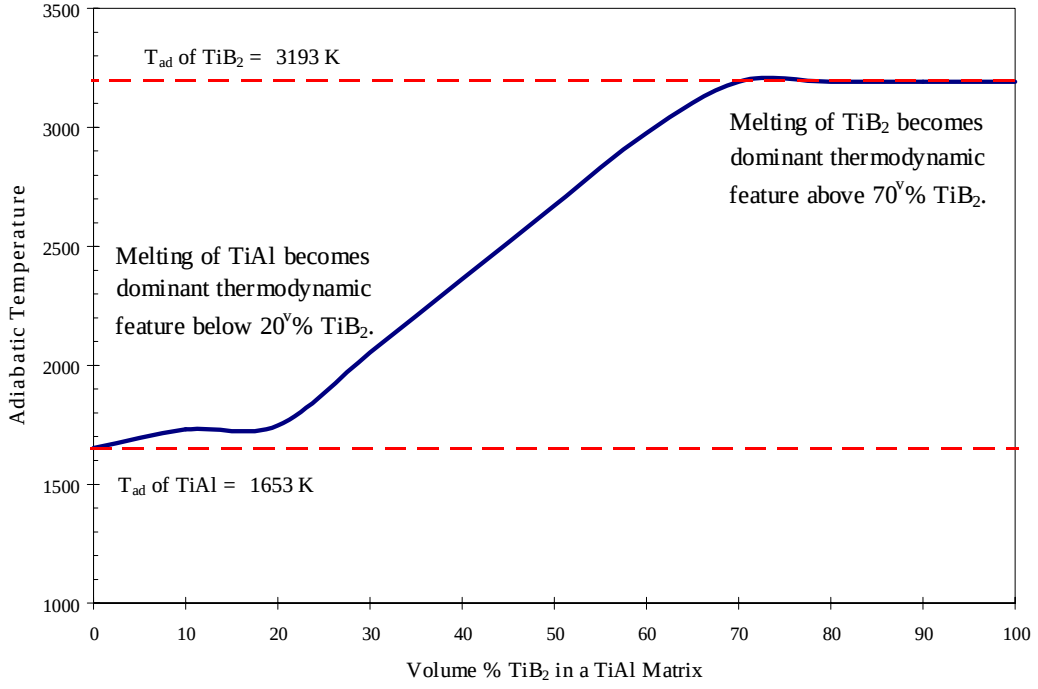

(b)

Figure 9: The calculated adiabatic temperature as a function of nominal TiB_2 volume percentage in a.) Al_3Ti and b.) $Ti_{54}Al_{46}$ matrices.

Figure 10 and Figure 11 show the experimentally-determined values of resulting particle size and edge-to-edge spacing as a function of the adiabatic temperatures calculated for

the corresponding composite variants. As shown, a reasonably strong correlation between both as-synthesized particle size and interparticle spacing with adiabatic temperature is noted.

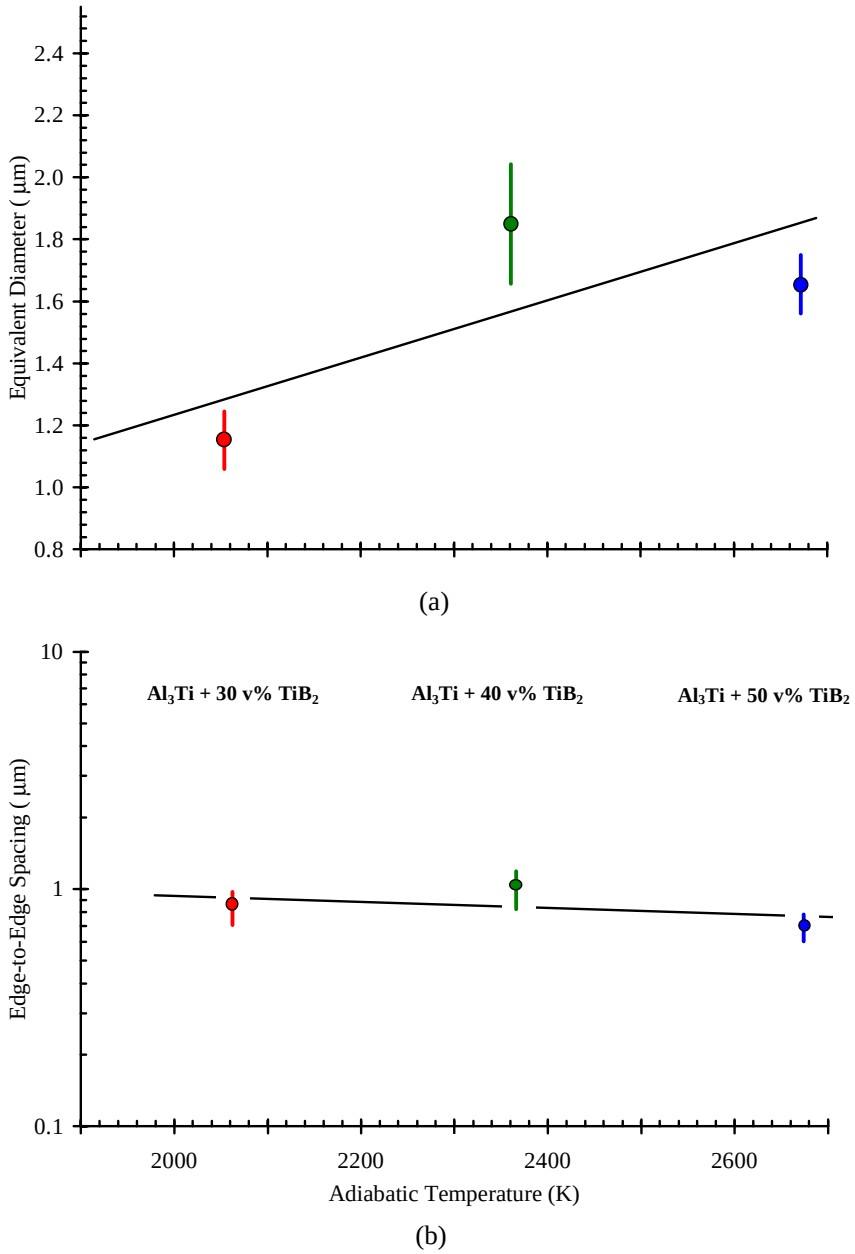

Figure 10: The measured TiB_2 size (a) and edge-to-edge interparticle spacing (b) as a function of calculated adiabatic temperature for the Al_3Ti-matrix composites.

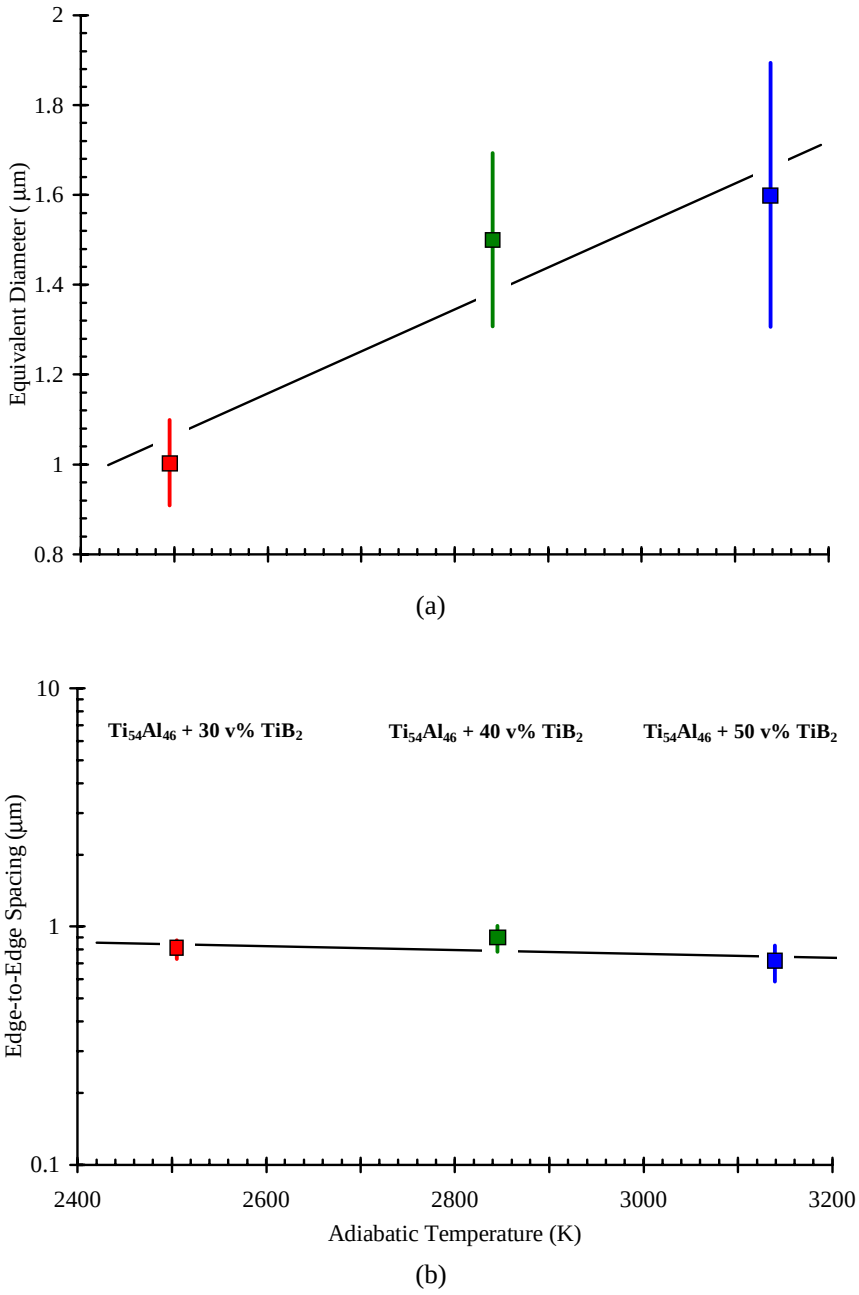

Figure 11: The measured TiB_2 size (a) and edge-to-edge interparticle spacing (b) as a function of calculated adiabatic temperature for the $Ti_{54}Al_{46}$-matrix composites.

3.4. Discussion

3.4.1. Synthesis Mechanism for the Metal and Intermetallic Matrix Composites

The proposed mechanism by which the reactive synthesis processing of in-situ metal and intermetallic matrix composites occurs is illustrated sequentially as Equation 6, for the

specific example of a TiB_2-reinforced TiAl (equiatomic, for simplicity of illustration) composite. As shown in Equation 6a, elemental powders are blended and external heat is supplied. Incipient dissolution of the titanium and boron occurs as the aluminum begins to melt (Equation 6b). The molten aluminum acts as an effective transport medium for the reaction between Ti and B in the formation of TiB_2 (Equation 6c). Accompanying the TiB_2 formation is an increment of enthalpy release that serves to increase the temperature of the compact further, thus acting to bring reaction 6c to completion. A secondary (i.e., less thermodynamically-favored relative to the formation of TiB_2) reaction between the remaining aluminum and titanium to form the titanium aluminide matrix brings the system to its lowest thermodynamic energy state. Due to the exothermicity of the reaction, the temperature may be sufficient to cause melting of the TiAl matrix (6d), as well as, in some instances, melting of the TiB_2. The matrix solidifies upon cooling (6e), completing the creation of the in-situ composite, in this case TiAl + TiB_2.

$$x \cdot Al_s + (x-y) \cdot Ti_s + \frac{y}{2} \cdot B_s + heat \rightarrow \qquad \text{Equation 6a}$$

$$x \cdot Al_l + (x-y) \cdot [Ti]_{Al} + \frac{y}{2} \cdot [B]_{Al} \rightarrow \qquad 6b$$

$$x \cdot Al_l + x \cdot [Ti]_{Al} + y \cdot TiB_2 + y \cdot \Delta H_{TiB_2} \rightarrow \qquad 6c$$

$$x \cdot TiAl_l + y \cdot TiB_2 + y \cdot \Delta H_{TiAl} \rightarrow \qquad 6d$$

$$x \cdot TiAl_l + y \cdot TiB_2 \qquad 6e$$

As noted in the sequence illustrated in Equation 6, TiB_2 formation begins within a molten form of the aluminum. Given this mechanism, it is realistic to assume that the temperature at the time of, and subsequent to, nucleation of TiB_2 particulate will have a strong influence on TiB_2 particle size and interparticle spacing. It is noted that the temperature increase due to the exothermicity of TiB_2 and TiAl formation occurs very quickly. Based on visual observations, this occurs over the course of only a few seconds.

3.4.2. Adiabatic Temperature as a Processing Variable

The adiabatic temperature represents a processing variable initially introduced by Merzhanov as a means to gauge the relative vigor and/or exothermicity of an SHS reaction.[1] Specifically, Merzhanov used the adiabatic temperature calculation to establish a criterion to predict whether a certain reaction will create sufficiently thermally-derived energy to sustain it to completion. The adiabatic temperature has also been used as a means to categorize SHS reactions on the basis of the respective state-of-matter (i.e., solid, liquid, or gas) for the participating components during synthesis. In the present study, the adiabatic temperature is used as an estimate of the maximum temperature that the formulated compact experiences during the synthesis reaction. Subrahmanyam and Vijaykumar[1] report in their review of SHS, that experimentally-measured temperatures are generally essentially equal-to or only slightly less than the calculated values. Despite the fact that the adiabatic temperature calculation provides a theoretical maximum, the strong agreement between experimental and calculated values is likely a consequence of the relatively instantaneous and rigorous release of heat associated with these reactions. Thus, the calculated values likely represent a reasonably accurate prediction of the temperatures experienced by the formulated compacts, albeit for a relatively limited increment of time.

The adiabatic temperature calculations shown in Figure 9 indicate that within a range of composite formulations experimentally produced in this study, i.e., 30-50 vol %, adiabatic temperature is a strong function of formulation. Above approximately 50 vol% TiB_2, however, temperatures are generated which are sufficient to initiate melting of the TiB_2; thus temperature becomes essentially invariant at all percentages in excess of this amount as heat supplied to sustain the “thermal arrest” associated with melting. Likewise at percentages less than approximately 10 vol%, adiabatic temperature is similarly invariant as melting of the Al_3Ti is occurring through this range. Similar effects over differing ranges of TiB_2 percent are noted on Figure 9 for the $Ti_{54}Al_{46}$, where a strong dependency of T_{ad} occurs for compositions containing 20-70 vol% TiB_2.

3.4.3. Correlation of Microstructure to Adiabatic Temperature

Figure 10 and Figure 11 illustrate that the size of the resulting particulate composite can be a strong function of its formulation by way of the temperature that is attained during synthesis. While a strong correlation is especially noted for the $Ti_{54}Al_{46}$-based composite (Figure 11), the Al_3Ti variants show a reduced dependency of size on temperature, mainly as a consequence of the measured size data at the 50 Vol% TiB_2 formulation. The reduced dependency may indicate that this particular Al_3Ti composite experiences some degree of TiB_2 melting during synthesis. This is illustrated in Figure 12, which shows equilibrium phase transition temperatures for both reactants and products for the titanium aluminide matrix composites, with the calculated adiabatic temperature for each experimental formulation indicated. The figure shows that the temperatures generated by synthesis of an Al_3Ti + 50 vol% TiB_2 formulation approaches 3193 K, the melting temperature of TiB_2. In this instance, melting and the subsequent post-synthesis solidification may lead to a reduced TiB_2 particle size, consistent with results previously reported for rapidly-solidified TiB_2-containing titanium aluminides.[69] However, no evidence of this is apparent in the examined microstructures. Likewise, Figure 12 suggests that TiB_2 melting will likely not occur for the $Ti_{54}Al_{46}$-composites within the range of formulations examined in this study. These data suggest that correlation of reinforcement size to adiabatic temperature will only occur within specific formulation ranges where reactant and product phase states are approximately common. In a separate study, the reinforcement particle size in IMCs of NiAl reinforced by TiB_2 was examined.[70] Adiabatc temperature calculations revealed a very narrow range of volume percentage reinforcement (80 to 100 v%) in which variation in adiabatic temperature is observed. In this system, the melting of NiAl, at 1911 K, dominates the adiabatic temperature up until 80 % TiB_2 reinforcement. The samples examined were reinforced with 10, 20, and 40 v% TiB_2, thus all had the same adiabatic temperature, 1911 K. No statistically significant variation in TiB_2 particle size was observed in these samples. In further support of the correlation of adiabatic temperature to particle size, Figure 13 shows TiC size data from a study of aluminum matrix composites by Aiken[71], showing a strong correlation to adiabatic temperature.

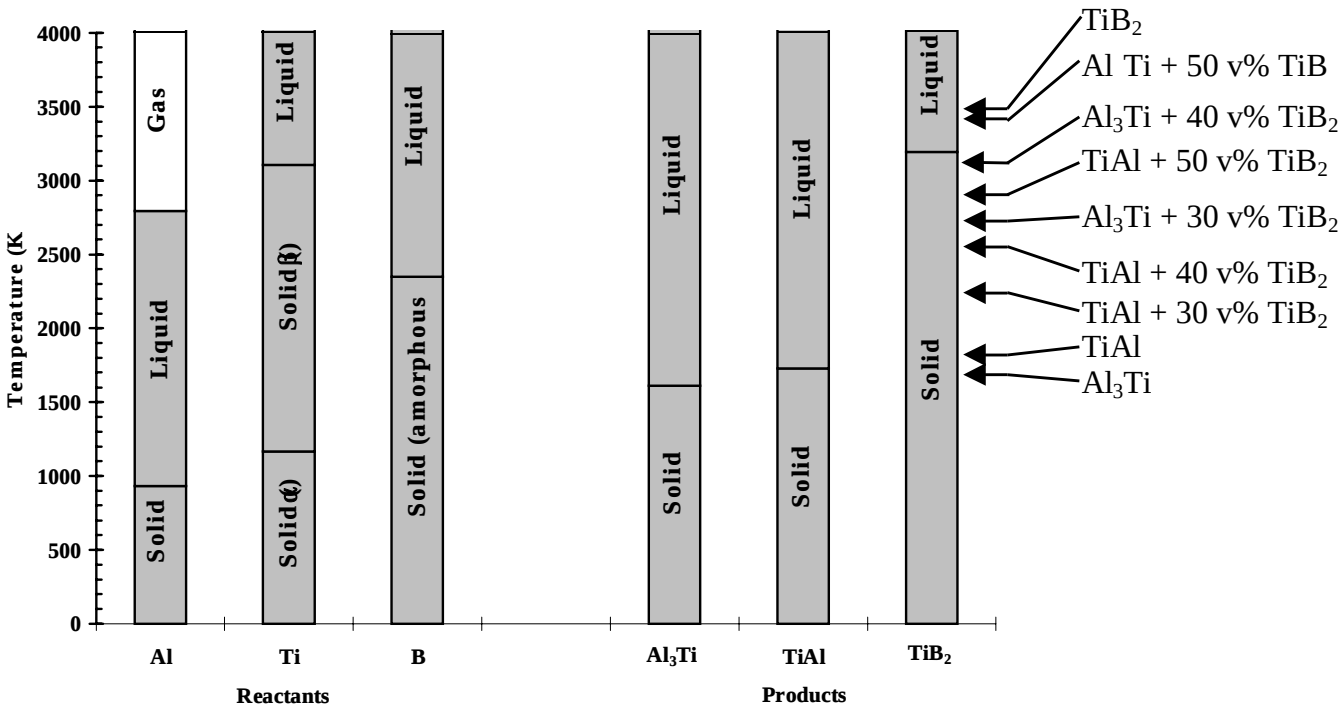

Figure 12: Phase transitions that occur within the reactants (Al, Ti, B) and products (Al_3Ti, TiAl, TiB_2) for reaction-synthesized titanium aluminide composites. Indicated on the right are the predicted values of the adiabatic temperature attained for each formulation examined in the present study.

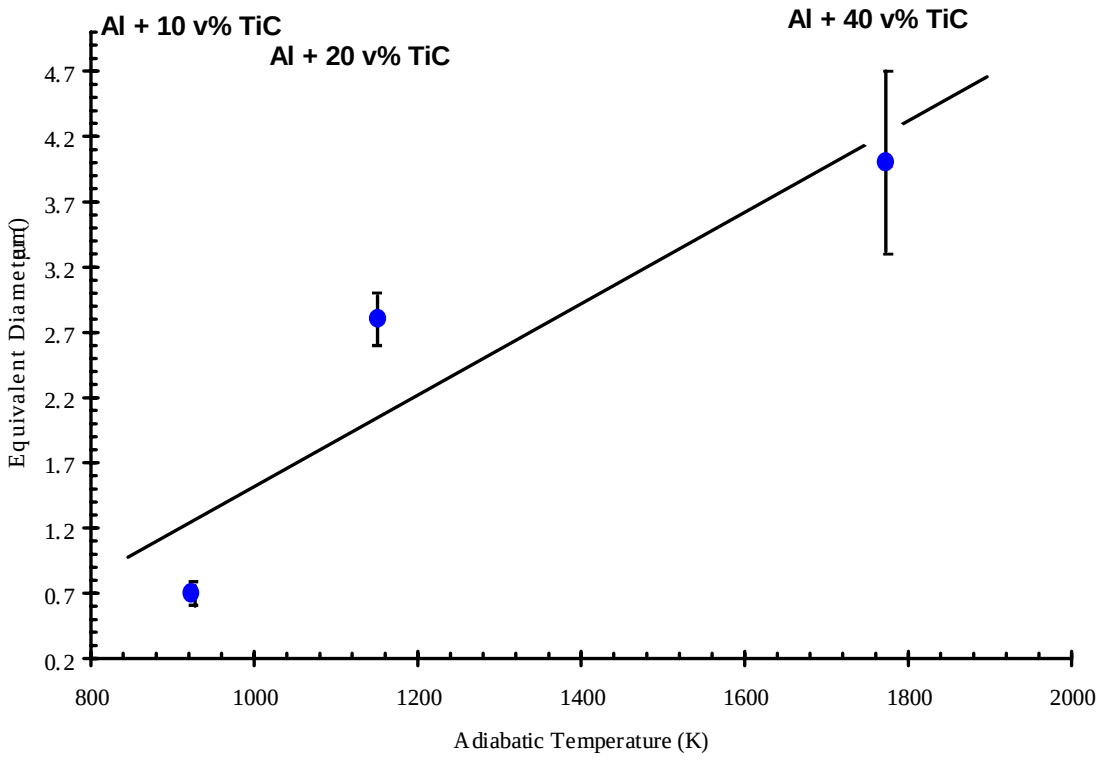

Figure 13: The measured TiC size as a function of calculated adiabatic temperature for the Al + TiC composites. The size data is from a separate study by Aiken.[8]

Perhaps the most important and useful information provided by the data of this study is the interparticle spacing data provided in Table III. Interparticle spacing can provide a direct link to performance, notably flow strength information.[4] Previous work has shown that in-situ-derived TiB_2 reinforcement is both thermodynamically and microstructurally-stable within the aluminide matrices.[4, 72] That is, over a broad range of subsequent primary and secondary processing methodologies (e.g., casting, powder-based consolidation, thermomechanical densification) as well as heat-treating strategies, TiB_2 size and spacing remains essentially constant. Thus, given appropriate empirical calibration, properties can be directly predicted for certain processing methodologies.

3.5. Summary

- The size of in-situ-derived TiB_2 reinforcement in Al_3Ti- and $Ti_{54}Al_{46}$-titanium aluminide composites produced by reaction synthesis tend to increase as its nominal volume percentage in the composite increases.

- The increase in TiB_2 size with increasing nominal volume percentage is a consequence of the higher temperatures associated with these formulations during the reaction synthesis process. The influence of temperature is evaluated through calculation of the adiabatic temperature of reaction for the titanium aluminide composites.
- The analysis indicates that the process-inherent temperature effects will occur only over certain ranges of TiB_2 formulation, that is, in ranges of reinforcement percentage where adiabatic temperature exhibits a strong dependency on composite composition.

3.6. References

[61] J. Subrahmanyam and M. Vijakumar: *J. Mater.Sci.*, Vol. 27, pp. 6249-6273, 1992.

[62] A.R.C. Westwood: *Mater. Trans. A*, Vol 19A, pp. 749-758, 1988.

[63] O.P. Poola, C. Cordier, P. Pirouz, and A.H. Heuer: *in Interfaces in Metal-Ceramic Matrix Composites*, TMS, Warrendale, PA, pp. 465-473, 1990.

[64] *Mechanical Metallurgy*, M.A. Meyers and K.K. Chawla, Prentice-Hall, New Jersey, p. 409, 1984.

[65] S.L. Kampe, P.Sadler, D.E. Larsen, and L. Christodoulou: *Metall. Mater. Trans.*, Vol. 25A, pp. 2184-2197, 1994.

[66] W.L. Frankhouser, K.W. Brendley, and M.C. Kieszek, *Gasless Combustion Synthesis of Refractory Compounds*, Noyes Publications, Park Ridge, NJ, p. 52, 1985.

[67] *JANAF Thermochemical Tables*, Second Edition, NBS, Washington, D.C., p. 10, 1971.

[68] R. Martin, *Synthesis and Processing of Intermetallic Matrix Composites as Reinforcements in Metallic Matrices*, Master's Thesis, Virginia Tech, pp. 105-10, 1994.

[69] M.L. Adams, S.L. Kampe, and L. Christodoulou: *Int. J. Powder Metall.*, Vol 26/2, pp. 105-114, 1990.

[70] J. Haeberle, senior project, Virginia Tech MSE Department, 1998.

[71] R.M. Aiken, private communication, 1998.

[72] S.L. Kampe, J.D. Bryant, and L. Christodoulou: *Metall. Trans.*, Vol 22A, pp. 447-454, 1991.

4. Characterization of Component Flow Behavior

4.1. Introduction

Flow behavior describes the plastic deformation a material undergoes given specific processing conditions. In a more generic sense, this is referred to as the yield criteria for the material. The yield criteria defines the stress condition whereby dislocation and, under certain conditions, diffusion mechanisms can permanently rearrange the structure of the material. This yield criterion is normally directionally specific (anisotropic) because of the directional nature of most crystalline structures. However, the polycrystallinity common in most structural metallic components, permits these materials to be considered non-directional, i.e., isotropic. In metal-forming processes, the range of plastic stresses beyond the yield criteria is called the flow stress.

The relative flow of the composite phases are of considerable importance in the prediction of codeformation behavior. Hence, the independent characterization of the flow stresses of these components, under relevant temperature and strain conditions, is necessary. This chapter examines the flow behavior of the IMCs, under relevant processing conditions, in terms of their composition and constituency. The flow behavior of Ti-6Al-4V, as described in the available literature, is also described.

In an earlier study[73], it was shown that near-γ titanium aluminide intermetallic matrix composites (IMCs) are capable of exhibiting strengths and stiffnesses (moduli) similar to, or exceeding those of structural ceramics (e.g., Al_2O_3 or SiC), given a suitable volume fraction (e.g., 30–50 volume percent) of dispersed ceramic (TiB_2) reinforcement. However, unlike such ceramics, the titanium aluminide matrix composites should be routinely processable using conventional metal-working techniques if the processing is conducted at temperatures which exceed the brittle to ductile temperature (BDT) of the continuous intermetallic matrix.

This chapter seeks to characterize the flow behavior of a series of titanium aluminide matrix composites (based on the near-γ and Al_3Ti compositons) at ranges of temperature

and strain rate which might be typical of an elevated temperature themomechanical process such as hot extrusion or forging.

4.2. Experimental

The TiB_2-reinforced titanium aluminide matrix composites were produced in situ using reaction synthesis techniques, as described in Chapter 3. The as-reacted composite sponge was communitively reduced into a fine powder (-100 mesh) through jaw crushing and subsequent disc milling. The powders were placed into commercially pure titanium tubes and hot isostatically pressed (HIP'd) for a period of 2 hours at 1300°C and 205 MPa (30.6 ksi), to consolidate the powder. The phase constituency of each variant was confirmed using x-ray diffraction and optical microscopy.

Quantitative microscopy techniques were used to determine the size and interparticle spacing of a random population of the titanium diboride crystals in each IMC composition, as described in Chapter 3.

Compression samples were sectioned from the consolidated tubing so as to have an aspect ratio between 1.5 and 2.0 with respect to the diameter of the consolidated powder cylinder within the tube. Compression tests were performed on a screw-driven Instron® universal test machine with an integrated furnace and fully densified SiC rams. Tests were performed at 1000, 1100 and 1200°C and strain-rates of 10^{-4} and 10^{-3} sec^{-1}. Temperature was maintained to within ± 5°C following a 15 minute soak at the test temperature.

4.3. Results

4.3.1. Mechanical Behavior

Of interest to this study is the peak flow stress reached by the composite at the initiation of plasticity. Figure 14 shows representative true stress versus true strain plots for the $Ti_{54}Al_{46}$ + 40 vol% TiB_2 composite (Figure 14a) and the Al_3Ti + 40 vol% TiB_2 composites tested at 1200°C and 0.0001 sec^{-1}. A list of these peak flow stresses is shown as Table IV.

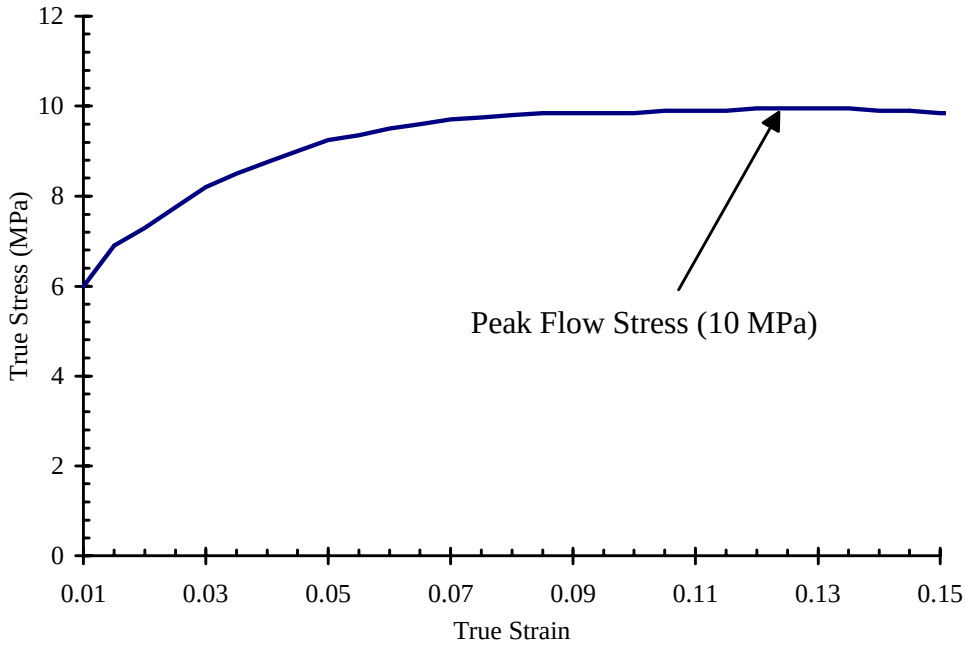

(a)

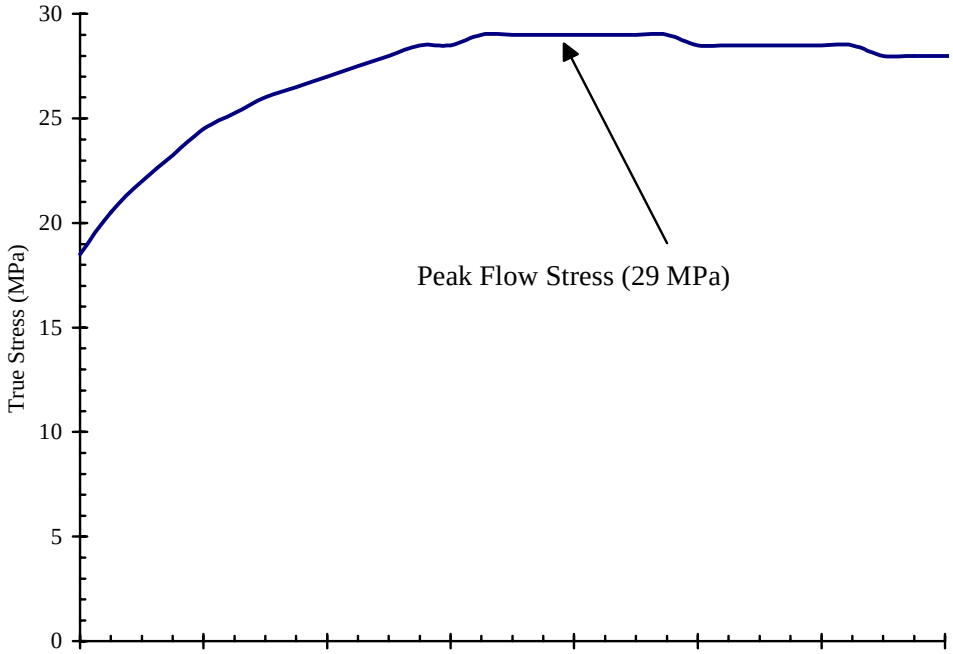

(b)

Figure 14: True stress versus true plastic strain plots for (a) Al_3Ti + 40 vol% TiB_2 and (b) $Ti_{54}Al_{46}$ + 40 vol% TiB_2 both at 1200°C and 0.0001 sec^{-1}. The peak flow stress is indicated in each plot.

Table IV: The true plastic stress peaks for each compression test at the various test conditions.

	True Peak Flow Stress (MPa)					
IMC Designation	*1000°C 0.0001/s*	*1100°C 0.0001/s*	*1200°C 0.0001/s*	*1000°C 0.001/s*	*1100°C 0.001/s*	*1200°C 0.001/s*
Al_3Ti + 30 v% TiB_2	153	67	3	>152	106	
Al_3Ti + 40 v% TiB_2	48	17	10	57	33	15
Al_3Ti + 50 v% TiB_2	116	39	8		76	
TiAl + 30 v% TiB_2	270	103	32		208	
TiAl + 40 v% TiB_2	255	94	30		185	

These stresses were used to develop phenomenologically-based constitutive equations based upon the flow stress equation:[74]

$$\sigma_{flow} = A \cdot \dot{\varepsilon}^{m} \exp\left[\frac{mQ}{RT}\right] \qquad \text{(Equation 7)}$$

Use of this equation requires the determination of the strain-rate sensitivity, m, the activation energy required for deformation, Q, and a structure constant, A. The strain-rate sensitivity and the activation energy may be derived by isolating each part using equations 8 and 9, respectively:

$$m = \left(\frac{\partial \ln \sigma}{\partial \ln \dot{\varepsilon}}\right)_{T} \qquad \text{(Equation } \mathbf{8}\text{)}$$

$$Q = \frac{R}{m}\left(\frac{\partial \ln \sigma}{\partial \frac{1}{T}}\right)_{\dot{\varepsilon}} \qquad \text{(Equation 9)}$$

Where R is the universal gas constant, $\dot{\varepsilon}$ is the strain-rate and T is the absolute temperature. Graphical representations of the strain-rate sensitivity calculation and the activation energy calculation are shown in Figure 15 and Figure 16, respectively. The slopes of the lines shown in Figure 15 represent the strain-rate sensitivity of the material. The slopes of the lines traced in Figure 16 are proportional to the activation energies of the composites. The average strain-rate sensitivity and activation energy for each IMC was used to determine the structure parameter, A, for that IMC. This same methodology was employed in evaluating the available data for Ti-6Al-4V[75]. The values calculated for each of these variables (i.e., m, Q, and A) are shown in Table V.

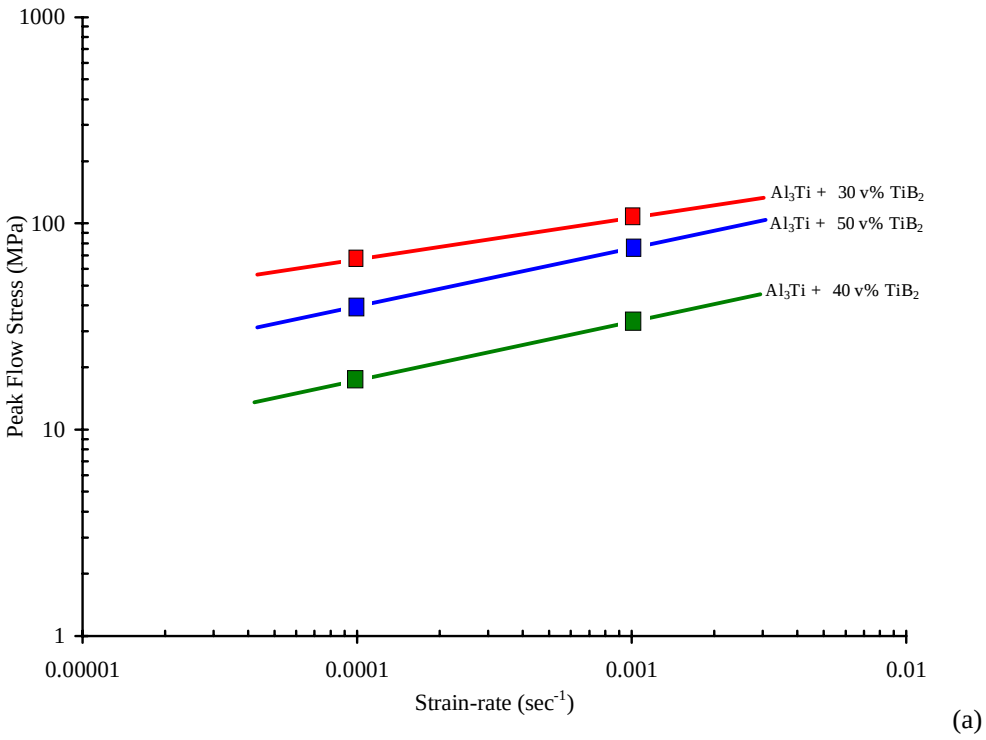

(a)

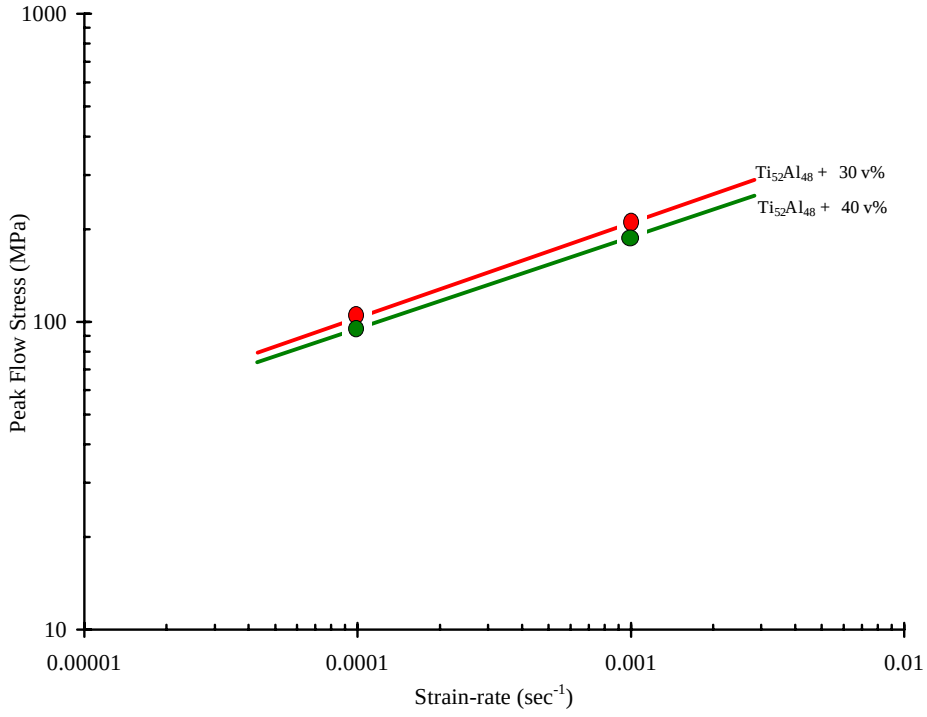

(b)

Figure 15: A plot of the peak flow stress as a function of the strain-rate for tests performed at 1100°C: (a) $Ti_{54}Al_{46}$-matrix composites and (b) Al_3Ti-matrix composites. The slopes of the trace lines shown represent the strain-rate sensitivity of each composite variant.

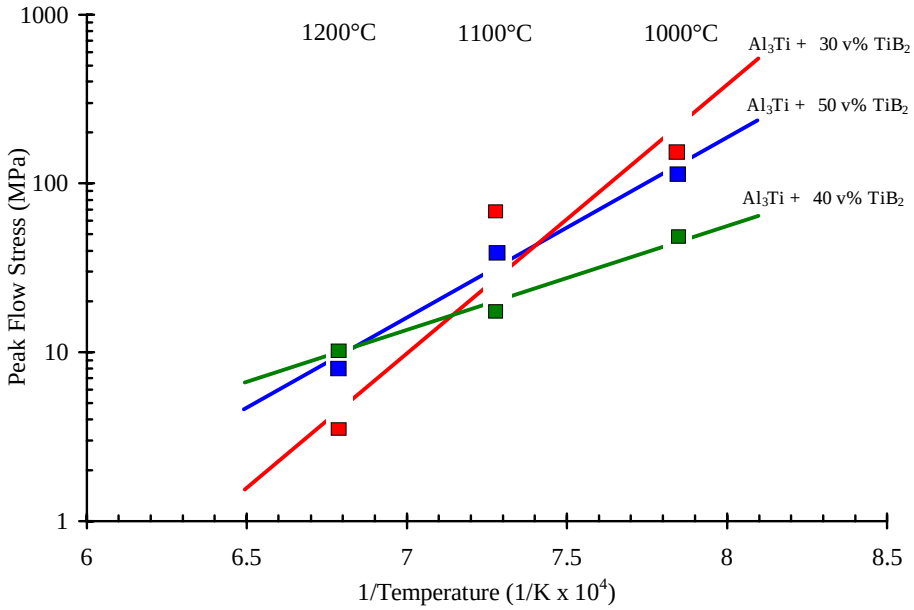

(a)

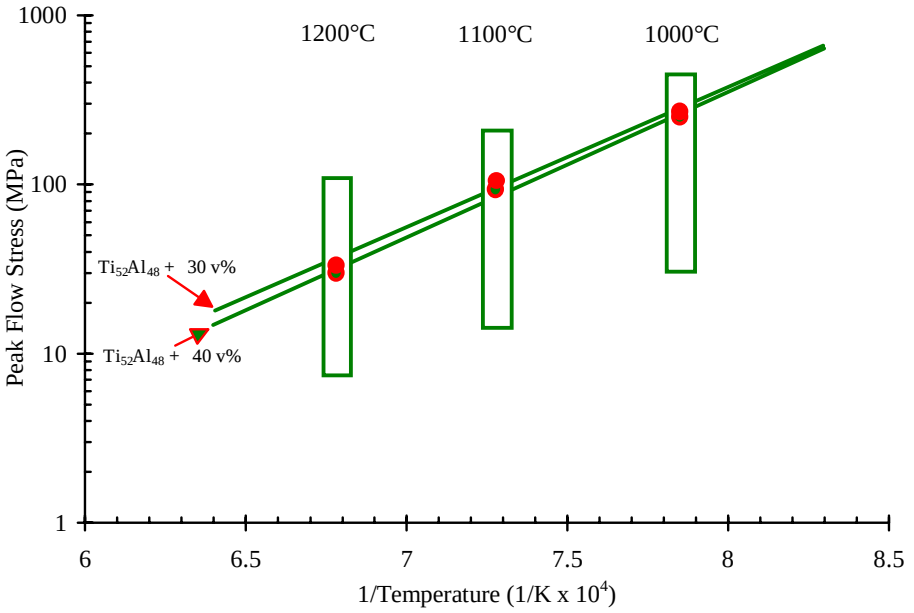

(b)

Figure 16: A plot of the peak flow stress as a function of temperature in the (a) $Ti_{54}Al_{46}$-matrix composites and (b) Al_3Ti-matrix composites for all temperatures tested. The slopes of the trace lines shown is related to the activation energy required for plastic deformation in each composite variant.

Table V: Values of the variables used to develop the constitutive flow stress equation for each IMC composition.

IMC Designation	*A (MPa) x 10^{-3}*	*m*	*Q (kJ/mol)*
Al_3Ti + 30 v% TiB_2	1.84	0.139	941
Al_3Ti + 40 v% TiB_2	5.14	0.198	575
Al_3Ti + 50 v% TiB_2	10.96	0.265	1093
Al_3Ti matrix average	5.98	0.201	870
TiAl + 30 v% TiB_2	1.95	0.257	536
TiAl + 40 v% TiB_2	1.67	0.280	549
TiAl matrix average	1.81	0.269	543
Ti-6Al-4V	29.6	0.148	535

4.4. Discussion

4.4.1. Effect of TiB_2 on Composite Flow Behavior

The temperatures at which the compression tests were performed are above the ductile to brittle transition temperatures of both intermetallic matrices. Thus, while these matrices will readily deform, the titanium diboride reinforcing them should remain rigid. Figure 17 shows the flow stress as a function of vol% TiB_2 for both intermetallic matrices. In the Al_3Ti-matrix composites (Figure 17a), the flow stress is a minimum at, or near, 40 vol% TiB_2 reinforcement. This trend may also appear in the $Ti_{54}Al_{46}$-matrix samples, although this cannot be concluded from the available test data. This trend may be a result of the TiB_2 interparticle spacing. Current micromechanical models predict that strength is a function of interparticle spacing of the rigid phase, due to the obstacle smaller spacing imposes upon dislocation motion.

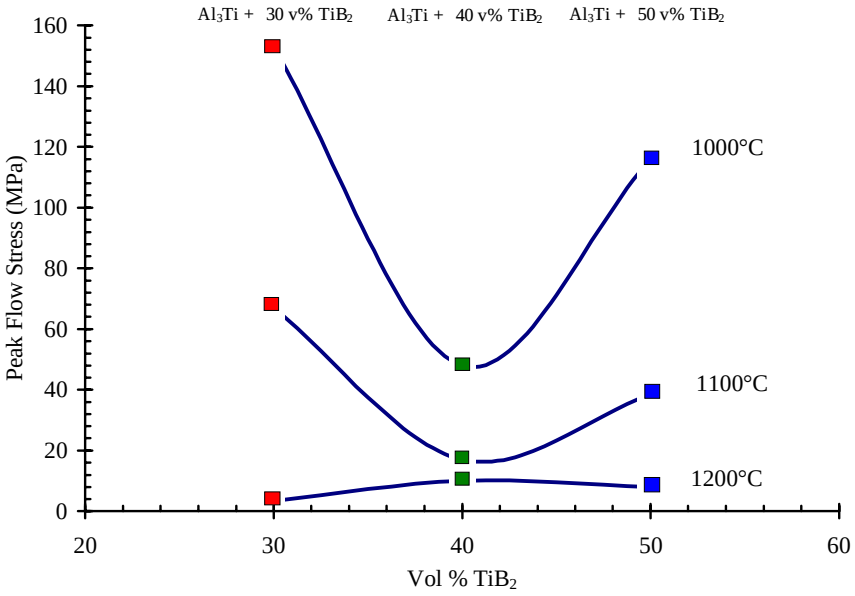

(a)

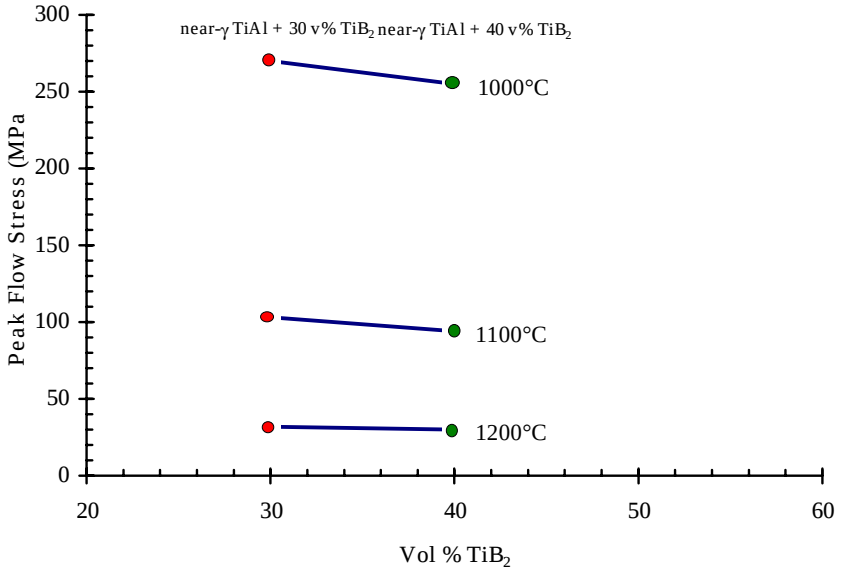

(b)

Figure 17: Flow stresses for the (a) Al_3Ti-based IMCs and the (b) $Ti_{54}Al_{46}$-based composites shown as a function of the volume percentage of TiB_2 reinforcement as determined at a strain-rate of 10^{-4} sec^{-1} for all test temperatures.

The interparticle spacing takes into account both the volume fraction of the reinforcement, as well as the reinforcement size. Both the volume fraction of the reinforcement is controlled by the chemistry of the composition prior to reaction synethesis, as described in chapter 3. The size and spacing of these particles appears to be controlled by the thermal energy available during this synthesis. Figure 18 shows the flow stress of the IMCs as a function of the TiB_2 interparticle spacing for tests performed at 10^{-4} sec^{-1} strain-rate and all temperatures. In the Al_3Ti-based IMCs, the TiB_2 spacing was observed to be the greatest in the sample reinforced with 40 vol% TiB_2, and somewhat lower in both the 30 and 50 vol% reinforced IMCs. In the case of the Al_3Ti-based IMCs (Figure 18a), the flow stress generally decreases as the spacing increases. A discrepancy in the mechanical response in the 30 vol% TiB_2 sample was found as a result of poor pre-synthesis blending in that batch of IMC powder. The spacing of the as-consolidated and mechanically tested Al_3Ti + 30 vol% TiB_2 was not consistent with the spacing observed in the as-reacted samples, and is shown in Figure 18a as lightly shaded marks. Figure 18b shows the flow stress as a function of interparticle spacing in the $Ti_{54}Al_{46}$-matrix composites. In this case, the flow stress appears to increase as the interparticle spacing increases. This is inconsistent with current models of discontinuously reinforced composites. This trend may indicate the presence of a phenomenon not associated with the presence of TiB_2 particles. However, to speculate on the mechanism of the increased flow stress would be fruitless as the variation in these data are believed to lie within the error of measurements (both interparticle spacing and peak flow stress), hence, no trend can be determined. What can be noted is the distinct decrease in flow stress with increasing temperature.

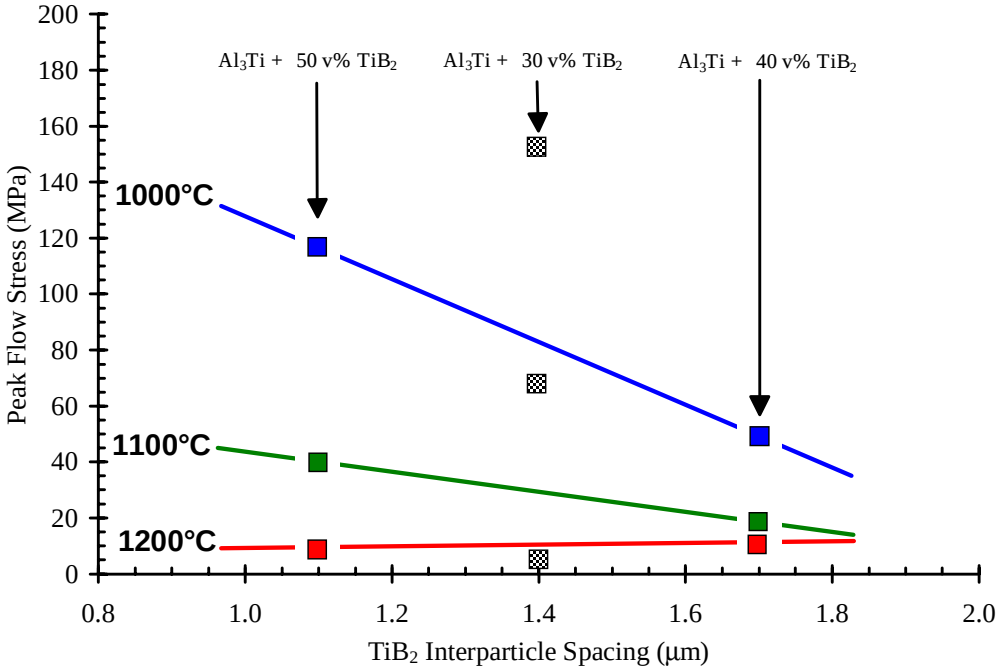

(a)

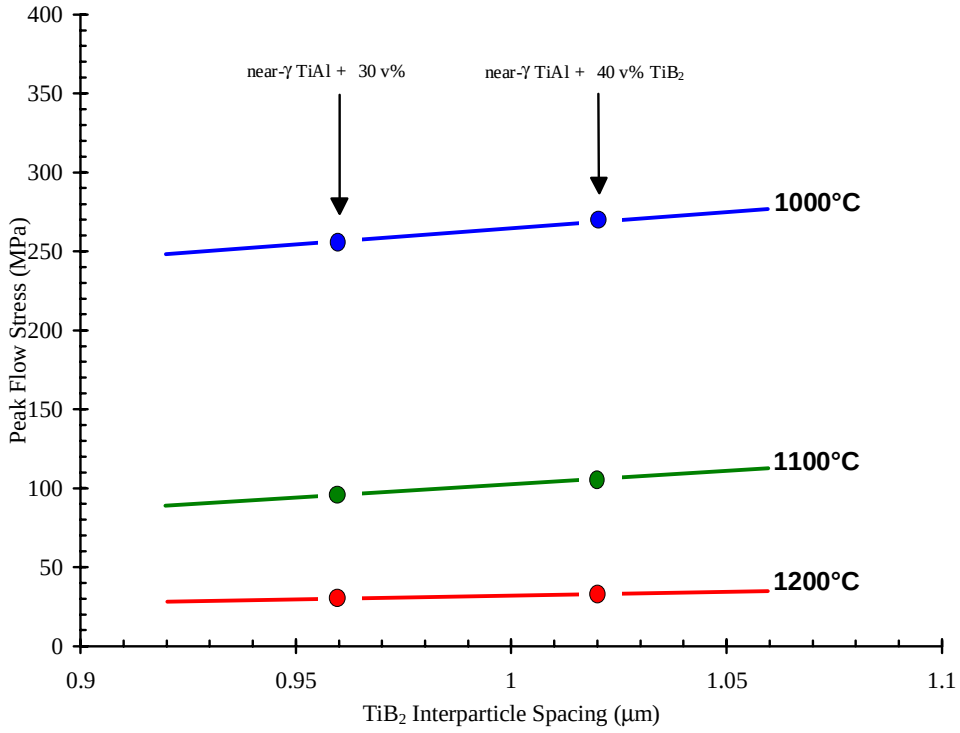

(b)

Figure 18: Flow stresses for the (a) Al_3Ti-based IMCs and (b) $Ti_{54}Al_{46}$-based IMCs shown as a function of the interparticle spacing of TiB_2 reinforcement as determined at a strain-rate of 10^{-4} sec^{-1} for all test temperatures.

4.4.2. Correlation of IMC Flow Stress to Temperature and Strain-rate

The temperatures at which the compression tests were performed are above the brittle to ductile temperature (BDT) for both of the intermetallic matrices[76]. These temperatures are also close to the melting temperatures of the titanium aluminide matrices, and therefore represent high homologous temperatures (T/T_{melt}), as well. At these temperatures the composite is extremely deformable, regardless of the reinforcement used. Due to the extreme temperatures and consequential deformability of the matrix, the results of these mechanical tests have some inherent scatter. The most significant trend to be observed is the decrease in flow stress with increasing temperature for a given composition. The strain-rate is also shown to effect the flow stress. The increase in flow stress as a function of increasing strain-rate is as one would expect. The consistency of these trends suggests that a quantitative description of the flow stress, in terms of temperature and strain-rate, can be made.

The microstructural variation which has the greatest effect on the flow behavior of the composites is the matrix composition. The effect of matrix composition is tied to the BDT, and hence, the melting temperature of the material. As a result, the $Ti_{54}Al_{46}$-matrix composites have higher peak flow stresses at all temperatures and strain-rates. This is due to the higher homologous temperature of this matrix. Figure 19 shows the flow stress as a function of temperature for the slower strain-rate (0.0001 sec^{-1}). This figure illustrates the effects of homologous temperature and volume % TiB_2 reinforcement. The flow stress decreases rapidly with increasing homologous temperature, as expected.

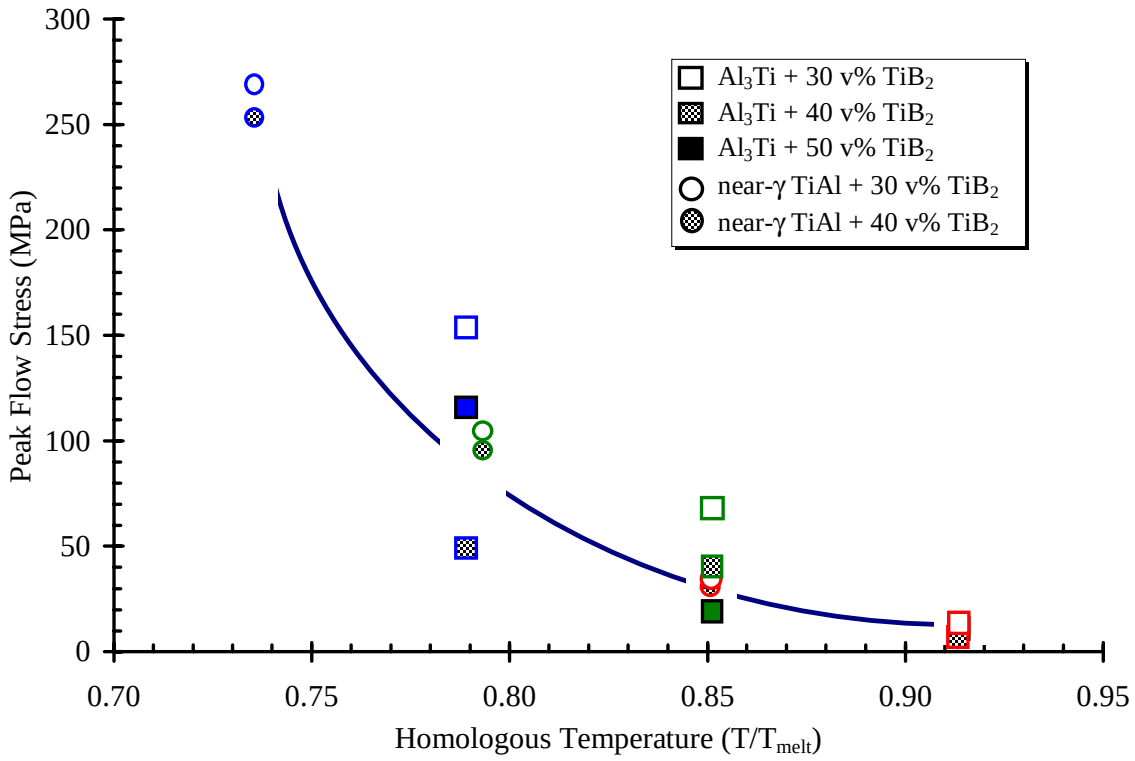

Figure 19: Variation of the peak flow stress as a function of the homologous temperature for all composites at a strain-rate of 0.0001sec^{-1}.

4.4.3. Development of Flow Stress Maps

The average values of the structure constant (A), the strain-rate sensitivity (m), and the activation energy (Q) as shown in the shaded regions of Table V are used to develop a processing map of the flow stress as a function of both strain-rate and temperature. The phenomenologically-based flow stress equation (Equation 7) has been used to evaluate the flow stress as a function of the temperature and strain-rate. This data is graphically represented as a three dimensional surface in strain-rate and temperature space. This data will be vital to the correlation of the experimentally codeformed metal/IMC composites' flow stress ratio to the degree of IMC particle deformation. Figures 19 through 21 show the flow stress maps for Al_3Ti-based composites. Similarly, Figures 22 and 23 show the flow stress maps for the $Ti_{54}Al_{46}$-based composites. The flow stress values predicted are consistent with experimental results, upon which they are based. One notable exception is the Al_3Ti reinforced by 50 volume percent TiB_2. In this case,

inaccuracy resulting from activation energy calculations is reflected in the predicted significantly higher flow stresses than were experimentally observed. Figure 22 shows a flow stress map for the Ti-6Al-4V alloy matrix. As noted earlier, this data was extrapolated from available data. The available data did not extend into temperature ranges above the beta transus (1066°C). The data presented assumes that the flow stress is independent of this microstructural change. This is not the case. In fact, room temperature measurements of Ti-6Al-4V alloys which were heat treated to increase the amount of beta phase at room temperature, have exhibited more ductile behavior than non-treated alloys at similar temperatures[77]. It is believed that at elevated temperatures these phases exhibit sufficiently low flow stresses (below 5 MPa) such that differences are negligible.

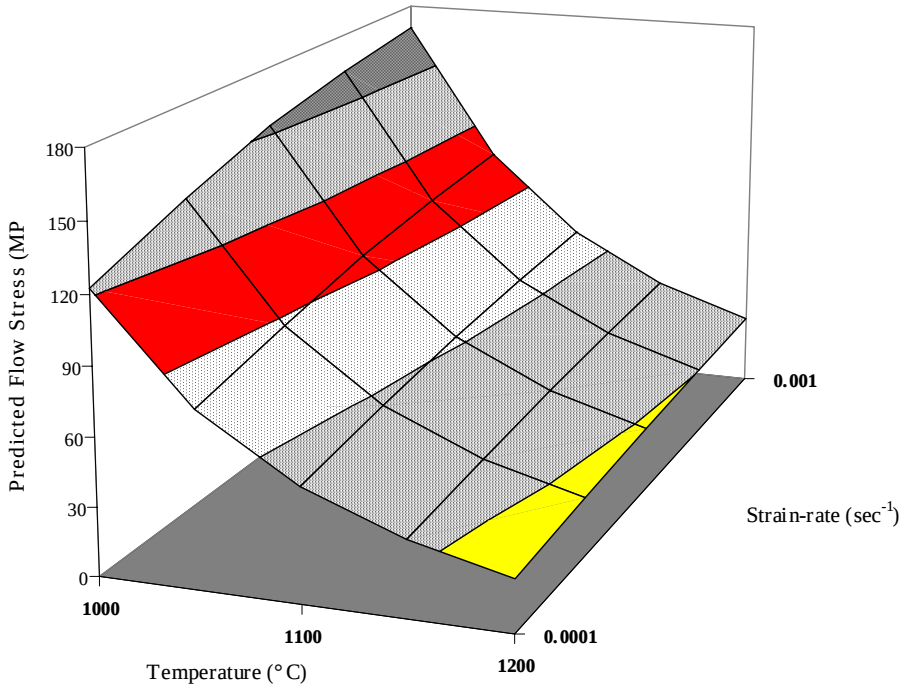

Figure 20: Variation of the flow stress as a function of the strain-rate and temperature for Al_3Ti + 30 volume % TiB_2.

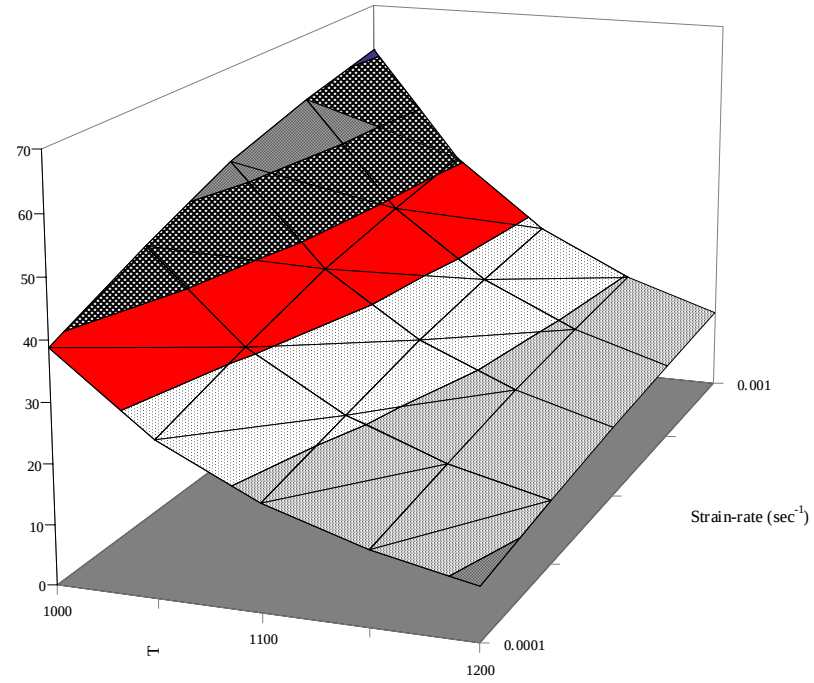

Figure 21: Variation of the flow stress as a function of the strain-rate and temperature for Al_3Ti + 40 volume % TiB_2.

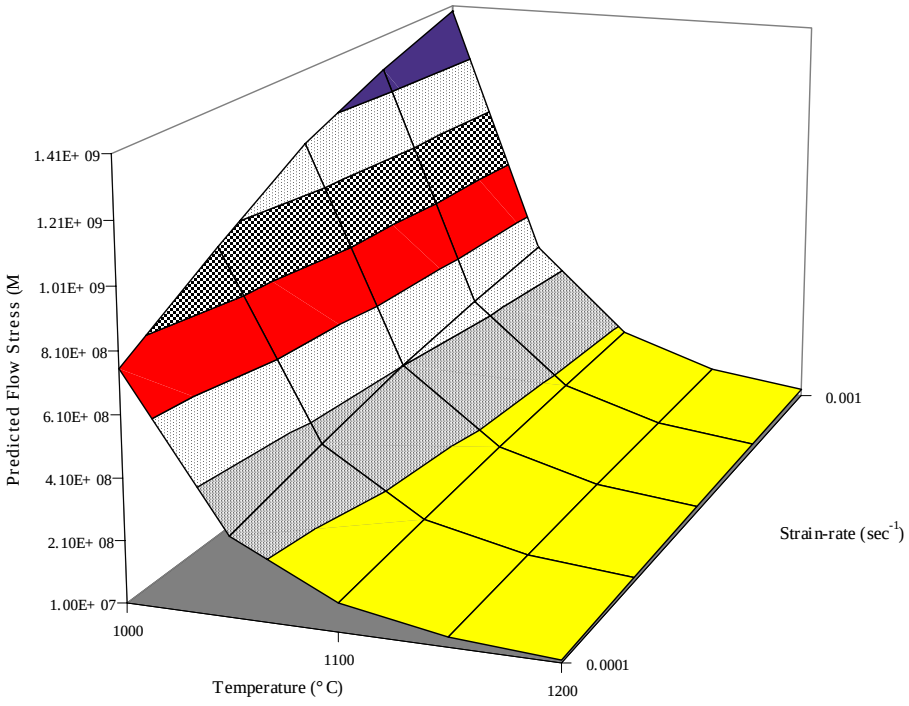

Figure 22: Variation of the flow stress as a function of the strain-rate and temperature for Al_3Ti + 50 volume % TiB_2.

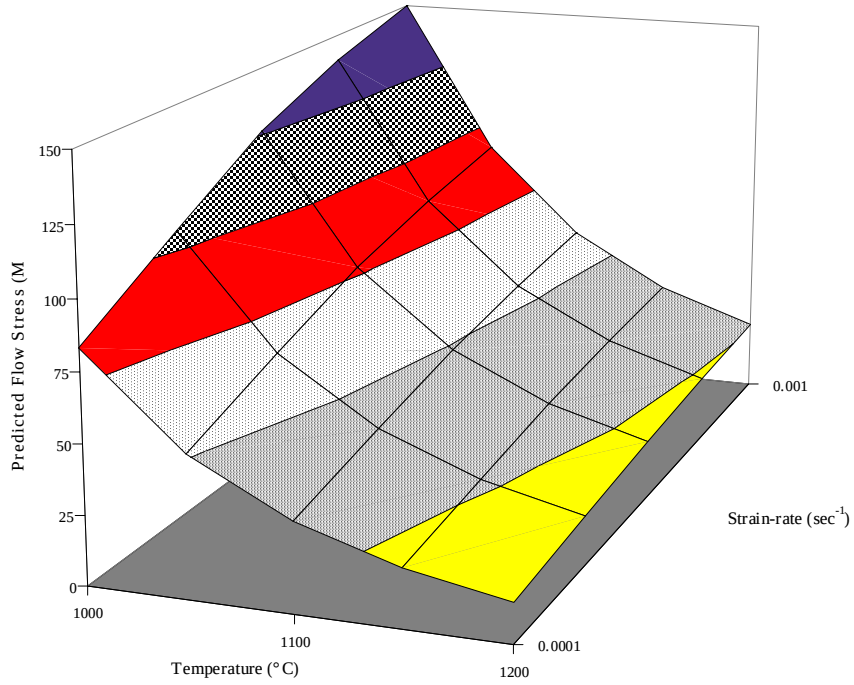

Figure 23: Variation of the flow stress as a function of the strain-rate and temperature for $Ti_{54}Al_{46}$ + 30 volume % TiB_2.

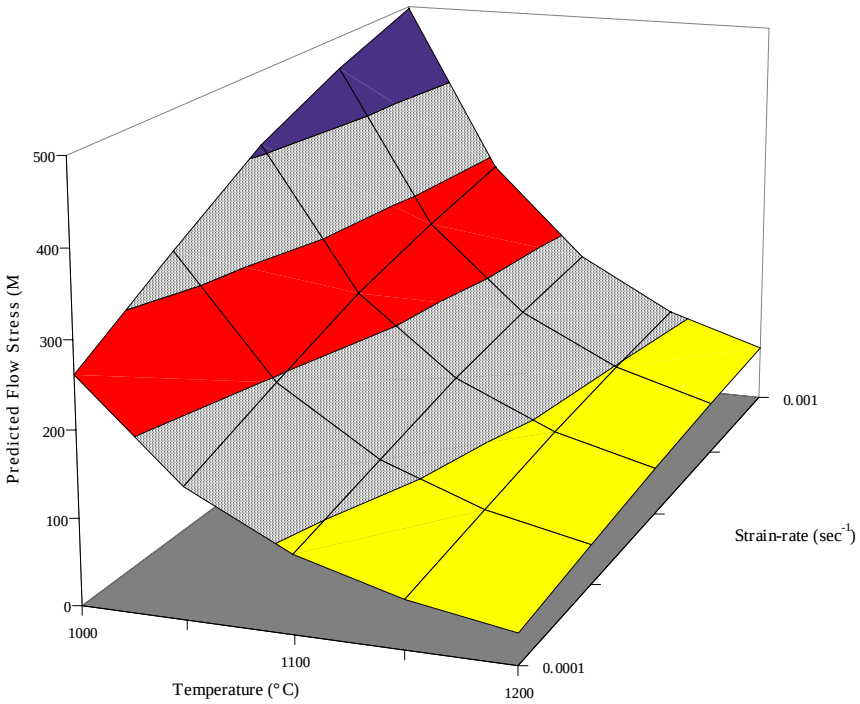

Figure 24: Variation of the flow stress as a function of the strain-rate and temperature for $Ti_{54}Al_{46}$ + 40 volume % TiB_2.

Figure 25: An extrapolation of available data for the flow stress as a function of the strain-rate and temperature for Ti-6Al-4V.

4.5. Summary

- Compression tests were performed at a series of temperatures and strain-rates to evaluate the flow behavior of the IMCs under conditions similar to those observed for deformation processes.
- Flow in these materials occurs readily above their ductile to brittle transition temperatures.
- An analysis of the volume fraction, size, and interparticle spacing of the TiB_2 reinforcement within the IMCs has been shown to have marginal influence on the high temperature flow behavior of these composites.
- The high temperature flow behavior of these composites was most affected by the matrix composition, and its subsequential influence on homologous temperature.

- The development of constitutive equations to describe the deformation behavior of these materials in terms of strain-rate and temperature on the flow stress revealed that the flow behavior of the composites was highly dependent on matrix composition and temperature.
- The effects of strain-rate were not evident at higher temperatures but appeared to effect limited influence at the lower test temperatures.

4.6. References

[73] M.L. VanMeter, S.L. Kampe, & L. Christodoulou, *Scripta Mater.*, Vol 34, No 8, pp. 1251-6, 1996.

[74] C. Zener & H.H. Hollomon, J Appl Phys, vol. 15, pp. 22-32, (1944).

[75] *Atlas of Formability: Ti-6Al-4V ELI*, National Center for Excellence in Metalworking Technology (NCEMT), Johnston, PA, 1993.

[76] D.M. Dimiduk, D.B. Miracle, Y-W. Kim & M.G. Mendiratta, *ISIJ International*, pp.1223-34, 1991.

[77] *Titanium Alloys: Material Properties Handbook*, ed. R. Boyer, G. Welsch, & E.W. Collings, pp. 592-4, 1994.

5. Extrusion Processing

Thus far, this study has examined the synthesis and flow behavior of the metal and IMC components of the proposed composite seperately. This chapter will evaluate the effects of material properties and processing conditions, discussed in previous chapters, on the codeformation of the composite as a whole. The experimental codeformation will be accomplished via the extrusion of a blended powder metal/IMC composite. The results will be analyzed in terms of the degree of deformation achieved within the IMC phase of the as-extruded material.

5.1. Introduction

Deformation processes induce shape changes through the application of forces by various tools.[78] In its most basic form, extrusion processing is a deformation process in which a cylindrical billet is forced through a small circular hole by a ram, reducing the cross-sectional area of the billet and increasing its length, to form a rod.

One particularly useful approach to the deformation processing of composite materials is canned powder extrusion.[79] This compositing strategy permits the dispersion of one species within another through powder blending. Further, the development of unique microstructural features, unfeasible or impossible using non-powder based techniques, is possible through this in-situ morphological deformation processing.

Morphological in-situ deformation processes are those which affect changes in the shape of the microstructural features of the composite, specifically the reinforcement. Well-documented studies of systems processed in this manner to codeform an ostensibly brittle, phase within a ductile matrix, are described in the literature.[80] In order to obtain a superior deformation processed composite, the reinforcement phase must be uniformly distributed through the matrix; and both phases need to exhibit similar flow behaviors under the deformation conditions, i.e., temperature, strain, and strain-rate. Advantages of morphological processing techniques include the preservation of clean matrix-reinforcement interfaces, and the development of unique reinforcing morphologies in

difficult to process materials. The present study seeks to exploit the latter feature of this processing strategy.

In this study, codeformation experiments have been performed by extruding blended metal/IMC composite powders. The high temperature mechanical behaviors of the metal and IMC components have been used as a basis for the selection of extrusion parameters (i.e., die ratio, temperature, ram speed, etc.) Ideal codeformation is believed to occur when the flow stresses in the metal matrix and the IMC reinforcement are equal. This condition results in deformation behavior similar to the case of a monolithic billet.

Codeformation behavior is controlled by the interactions of material properties and processing conditions. Material properties which influence codeformation include intermetallic matrix composition and the volume % TiB_2 reinforcement within the intermetallic alloy. Several IMC compositions have been tested to evaluate the impact of these factors. Some processing conditions which influence codeformation include the billet temperature during the extrusion, strain-rate (as determined by the ram speed and die ratio), and the amount of IMC blended with the Ti-6Al-4V alloy matrix. These, too, have been systematically varied to evaluate their impact on codeformation.

The degree of codeformation has been examined in terms of the as-extruded IMC particle aspect ratio. An attempt to relate the influence of material properties and processing conditions to the relative flow stress of the metal and IMC components has been made. An effort to correlate the IMC codeformation to the relative flow stress is also discussed.

5.2. Experimental

Flow stress maps have been created for the IMC "reinforcement" and the Ti-6Al-4V matrix, as illustrated in the previous chapter. Commensurate deformation should occur when the flow stress of the metal matrix approaches that of the IMC reinforcement. Flow stress maps have been used to identify temperatures and strain-rates where this condition will be met. Figure 26 shows the flow stress ratios for Al_3Ti + 40 v% TiB_2 (Figure 26a) and $Ti_{54}Al_{46}$ + 40 v% TiB_2 (Figure 26b) to the conventional Ti-6Al-4V alloy. These plots suggest that codeformation is likely to occur for all strain-rates, though higher rates

should produce slightly more codeformation. The extrusion temperature is much more influential, according to the flow stress maps, and higher temperatures are more likely to achieve codeformation. One further comparison between Figure 26a and Figure 26b illustrates that codeformation is more likely to occur for compositions reinforced with the Al_3Ti-based IMCs.

5.2.1. Composite Powder Preparation

Prior to blending, the as-reacted IMC sponge was ground into a fine powder. These powders were sieve-analyzed to generate information on the particle size distribution of the IMC powder particles. All IMC particulates were under 300 μm, but averaged between 125 and 300 μm, in their smallest dimension. The Ti-6Al-4V matrix was obtained as [500 μm spherical prealloyed powder form from Nuclear Metals (Concord, MA).

To achieve the desired volume percentage of IMC within the Ti-6Al-4V matrix, the appropriate volume of powder was measured using a graduated cylinder and tapped to settle the powder. The powders were then mixed and blended in a sealed bottle for 1 hour on a set of rollers.

The blended composite powders were transferred to a mild steel or titanium can. Before the cans were sealed, the powder was placed under a vacuum ([100 mtorr). The 304 stainless steel or titanium cap was then electron beam welded in place.

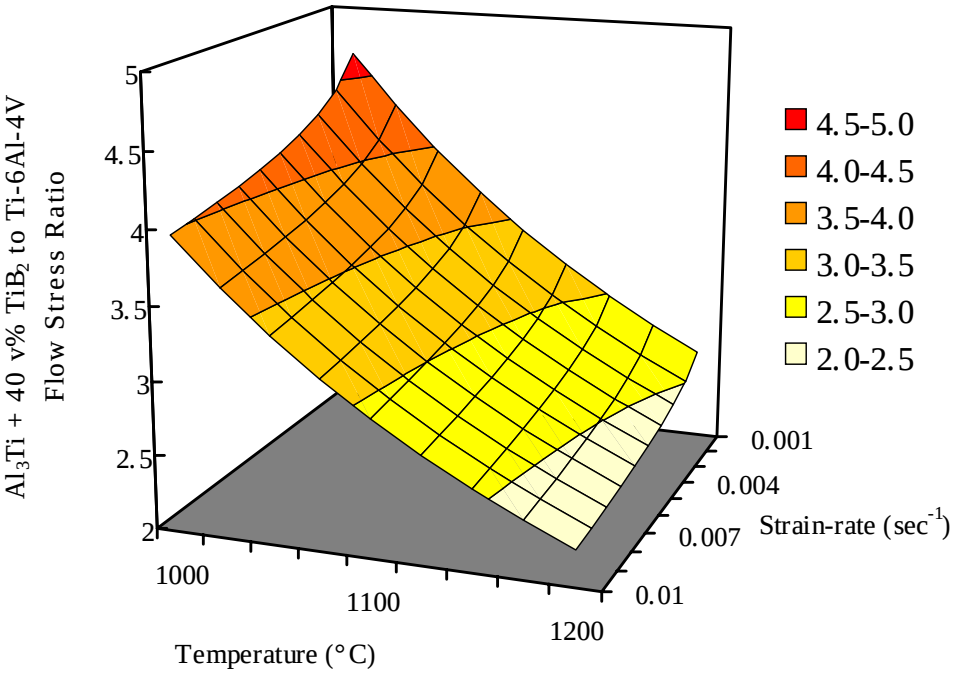

(a)

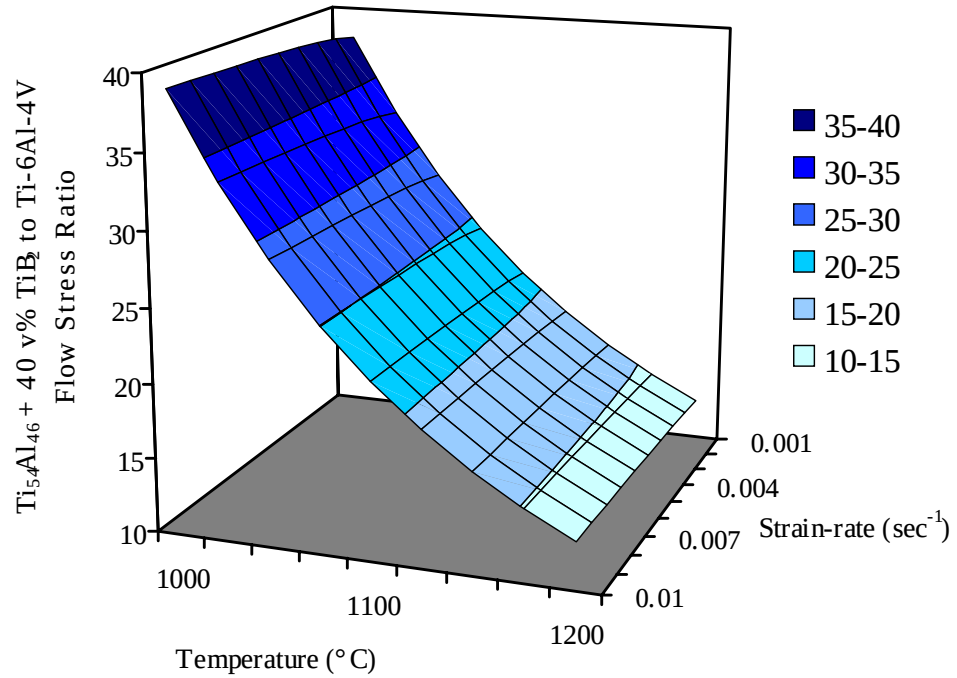

(b)

Figure 26: The flow stress ratio of (a) Al_3Ti + 40 v% TiB_2 and (b) $Ti_{54}Al_{46}$ + 40 v% TiB_2 to that of Ti-6Al-4V for temperatures from 1000° to 1200° and strain-rates from 0.001 sec-1 to 0.01 sec-1. This data was generated from the flow stresses calculated in Chapter 4.

5.2.2. Extrusion Trials

Prior to extrusion, each billet was coated with DAG, a graphite-based lubricant, and placed in a furnace where they had been held at the selected temperature for one hour. After soaking at temperature, the billet was quickly transferred to the extrusion tooling. Extrusions were performed using the Banyard Metalheat, Ltd. hydraulic extrusion press of the Materials Processing Group at the Imperial College of Science, Technology and Medicine (London, UK). A glass plug was placed before the billet in the extrusion press to act as a lubricant. The extrusion tooling was held at 500°C. The billet was immediately extruded at a ram speed of 2.5-4.7 mm/sec. The deformation of the billet was halted prior to full extrusion to provide samples of the material as it proceeds through the extrusion die. The extruded rods were allowed to cool to ambient temperature in air. A picture of the extrusion press with a still hot extruded billet is shown as Figure 27. Appendix C shows a complete list of the extrusions performed, the sample designation, date, composition, can/cap material, extrusion temperature, extrusion ratio, and facility.

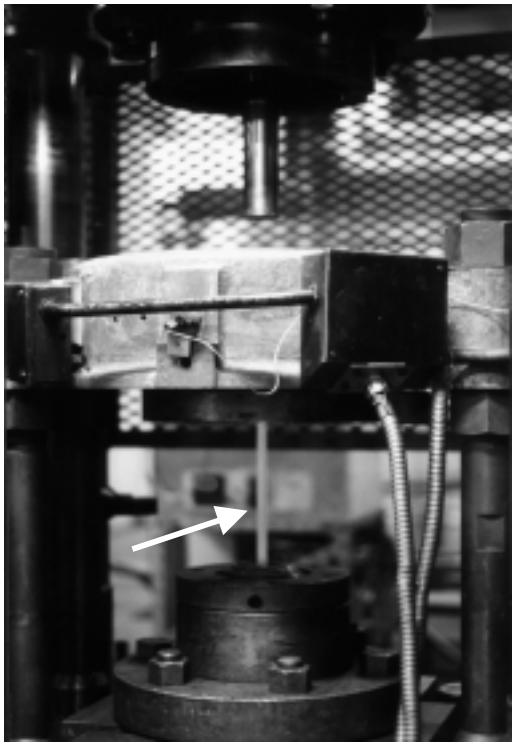

Figure 27: A picture of the Banyard Metalheat hydraulic extrusion press used for experimental codeforation trials. The region specified by the arrow, is a still-hot extrusion of the metal/IMC composite.

5.2.3. Microstructural Analysis Protocol

Transverse sections were taken from the approximate center of each extrusion and polished using conventional metallographic techniques. The samples were immersed with a 2 % solution of HF, as an etch until small bubbles started to form (approximately 2 seconds.) Optical microscopy was performed on these cross-sections to evaluate the degree of codeformation within the composite. This was assessed in terms of the IMC particle aspect ratio.

The particle aspect ratio data was generated via quantitative optical microscopy. Figure 28 serves to illustrate the measurement protocol. The cross-section was divided into four roughly-equivalent regions as shown in Figure 28a, to maintain a random sample across the diameter of the specimen. Fifteen particles in each region were randomly selected through their coincidence with a regularly-spaced series of overlayed points. Four measurements were on each particle. Figure 28b shows the measurement of hypothetical IMC particle. The entire length of the particle was measured, as well as 3 diametrical measurements at ¼, ½, and ¾ of the particle's length. Multiple diametrical measurements were deamed necessary because of the wide variation in width across non-uniform particles. The particle aspect ratio was calculated by dividing the total length of a particle by that particle's average width. This aspect ratio serves as a measure of particle deformation, from which IMC strain can be calculated.

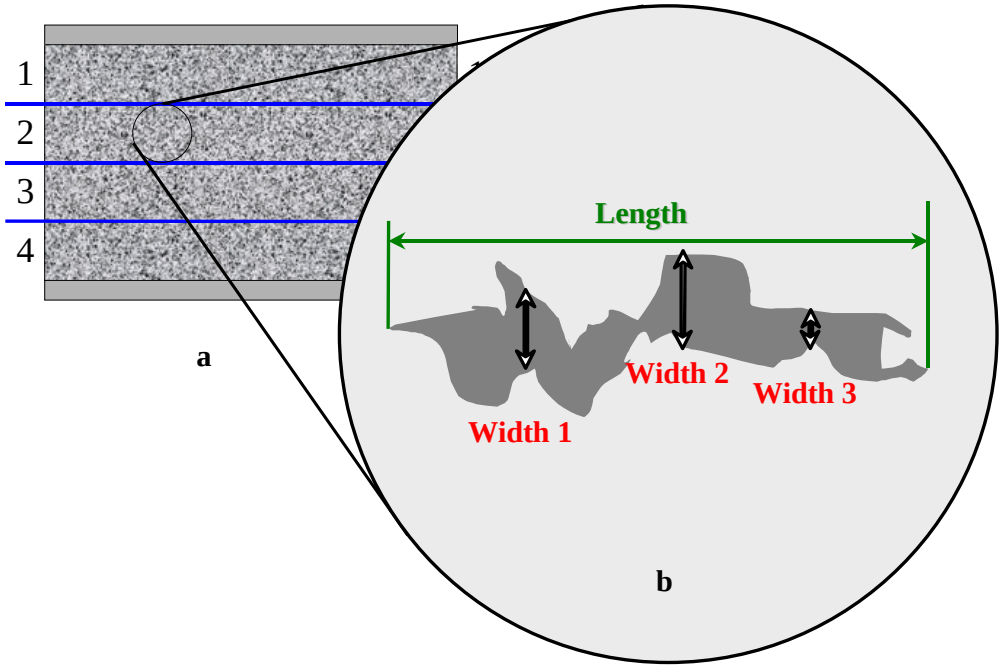

Figure 28: A schematic showing the selection and measurement of a hypothetical as-codeformed IMC particle. (a) Samples were taken from transverse sections divided in 4 regions. (b) The length and 3 widths were measured for a random sample of IMC particles.

5.3. Results

Several extrusion campaigns were undertaken to evaluate the feasibility of codeformation via hot extrusion under particular extrusion parameters (i.e., facility and canning material.) These trials showed that the expense of titanium cans was not necessary. As a result, remaining extrusions were performed in steel cans. Preliminary trials showed that the facilities at Imperial College produced better results than the facilities of Oak Ridge National Laboratory due to their instrumentation and slower ram speeds. A sample of the extrusions performed were selected for quantitative codeformation analysis. The extrusions quantitatively examined to systematically evaluate codeformation are shown in Table VI.

Table VI: A list of the extrusions utilized in this study.

Sample Designation	***Matrix + volume % (IMC reinforcement)***	***Extrusion Temperature (°C)***	***Extrusion Ratio****
T4040A-Lo	Ti-6Al-4V + 40 v% (Al_3Ti + 40 v% TiB_2)	1200	18:1
T4040A-Hi	Ti-6Al-4V + 40 v% (Al_3Ti + 40 v% TiB_2)	1200	25:1
T4040γ-Lo	Ti-6Al-4V + 40 v% ($Ti_{54}Al_{46}$ + 40 v% TiB_2)	1200	9:1
T4040γ-Hi	Ti-6Al-4V + 40 v% ($Ti_{54}Al_{46}$ + 40 v% TiB_2)	1200	25:1
T4000A	Ti-6Al-4V + 40 v% Al_3Ti	1200	16:1
T4020A	Ti-6Al-4V + 40 v% (Al_3Ti + 20 v% TiB_2)	1200	11:1
T2040A	Ti-6Al-4V + 20 v% (Al_3Ti + 40 v% TiB_2)	1200	21:1
T3040A	Ti-6Al-4V + 30 v% (Al_3Ti + 40 v% TiB_2)	1200	23:1
T3040A-1180	Ti-6Al-4V + 30 v% (Al_3Ti + 40 v% TiB_2)	1180	20:1
T3040A-Large	Ti-6Al-4V + 30 v% (Al_3Ti + 40 v% TiB_2)	1200	36:1
T3040A-Small	Ti-6Al-4V + 30 v% (Al_3Ti + 40 v% TiB_2)	1200	36:1

*Extrusion ratio measured as initial billet cross-sectional area to the as-extruded cross-sectional area.

5.3.1. Extrusion Press Data

Each extrusion operation required approximately 50 seconds of operational press time, however, considerably more time was spent extracating the as-extruded rods from the container and die. The extrusion ram loads, pressures, and displacements were recorded and used to calculate the strain-rate of the process. The strain-rate was calculated by dividing the ram speed by the change in billet length. This data is presented in Table VII.

Figure 29 shows one example of the data relating the extrusion ram load to the ram displacement. The initial peak (Figure 29a) is the break-through pressure and represents the moment when the nose of the billet begins to exit the die. There is a small "steady-state" region following this initial peak (Figure 29b) followed by a gradual increase (Figure 29c) believed to be a result of billet cooling. Because the die is held at 500°C and, initially, the billet is at a temperature more than twice that temperature, billet cooling has a significant effect on the overall flow. The full range of data generated during the extrusion trials is presented in Appendix C.

Table VII: Extrusion press loading and displaceent data and the calculated extrusion strain-rate.

Sample Designation	*Ram Speed (mm/sec)*	*Strain-rate (sec^{-1})*	*Maximum Ram Pressure (MPa)*	*Extrusion Ratio*
T4040A-Lo	4.28	0.0041	569	18:1
T4040A-Hi	2.50	0.0058	1553	25:1
T4040γ-Lo	4.65	0.0095	485	9:1
T4040γ-Hi	4.28	0.0028	1408	25:1
T4000A	2.72	0.0042	813	16:1
T4020A	2.93	0.0081	697	11:1
T2040A	3.03	0.0041	545	21:1
T3040A	3.01	0.0055	545	23:1
T3040A-1180	2.57	0.0038	821	20:1
T3040A-Large	4.93	0.0031	545	36:1
T3040A-Small	4.75	0.0029	753	36:1

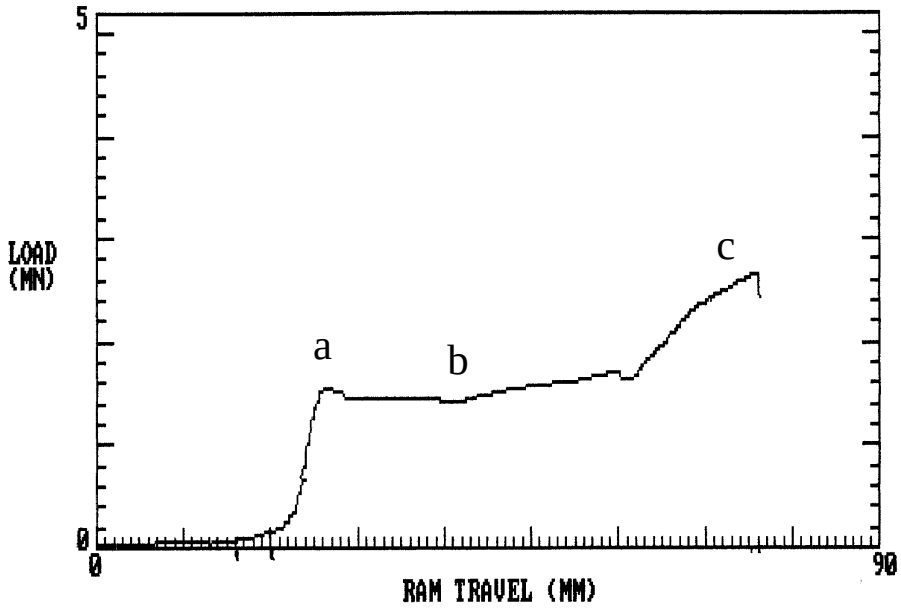

Figure 29: Data generated during the extrusion process showing the extrusion ram loading as a function of the ram displacement.

The extrusions produced were rod-shaped, between 0.5 and 2 meters in length and 8 to 20 mm in cross-sectional diameter, and were generally straight. A photograph of several extrudes is shown in Figure 30. In all cases the extrudes exhibited a rough, dark gray

surface finish. This surface was a result of the glass and graphite lubrication used in the extrusion process and was easily removed by sand blasting prior to sectioning.

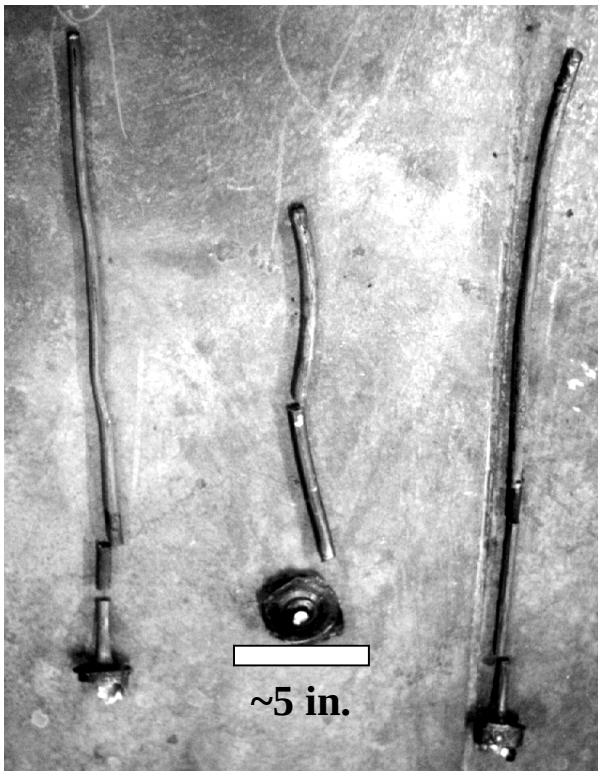

Figure 30: Several as-extruded billets shown cooling: (from left to right) Ti-6Al-4V + 30 v% (Al_3Ti + 40 v% TiB_2, Ti-6Al-4V + 40 v% (Al_3Ti + 20 v% TiB_2), Ti-6Al-4V + 40 v% Al_3Ti.

5.3.2. Microstructural Analyses

All samples exhibited porosity associated with the IMC particles. Figures 30 through 35 show optical micrographs of as-polished and etched transverse cross-sections taken from each sample. In all microgrpahs the IMC component appears as the darker microstructural feature. The effect of IMC particle size was examined using samples similar to those illustrated in Figure 35. These micrographs show Ti-6Al-4V + 30 v% (Al_3Ti + 40 v% TiB_2) with two distinct reinforcement sizes. The smaller IMC particle size (Figure 31a) was below 45 μm (-325 mesh or sub-sieve) and the larger (Figure 31b) was between 125 and 300 μm (-50 to +120 mesh).

The effects of volume percentage IMC reinforcement on codeformation was analyzed through measurement of samples similar to those shown in Figure 32. Ti-6Al-4V + 20 v% (Al_3Ti + 40 v% TiB_2) (Figure 32a), Ti-6Al-4V + 30 v% (Al_3Ti + 40 v% TiB_2) (Figure 32b), and Ti-6Al-4V + 40 v% (Al_3Ti + 40 v% TiB_2) (Figure 32c) illustrate the increasing volume percentage of IMC within the titanium alloy matrix. A general increase in particle elongation can be observed qualitatively in these micrographs.

Sections taken from extrusions reinforced with 40 v% (Al_3Ti + 40 v% TiB_2) (Figure 33a) and 40 v% ($Ti_{54}Al_{46}$ + 40 v% TiB_2) (Figure 33b) illustrate the effects of intermetallic matrix composition on codeformation. Figure 34 shows samples used to evaluate the effects of extrusion temperature on codeformation. Two temperatures were tested, 1180°C (Figure 34a) and 1200°C (Figure 34b), both for composites reinforced with 30 v% (Al_3Ti + 40 v% TiB_2).

The effect of die ratio, which affects the extrusion strain-rate for each extrusion was examined by looking at samples as illustrated in Figure 35. Several examples of die ratios for the Ti-6Al-4V + 40 v% (Al_3Ti + 40 v% TiB_2) samples are shown. The micrographs shown correspond to 18:1 (Figure 35a) and 25:1 (Figure 35b).

Figure 36 shows samples used to assess the influence which the volume percentage of TiB_2 (within the IMC) had on codeformation. Three micrographs are shown: Ti-6Al-4V + Al3Ti (Figure 36a), Ti-6Al-4V+ (Al_3Ti + 20 v% TiB_2) (Figure 36b), and Ti-6Al-4V+ (Al_3Ti + 40 v% TiB_2) (Figure 36c). Figures 35a and 35c were taken using Nemarsky polarization to better show the topography of the sample. In these micrographs the darker IMC component appears to be raised above the lighter Ti-6Al-4V matrix.

Particle aspect ratios were measured using a video monitor (CRT) attached directly to the microscope, rather than from micrographs which fail to show particles in their entirety. This technique allowed for the sample to be traversed, aiding in the measurement of longer particles.

(a)

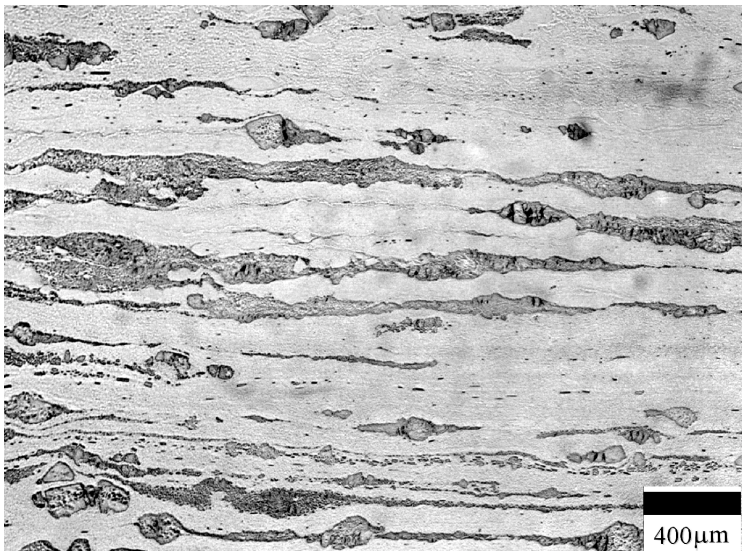

(b)

Figure 31: Micrographs of as-polished and etched transverse planar cross-sections of Ti-6Al-4V + 30 v% (Al_3Ti + 40 v% TiB_2) samples. The pre-extrusion IMC particles blended into these M/IMC composites had dimensions (a) less than 45 μm and (b) between 125 and 300 μm.

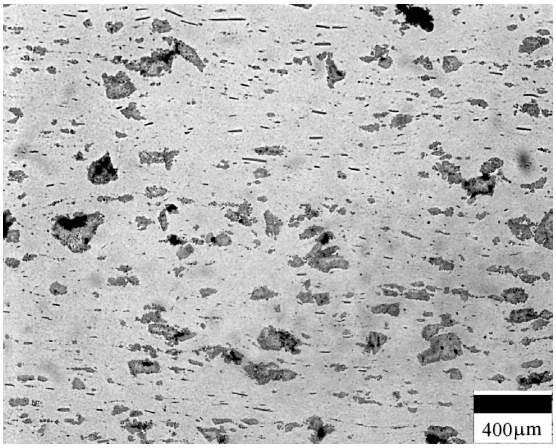

(a)

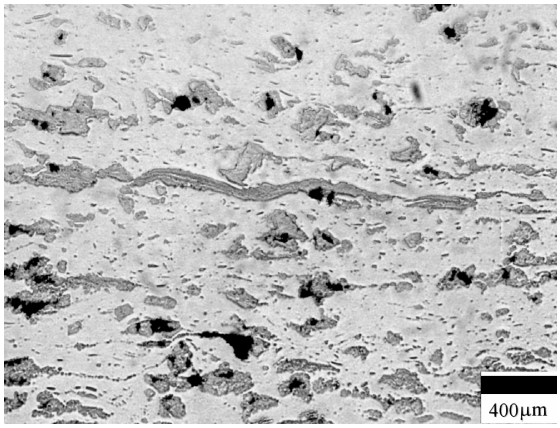

(b)

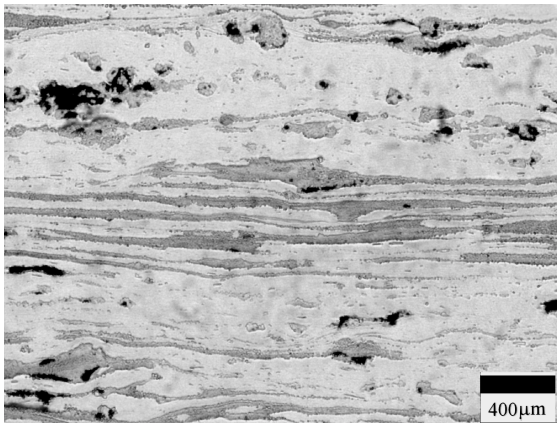

(c)

Figure 32: Micrographs of as-polished and etched transverse planar cross-sections of (a) Ti-6Al-4V + 20 v% (Al_3Ti + 40 v% TiB_2), (b) Ti-6Al-4V + 30 v% (Al_3Ti + 40 v% TiB_2), and (c) Ti-6Al-4V + 40 v% (Al_3Ti + 40 v% TiB_2) composites.

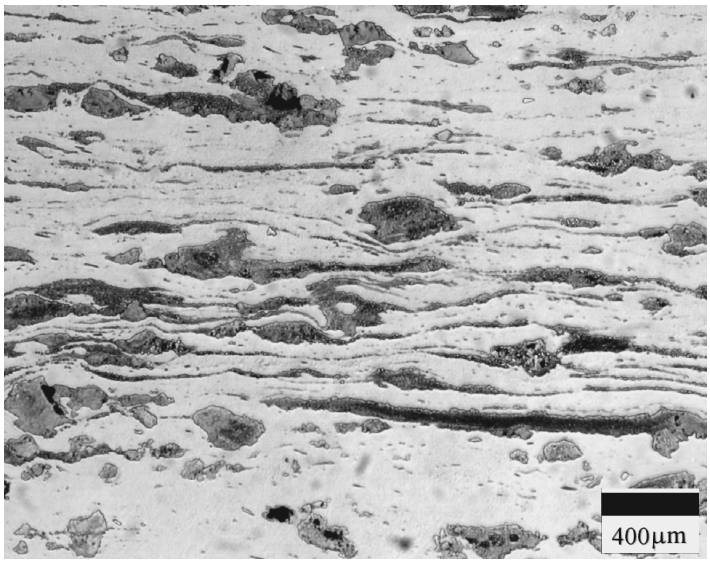

(a)

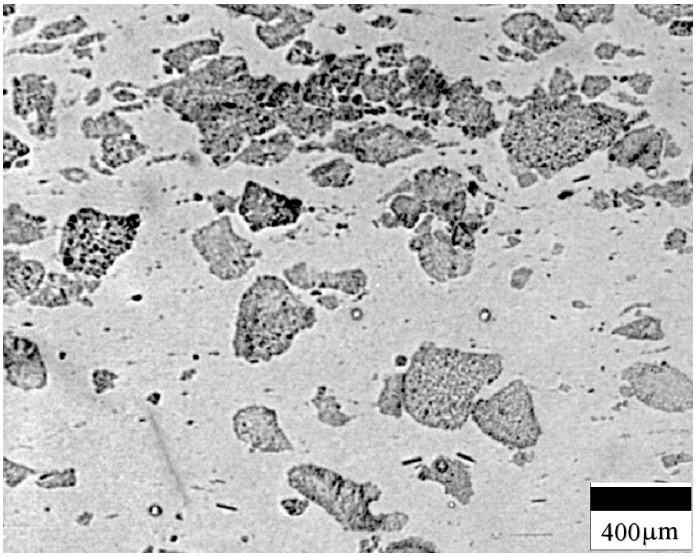

(b)

Figure 33: Micrographs of as-polished and etched transverse planar cross-sections of (a) Ti-6Al-4V + 40 v% (Al_3Ti + 40 v% TiB_2) and (b) Ti-6Al-4V + 40 v% ($Ti_{54}Al_{46}$ + 40 v% TiB_2) samples.

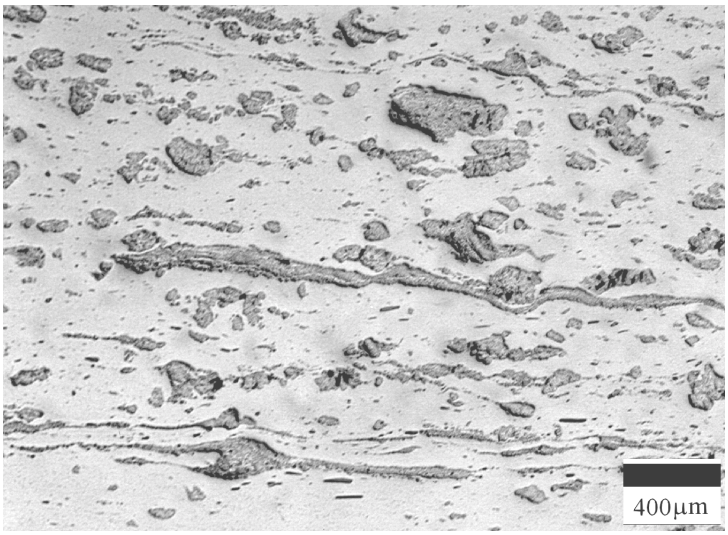

(a)

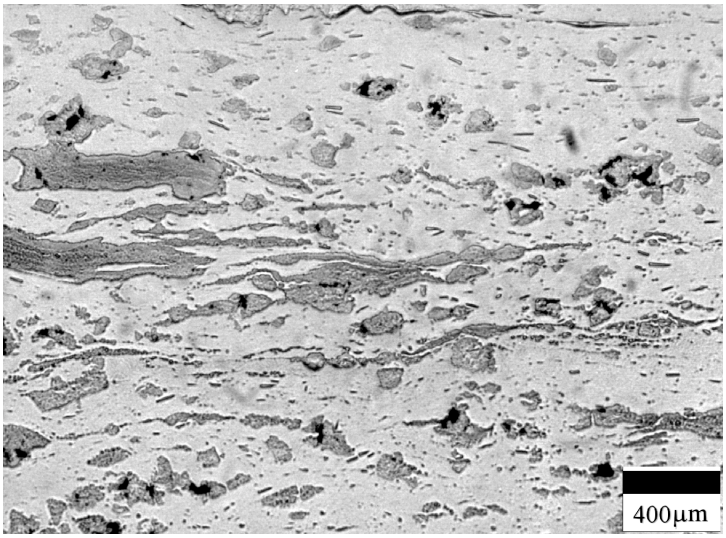

(b)

Figure 34: Micrographs of as-polished and etched transverse planar cross-sections of Ti-6Al-4V + 30 v% (Al_3Ti + 40 v% TiB_2) samples extruded at (a) 1180°C, and (b) 1200°C.

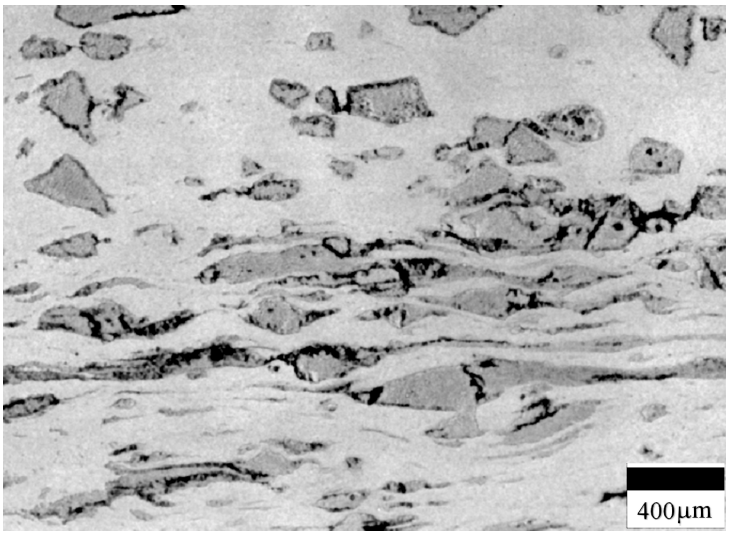

(a)

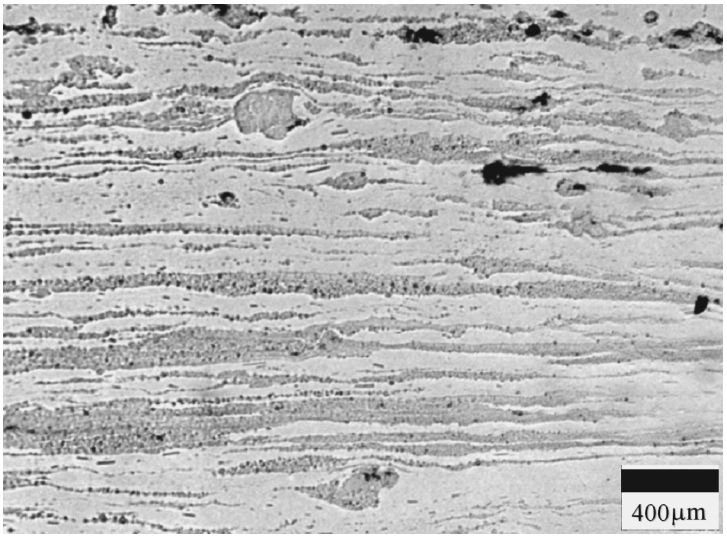

(b)

Figure 35: Micrographs of as-polished and etched transverse planar cross-sections of Ti-6Al-4V + 40 v% (Al_3Ti + 40 v% TiB_2) samples having extrusion ratios of (a) 18:1, and (b) 25:1.

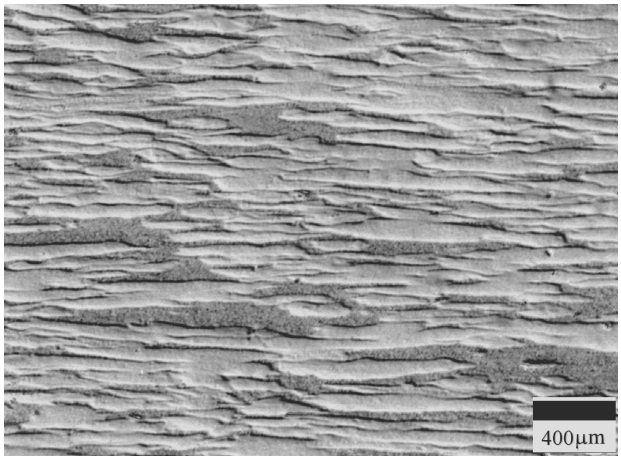

(a)

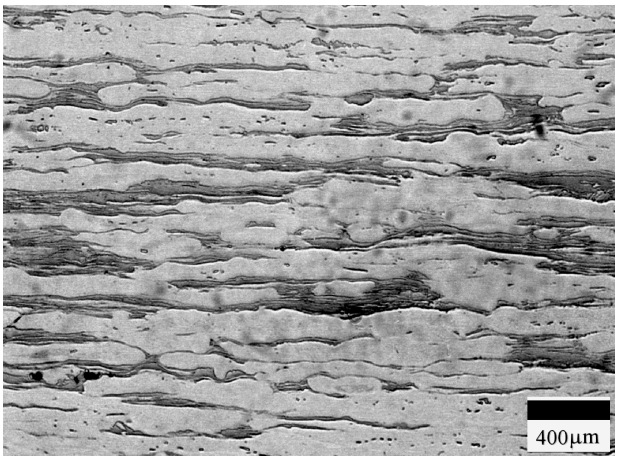

(b)

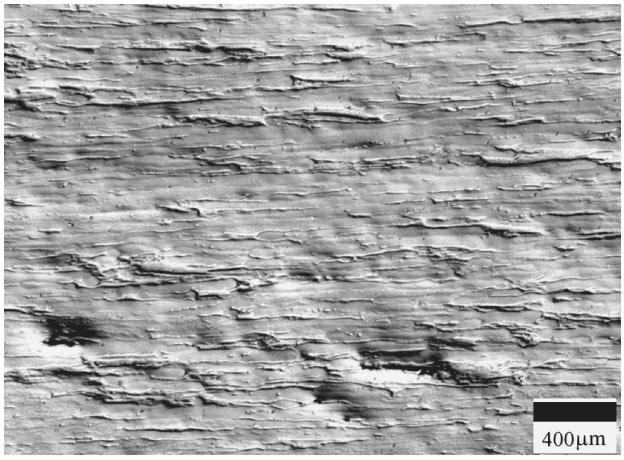

(c)

Figure 36: Micrographs of as-polished and etched transverse planar cross-sections of (a) Ti-6Al-4V + 40 v% Al_3Ti, (b) Ti-6Al-4V + 40 v% (Al_3Ti + 20 v% TiB_2), and (c) Ti-6Al-4V + 40 v% (Al_3Ti + 40 v% TiB_2) as-extruded composites.

Prior to deformation processing, the IMC particles are assumed to be nearly spherical in shape and uniformly distributed within the Ti-6Al-4V metal powder. The IMC particle aspect ratio can be related to the plastic strain resulting from codeformation processing. Figure 37 shows this relationship in terms of the IMC particle dimensions:

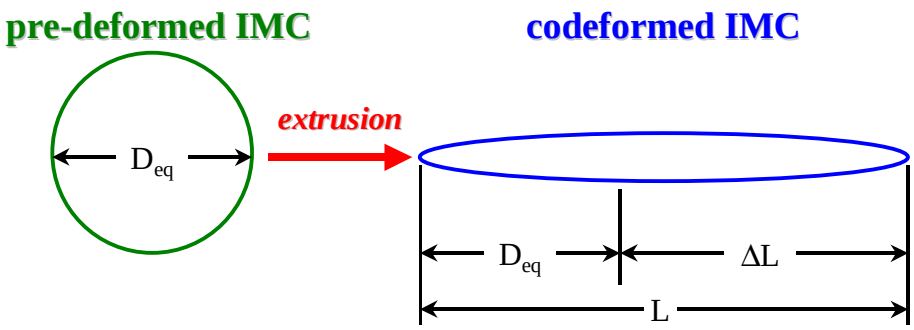

$$\varepsilon_{tensile} = \frac{\Delta L}{L_0} = \frac{L - D_{eq}}{D_{eq}}$$

Figure 37: A schematic and equation illustrating the relationship between particle aspect ratio and tensile strain.

In the equation shown in Figure 37, $\varepsilon_{tensile}$ is the tensile strain, i.e., strain in the extrusion direction, and is defined as the change in particle length, ΔL, over the initial length, L_0. The initial length is calculated under a conservation of volume assumption. This is used to determine the equivalent spherical diameter, D_{eq}, of that particle prior to deformation and is used as the initial particle "length". Tensile strain refers to the strain in the extrusion direction.

Table VIII shows the results of the particle aspect ratio measurements for each sample examined, the error, the calculated tensile strain and the average length and width of the codeformed IMC particles.

Table VIII: The extrusion conditions and IMC particle aspect ratios, strains and dimensions for the series of metal/IMC composites quantitatively examined.

Metal/IMC Designation	*Temperature (°C)*	*Extrusion Ratio*	*Particle Aspect Ratio*	*% Error*	*Tensile Strain*	*Average Length (μm)*	*Average Width (μm)*
T4040A	1200	18:1	16 ± 4	26	1.59±0.30	469	37
T4040A	1200	25:1	40 ± 15	38	2.62±0.66	886	31
T4040γ	1200	9:1	3 ± 0.3	11	0.13±0.05	176	62
T4040γ	1200	25:1	3 ± 0.3	11	0.12±0.06	164	62
T4000A	1200	16:1	400*		>13	>13000*	30*
T4020A	1200	11:1	75 ± 16	22	4.64±0.60	1098	15
T2040A	1200	21:1	5 ± 1	27	0.49±0.15	128	34
T3040A	1200	23:1	11 ± 4	35	1.04±0.28	302	32
T3040A	1180	20:1	12 ± 4	48	1.02±0.35	569	36
T3040A-L	1200	36:1	9 ± 2	23	1.70±0.36	678	43
T3040A-S	1200	36:1	19 ± 4	23	0.93±0.21	125	16

* IMC phase was co-continuous with Ti-6Al-4V matrix. This number represents the average measured particle width versus the section length (maximum possible measurable length).

5.4. Discussion

5.4.1. The effect of pre-processing IMC particle size on codeformation

Figure 38 shows the effect of pre-processing IMC particle size on the codeformation behavior of the IMC particles. IMC particle size measurements were performed via mechanical screen sieving (ASTM standard B214-92[81]). This technique has a tendency to give results with approximately 5% error skewed toward coarser particles.[82] Therefore, the imprecision of this technique lends itself to qualitative guidelines for IMC size effects.

Metallograhic comparison of these composites shows significantly more porosity in the samples reinforced with larger IMC particles. This tendency is likely due to pores acting as fracture initiation sites during the reduction of the smaller particles, thereby diminishing their presence. Consolidation of the pores present in larger particles offers one explanation to the larger degree of codeformation achieved by these particles. Another proposed explanation can be found in the interaction between particle and matrix. Hypothetically, the surface area to volume ratio of a large particle is much less than that of a smaller particle. During processing, there are many modes of loading placed on the particles. Under shearing, friction between particle and matrix will be

more pronounced for particles with higher surface areas, i.e., larger particles. This increased friction would result in more efficient load transfer to larger particles, hence more codeformation. In this case, smaller particles may actually "tumble" rather than deforming due to rotational moments imposed upon them. This would lead to less codeformation.

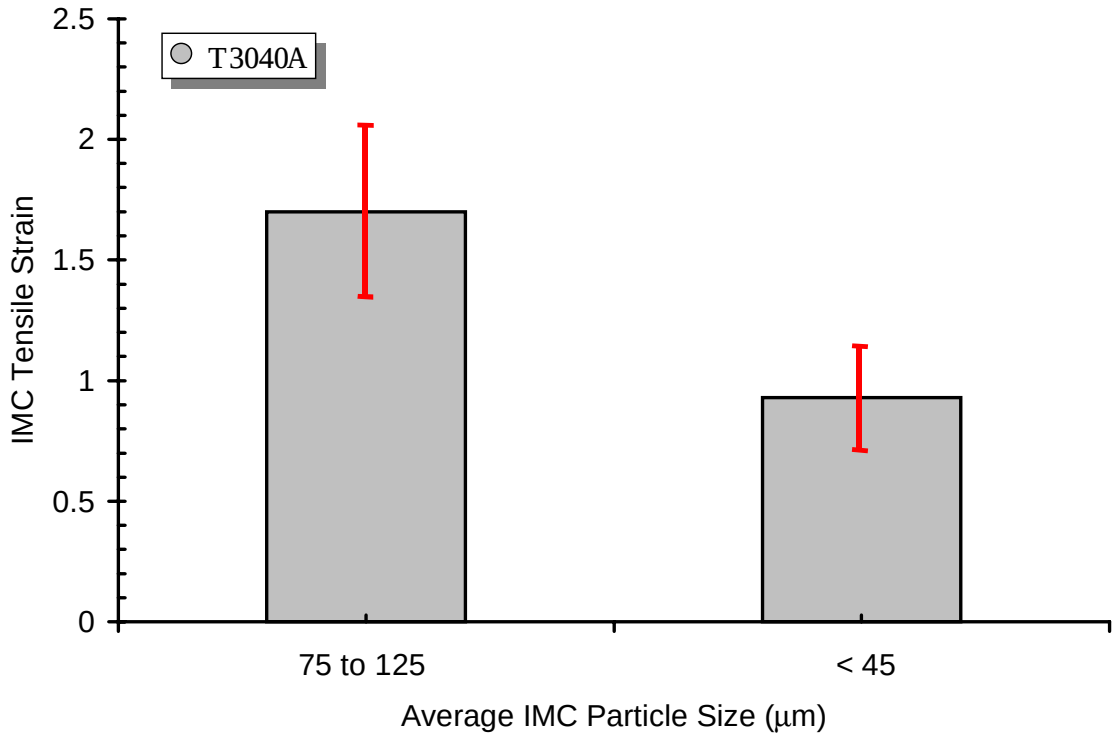

Figure 38: The average IMC tensile strain, resulting from extrusion, as a function of the average IMC particle size. The IMC particle size in this chart represents a range of particle sizes.

5.4.2. The effect of volume % IMC on codeformation

The amount of IMC reinforcement in the composite also effects the codeformation behavior. Figure 39 shows the tensile strain as a function of the volume % (Al_3Ti + 40 v% TiB_2). As the volume percentage of IMC increases, there is an increase in the average IMC tensile strain. It is likely that this is an effect of the increased presence of Ti-6Al-4V. The Ti-6Al-4V has a lower flow stress than the IMC phase at these temperatures. This limits the ability of the titanium alloy to effectively transfer load to

the IMC phase as effectively. This results in the Ti-6Al-4V matrix deforming more than the IMC particles, i.e., less commensurate deformation.

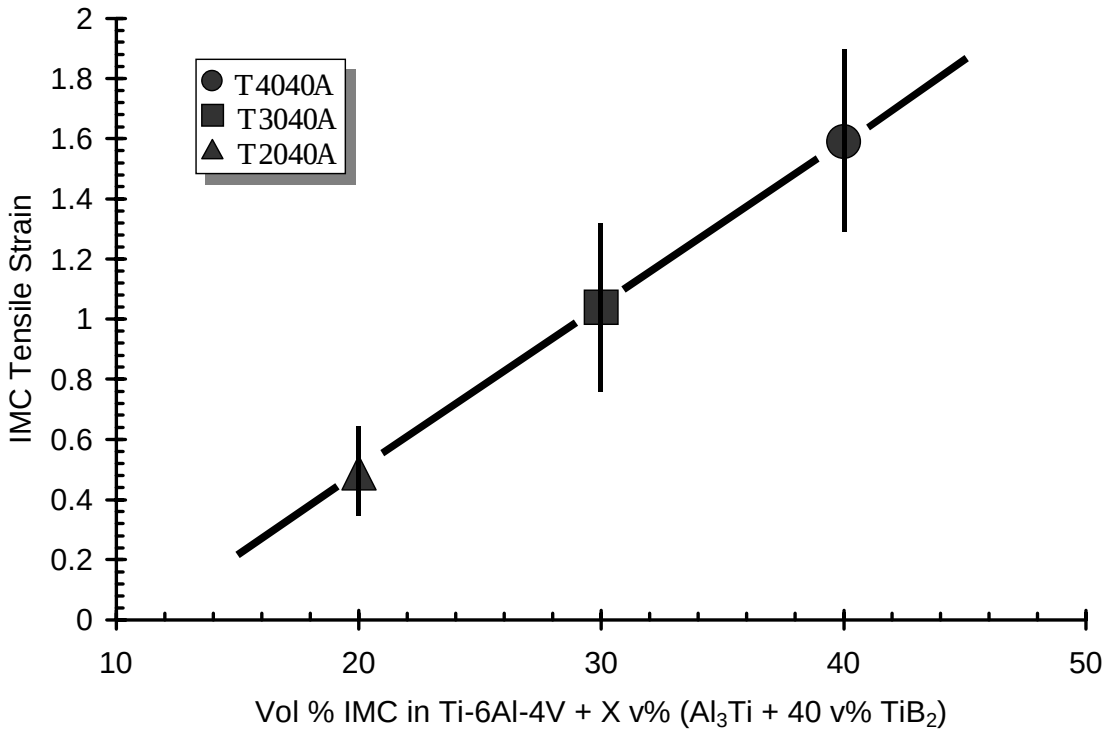

Figure 39: The average IMC tensile strain, resulting from extrusion, as a function of the nominal volume percentage of IMC.

5.4.3. The effect of temperature and matrix composition on codeformation

All composites were extruded well above the brittle to ductile temperature (BDT) for the intermetallic matrices used in the IMCs. The influence of temperature on deformation behavior is often measured in terms of the homologous temperature. In this case, the homologous temperature is defined as the ratio of initial billet temperature to the melting temperature of the intermetallic alloy used in the IMC "reinforcement". Figure 40 shows the influence of homologous temperature on the codeformation behavior in terms of the particle aspect ratio and the tensile strain. The effect of extrusion temperature also reveals the effect of matrix composition. The melting temperature of the $Ti_{54}Al_{46}$ intermetallic matrix is higher than that of the Al_3Ti, and the homologous temperatures are affected accordingly. Figure 40 shows that as the homologous temperature increases,

the IMC phase exhibits more deformation. The slight deviation from the trend shown by the two Al_3Ti-based IMC samples is likely due to the small temperature variation (1180° versus 1200°C).

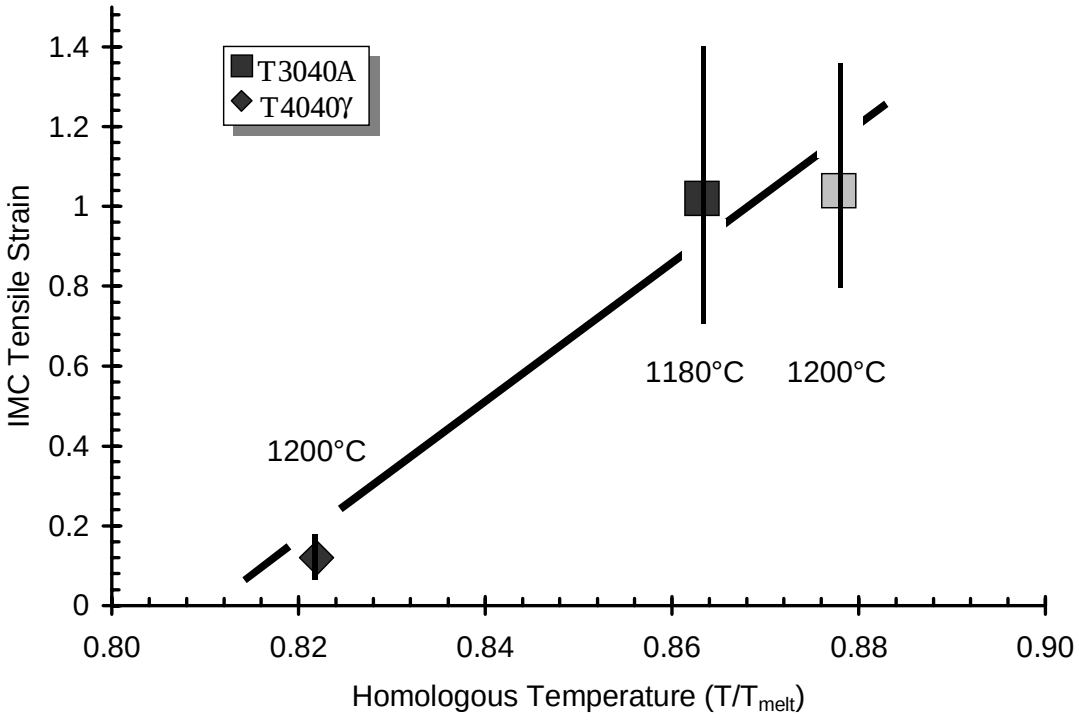

Figure 40: The IMC particle strain as a function of the homologous temperature for Ti-6Al-4V + 30 v% (Al_3Ti + 40 v% TiB_2) extruded at 1180°C, Ti-6Al-4V + 30 v% (Al_3Ti + 40 v% TiB_2) extruded at 1200°C, and Ti-6Al-4V + 40 v% ($Ti_{54}Al_{46}$ + 40 v% TiB_2) extruded at 1200°C.

5.4.4. The effect of strain-rate on codeformation

The extrusion strain-rate is determined by dividing the extrusion ram speed by the change in the extrusion length (as determined by the amount of billet which was extruded versus the extruded length). Samples reinforced with 40 v% (Al_3Ti + 40 v% TiB_2) were examined in terms of the applied extrusion strain-rate. The results of this analysis are shown in Figure 41. Although no strong correlation is observed, a general increase in the amount of IMC strain as the extrusion strain-rate increases. This may be linked to the slightly decreasing flow stress ratio shown to occur with increasing strain-

rate, as shown previously in Figure 26a. However, the lack of a significant trend is more likely due to the narrow range of strain-rates observed and the limited influence this processing variable has on codeformation in these conditions (i.e., high temperature, low strain-rate).

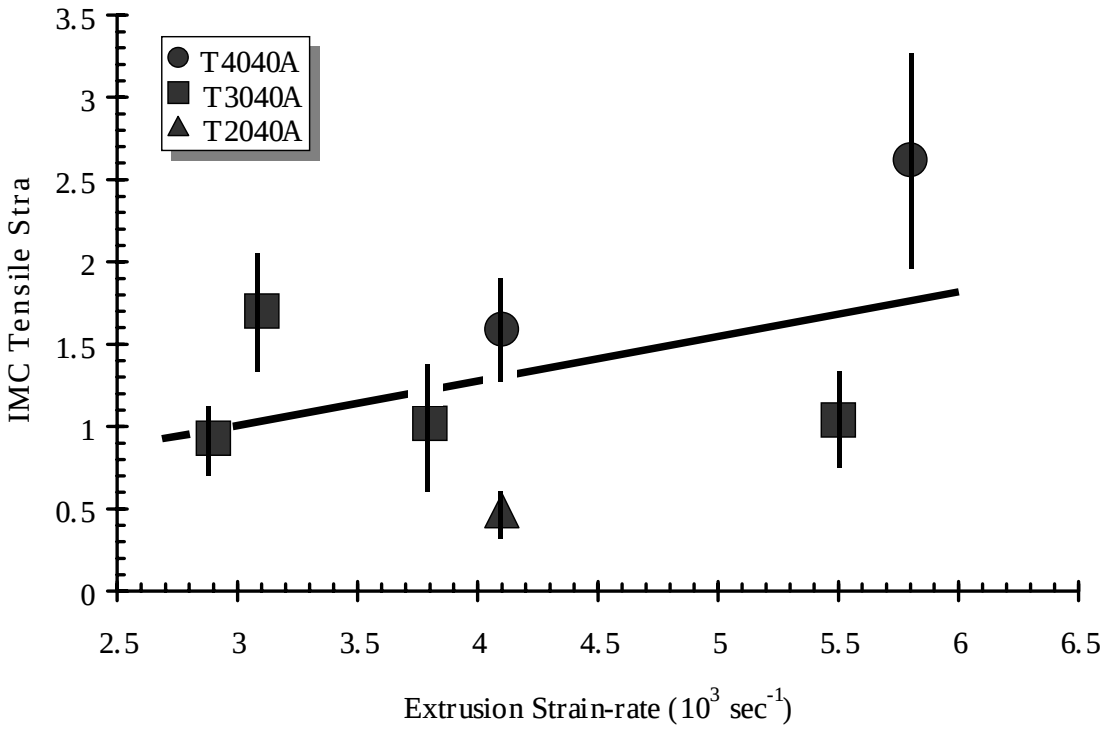

Figure 41: The IMC particle strain as a function of strain-rate for Ti-6Al-4V + 40 v% (Al_3Ti + 40 v% TiB_2), Ti-6Al-4V + 30 v% (Al_3Ti + 40 v% TiB_2), and Ti-6Al-4V + 20 v% ($Ti_{54}Al_{46}$ + 40 v% TiB_2).

5.4.5. The effect of volume % TiB_2 on codeformation

The effect of volume percentage TiB_2 within an Al_3Ti matrix IMC was analyzed for a series of Ti-6Al-4V + 40 v% (Al_3Ti + *X* v% TiB_2) composites. Actual particle aspect ratio measurements were impossible for the Ti-6Al-4V sample reinforced with Al_3Ti because the two components were co-continuous, and so an estimate was employed. This co-continuous microstructure is shown in Figure 42. An estimate, based upon the measured average width of Al_3Ti particles and the total possible length given the length of the transverse section, was employed to discuss trends.

Figure 43 shows the effect of TiB_2 on the codeformation of the metal/IMC composites. A significant increase in IMC particle deformation is observed with decreasing volume % TiB_2. This is an effect of the volume occupied by the non-deformable TiB_2 particulates.

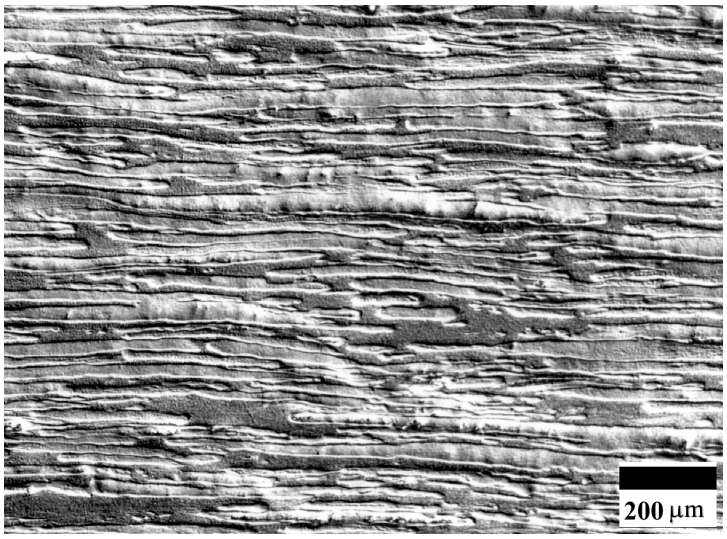

Figure 42: A micrograph of an as-polished and etched transverse cross-section taken from the center of the Ti-6Al-4V + 40 v% Al_3Ti extrusion. The Al_3Ti is shown as the darker gray component and is co-continuous with the Ti-6Al-4V component (lighter gray).

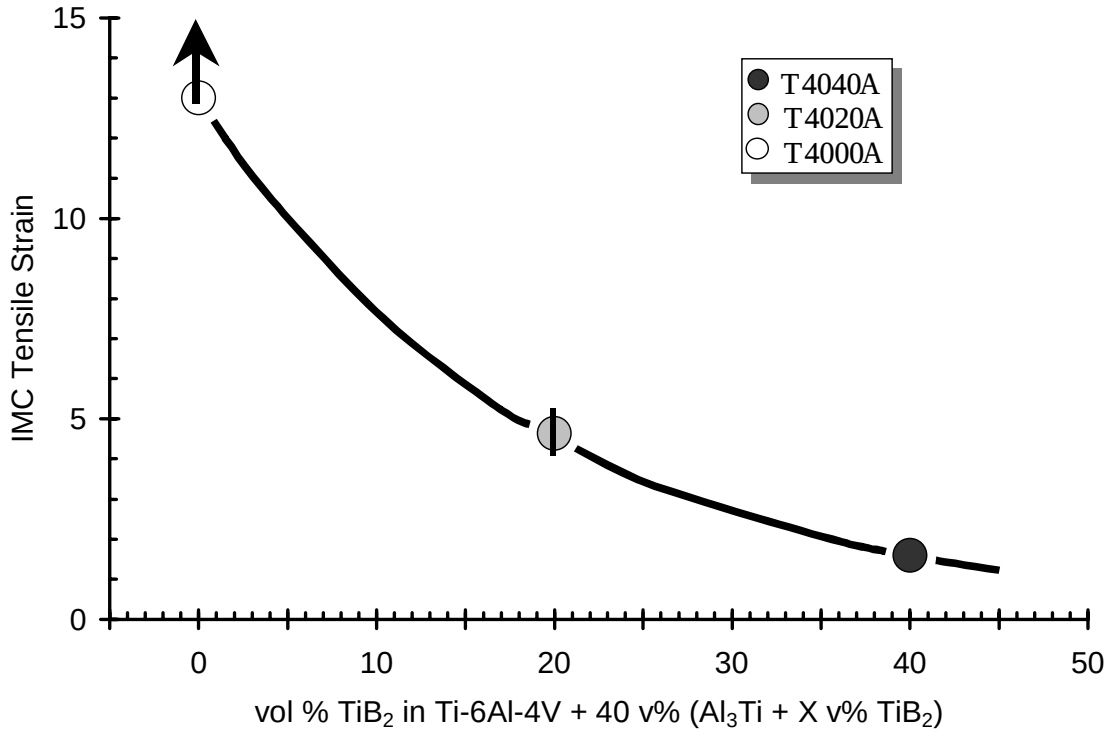

Figure 43: The tensile strain as a function of the v% TiB_2 for Ti-6Al-4V + 40 v% (Al_3Ti + 40 v% TiB_2), Ti-6Al-4V + 40 v% (Al_3Ti + 20 v% TiB_2), and Ti-6Al-4V + 40 v% Al_3Ti. Each of these composites were extruded at 1200°C.

The effect of TiB_2 presence is illustrated schematically in Figure 44. Figure 44a shows an IMC particle with 40 v% ceramic reinforcement. This particle can be examined as 2 components, one deformable (intermetallic) and one rigid (ceramic reinforcement). These 2 slabs are shown in Figure 44b. As the particle is deformed, the deformable component, represented by 60 % of the volume, must accommodate 100% of the imposed strain. The result is that increasing the volume percentage of deformable Al_3Ti in the IMC (i.e., $Al_3Ti \rightarrow Al_3Ti$ + 20 v% $TiB_2 \rightarrow Al_3Ti$ + 40 v% TiB_2, in decreasing order) increases the plastic strain accumulated by the particle.

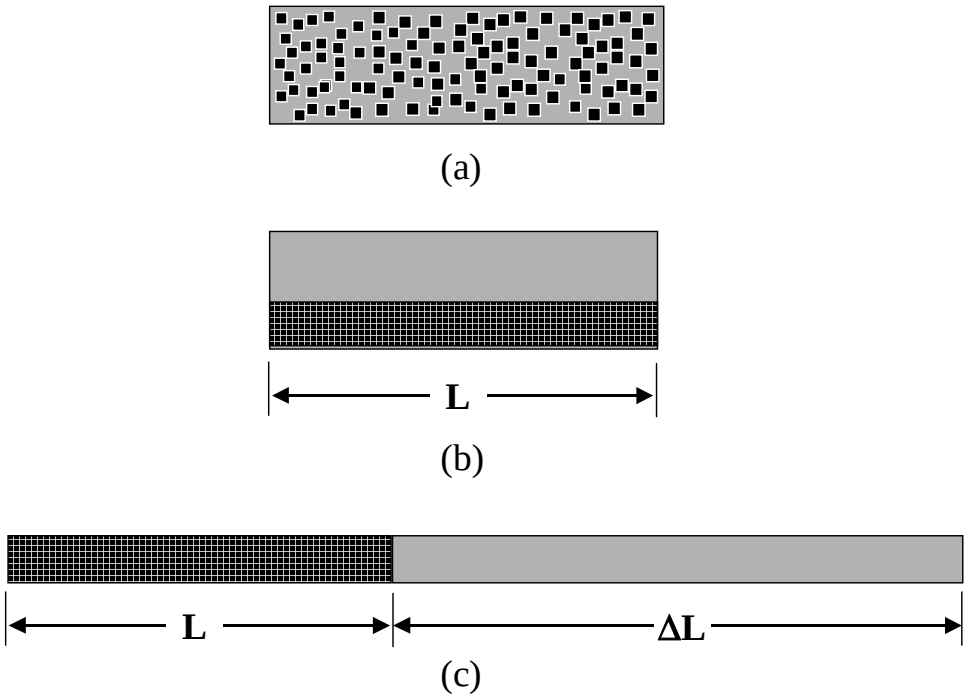

Figure 44: An analysis illustrating the effect of 40 v% TiB_2 on the deformation behavior of a codeformed IMC. (a) The IMC particle consists of 2 components: one deformable (light) the other rigid (dark). (b) A continuum approach would represent this system as 2 slabs of material. The amount of deformation (c) is limited by the amount of deformable (e.g., orange, intermetallic matrix) component, which is forced to absorb 100% of the applied strain.

5.4.6. Correlation of Codeformation to Relative Flow Stress

The relative flow stress is the ratio of the flow stress of the reinforcment to the matrix and is believed to be the controlling factor in the codeformation of materials. As discussed in Chapter 4, flow stresses are influenced by composition, temperature and strain-rate. Flow stress ratios can be examined as a function of temperature and strain-rate, using the phenomenologically-based flow stress equation described earlier. Initially, the flow stress ratios were used to aid in the determination of extrusion parameters likely to induce commensurate deformation. These same plots (i.e., Figure 26a and b) graphically show the flow stress ratios examined here. The current discussion is limited to data available from testing performed in Chapter 4, specifically data for Al_3Ti + 40 v% TiB_2 shown in Figure 26a. In determining the flow stress ratio, two assumptions are made: the extrusion temperature remains close to that of the initial billet

temperature and the strain-rate is as described in section 5.4.4. The extrusion conditions and the resultant flow stress ratios are shown in Table IX.

Table IX: Flow stress ratio data for the series of examined extrusions.

M/IMC Designation	***Temperature (°C)***	***Strain-rate ($x\ 10^{-3}\ sec^{-1}$)***	***Flow Stress Ratio***	***Average IMC Tensile Strain***
T4040A-Lo	1200	4.06	2.39	1.59 ± 0.20
T4040A-Hi	1200	5.79	2.33	2.62 ± 0.66
T2040A	1200	4.11	2.39	0.49 ± 0.15
T3040A	1200	5.50	2.34	1.04 ± 0.28
T3040A-1180	1180	3.78	2.40	1.02 ± 0.35
T3040A-Large	1200	3.09	2.43	1.70 ± 0.36
T3040A-Small	1200	2.90	2.44	0.93 ± 0.21

Figure 45 shows the IMC tensile strain as a function of the flow stress ratio of Al_3Ti + 40 v% TiB_2 to Ti-6Al-4V. No correlation is observed. This is likely due to the extreme ductility of the IMC at these temperatures and strain-rates, even relative to the even more deformable Ti-6Al-4V. Recall from Chapter 4 that the range of flow stresses observed for the Al_3Ti-matrix samples reinforced with 30, 40, and 50 v% TiB_2 at 1200°C and 0.0001 sec^{-1} was from 4 to 10 MPa. This corresponds to a flow stress ratio of 1 to 3 (to Ti-6Al-4V) under similar conditions. This lack of a trend indicates that the effect of TiB_2 on the flow stress at this extreme temperature is small and other factors play a greater role in controlling codeformation behavior. Factors such as volume % TiB_2 and volume % IMC, which have a limiting effect on the degree of IMC deformation, are a more effective predictor of codeformation.

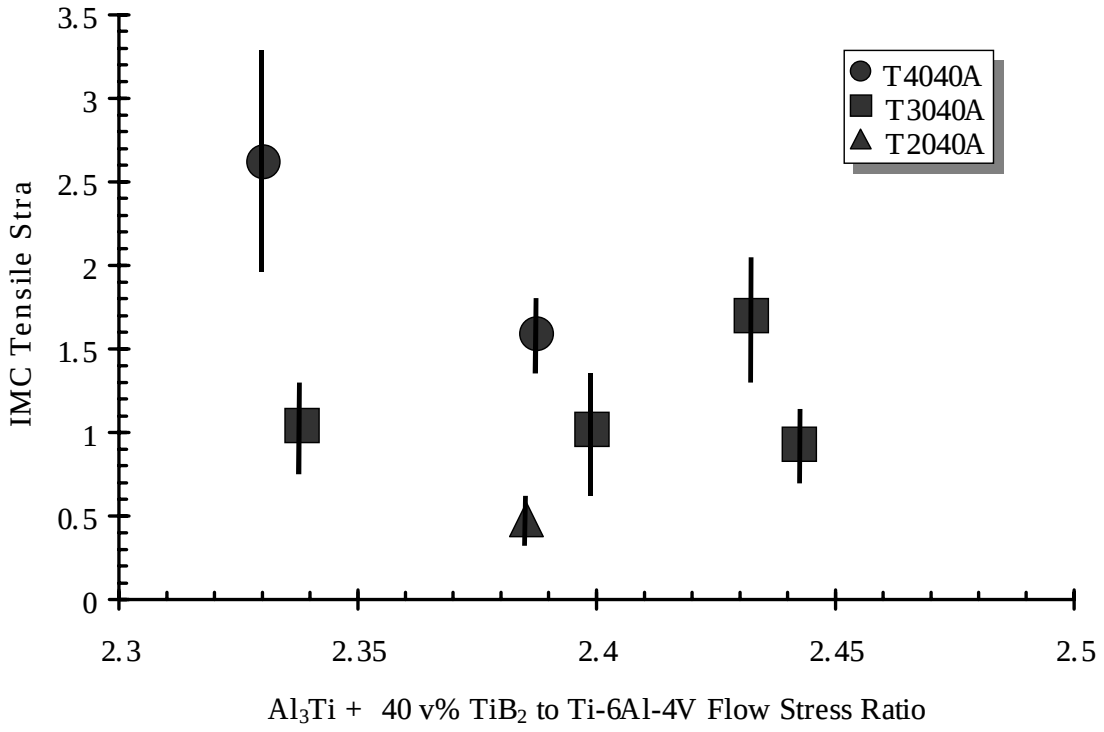

Figure 45: The IMC strain in samples reinforced with Al_3Ti + 40 v% TiB_2 as a function of the calculated relative flow stress.

The factor with the greatest influence on codeformation, though, is the intermetallic alloy composition. This factor is likely a flow stress related effect. There is a significant difference in the IMC strain between the two titanium aluminide matrix composites, as was shown in Figure 26. A more accurate measurement of codeformation would consist of a series of extrusions at constant homologous temperature. A comparison of codeformation behavior at constant flow stress ratio would conclusively show if the disparity between the two intermetallic matrices is a flow stress related phenomonon. This, however, is difficult using a Ti-6Al-4V matrix, as melting might occur in the $Ti_{54}Al_{46}$ intermetallic before this condition is achieved.

Although a correlation to flow stress is not plausible, it should be noted that even with flow stress ratios as high as 2.44, a significant degree of codeformation (nearly 100% strain) was observed. This degree codeformation is counter to the results predicted by Zahrah and colleagues using finite element simulation.[83] This feature of Zahrah's study

may be a result of the mesh used in the simulation. The development of a more accurate model, based upon Zahrah's model, will be the foundation of the final portion of this research.

5.5. Summary

- Flow stress maps, as calculated in Chapter 4, were used to select extrusion conditions under which codeformation was likely to occur. These conditions were used to successfully extrude a series of metal/IMC powder blend composites.
- Commensurate deformation of the metal and IMC components was observed to varying degrees in all cases. The degree of IMC codeformation was evaluated through quantitative microscopy of the final series of extrusions.
- The size of the IMC particles used to reinforce the metal/IMC composites was shown to have an effect on codeformation behavior. The degree of codeformation achieved was less for samples reinforced with fine IMC particles.
- Increasing the amount of IMC reinforcement was observed to affect the codeformation negatively. The limited ability of the Ti-6Al-4V to transfer loading, and hence deformation, onto the IMC particles was responsible for this tendency.
- Increasing homologous temperature, as shown through changes in extrusion temperature and intermetallic matrix alloy, was observed to greatly increase the ability of the IMC to codeform.
- The extrusion strain-rate was calculated and shown to have little effect on the codeformation of the IMC particulate in this elevated temperature regime.
- The volume % of TiB_2 used to reinforce the metal/IMC composites was shown to have the greates effect on codeformation. This effect was explained as a volumetric phenomenon, in which the quantity of deformable intermetallic alloy decided the degree to which codeformation was possible. Samples reinforced with no TiB_2 were shown to have a co-continuous microstructure; having achieved ideal commensurate deformation.

- The flow stress ratios of samples reinforced with Al_3Ti + 40 v% TiB_2 was calculated. No discernable trend was noted with regard to the degree of IMC deformation. This was attributed to the extreme ductility of the IMC particles at these tempeartures and strain-rates.

5.6. References

[78] S. Kalpakjian, *Manufacturing Processes for Engineering Materials, Third Edition*, Addison-Wesley-Longman, Inc. Menlo Park, CA, 1997.

[79] P.R. Roberts, B.L. Ferguson, "Extrusion of Metal Powders", International Materials Reviews, vol. 36, no. 2, pp. 62-79, 1990.

[80] T.H. Courtney, "Strengthening Behavior of In-Situ Composites", in *Metal Matrix Composites: Mechanisms and Properties*. Academic Press, Inc., pp. 101-131, 1991.

[81] ASTM Standard B214-92, "Standard Test Method for Sieve Analysis of Granular Metal Powders", pp. 49-51, 1992.

[82] R.M. German, *Powder Metallurgy Science* 2nd *Edition*, Metal Powder Industries Foundation, Princeton, NJ, pp. 37-40, 1994.

[83] T. Zahrah, et.al. "Development of Intelligent Processing Methodology for Intermetallic Matrix Composites" *ONR Progress Report #N00014-96-C-0427*, MATSYS, Inc. 1998.

6. Simulation of Codeformation Processes

This study has been used to develop a systematic and scientific approach to the study of codeformation processes. Metal/IMC component flow stress data generated in Chapter 4, were used in the advancement of a finite element model of the codeformation process. The experimental results obtained from the actual extrusions, as described in Chapter 5, were utilized to assess the accuracy of the model.

6.1. Introduction

The ability to perform engineering analyses on large complex structures without the need for extensive prototyping has been the driving force behind the development of the finite element method. The finite element method (FEM) or finite element analysis (FEA) refers to a problem solving technique in which a complicated continuum problem, can be discretized into smaller "finite elements" each having some simple shape. Using this technique, the continuum problem, represented by a series of complex differential equations, is transformed into a series of interdependent algebraic equations. The interdependent relationships of the important variables for the finite elements can then be assembled into a large matrix of interdependent algebraic equations.[84] These equations are solved simultaneously until a convergent solution is found. The finite elements are then reassembled and the individual solutions interpreted to formulate a complete solution.

Only recently has this method begun to be applied to metal-forming processes. The primary objective of any metal-forming analysis is to predict the kinematic relationships between the undeformed billet and the as-deformed piece.[85] This generally includes the prediction of temperature and heat flow, as these factors influence material flow behavior.

In the modelling of most hot deformation processes, an assumption of rigid-plastic material behavior is practical. The amount of elastic strain is considered negligible in comparison to the total strain, and at processing temperatures greater than the

recrystallization temperature of the metal, an assumption of limited linear work hardening (i.e., plastic flow behavior) is also valid.[86]

The Zahrah model, described briefly in Chapter 2, provides a method for evaluating the influence of relative flow behavior, volume percentage of reinforcement, and reinforcement particle size on the equivalent strain of the extruded model. The model allows the user to define the flow behavior of specific elements relative to other elements. In this manner, the properties of the matrix and reinforcement materials can be applied to elements defined as "matrix" or "reinforcement". A unique feature of Zahrah's work is the method used to interpret the interaction of matrix/reinforcement elements. The interpretation is performed by applying the equivalent strain-distribution resulting from deformation onto the original finite element mesh. Zahrah interprets the strain gradients along regions of matrix/reinforcement contact as being indicative of the degree of commensurate deformation and hence, IMC particle elongation.

A finite element model has been developed based on the model developed by Zahrah, *et. al*.[87] The function of this finite element model is highlighted by its ability to predict favorable process conditions leading to commensurately deformed structures. This type of model can be altered to independently assess the influence of material properties and process conditions on codeformation, thereby assisting in process optimization. Furthermore, the concepts behind the model are adaptable to other codeformation operations, such as rolling, wire drawing, or forging.

In the present study, the finite element method was used to independently evaluate the influence of metal/IMC composition, temperature, ram speed, and extrusion ratio in terms of the influence these parameters have on component (i.e., matrix and reinforcement) flow stress. The Ti-6Al-4V matrix and the IMC reinforcements are mechanically dissimilar materials; therefore, the relative flow stresses of these materials will have considerable influence on codeformation. Additionally, it is reasonable to assume that variations in the size, and volume percentage of the reinforcement elements will also have an effect on the degree of achievable codeformation. Each of these factors was independently evaluated in the series of models developed.

6.2. Experimental

An axisymmetric finite element model developed to simulate extrusion is shown in Figure 46. The finite element model consists of a 60 by 20 mesh combining three types of elements: four-noded axisymmetric elements (shown red in Figure 46) contact elements (shown blue in Figure 46), and rigid surface (shown green in Figure 46). The axisymmetric elements describe the workpiece, the rigid surface represents the extrusion tooling, and the contact elements represent the frictional interaction between the two.

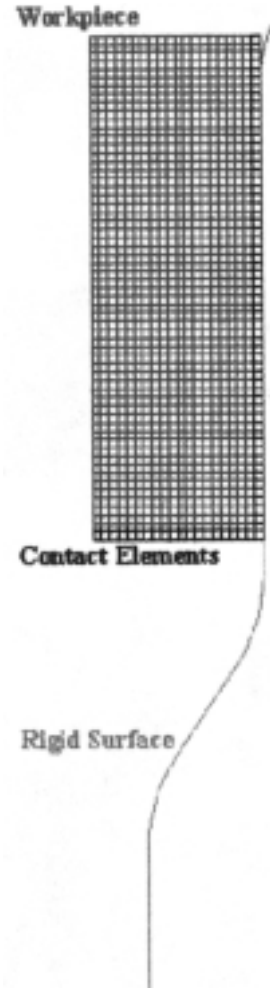

Figure 46: The finite element model mesh used in the simulation of codeformation via extrusion.

The simulation was performed using the commercial FEM code, ABAQUS®. Downward displacements were applied to the top of the workpiece force it through the smaller area, representing the die, at the bottom half of the model. A friction coefficient is applied to

the contact elements to simulation the shear forces between the workpiece and the extrusion chamber.

Simulations were performed with 20, 30, or 40 v% IMC reinforcement. A random number generator was used to define elements as "matrix" or "reinforcement" in a randomly dispersed "particle reinforced" mesh, having the appropriate volume percentage of fine or coarse particles.[88] Alterations to the model provide the ability to explicitly define the initial yield stress of each component.

Models were developed to simulate several of the experimental extrusions described in Chapter 5. Recall that in Chapter 4, flow stresses were calculated for Ti-6Al-4V and the IMCs as a function of temperature and strain-rate. In each of the models developed, the experimentally-derived flow stress for each component was used to describe the flow behavior of that component for the conditions of the specific extrusion. The details of each finite element models are shown in Table X.

Table X: A list of the extrusion simulations and the conditions under which the simulations were performed. In all cases, the flow stress for the matrix was 45-50 MPa.

Extrusion Simulation	***Particle size (fine/coarse)***	***Vol % particle reinforcement (20, 30, 40)***	***Initial temperature (°C)***	***Extrusion strain-rate (sec^{-1})***	***Flow stress ratio (σ_r/σ_m)***	***Flow stress of the reinforcement (MPa) *****
Ti-6Al-4V	n/a	n/a	1200	0.005	1	45-50
T4040A-Lo	fine	40	1200	0.0041	2.39	108-120
T4040A-Hi	fine	40	1200	0.0058	2.33	105-117
T4040γ-Lo*	fine	40	1200	0.0095	13.18	593-659
T2040A	fine	20	1200	0.0041	2.39	108-120
T3040A	fine	30	1200	0.0055	2.34	105-117
T3040A-1180	fine	30	1180	0.0038	2.52	113-126
T3040A-Lg	coarse	30	1200	0.0031	2.43	109-122
T3040A-Sm	fine	30	1200	0.0029	2.44	110-122

* Simulations of samples reinforced with 40 vol% ($Ti_{54}Al_{46}$ + 40 vol% TiB_2).
** The flow stress range accounts for linear work hardening from the initial yield stress to a maximum value at a strain of 2.0.

6.3. Results

The results of extrusion simulation are displayed as contours of effective or equivalent plastic strain:

$$\bar{\varepsilon} = \frac{\sqrt{2}}{3}\sqrt{\left(\varepsilon_{p1}-\varepsilon_{p2}\right)^2+\left(\varepsilon_{p2}-\varepsilon_{p3}\right)^2+\left(\varepsilon_{p3}-\varepsilon_{p1}\right)^2} \qquad \text{(Equation 10)}$$

The equivalent strain provides an adequate representation of the accumulated plastic strain in two dimensions. Although the strain values are not quantitatively accurate, their values may be used to illuminate trends in codeformation behavior. Of particular interest to this study is the difference in strain between elements representing the matrix and the reinforcement. The relative amount of codeformation between extrusion simulations can be assessed through comparison of the matrix to reinforcement strain ratio. As this ratio increases, the matrix absorbs more strain, hence less codeformation is predicted to occur. The equivalent plastic strains for each component, the average strain for the entire mesh, and the matrix to reinforcement strain ratios for each simulation are shown in Table XI.

Table XI: The results of extrusion simulations for the finite element models shown in Table X in terms of the equivalent plastic strain for each element type, the average total strain, and the strain ratio.

Extrusion Simulation	*Average Matrix Element Strain*	*Average Reinforcement Element Strain*	*Average Total Strain*	*Matrix to Reinforcement Strain Ratio*
Ti-6Al-4V	1.94	N/A	1.94	1
T4040A-Lo	1.92	1.57	1.78	1.22
T4040A-Hi	1.91	1.56	1.77	1.22
T4040γ-Lo*	1.28	0.67	1.03	1.91
T2040A	2.17	1.69	2.07	1.28
T3040A	2.20	1.78	2.07	1.24
T3040A-1180	2.23	1.78	2.07	1.25
T3040A-Lg	2.23	1.77	2.09	1.26
T3040A-Sm	2.40	1.72	2.09	1.40

6.3.1. Simulated extrusion of a monolithic billet

Ideal codeformation, as would occur in a monolithic billet, is homogeneous; having very little strain gradient between the different element types. The results of a simulation of the extrusion of a monolithic Ti-6Al-4V billet at 1200°C and 0.005 sec^{-1} are shown in Figure 47. These results show homogeneous deformation, and an overall average strain of 1.94.

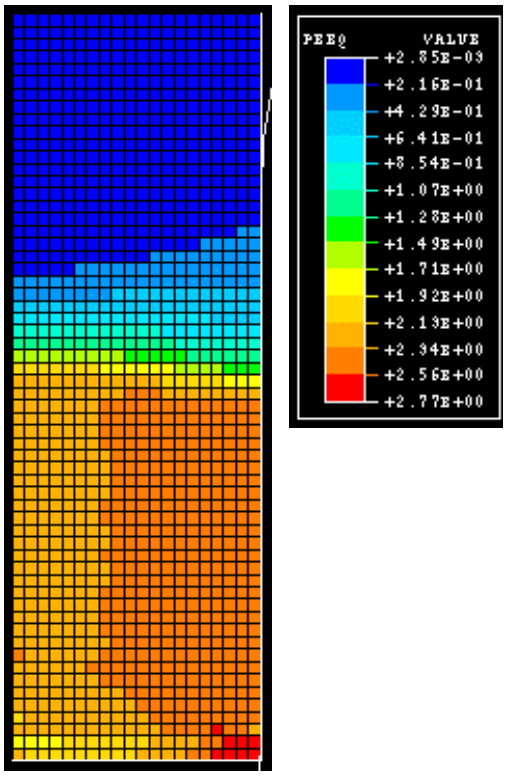

Figure 47: The equivalent strain results of a finite element simulation of monolithic Ti-6Al-4V at 1200°C and 0.005 sec^{-1}. Note that there is very little variation in strain, indicating homogeneous deformation.

6.3.2. Effect of reinforcement volume percentage

Extrusions of 20, 30, and 40 v% IMC reinforcement were simulated to evaluate the influence of volume percentage reinforcement on codeformation. Process conditions vary slightly from one extrusion to the other. The conditions (i.e., temperature and strain-rate) set for each extrusion were as outlined in Table X. The finite element mesh and results for these simulations are shown as Figure 48 (20 v% IMC), Figure 49 (30 v% IMC) and Figure 50 (40 v% IMC). Simulations of the 20 v% reinforced samples reveal that the strain in the matrix is 28% higher than the average strain in the reinforcements. This percentage decreases with increasing v% of reinforcement, from 24% higher than the reinforcement in the samples reinforced with 30 v% IMC to 22% higher in samples reinforced with 40 v% IMC.

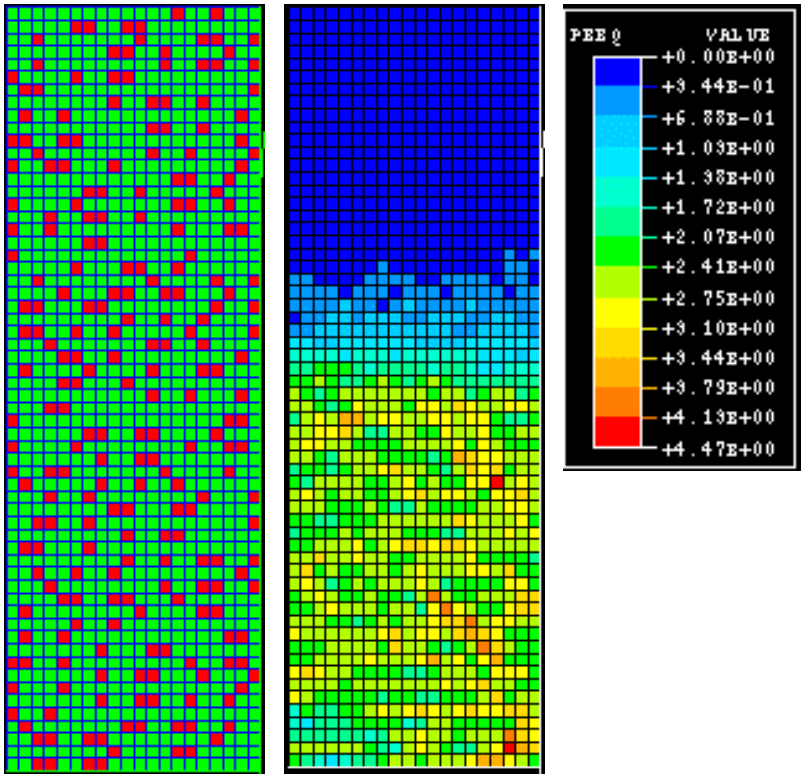

(a) (b)

Figure 48: The (a) initial mesh and the (b) resulting equivalent strain from a simulation of the extrusion of a Ti-6Al-4V + 20 v% (Al_3Ti + 40 v% TiB_2) billet extruded at 1200°C and 0.0041 sec^{-1}.

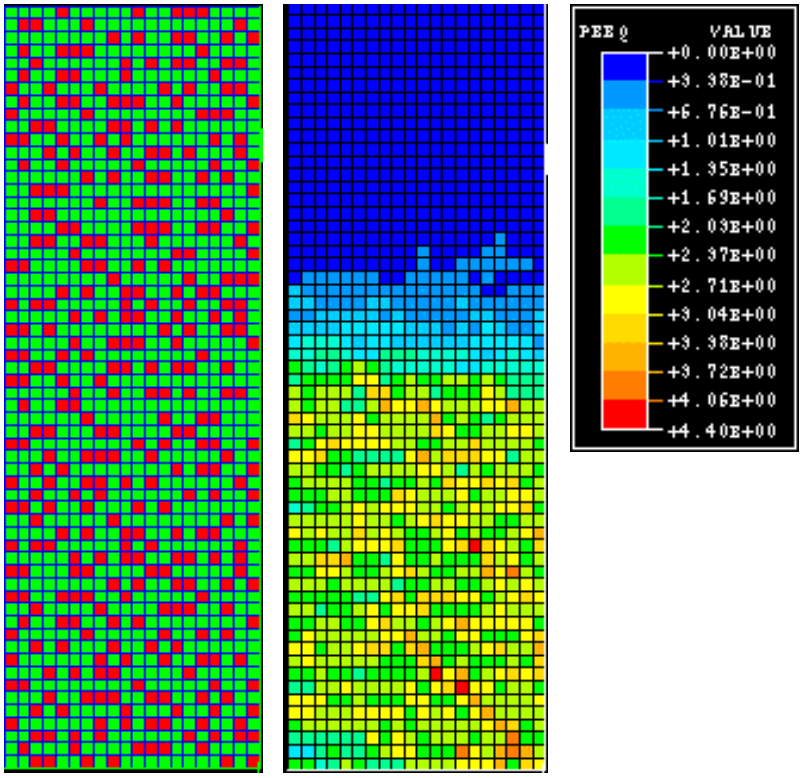

(a) (b)

Figure 49: The (a) initial mesh with fine reinforcement and the (b) resulting equivalent strain from a simulation of the extrusion of a Ti-6Al-4V + 30 v% (Al_3Ti + 40 v% TiB_2) billet extruded at 1200°C and 0.0055 sec^{-1}.

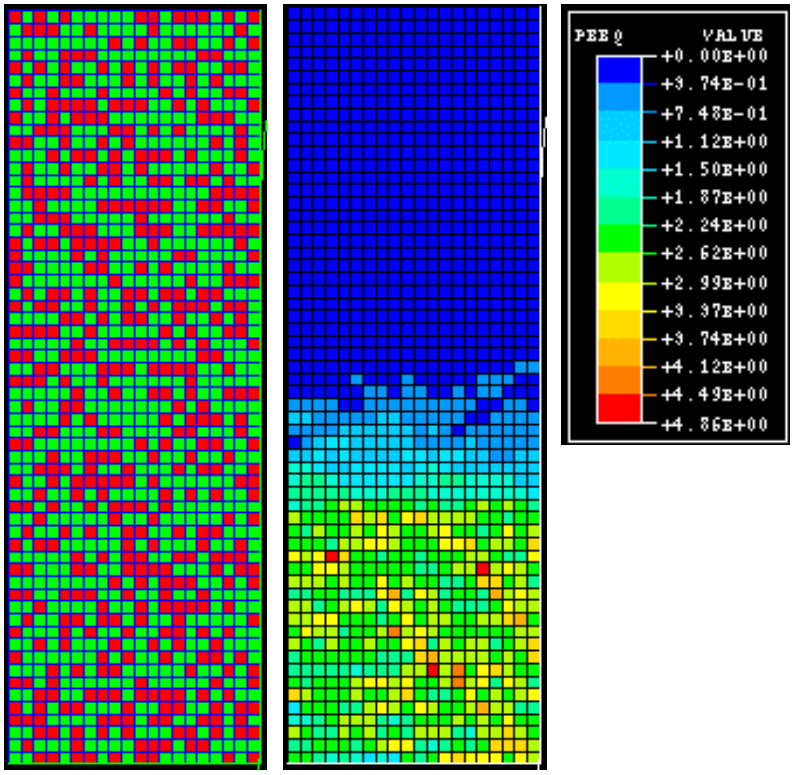

(a) (b)

Figure 50: The (a) initial mesh and the (b) resulting equivalent strain from a simulation of the extrusion of a Ti-6Al-4V + 40 v% (Al_3Ti + 40 v% TiB_2) billet extruded at 1200°C and 0.0041 sec^{-1}.

6.3.3. Effect of reinforcement particle size

Extrusions of coarse and fine 30 v% IMC reinforcement were simulated to evaluate the influence of reinforcement particle size on codeformation. The simulations were run using the flow stresses of the components for conditions as specified in Table X. The finite element meshes and equivalent strain results of the coarse particulate simulation are shown in Figure 51. The mesh and results of the fine particulate simulation are shown in Figure 52. The average equivalent strain in the matrix is about 26% higher than the reinforcement for the fine particulates and 40% higher for the coarse particulates.

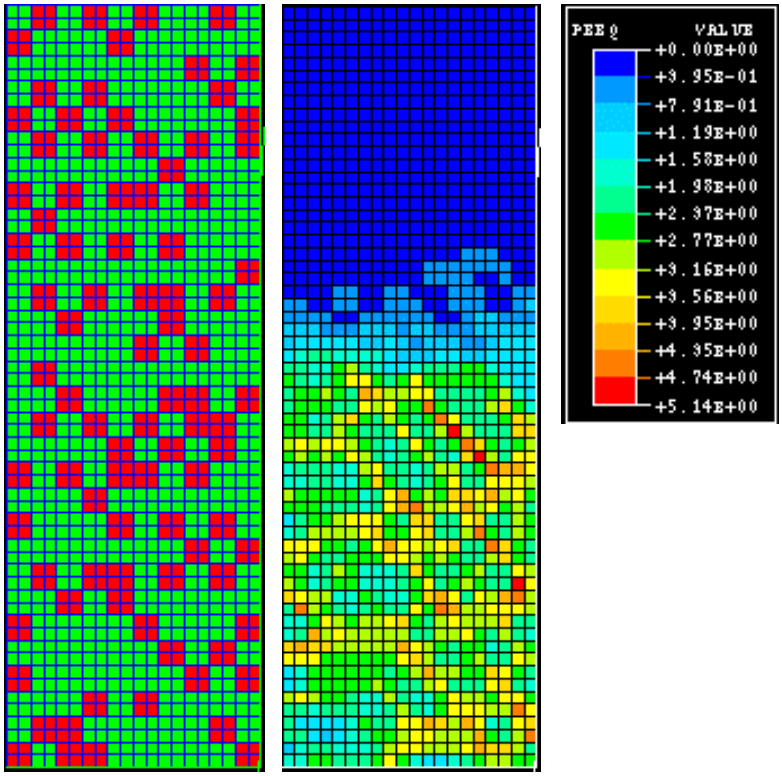

(a) (b)

Figure 51: The (a) coarse initial mesh and the (b) resulting equivalent strain from a simulation of the extrusion of a Ti-6Al-4V + 30 v% (Al_3Ti + 40 v% TiB_2) billet extruded at 1200°C and 0.0031 sec^{-1}.

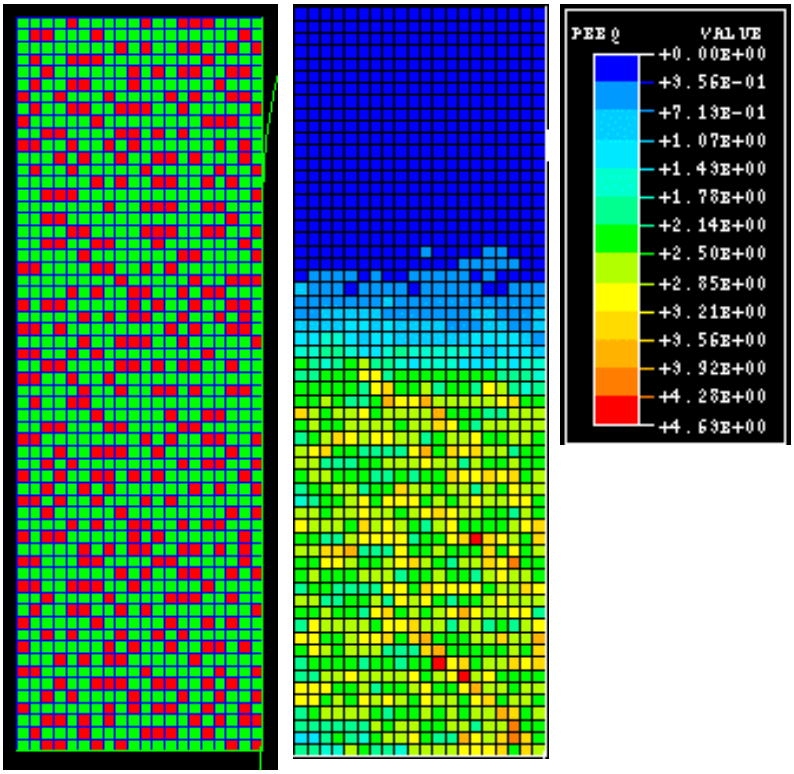

(a) (b)

Figure 52: The (a) fine initial mesh and the (b) resulting equivalent strain from a simulation of the extrusion of a Ti-6Al-4V + 30 v% (Al_3Ti + 40 v% TiB_2) billet extruded at 1200°C and 0.0029 sec^{-1}.

6.3.4. Effect of IMC composition

The effect of IMC composition was evaluated through the simulation of extrusions reinforced with 40v% (Al_3Ti + 40v% TiB_2) and 40v% ($Ti_{54}Al_{46}$ + 40 v% TiB_2). These models are shown as Figure 50 and Figure 53, respectively. The average equivalent strain of the matrix is 22% higher than the IMC reinforcement in the Al_3Ti + 40v% TiB_2 reinforced samples, but this increases to 91% for samples reinforced with $Ti_{54}Al_{46}$ + 40 v% TiB_2.

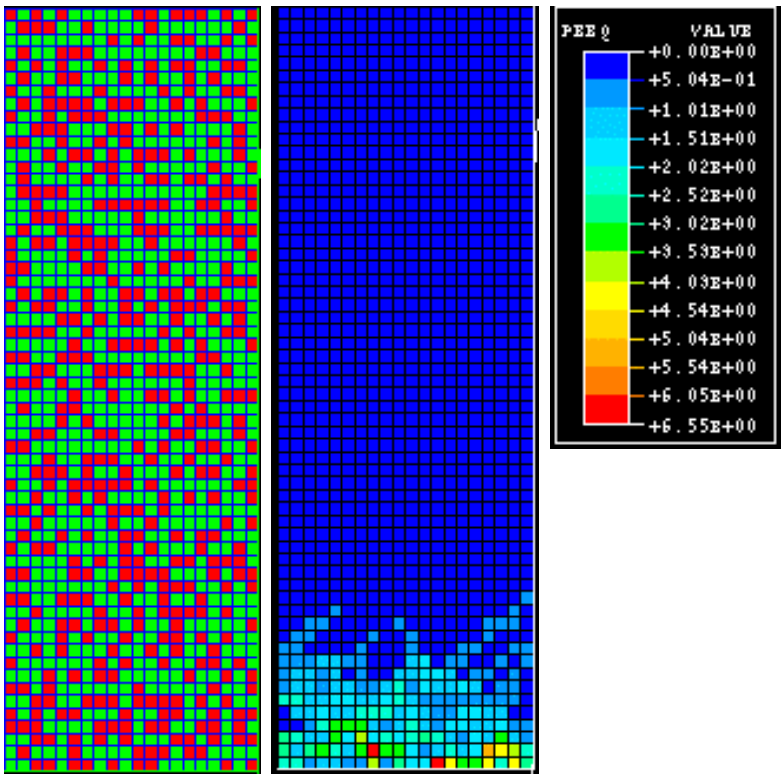

(a) (b)

Figure 53: The (a) initial mesh and the (b) resulting equivalent strain from a simulation of the extrusion of a Ti-6Al-4V + 40 v% ($Ti_{54}Al_{46}$ + 40 v% TiB_2) billet extruded at 1200°C and 0.0028 sec^{-1}.

6.3.5. Effect of Process Conditions

The influence of two process conditions, temperature and strain-rate, were examined in the extrusion simulations. The finite element model developed does not currently support alterations in the strain-rate or temperature directly. Therefore, the relative component flow stress was used to accommodate variations in each. The flow stress was altered through the use of the flow stress equation, as described in Chapter 4. The reader is referred to Chapter 4 for detailed information on these calculations. The flow stresses ratios utilized to simulate these conditions are shown in Table X.

The strain-rate is influence by the ram speed and the die ratio in actual extrusion processes. In the models developed to simulate the effect of strain-rate, the ram speed

and extrusion ratios were held constant. Simulations of 40 v% fine IMC-reinforced samples were performed with flow stresses calculated for strain-rates of 0.0041 and 0.0058 sec^{-1}. The meshes and results for each are shown as Figure 50 and Figure 54, respectively. The average equivalent strain of the matrix was 22% higher than the reinforcement in both cases.

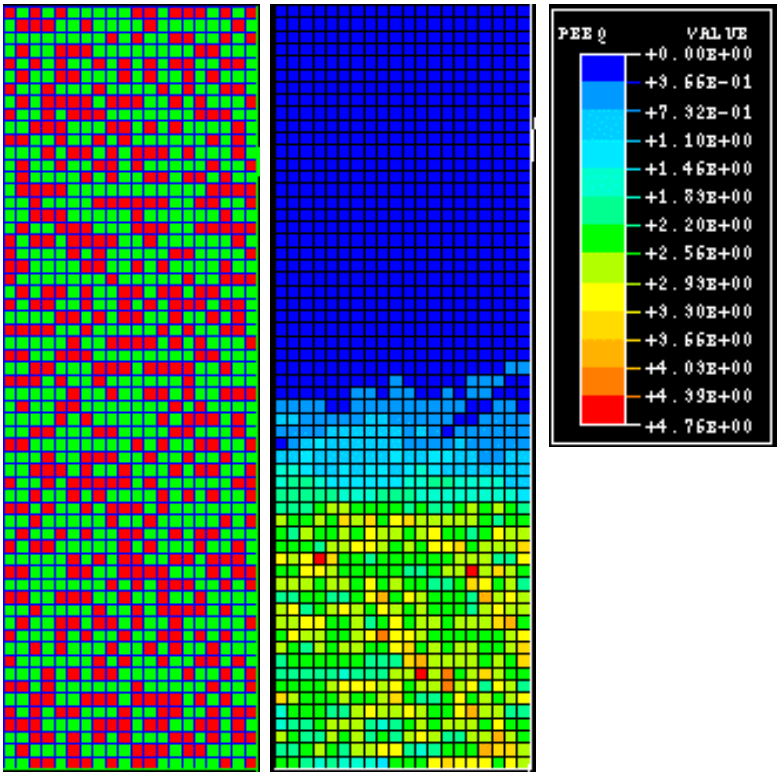

(a) (b)

Figure 54: The (a) initial mesh and the (b) resulting equivalent strain from a simulation of the extrusion of a Ti-6Al-4V + 40 v% (Al_3Ti + 40 v% TiB_2) billet extruded at 1200°C and 0.0058 sec^{-1}.

Two extrusions of samples reinforced with 30v% IMC were simulated with flow stresses corresponding to material behavior at 1200°C and 1180°C. These models and their results are shown as Figure 49 and Figure 55, respectively. The average equivalent strain in the matrix increased only slightly from 24% higher than that of the reinforcement to 25% higher than that of the reinforcement as the simulated extrusion temperature decreased from 1200°C to 1180°C.

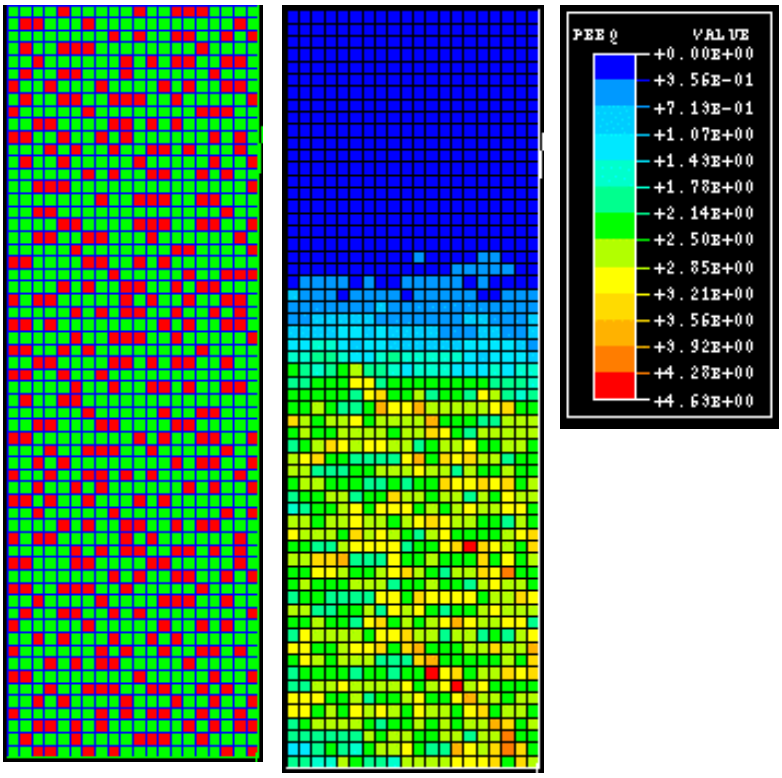

(a) (b)

Figure 55: The (a) initial mesh and the (b) resulting equivalent strain from a simulation of the extrusion of a Ti-6Al-4V + 30 v% (Al_3Ti + 40 v% TiB_2) billet extruded at 1180°C and 0.0038 sec^{-1}.

6.4. Discussion

6.4.1. Correlation of Simulations to Experimental Codeformation

The results of the extrusion simulations are presented in terms of the equivalent strain. In examining the simulation results, it is important to compare the equivalent strain in the composites to that of the monolithic billet (Figure 47). The monolithic billet simulation reveals that there is slightly more strain in regions adjacent to the extrusion tooling. This observation is in agreement with microstructural analyses of the codeformed composites.

Non-homogeneity in the strain distributions, as observed in the composite billet simulations, is due to differences in mechanical response between the matrix and the reinforcements. Comparisons between the average equivalent strain in the matrix and reinforcement provide a means to assess the deformation of the IMC reinforcements.

Higher matrix strains indicate that the matrix absorbed most of the imposed deformation. Hence, less commensurate deformation occurred, resulting in less IMC particle strain.

6.4.1.1. v% IMC Reinforcement

The presence of a flow resistant component in a composite to be codeformed has the effect of changing the strain distribution in the composite. Likewise, changes in the amount of that flow resistant component should also affect the codeformation. Quantitative microscopy of the experimentally codeformed composites showed a roughly linear increase in IMC particle strain with increasing volume percentage (Figure 39). This was attributed to a decrease in the amount of deformable Ti-6Al-4V matrix available to accommodate the imposed deformation. The simulations showed similar results. Increases in the vol% of reinforcement result in lower equivalent strain ratios, and consequentially, a higher degree of codeformation.

6.4.1.2. Reinforcement Size

Simulations were also used to study the effect of the reinforcement element size. These simulations were performed by increasing the reinforcement "particles" from 1 element to 4 elements, i.e., a square 4 times the size of a single element. The meshes, and results, for coarse and fine 30 vol% reinforcement scenarios are shown in Figure 51 and Figure 52, respectively. The equivalent strain in the matrix was shown to increase relative to that of the reinforcement as the reinforcement element size was increased from fine to coarse. The results of the simulations show that as the size of the reinforcement increases, the strain in the matrix climbs from 26% higher than the reinforcement to 40% higher. These results predict that commensurate deformation is more likely to occur for smaller reinforcement particles. Metallographic observations of actual extrusions suggest that larger particles are more codeformed than smaller particles of the same composition. The disagreement of the model to metallographic observations may be attributed to the inability of reinforcement elements in the simulations to rotate within the matrix. The "tumbling" of smaller reinforcement particles was thought to be one factor which lead to decreased deformation in these particles. Similarly, some of the

porosity present in larger particles, which may collapse and lead to increased particle elongation, has not been accounted for in the models.

6.4.1.3. IMC Composition

The composition of the intermetallic matrix (e.g., Al_3Ti or $Ti_{54}Al_{46}$) greatly effects the flow behavior of the IMC reinforcement, as was shown in Chapter 4. Simulations of composites reinforced with 40 v% (Al_3Ti + 40 v% TiB_2) and 40 v% ($Ti_{54}Al_{46}$ + 40 v% TiB_2) were used to test the effects of matrix composition on codeformation. These simulations are shown in Figure 50 and Figure 53, respectively. The great difference in the flow stresses of these materials is evident in the results of these simulations. The Al_3Ti-based IMCs have a flow stress approximately 1.5 times that of the Ti-6Al-4V matrix. This results in a codeformed composite in which the average equivalent strain in the matrix is predicted to be 1.24 times that of the reinforcement. The $Ti_{54}Al_{46}$-based IMC-reinforced samples have flow stresses that are almost 10 times that of the Ti-6Al-4V matrix. The resulting equivalent strains show that the strain in the matrix is 1.91 times that of the $Ti_{54}Al_{46}$-based IMC. These results indicate that the Al_3Ti-matrix IMCs could be commensurately deformed, but the $Ti_{54}Al_{46}$-matrix IMCs should not. This is consistent with the quantitative microscopically observed results from the experimental extrusions.

6.4.1.4. Processing Conditions

The die ratio, ram speed, and temperature of several extrusions were varied to assess the influence such processing parameters on codeformation. Currently, these processing conditions cannot be directly applied to the finite element model. However, the effects of these parameters can be applied through alteration of the flow stress, which is a function of the strain-rate and temperature. Two simulations were investigated to evaluate the influence of strain-rate on codeformation. Simulations of samples reinforced with 40 v% (Al_3Ti + 40 v% TiB_2) and strain-rates of 0.0041 and 0.0058 sec^{-1} showed little change in the amount of commensurate deformation to be expected. Quantitative microscopy of the actual extrusions showed an increase in IMC codeformation of over 50% with increasing flow stress. This disparity is likely a

consequence of the narrow range of flow stresses used in the model. These results could be improved by modification of the model to define changes in die geometry directly.

Two simulations were also performed to assess the influence of initial billet temperature on codeformation. The narrow range of temperatures studied results in a narrow range of flow stresses applied to the models. The results of the quantitative microscopy and the finite element models both proved to be inconclusive. However, the homologous temperature has been shown to have a significant influence upon codeformation. This is evident in a comparison the 40 v% (Al_3Ti + 40 v% TiB_2) and 40 v% ($Ti_{54}Al_{46}$ + 40 v% TiB_2) extrusions and simulations. The former was extruded at a homologous temperature of 0.84, the latter at 0.76. Trends in the experimental extrusions and the corresponding finite element models show that the higher homologous temperature, yield lower flow stresses, and consequentially increased IMC codeformation. This is due to a decrease in the component flow stress ratio with increasing homologous temperature.

6.4.2. Suggestions for Improved FEM's

There are several flaws in the current model which prevent the accurate determination of codeformation behavior. The model used to perform the above simulations is 2 dimensional and, as a result, does not accurately account for out-of-plane interactions between matrix and reinforcement. Nor does the model account for particle-particle interactions in which previously separated particles collide. These collisions could result in particle fracture or irregularity in particle deformation. Thermally induced flow stress changes, which occur during the extrusion process process, are also not yet incorporated into the model. Specifically, the model does not address the competing effects of adiabatic heating, die contact cooling, and radiative cooling. These are factors that influence the flow behavior of both the matrix and reinforcement and the resulting degree of codeformation achieved.

6.5. Summary

- A finite element model of the extrusion process has been developed and used to simulate the codeformation of a discontinuously-reinforced composite. The model provides the ability to alter the volume percentage of randomly dispersed particles and define the flow stresses of both the particles and the surrounding matrix.
- The model has been used to simulate the codeformation processing of a series of metal/IMC composites having a various volume percentages of IMC reinforcement, initial billet temperatures, extrusion ratios, IMC particle sizes and intermetallic alloy compositions.
- The results of these simulations was examined by comparison of the average equivalent strains of matrix and reinforcement elements. This data was used to determine a strain ratio, which was used to identify trends with respect to the above-mentioned series of composites.
- The model predicts that the amount of codeformation will increase with increasing v% IMC. This prediction is supported by experimental extrusion results.
- The simulations predict that smaller IMC particles will achieve a higher degree of codeformation. This was not observed in the experimental extrusions. The difference between simulation and reality is likely due to the inability of the simulations to account for small particle “tumble”.
- Changes in IMC composition have a dramatic effect on the flow behavior of the IMCs, and result in different codeformation. IMCs with higher flow stresses at the processing conditions have correspondingly less IMC codeformation.
- The simulated processing conditions have only a marginal effect on the flow behavior of the IMC and matrix components.
- The homologous temperature was shown to have an effect on codeformation, because of its effect on the component flow stress ratio. As the homologous temperature increases, the ability to codeform the IMCs increases.

- The current finite element model is not ready to quantitatively predict the results of codeformation processes. This could change through the incorporation of better flow stress data, thermal effects, out-of-plane deformations, and particle-particle interactions.

6.6. References

[84] G.E. Barron, *in What Every Engineer Should Know about Finite Element Analysis,* ed. J.R. Brauer, Marcel Dekker, Inc., New York, p. 4, 1988.

[85] S. Kobayashi, S-I. Oh, & T. Altan, *Metal Forming and the Finite-Element Method*¸Oxford University Press, New York, p. 26, 1989.

[86] C.R. Bo□r, N. Rebelo, H. Rystad & G. Schr□der, *Process Modelling of Metal Forming and Thermomechanical Treatment,* Springer-Verlag, Berlin, p. 75, 1986.

[87] T. Zahrah, *et.al., Development of Intelligent Processing Methodology for Intermetallic Matrix Composites,* Progress Report #N00014-96-C-0427, MATSYS, Inc., Springfield, VA, 1998.

[88] ibid, pp. 5.

7. Summary and Conclusions

7.1. Summary of the Research

7.1.1. Approach

The primary objective of this project was to systematically and scientifically evaluate the effects of composition and processing on the codeformation behavior of mechanically-dissimilar, discontinuously-reinforced composites. This was studied experimentally through systematic variation of the composition of the discontinuous-IMC reinforcement, the volume percentage of that composite within the metal matrix, and the extrusion conditions (i.e., billet temperature, ram speed, and die design). The degree of codeformation in each composite was evaluated in terms of the average plastic deformation the IMC particles have undergone as a result of extrusion processing, and was correlated to the above-mentioned variables. Finally, a finite element model in which the relative flow stress, size, and distribution of multiple element types (i.e., "matrix" elements and "reinforcement" elements) could be independently controlled, as could the extrusion ratio and ram speed. Codeformation was analyzed by a comparison of equivalent strains between "matrix" and "reinforcement" elements. The results of the finite element simulation were shown to agree well with those of the experimental extrusions in most regards, but significant improvement is required for the models to be considered quantitatively reliable.

7.1.2. Reaction Synthesis

The reaction synthesis technique used to produce the IMCs was reviewed with particular attention paid to the effects of IMC composition on microstructure. The synthesis technique employed, called exothermic dispersion (XD™) synthesis, uses blended elemental powders to produce a fine dispersion of ceramic particulate within a metallic or intermetallic matrix.[90] This is accomplished by employing the exothermic heats of formation to provide a kinetic advantage, resulting in reaction self-sustenance. The heat generated during the reaction was presented in terms of the adiabatic temperature (i.e., the theoretical maximum temperature the reaction can attain assuming no heat losses to

the surroundings), and was shown to be a function of the highly exothermic $Ti + 2B \xrightarrow{\text{heat}} TiB_2$ reaction. Optical microscopy of the XD-synthesized IMCs showed that the size of the discontinuous TiB_2 reinforcement generally increased with their volume percentage, as did the adiabatic temperature. This observation, in combination with established models of discontinuous composite strengthening, provide a link between synthesis and room temperature strengthening potency.

7.1.3. Characterization of Flow Behavior

The works of Spitzig, *et.al*, and Avitzur[91] suggested that codeformability is strongly dependent upon the relative flow stresses of each component during processing. Therefore, knowledge of the flow stress of individual components, i.e., IMC (reinforcement) and Ti-6Al-4V (matrix), provides valuable insight into the flow behavior of the composite during codeformation processing. The data are especially important for the IMCs, as the literature provides little information on the high temperature flow behavior of these materials. The flow stress was characterized using high temperature compression tests, performed on a series of discontinuously-reinforced IMCs. The data were correlated to a flow stress equation based on the model of Zener and Hollomon.[92] Likewise, a model of the flow behavior of Ti-6Al-4V was developed using strength data available in the literature.[93] However, it should be noted that this model does not take the phase transformation of α titanium to the β phase which occurs at approximately 1060°C. From these models, flow stress maps were created to describe the flow behavior of the IMC and the Ti-6Al4V as a function of the temperature and strain-rate in ranges consistent with codeformation processing.

7.1.4. Codeformation Processing

Codeformation experiments were conducted through the extrusion of a series of Ti-6Al-4V and IMC powder mixtures under various conditions. A series of six metal/IMC compositions were used to assess the degree of codeformation with respect to volume percentage IMC reinforcement, volume percentage of TiB_2 within the IMC, size of the IMC reinforcement, and intermetallic matrix alloy composition. The influence of process conditions on codeformation was evaluated with respect to the initial billet

temperature and the extrusion ratio. These material- and process-related variables were also correlated to homologous temperature, imposed strain-rate, and relative flow stress.

The results of the experiments were quantified in terms of the plastic strain in the IMC particles as calculated from direct microscopic measurement of IMC particle aspect ratios. A comparison between trends observed for accumulated particle strain and the material- or process-related conditions reveal that increasing codeformation coincides with:

- increasing IMC particle size
- increasing extrusion temperature
- increasing homologous temperature
- increasing strain-rate
- decreasing v% TiB_2 within the IMC

Of these trends, variation in the volume percentage of TiB_2 within the IMC reinforcement had the greatest effect on particle deformation. The explanation for this behavior is related to the volume available for deformation. The TiB_2 is assumed to be rigid under the processing conditions imposed. As a result, the amount of the deformable intermetallic matrix and the related interactions between rigid TiB_2 particles become factors that greatly influence IMC deformation.

The relative flow stress was calculated as a function of initial billet temperature and strain-rate using the flow stress models described above. No conclusive correlation was observed between the relative flow stress and the particle strain was observed in samples having the same IMC composition. This is likely due to the narrow range of relative flow stresses tested and the large error (i.e., relative to the narrow flow stress ranges) in the flow stress models. There was little evidence of codeformation among samples reinforced with the $Ti_{54}Al_{46}$-based IMCs. The lack of codeformation is thought to be related to the significantly higher flow stress of the $Ti_{54}Al_{46}$ intermetallic matrix alloy at the extrusion temperature.

7.1.5. Finite Element Modelling

Finite element models of several extrusion were developed to provide the ability to qualitatively predict the results of codeformation processing. These models are used to independently evaluate the influence of metal/IMC composition, temperature, ram speed, and extrusion ratio in terms of the impact these parameters have on the relative flow stresses of the components. In addition, variations in reinforcement particle size and volume percentage have been incorporated into the model. The results of the finite element models are interpreted by superimposing the equivalent strains resulting from codeformation onto the original finite element mesh. Average values for the equivalent plastic strain in the elements representing the matrix and reinforcement are used to generate an equivalent strain ratio. In this manner, it is possible to relate the amount of codeformation to the presence of reinforcement particles and the processing conditions.

The results of the extrusion simulations have been correlated to the volume percentage of IMC reinforcement, the size of the IMC particles, the composition of the IMC, and the process conditions of temperature and strain-rate. The models predict that an increasing degree of codeformation will coincide with:

- increasing volume % IMC particulate
- finer IMC particles
- increased homologous temperature
- decreased reinforcement to matrix flow stress ratio

All results, with the exception of those for IMC particle size, were supported by microstructural observations in the experimental extrusions. The processing conditions of temperature and strain-rate have been shown to influence the relative flow stresses of the components. However, in the simulations and microstructures examined, these conditions did not show any conclusive effect on codeformation behavior.

7.2. Conclusions

- Codeformation of a discontinuous IMC-reinforced metal matrix composite is possible at temperatures above the BDT of the intermetallic matrix.

- The size of in-situ-derived TiB_2 reinforcement in Al_3Ti- and $Ti_{54}Al_{46}$-titanium aluminide composites produced by reaction synthesis tend to increase as its nominal volume percentage in the composite increases.
- The increase in TiB_2 size with increasing nominal volume percentage is a consequence of the higher temperatures associated with these formulations during the reaction synthesis process. The influence of temperature is evaluated through calculation of the adiabatic temperature of reaction for the titanium aluminide composites.
- The development of constitutive equations to describe the deformation behavior of these materials in terms of strain-rate and temperature on the flow stress reveals that the flow behavior of the composites is highly dependent on matrix composition and temperature.
- The size and spacing of the TiB_2 reinforcement within the IMCs were shown to have a marginal influence on the high temperature flow behavior of these composites.
- The size of the IMC particles used to reinforce the metal/IMC composites was shown to have an effect on codeformation behavior. The degree of codeformation achieved was greater for samples reinforced with larger IMC particles.
- Increasing the amount of IMC reinforcement was observed to affect the codeformation negatively. The limited ability of the Ti-6Al-4V to transfer loading, and hence deformation, onto the IMC particles was responsible for this tendency.
- Increasing homologous temperature, as shown through changes in extrusion temperature and intermetallic matrix alloy, was observed to increase the ability of the IMC to codeform.

- The volume % of TiB_2 used to reinforce the metal/IMC composites was shown to have a great effect on deformation. This effect was explained as a volumetric phenomenon, in which the quantity of deformable intermetallic alloy decided the degree to which codeformation was possible.
- The flow stress ratios of samples reinforced with Al_3Ti + 40 v% TiB_2 was calculated. No discernable trend was noted with regard to the degree of IMC deformation. This was attributed to the extreme ductility of the IMC particles at these tempeartures and strain-rates.
- Finite element models of codeformation predict that the amount of codeformation will increase with increasing v% IMC, smaller IMC particles, higher homologous temperatures, and decreased component flow stress ratios.
- The current finite element model is not ready to quantitatively predict the results of codeformation processes, but with the incorporation of better flow stress data, thermal effects, and out-of-plane deformation, and particle-particle interactions, the accuracy can be improved.

7.3. Directions for future research

The most logical extension of the current research is to develop an improved finite element model. This model could incorporate the three-dimensional aspects of codeformation. An improved model might also account for changes in the geometry of the codeformation process, especially with regard to the die ratio. Additionally, the ability to incorporate actual flow stress values, rather than a reliance on flow stress ratios, might improve the model substantially.

In the shorter term, mechanical testing of the extruded composites produced in this study should be undertaken. To obtain realistic strengths, however, the porosity associated with the IMC particulates must be eliminated. This will provide the means relate strengthening improvements to the presence of codeformed IMCs, rather than displaying near-immediate fracture due to porosity.

Other materials systems and codeformation processing strategies might be also attempted in the near-term. Some work has already begun on the codeformation via hot rolling of

an aluminum and brass laminar composite.[94] Adaptations and improvements in these and other processes could lead to the development of components codeformation engineered for specific tasks.

---

[90] O.P. Poola, C. Cordier, P. Pirouz, and A.H.Heuer: *in Interfaces in Metal-Ceramic Matrix Composites*, TMS, Warrendale, PA, 1990, pp. 465-73.

[91] B. Avitzur, *Handbook of Metal Forming Processes*, Wiley-Interscience, New York, 1983.

[92] C. Zener and J.H. Hollomon, *J. Appl. Physics*, vol. 15, no. 1, pp. 22-32, 1944.

[93] *Titanium Alloys: Material Properties Handbook*, ed. R. Boyer, G. Welsch, and E.W. Collings, pp. 592-4, 1994.

[94] A. Johnson, Senior Project, Virginia Tech, Spring, 1997.

A. IMC Thermodynamics

This appendix includes enthalpy loops for Al-, Al_3Ti-, and near-γ TiAl-based intermetallic matrix composites. It also includes charts which show the adiabatic temperature as a functions of volume percent reinforcement for these IMCs.

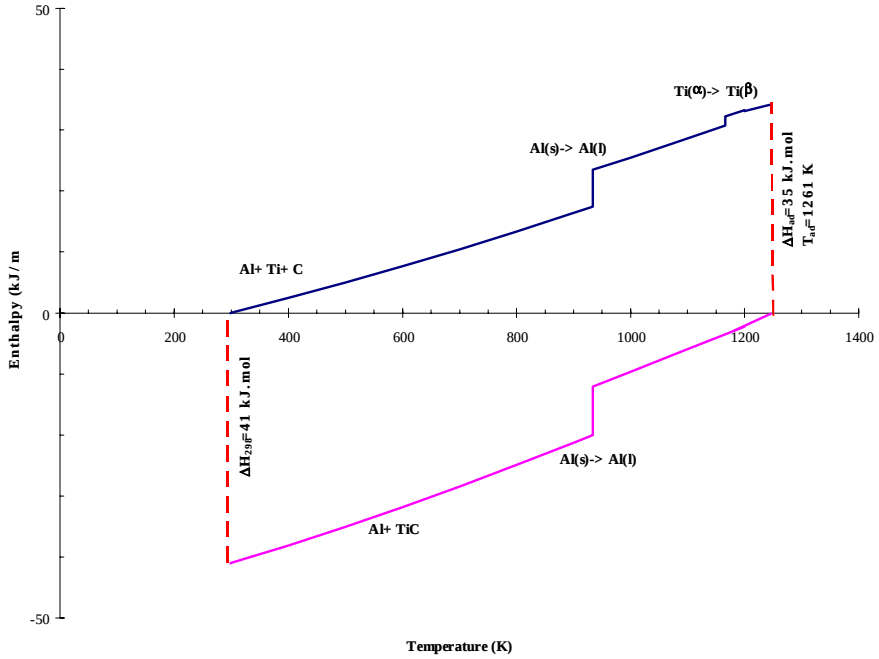

Figure 55: A plot of the change in enthalpy as a function of temperature for the reaction synthesis of the Al + 30 volume % TiC composite.

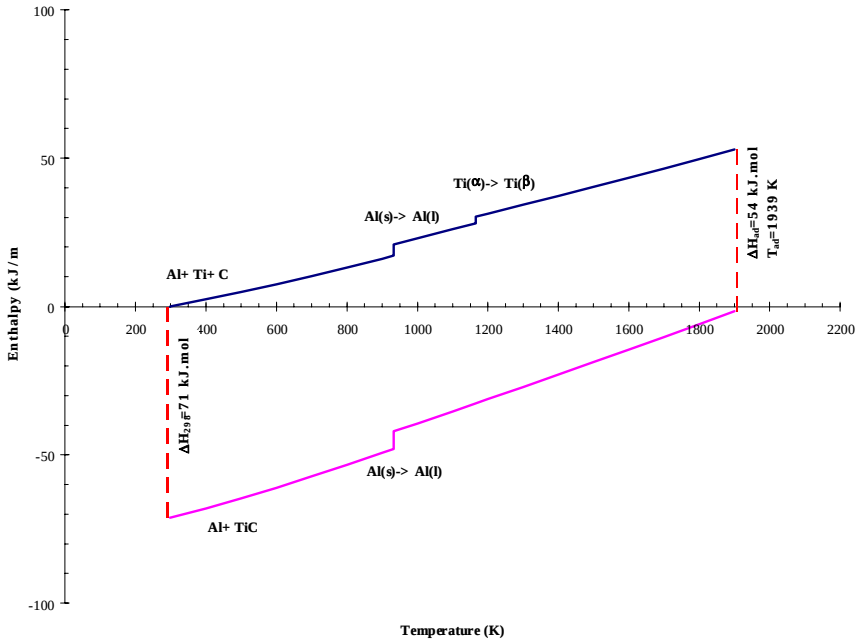

Figure 56: A plot of the change in enthalpy as a function of temperature for the reaction synthesis of the Al + 50 volume % TiC composite.

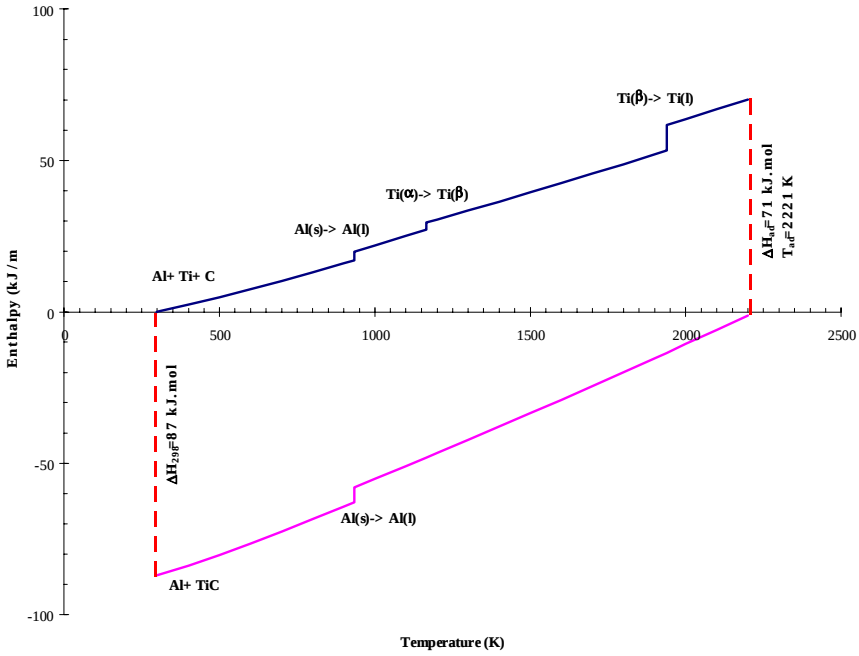

Figure 57: A plot of the change in enthalpy as a function of temperature for the reaction synthesis of the Al + 60 volume % TiC composite.

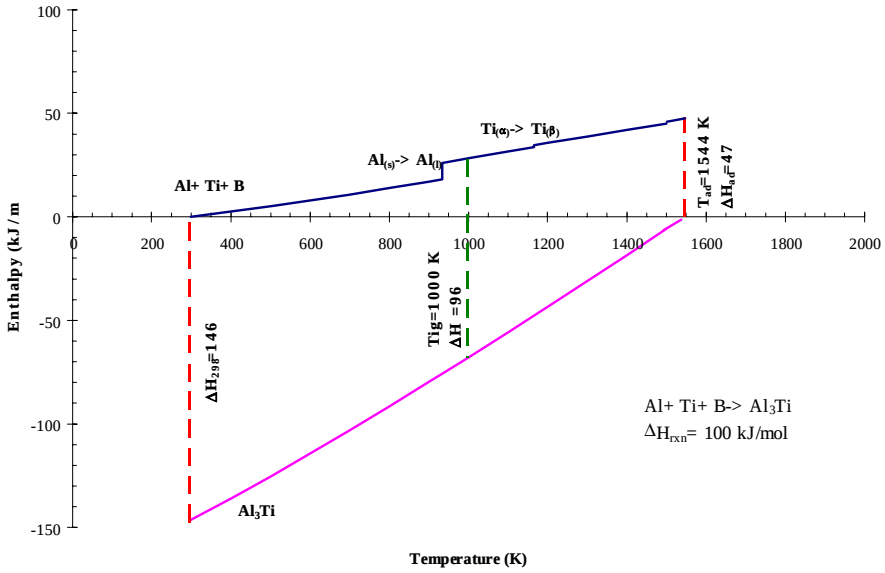

Figure 58: A plot of the change in enthalpy as a function of temperature for the reaction synthesis of the monolithic Al_3Ti.

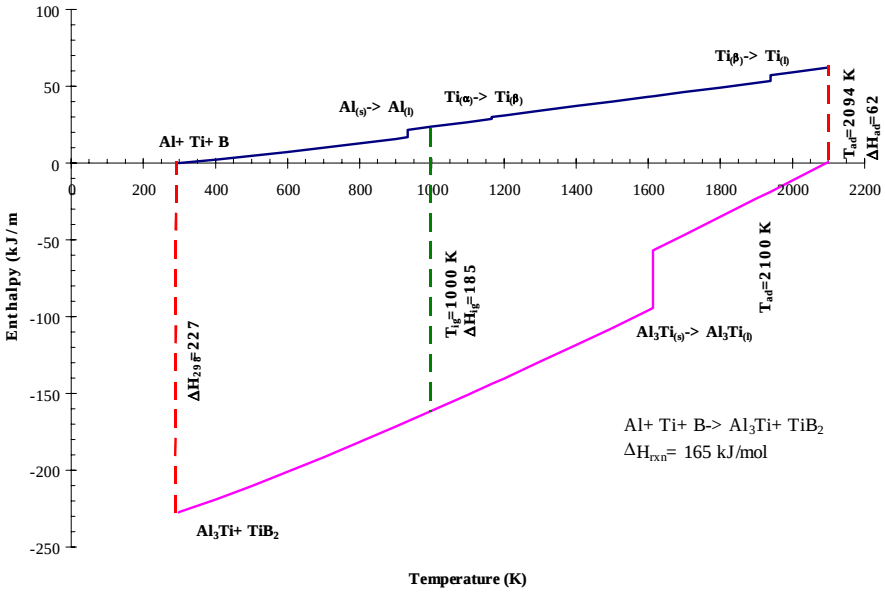

Figure 59: A plot of the change in enthalpy as a function of temperature for the reaction synthesis of the Al_3Ti + 20 volume % TiB_2 composite.

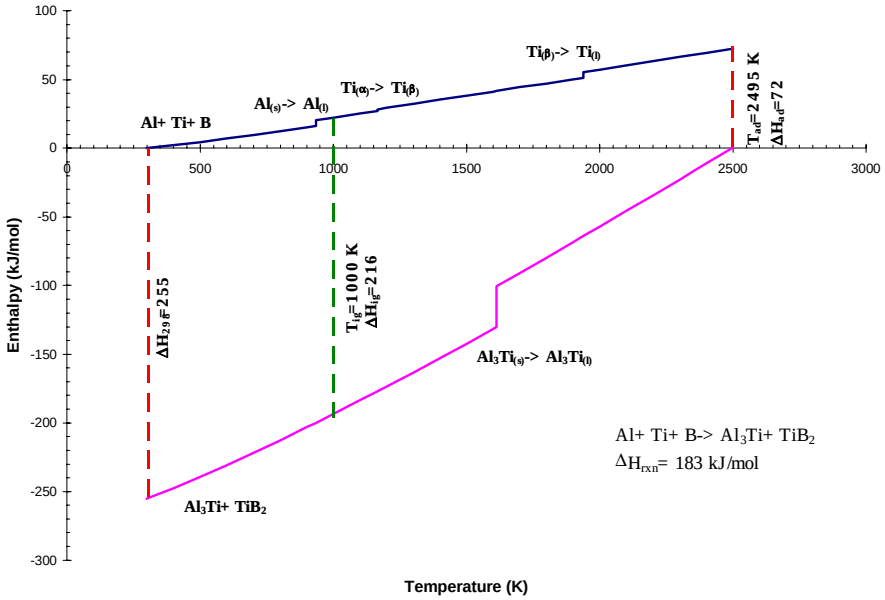

Figure 60: A plot of the change in enthalpy as a function of temperature for the reaction synthesis of the Al_3Ti + 30 volume % TiB_2 composite.

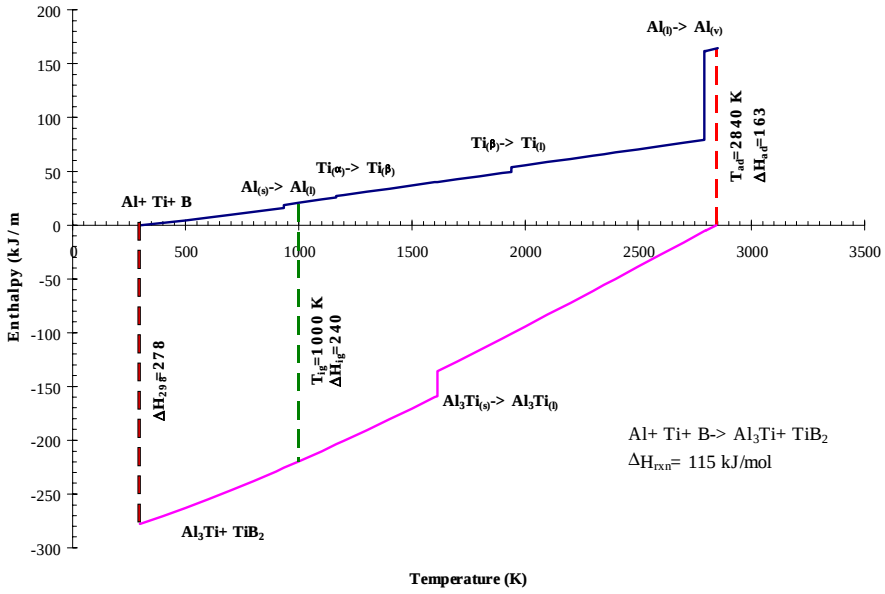

Figure 61: A plot of the change in enthalpy as a function of temperature for the reaction synthesis of the Al_3Ti + 40 volume % TiB_2 composite.

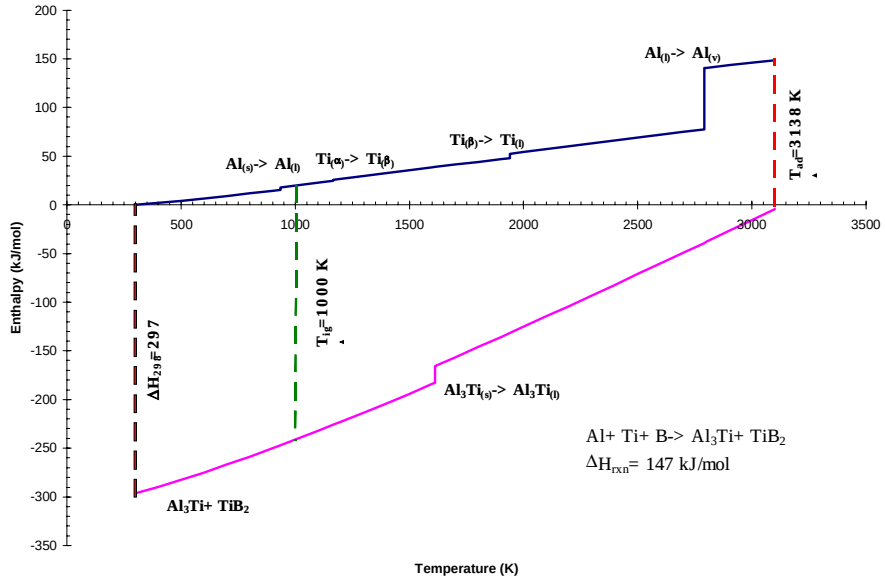

Figure 62: A plot of the change in enthalpy as a function of temperature for the reaction synthesis of the Al_3Ti + 50 volume % TiB_2 composite.

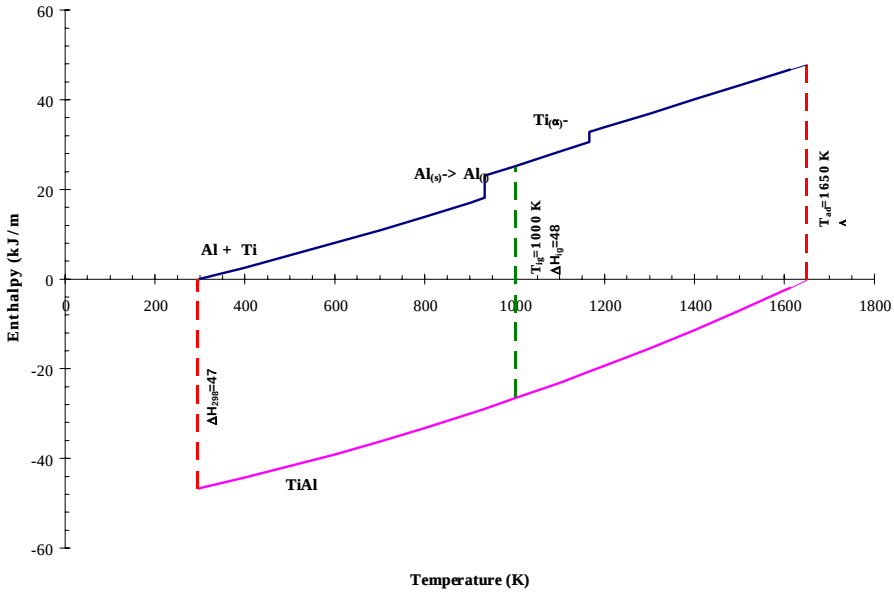

Figure 63: A plot of the change in enthalpy as a function of temperature for the reaction synthesis of the monolithic near-γ TiAl.

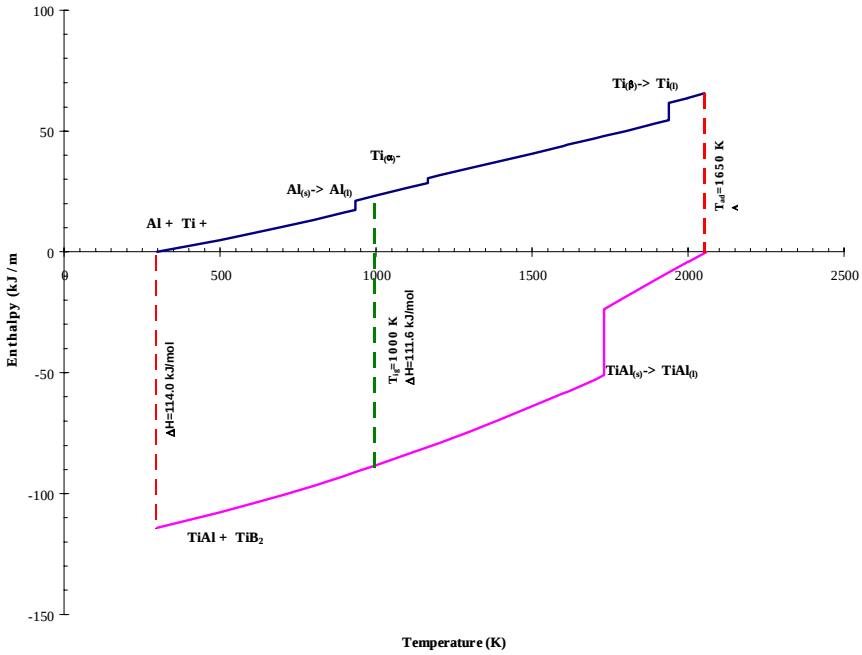

Figure 64: A plot of the change in enthalpy as a function of temperature for the reaction synthesis of the near-γ TiAl + 30 volume % TiB_2 composite.

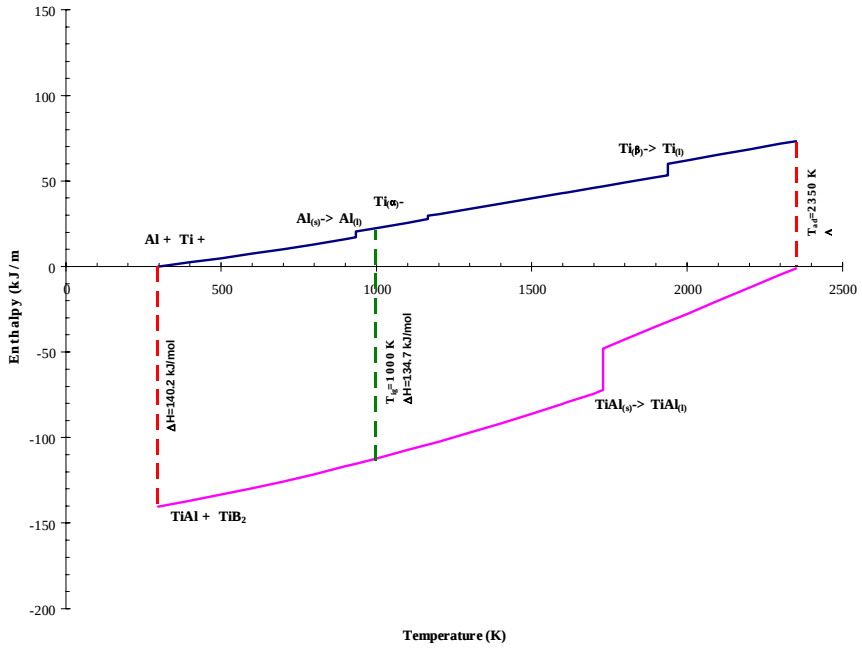

Figure 65: A plot of the change in enthalpy as a function of temperature for the reaction synthesis of the near-γ TiAl + 40 volume % TiB_2 composite.

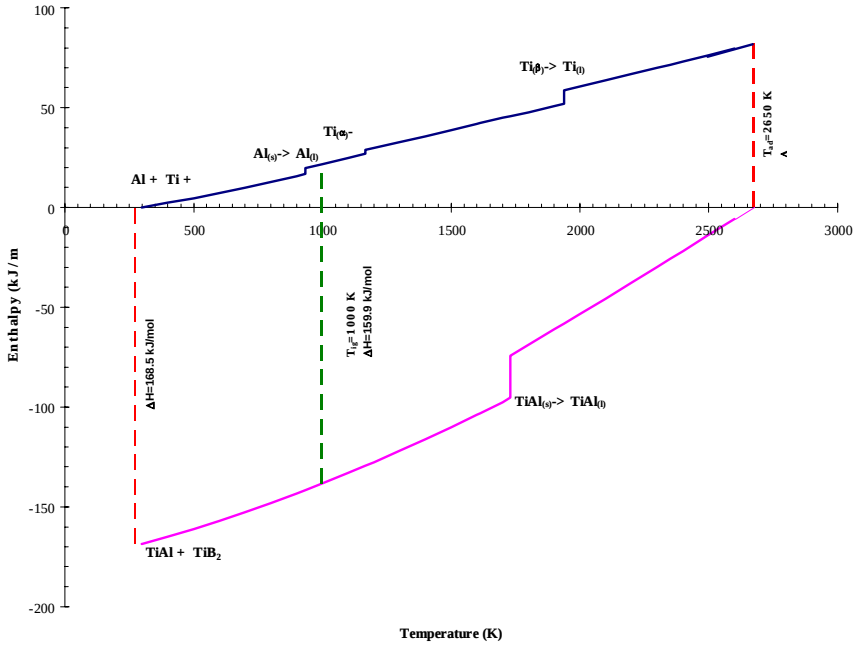

Figure 66: A plot of the change in enthalpy as a function of temperature for the reaction synthesis of the near-γ TiAl + 50 volume % TiB_2 composite.

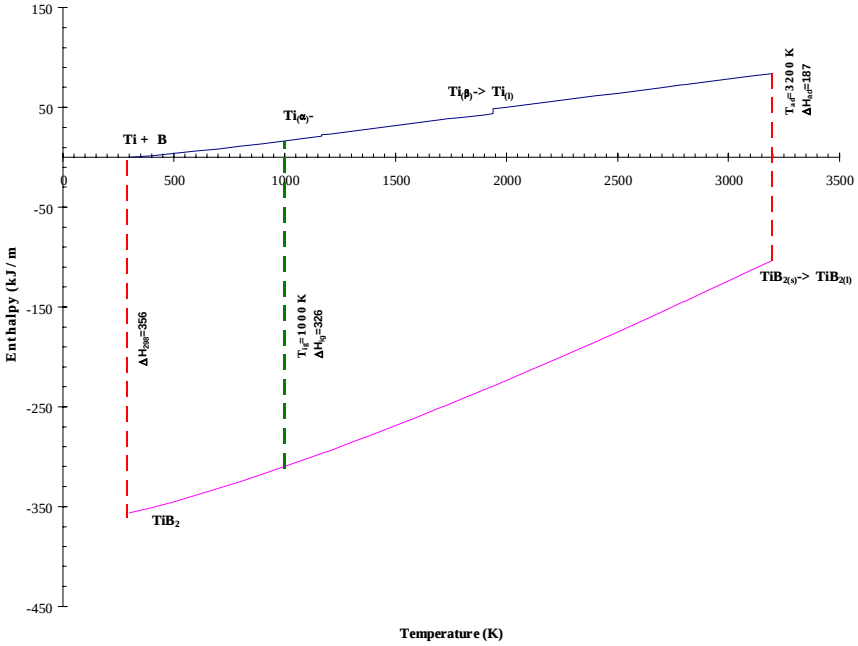

Figure 67: A plot of the change in enthalpy as a function of temperature for the reaction synthesis of the monolithic TiB_2, used for calculation purposes only.

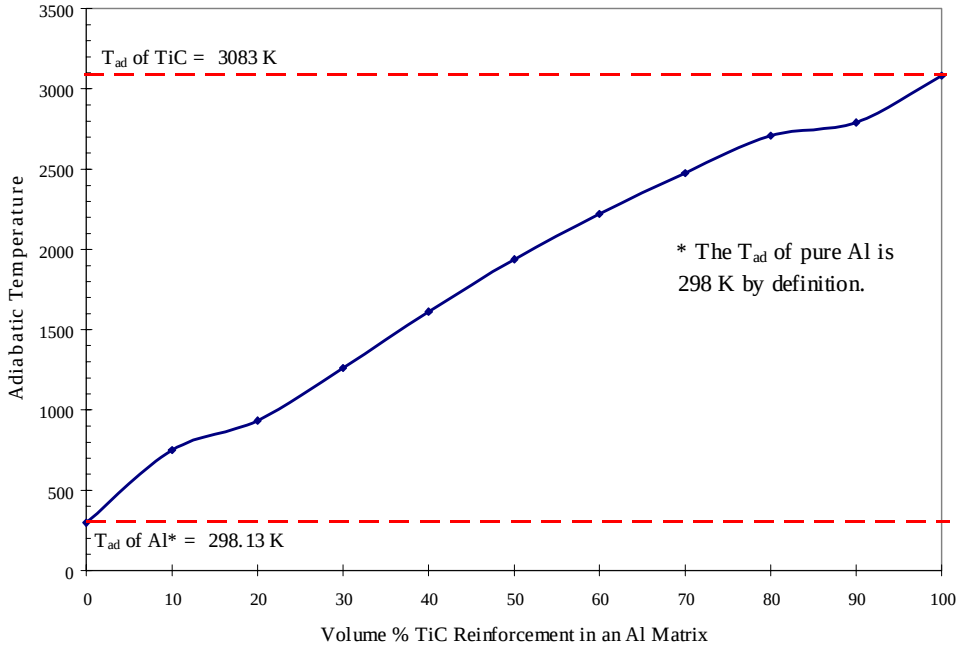

Figure 68: The calculated adiabatic temperature as a function of the volume percentage of TiC within an Al matrix.

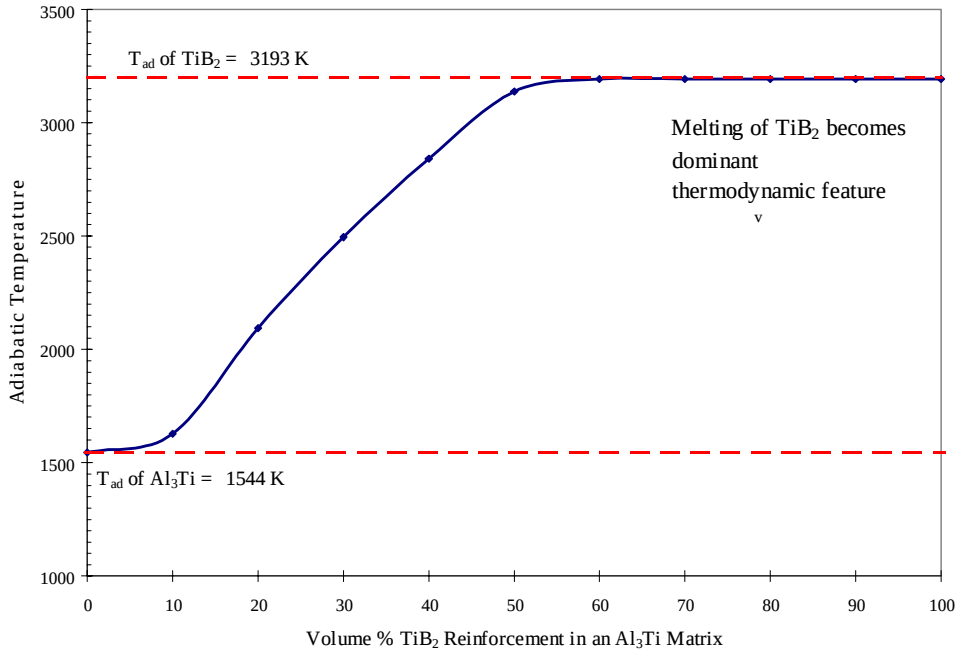

Figure 69: The calculated adiabatic temperature as a function of the volume percentage of TiB_2 within an Al_3Ti matrix.

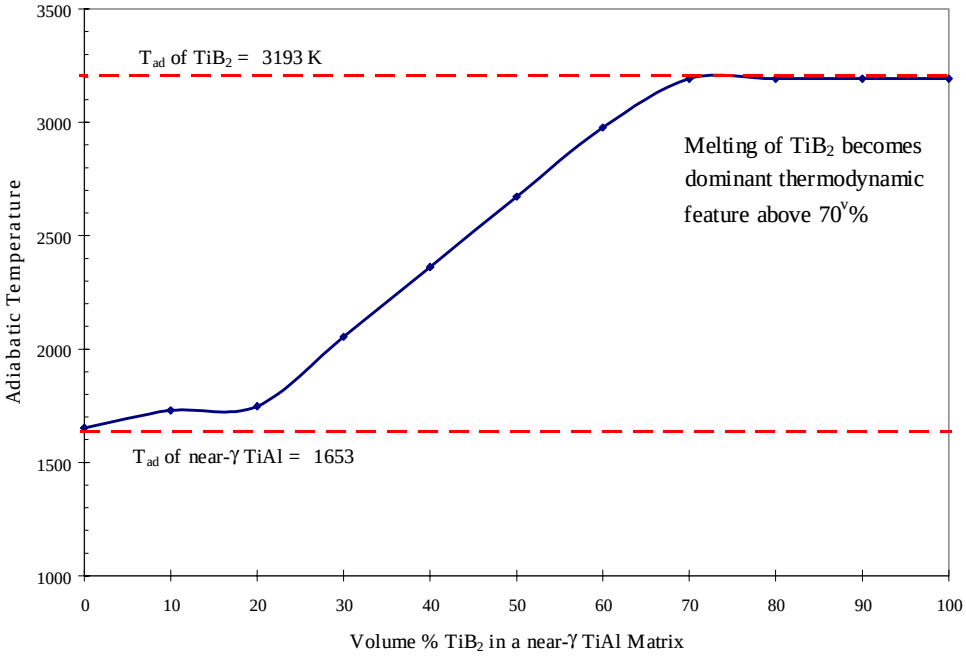

Figure 70: The calculated adiabatic temperature as a function of the volume percentage of TiB_2 within a near-γ TiAl matrix.

Appendix B: Flow Stress Behavior

This appendix contains the stress-strain diagrams for the Al_3Ti- and near-γ TiAl-based intermetallic matrix composites. It also contains the plots used to calculate the strain-rate sensitivity, m, and the activation energy required for deformation, Q. The flow stress maps, which describe the flow stress in terms of temperature and strain-rate, are also provided.

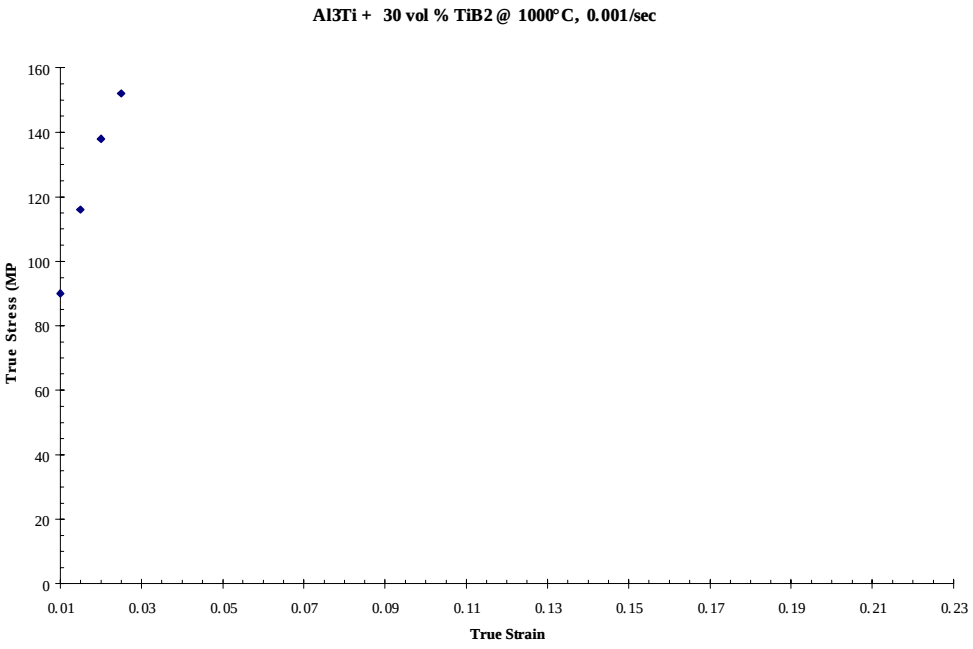

Figure 71: Corrected True Stress vs. True Plastic Strain for Al_3Ti + 30 volume % TiB_2 at 1000°C and a strain-rate of 0.0001 sec^{-1}.

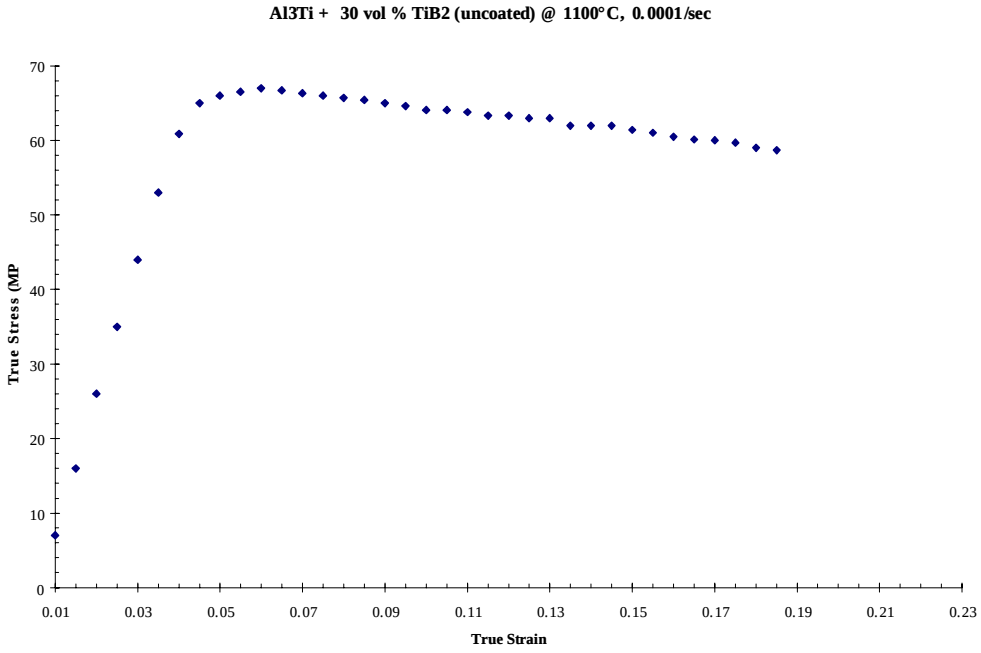

Figure 72: Corrected True Stress vs. True Plastic Strain for Al_3Ti + 30 volume % TiB_2 at 1100°C and a strain-rate of 0.0001 sec^{-1}.

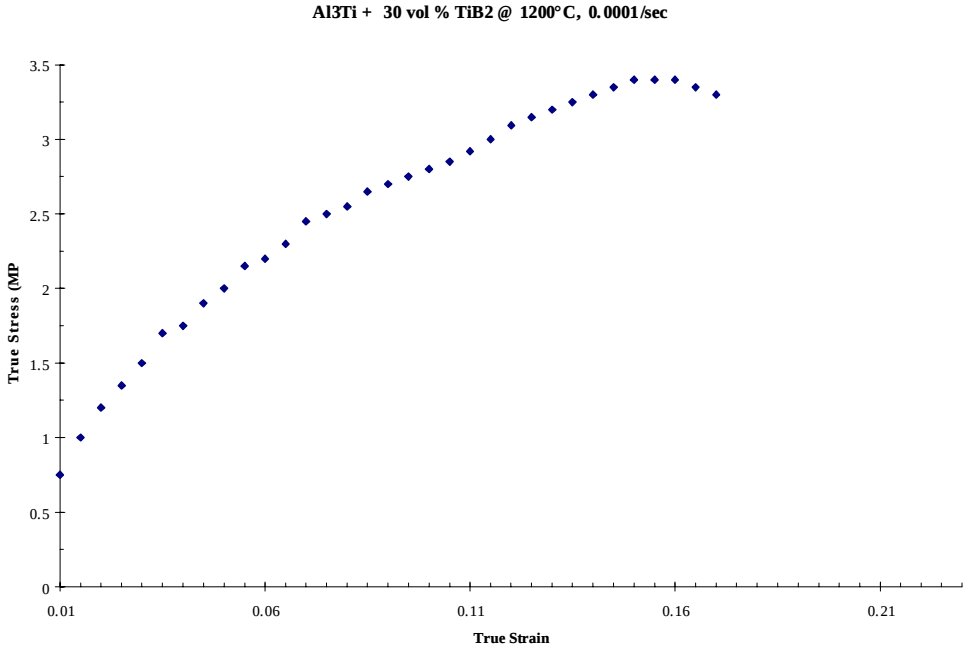

Figure 73: Corrected True Stress vs. True Plastic Strain for Al_3Ti + 30 volume % TiB_2 at 1200°C and a strain-rate of 0.0001 sec^{-1}.

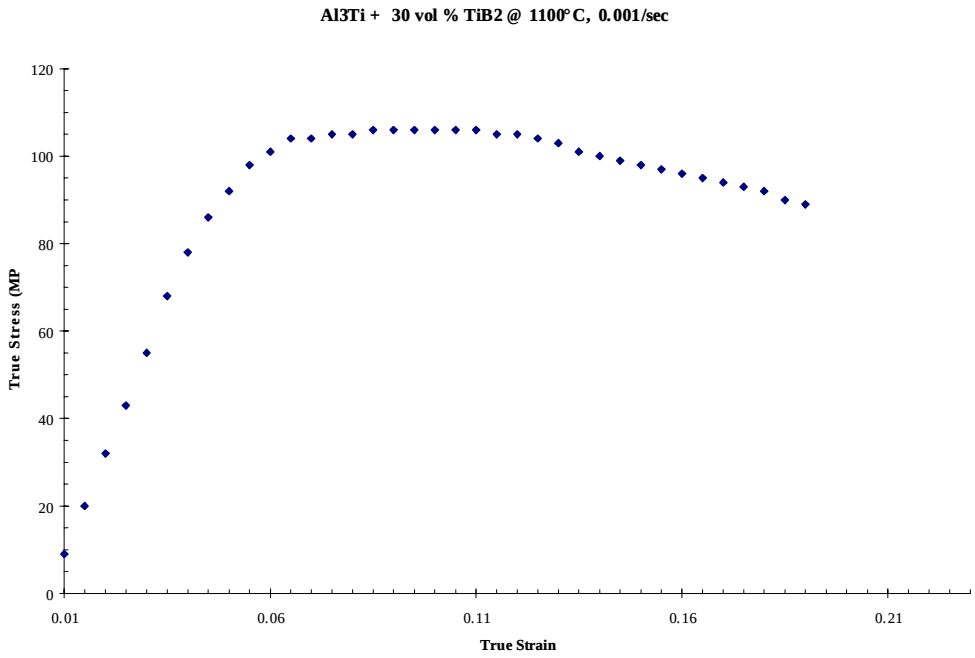

Figure 74: Corrected True Stress vs. True Plastic Strain for Al_3Ti + 30 volume % TiB_2 at 1000°C and a strain-rate of 0.001 sec^{-1}.

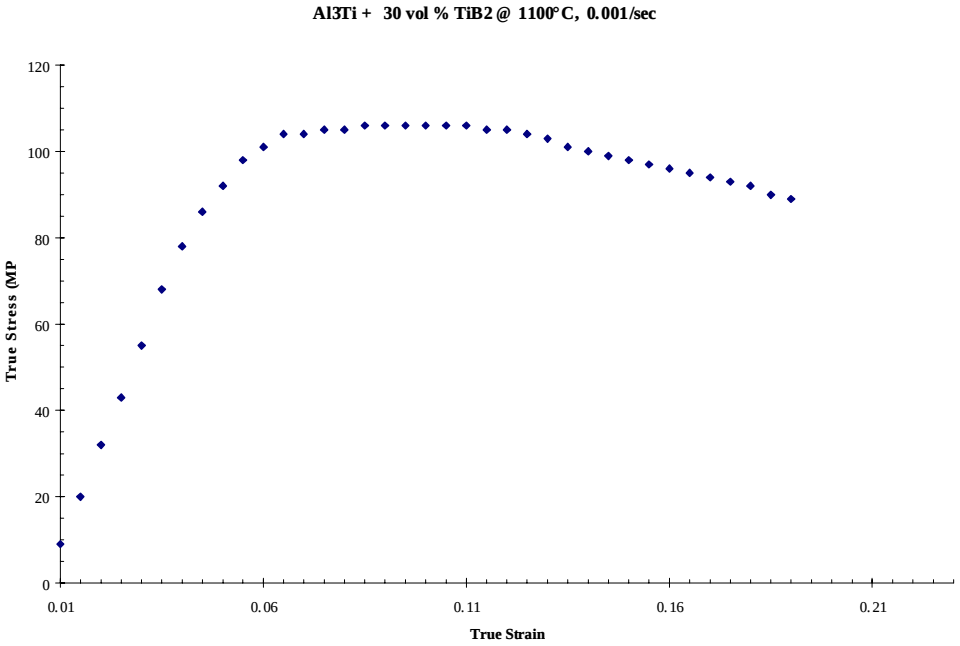

Figure 75: Corrected True Stress vs. True Plastic Strain for Al_3Ti + 30 volume % TiB_2 at 1000°C and a strain-rate of 0.001 sec^{-1}.

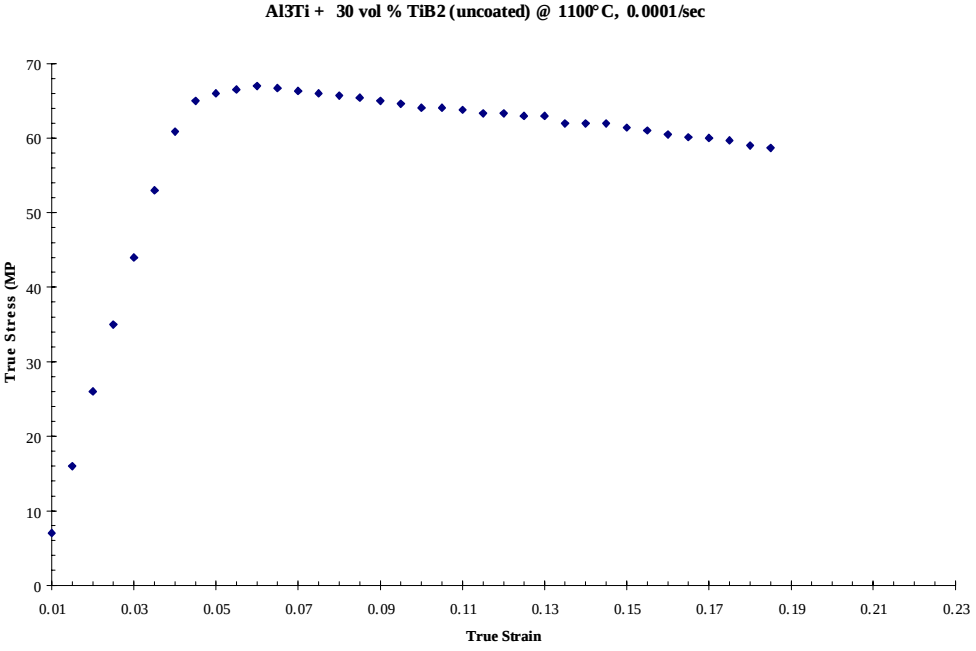

Figure 76: Corrected True Stress vs. True Plastic Strain for Al_3Ti + 30 volume % TiB_2 at 1100°C and a strain-rate of 0.001 sec^{-1}.

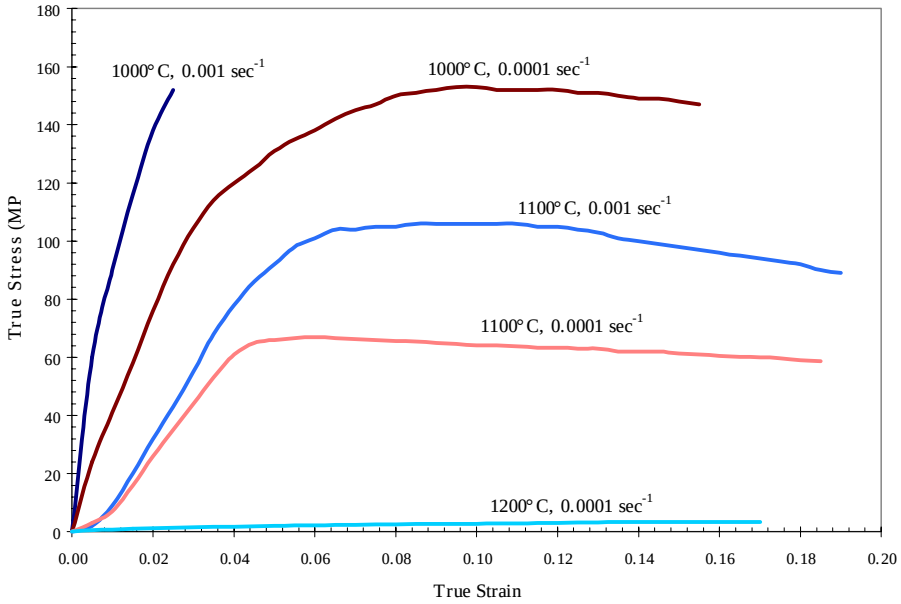

Figure 77: Corrected True Stress vs. True Strain for Al_3Ti + 30 volume % TiB_2 at all tested temperatures and strain-rates.

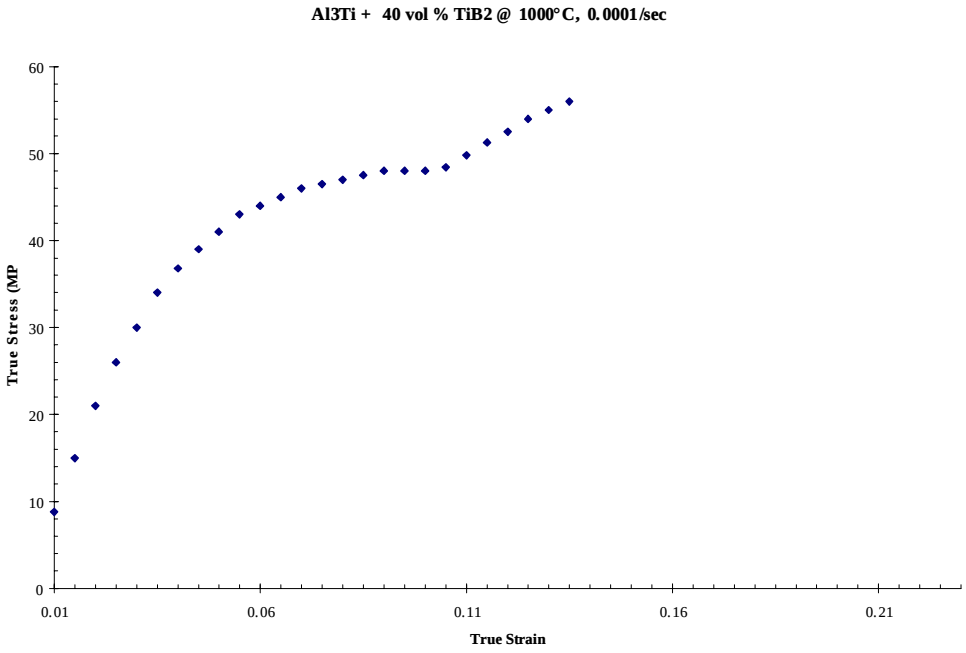

Figure 78: Corrected True Stress vs. True Plastic Strain for Al_3Ti + 40 volume % TiB_2 at 1000°C and a strain-rate of 0.0001 sec^{-1}.

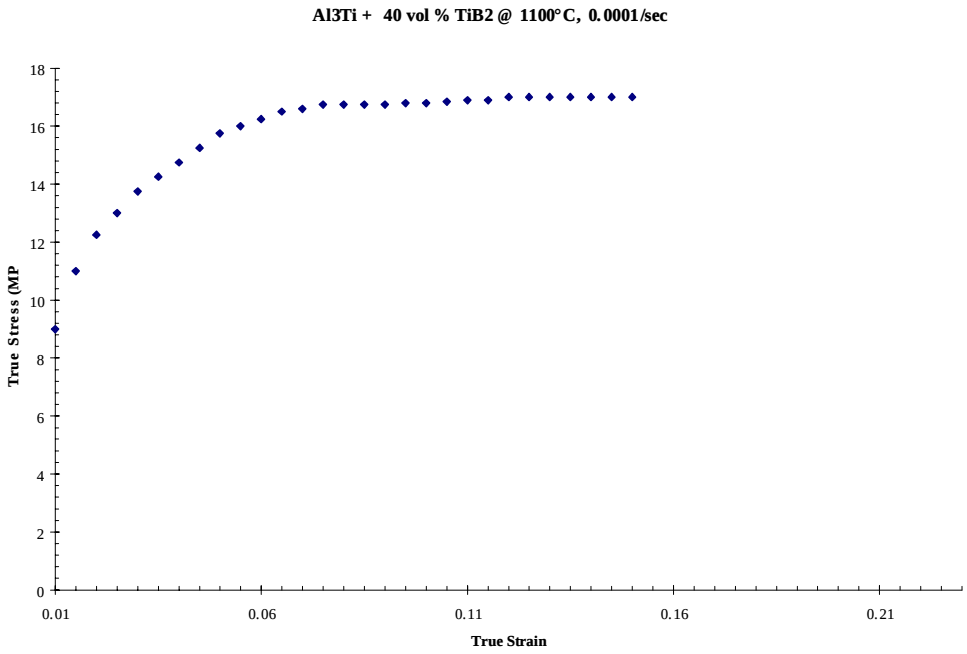

Figure 79: Corrected True Stress vs. True Plastic Strain for Al_3Ti + 40 volume % TiB_2 at 1100°C and a strain-rate of 0.0001 sec^{-1}.

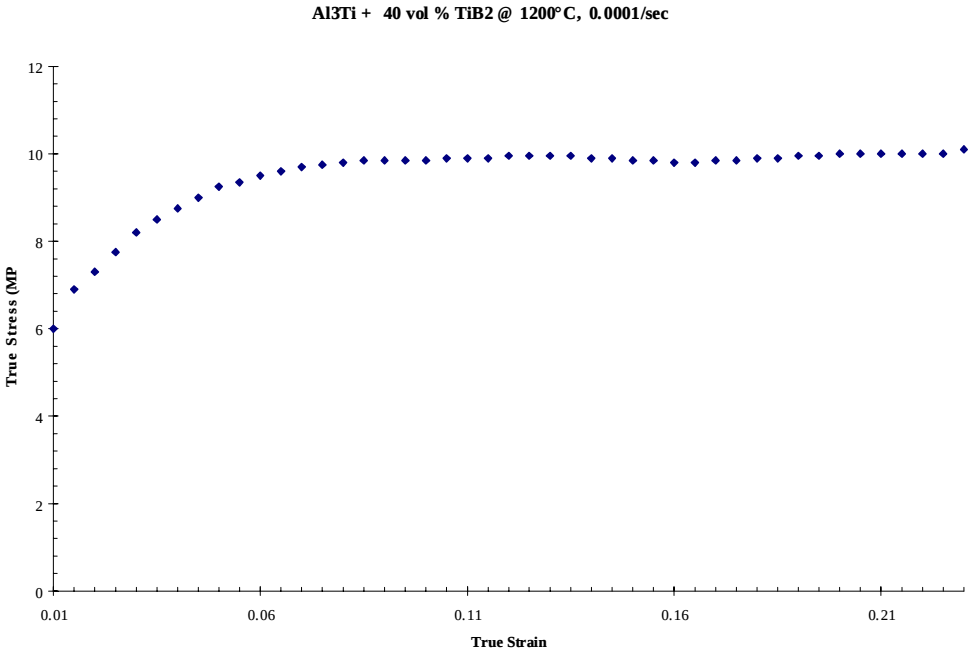

Figure 80: Corrected True Stress vs. True Plastic Strain for Al_3Ti + 40 volume % TiB_2 at 1200°C and a strain-rate of 0.0001 sec^{-1}.

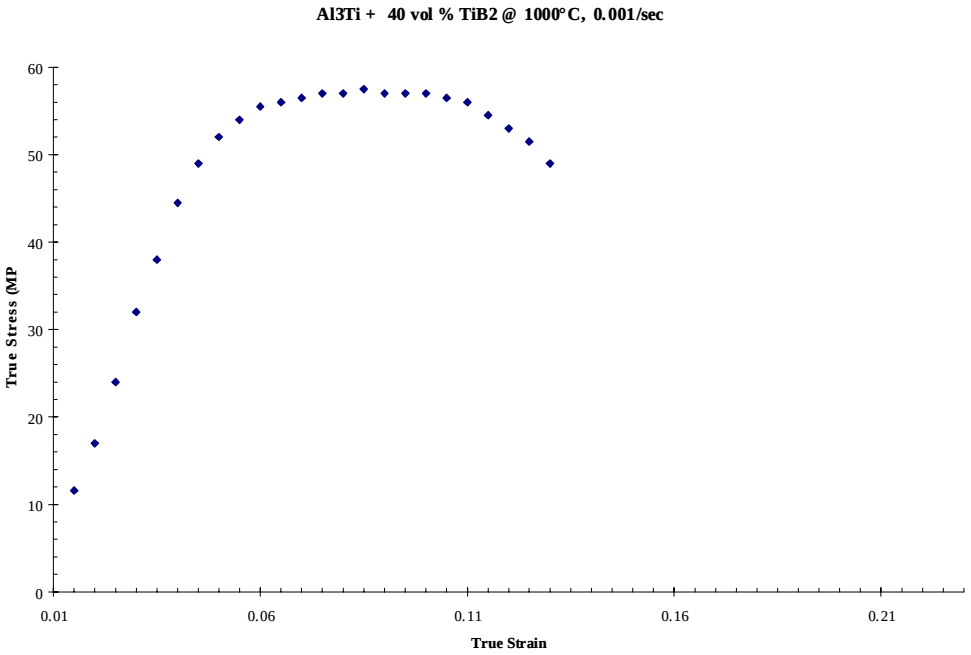

Figure 81: Corrected True Stress vs. True Plastic Strain for Al_3Ti + 40 volume % TiB_2 at 1000°C and a strain-rate of 0.001 sec^{-1}.

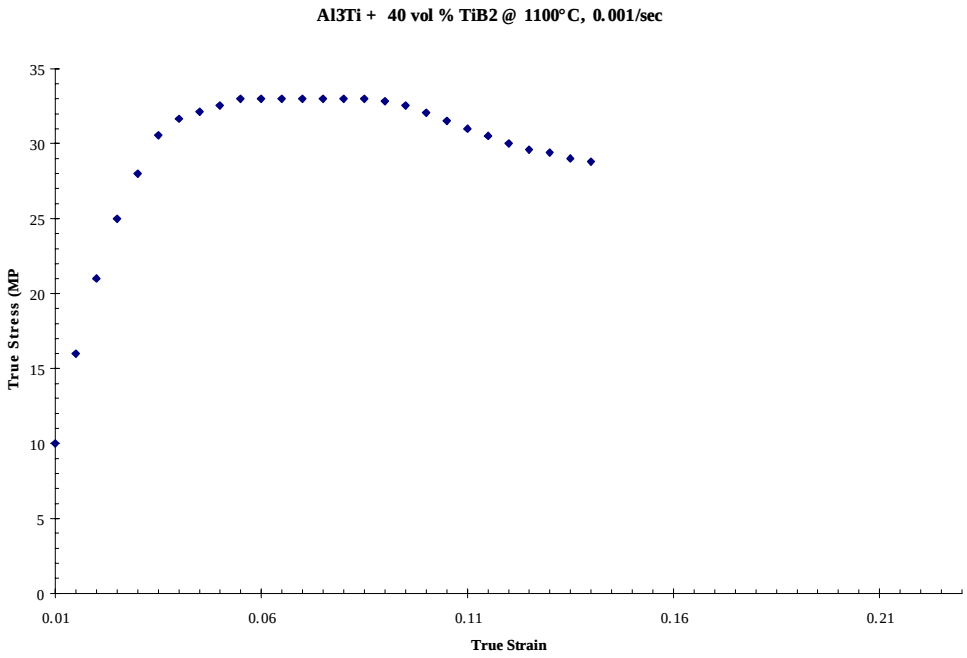

Figure 82: Corrected True Stress vs. True Plastic Strain for Al_3Ti + 40 volume % TiB_2 at 1100°C and a strain-rate of 0.001 sec^{-1}.

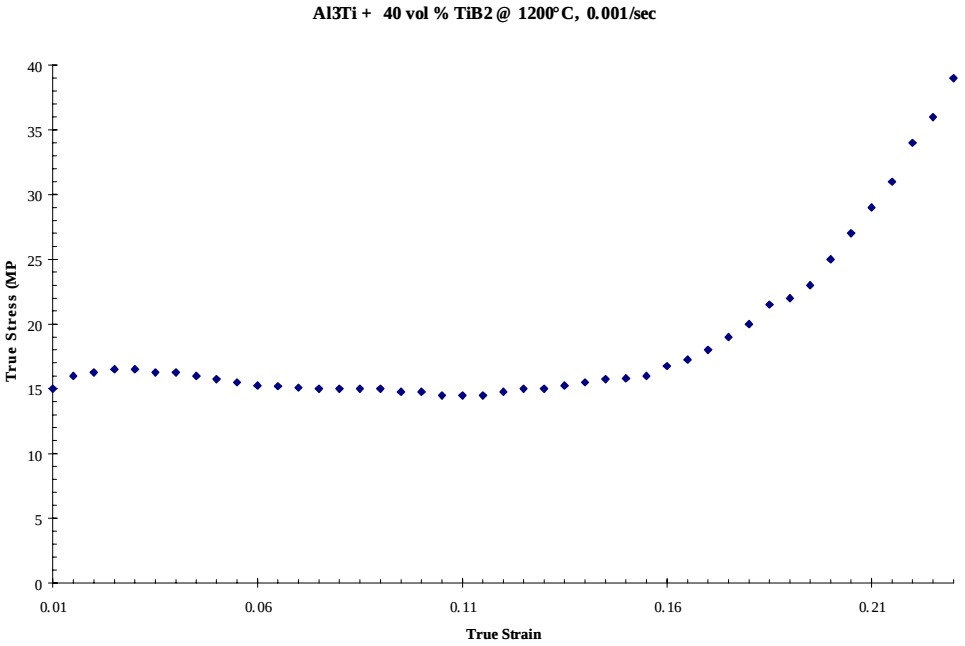

Figure 83: Corrected True Stress vs. True Plastic Strain for Al_3Ti + 40 volume % TiB_2 at 1200°C and a strain-rate of 0.001 sec^{-1}.

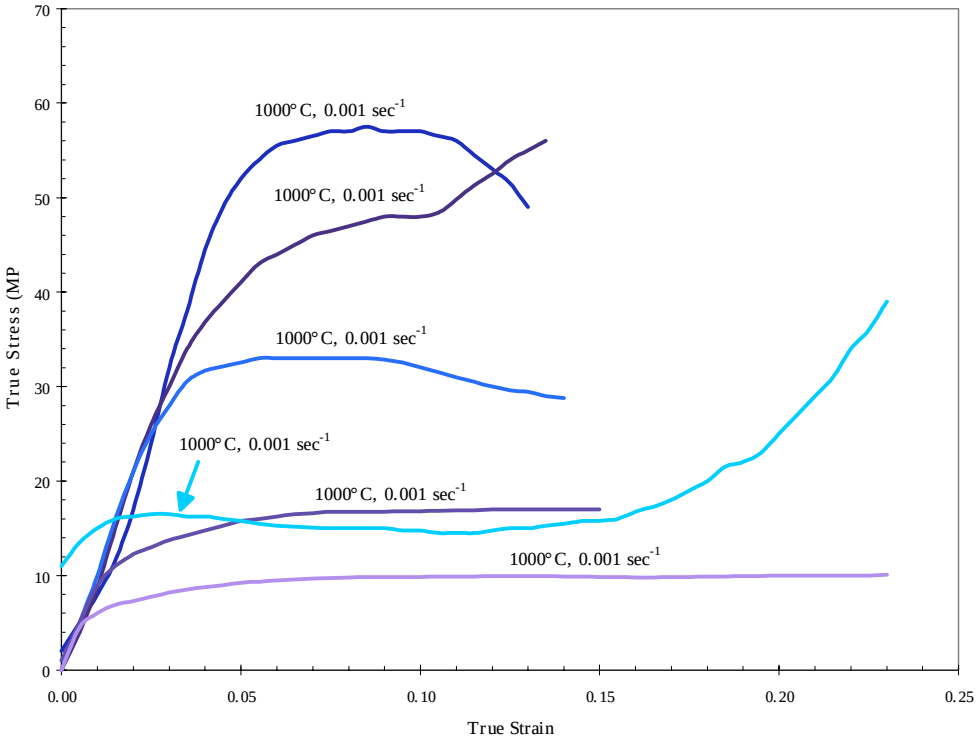

Figure 84: Corrected True Stress vs. True Strain for Al_3Ti + 40 volume % TiB_2 at all tested temperatures and strain-rates.

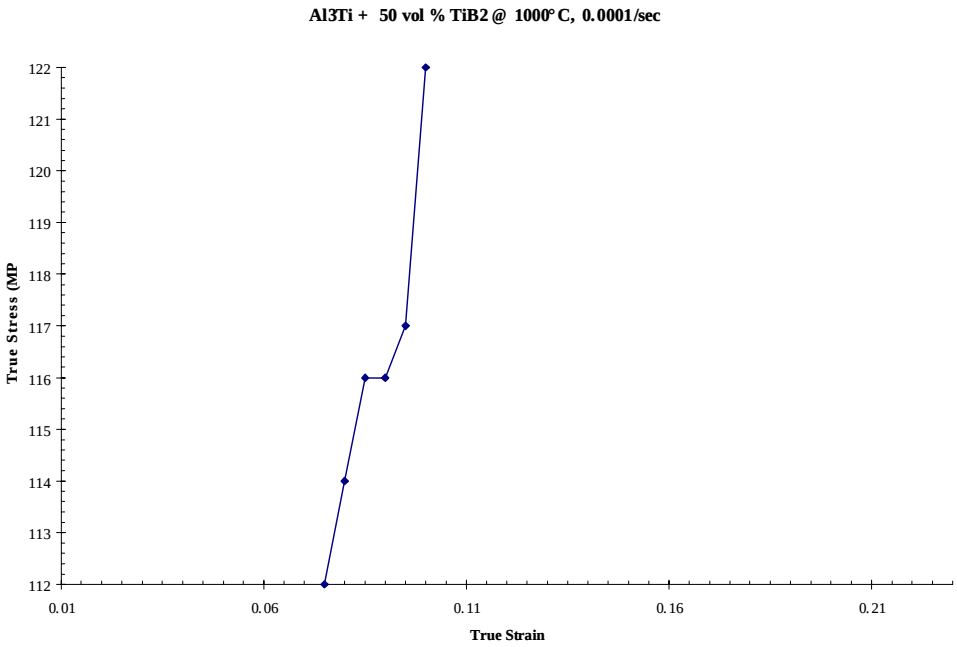

Figure 85: Corrected True Stress vs. True Plastic Strain for Al_3Ti + 50 volume % TiB_2 at 1000°C and a strain-rate of 0.0001 sec^{-1}.

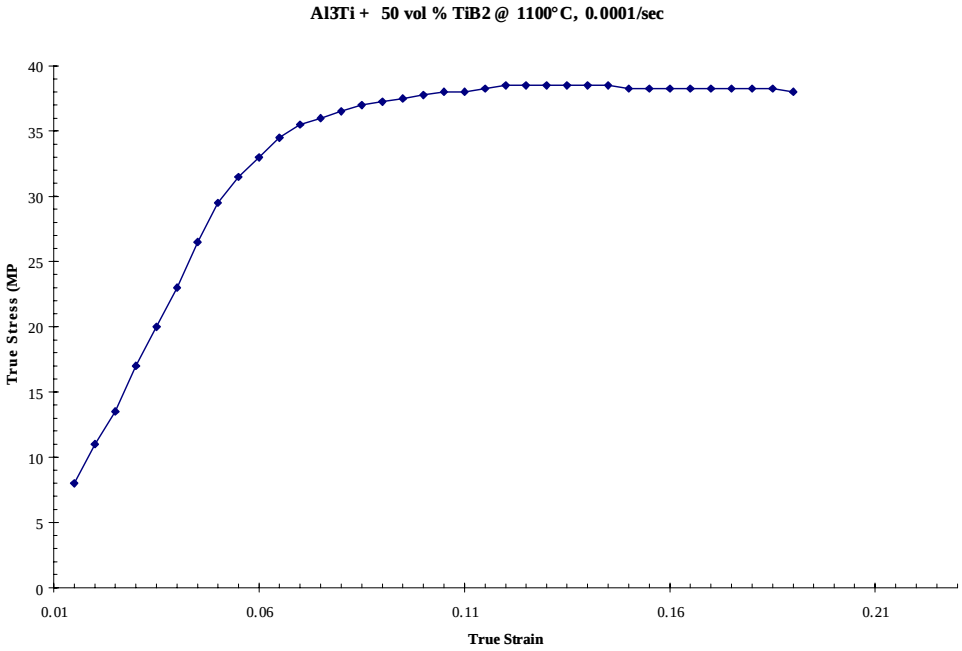

Figure 86: Corrected True Stress vs. True Plastic Strain for Al_3Ti + 50 volume % TiB_2 at 1100°C and a strain-rate of 0.0001 sec^{-1}.

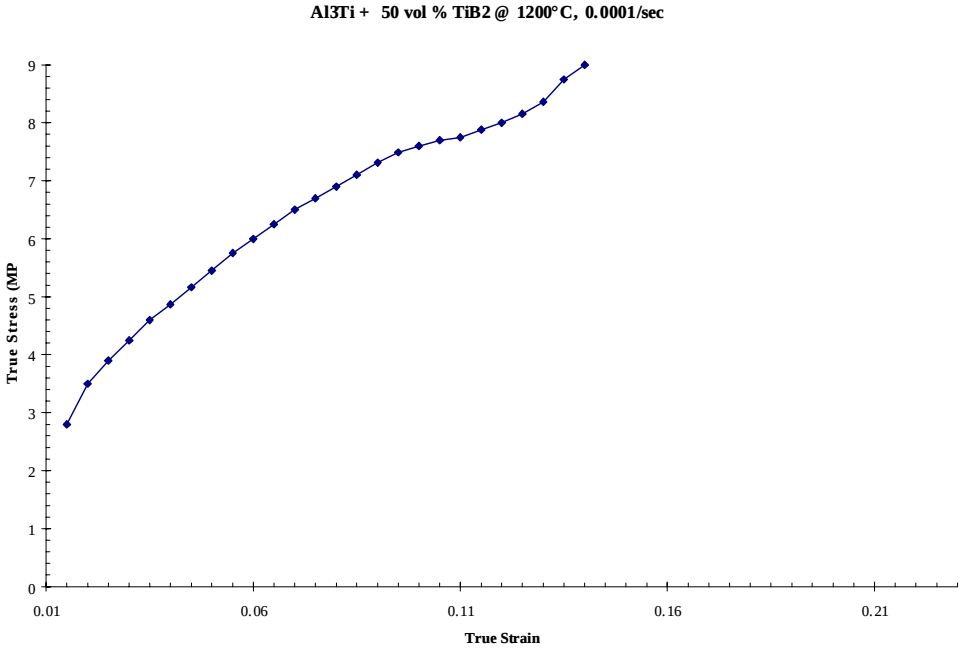

Figure 87: Corrected True Stress vs. True Plastic Strain for Al_3Ti + 50 volume % TiB_2 at 1200°C and a strain-rate of 0.0001 sec^{-1}.

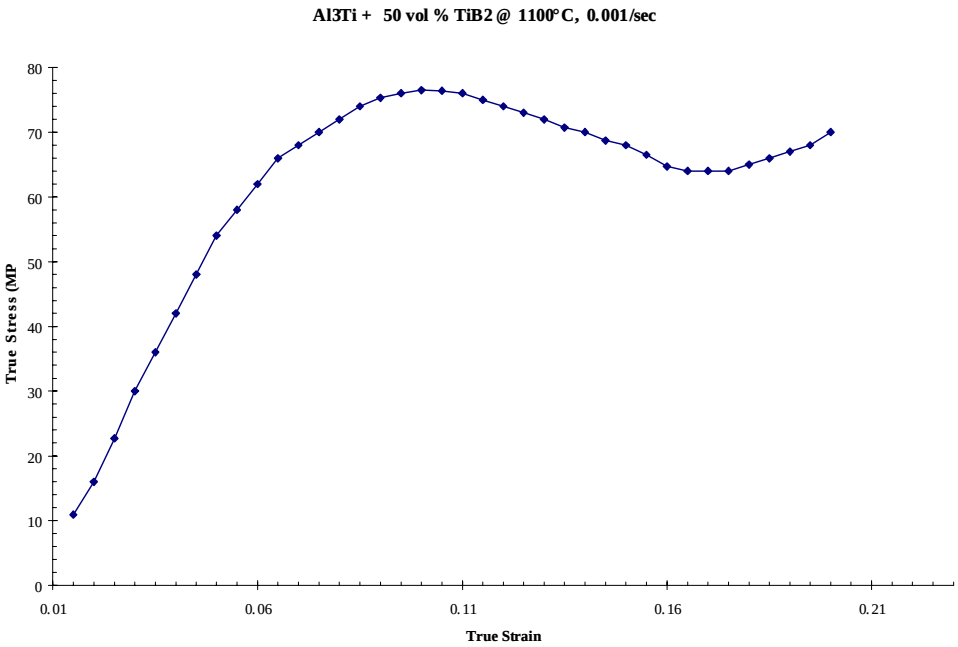

Figure 88: Corrected True Stress vs. True Plastic Strain for Al_3Ti + 50 volume % TiB_2 at 1100°C and a strain-rate of 0.001 sec^{-1}.

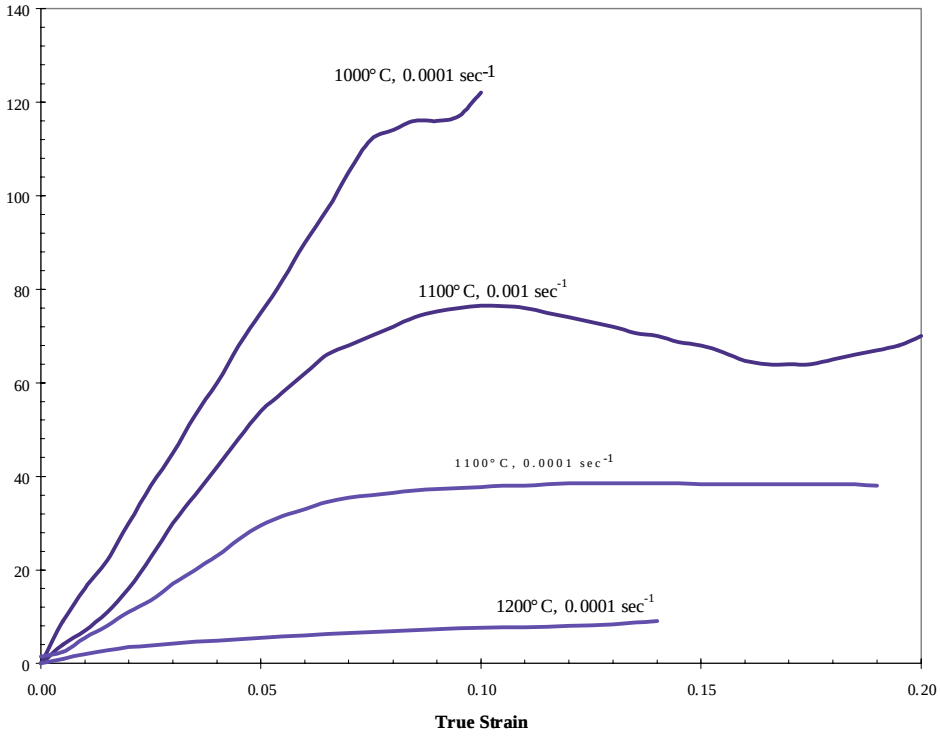

Figure 89: Corrected True Stress vs. True Strain for Al_3Ti + 50 volume % TiB_2 at all tested temperatures and strain-rates.

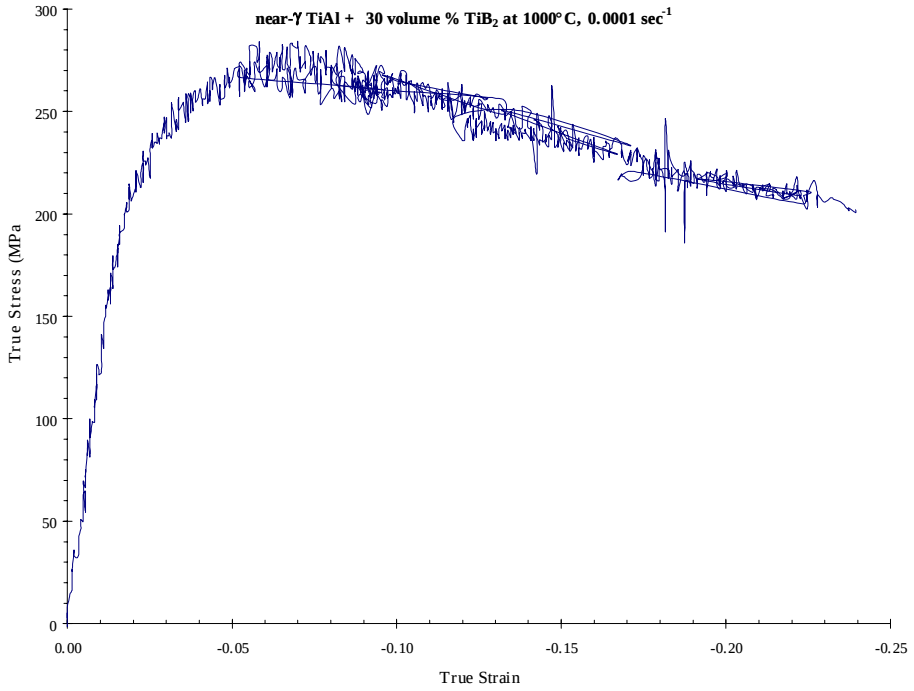

Figure 90: Corrected True Stress vs. True Plastic Strain for near-γ TiAl + 30 volume % TiB_2 at 1000°C and a strain-rate of 0.0001 sec^{-1}.

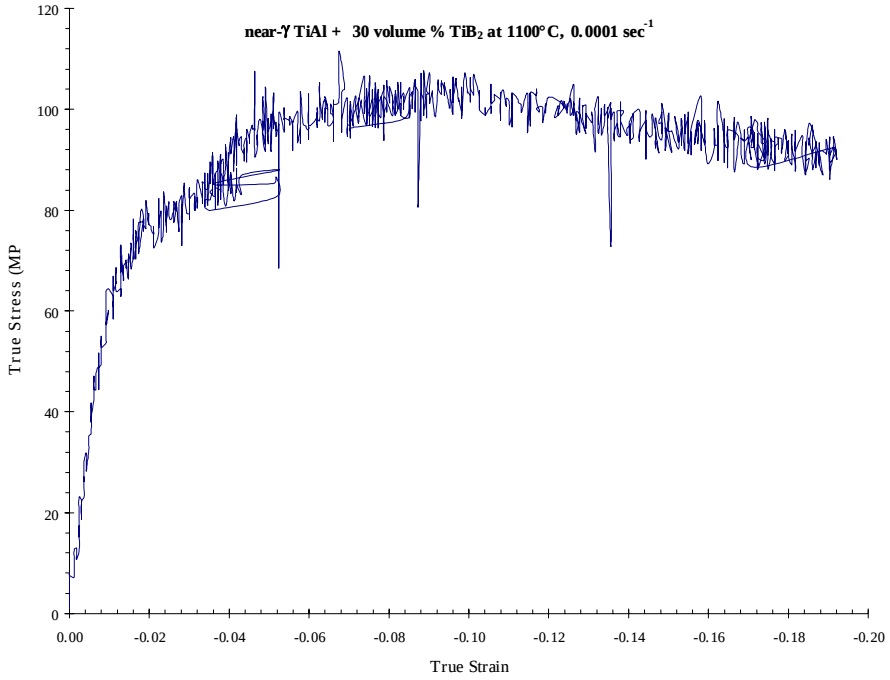

Figure 91: Corrected True Stress vs. True Plastic Strain for near-γ TiAl + 30 volume % TiB_2 at 1100°C and a strain-rate of 0.0001 sec^{-1}.

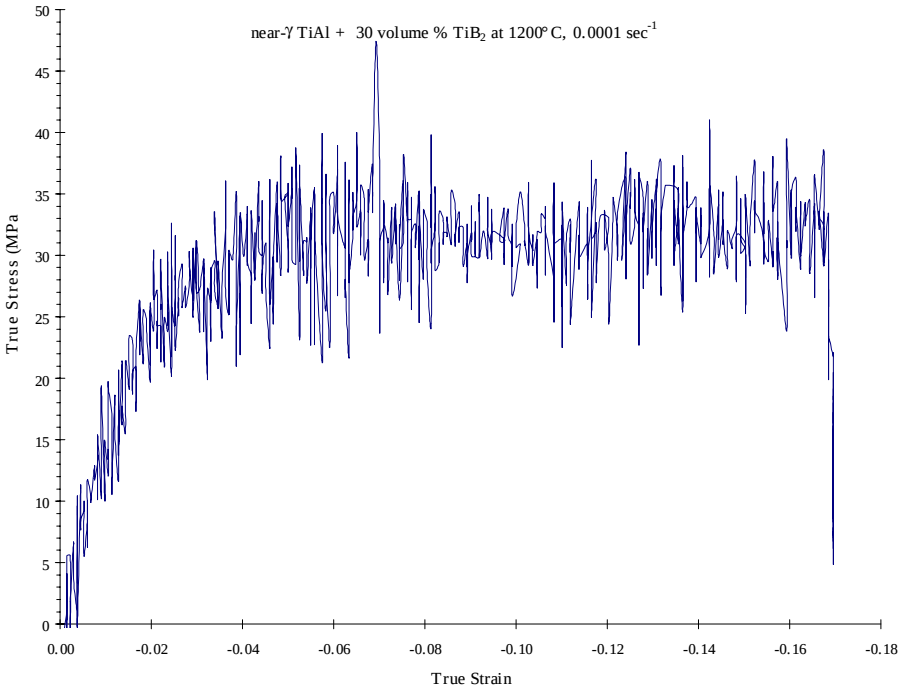

Figure 92: Corrected True Stress vs. True Plastic Strain for near-γ TiAl + 30 volume % TiB_2 at 1200°C and a strain-rate of 0.0001 sec^{-1}.

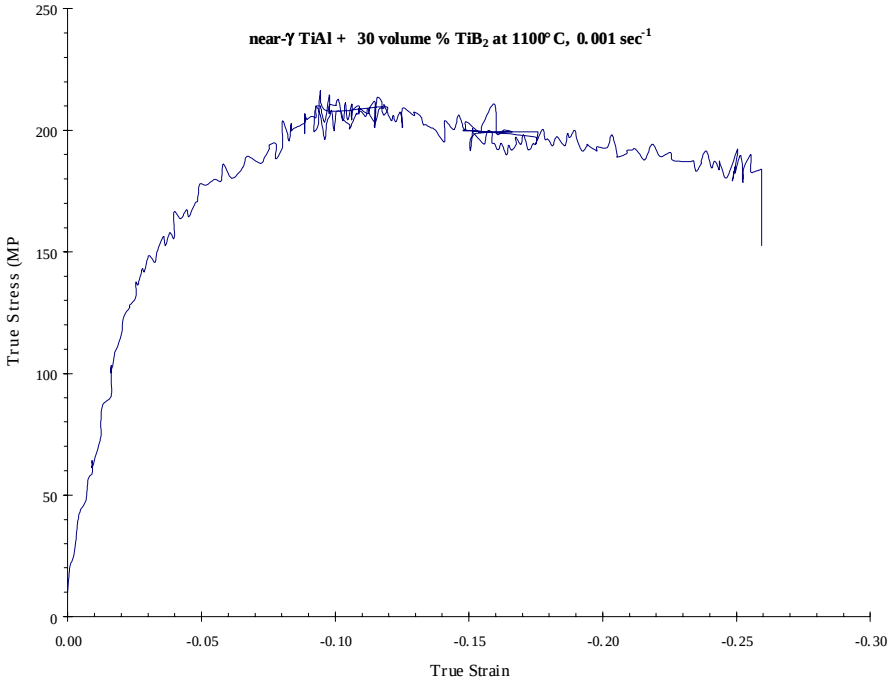

Figure 93: Corrected True Stress vs. True Plastic Strain for near-γ TiAl + 30 volume % TiB_2 at 1100°C and a strain-rate of 0.001 sec^{-1}.

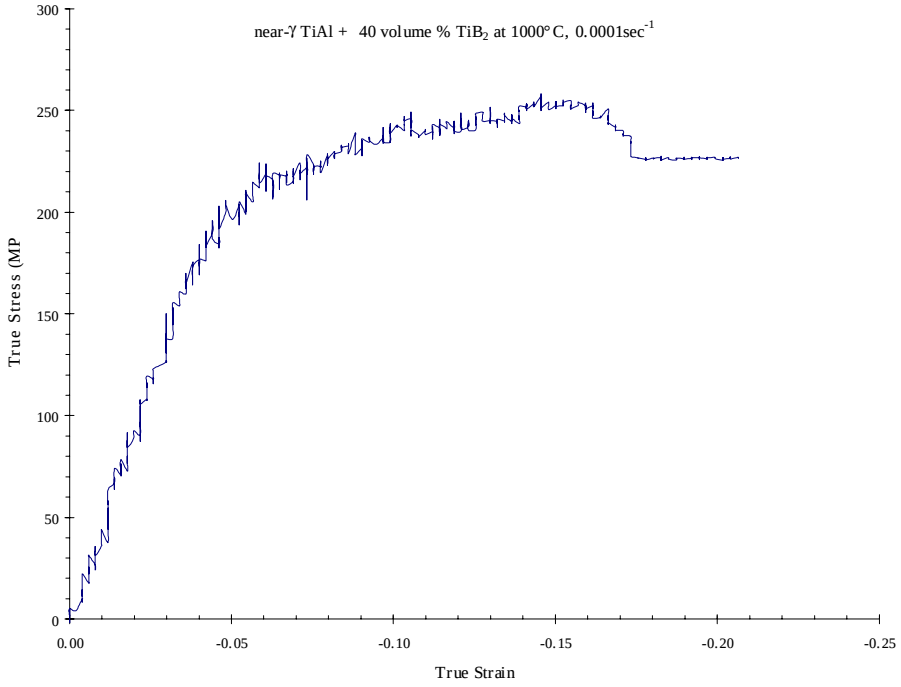

Figure 94: Corrected True Stress vs. True Plastic Strain for near-γ TiAl + 40 volume % TiB_2 at 1000°C and a strain-rate of 0.0001 sec^{-1}.

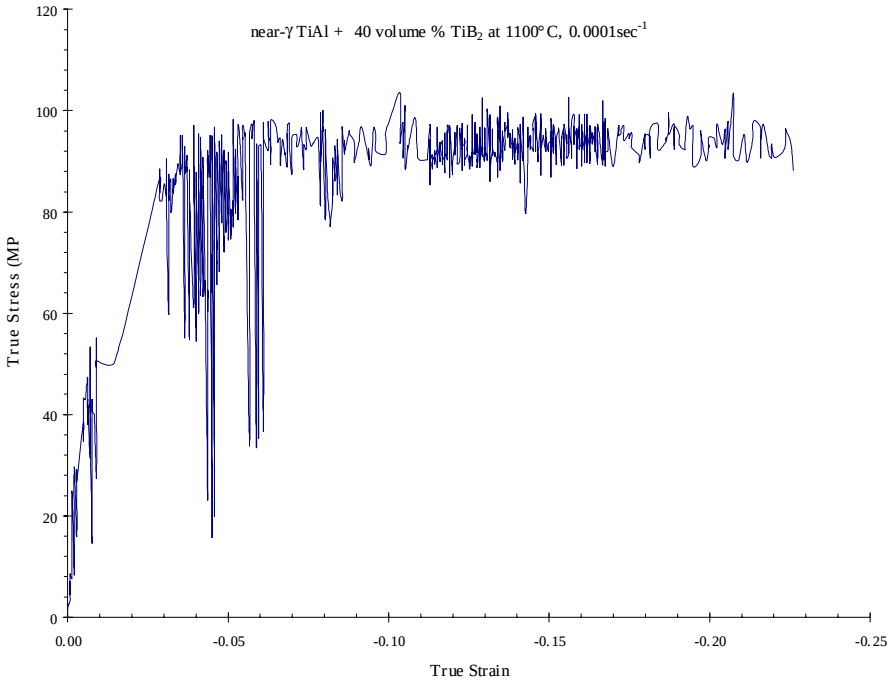

Figure 95: Corrected True Stress vs. True Plastic Strain for near-γ TiAl + 40 volume % TiB_2 at 1100°C and a strain-rate of 0.0001 sec^{-1}.

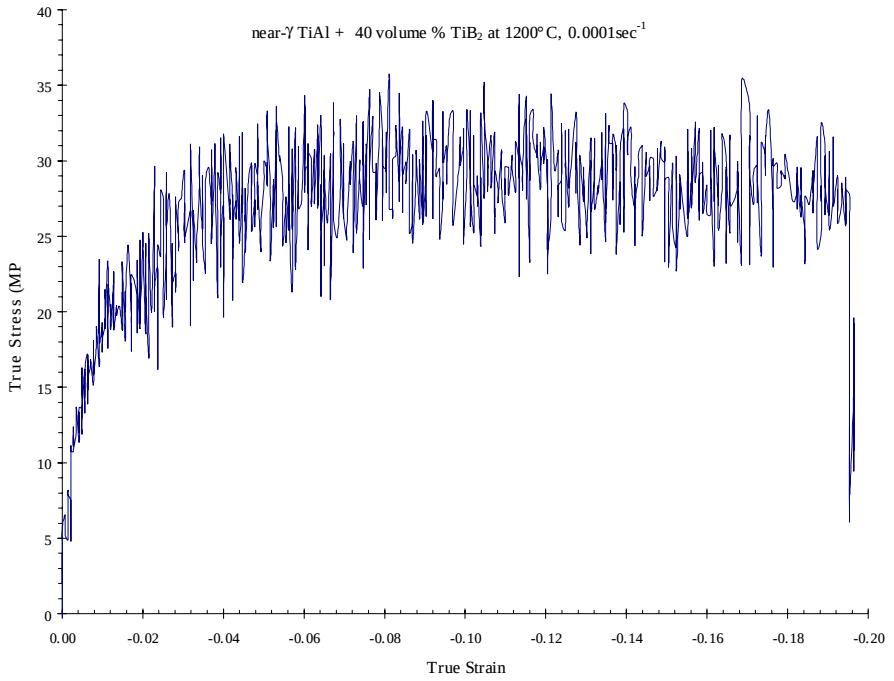

Figure 96: Corrected True Stress vs. True Plastic Strain for near-γ TiAl + 40 volume % TiB_2 at 1200°C and a strain-rate of 0.0001 sec^{-1}.

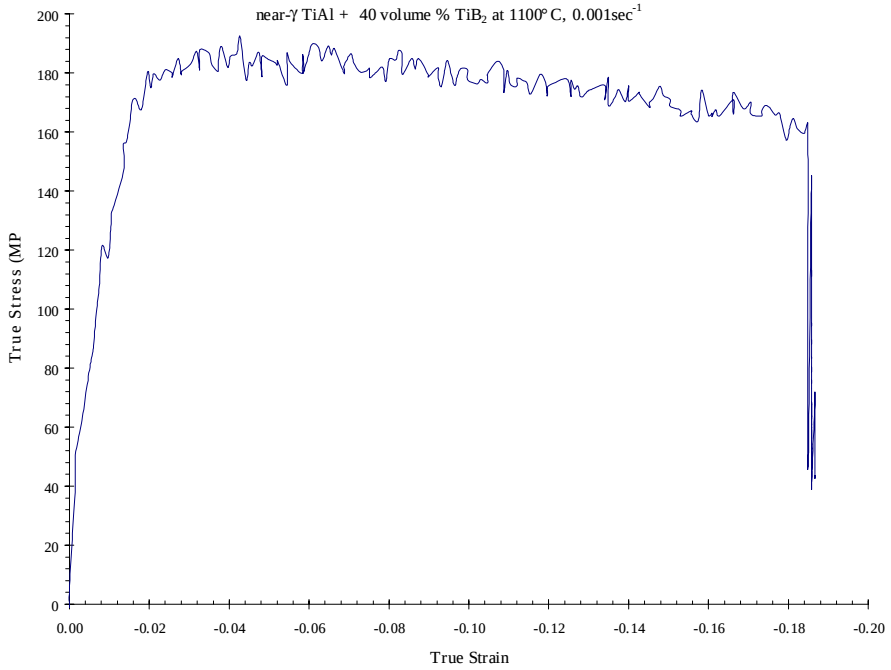

Figure 97: Corrected True Stress vs. True Plastic Strain for near-γ TiAl + 40 volume % TiB_2 at 1100°C and a strain-rate of 0.001 sec^{-1}.

Appendix C: Extrusion Data

This appendix contains a complete list of the extrusions performed, their sample designation, date, composition, can/cap material, extrusion temperature, extrusion ratio, and facility. This data is presented in Table XI. The extrusions used in the quantitative analysis presented in Chapter 5 are shaded. Raw extrusion data, as taken from the extrusion press, is shown in the following Tables and Figures.

Table XII: A list of extrusions performed to date, including notations of the extrusion parameters and sample designations.

Sample Designation	Date	Matrix + volume % (Reinforcement IMC)	Can/Cap Materials	Extrusion Temperature (°C)	Extrusion Die Ratio	Extrusion Facility
T-4040A (1)	*Apr-96*	*Ti-6Al-4V + 40 v% (Al_3Ti + 40v% TiB_2)*	*1020/304*	*1200*	*10:1 (flat)*	*Imperial College (London)*
T-4040A (2)	*Apr-96*	*Ti-6Al-4V + 40 v% (Al_3Ti + 40v% TiB_2)*	*1020/304*	*1200*	*16:1 (flat)*	*Imperial College (London)*
T-4040G (1)	*Apr-96*	*Ti-6Al-4V + 40 v% (TiAl + 40v% TiB_2)*	*1020/304*	*1200*	*10:1 (flat)*	*Imperial College (London)*
T-4040G (2)	*Apr-96*	*Ti-6Al-4V + 40 v% (TiAl + 40v% TiB_2)*	*1020/304*	*1200*	*16:1 (flat)*	*Imperial College (London)*
T-4040A (3)	Jun-96	Ti-6Al-4V + 40 v% (Al_3Ti + 40v% TiB_2)	Ti/Ti	1250	16:1 (flat)	Oak Ridge National Labs
T-4040A (4)	Jun-96	Ti-6Al-4V + 40 v% (Al_3Ti + 40v% TiB_2)	Ti/Ti	1300	16:1 (flat)	Oak Ridge National Labs
T-3040A (1)	Jun-96	Ti-6Al-4V + 40 v% (Al_3Ti + 30v% TiB_2)	Ti/Ti	1250	16:1 (flat)	Oak Ridge National Labs
T-3040A (2)	Jun-96	Ti-6Al-4V + 40 v% (Al_3Ti + 30v% TiB_2)	Ti/Ti	1300	16:1 (flat)	Oak Ridge National Labs
T-4040A (5)	Jun-96	Ti-6Al-4V + 40 v% (Al_3Ti + 40v% TiB_2)	1020/304	1250	16:1 (flat)	Oak Ridge National Labs
T-3040A (3)	Nov-96	Ti-6Al-4V + 40 v% (Al_3Ti + 30v% TiB_2)	1020/304	1200*	12:1 (cone)	Imperial College (London)
T-3040A (4)	Nov-96	Ti-6Al-4V + 40 v% (Al_3Ti + 30v% TiB_2)	1020/304	1250*	12:1 (cone)	Imperial College (London)
T-3040A (5)	Nov-96	Ti-6Al-4V + 40 v% (Al_3Ti + 30v% TiB_2)	1020/304	1300*	12:1 (cone)	Imperial College (London)
T-4040A (6)	Nov-96	Ti-6Al-4V + 40 v% (Al_3Ti + 40v% TiB_2)	1020/304	1200*	12:1 (cone)	Imperial College (London)
T-2040A (1)	Nov-96	Ti-6Al-4V + 40 v% (Al_3Ti + 40v% TiB_2)	1020/304	1200*	12:1 (cone)	Imperial College (London)
T-3040A-L	*Nov-96*	*Ti-6Al-4V + 40 v% (Al_3Ti + 30v% TiB_2)*	*1020/304*	*1200**	*12:1 (cone)*	*Imperial College (London)*
T-3040A-S	*Nov-96*	*Ti-6Al-4V + 40 v% (Al_3Ti + 30v% TiB_2)*	*1020/304*	*1200**	*12:1 (cone)*	*Imperial College (London)*
T-0040A	Nov-96	100 v% (Al_3Ti + 30v% TiB_2)	1020/304	1250*	12:1 (cone)	Imperial College (London)
T-4040A (7)	*Jul-97*	*Ti-6Al-4V + 40 v% (Al_3Ti + 40v% TiB_2)*	*1020/304*	*1200*	*25:1 (cone)*	*Imperial College (London)*
T-4040A (8)	Jul-97	Ti-6Al-4V + 40 v% (Al_3Ti + 40v% TiB_2)	1020/304	1200	12:1 (cone)	Imperial College (London)
T-3040A (6)	*Jul-97*	*Ti-6Al-4V + 30 v% (Al_3Ti + 40v% TiB_2)*	*1020/304*	*1180*	*12:1 (cone)*	*Imperial College (London)*
T-4000A	*Jul-97*	*Ti-6Al-4V + 40 v% (Al_3Ti)*	*1020/304*	*1200*	*12:1 (cone)*	*Imperial College (London)*
T-4020A	*Jul-97*	*Ti-6Al-4V + 40 v% (Al_3Ti + 20v% TiB_2)*	*1020/304*	*1200*	*12:1 (cone)*	*Imperial College (London)*
T-3040A (7)	*Jul-97*	*Ti-6Al-4V + 30 v% (Al_3Ti + 40v% TiB_2)*	*1020/304*	*1200*	*12:1 (cone)*	*Imperial College (London)*
T-2040A (2)	Jul-97	Ti-6Al-4V + 20 v% (Al_3Ti + 40v% TiB_2)	1020/304	1200	12:1 (cone)	Imperial College (London)
T-4040A (9)	N/A**	Ti-6Al-4V + 40 v% (Al_3Ti + 40v% TiB_2)	1020/304	N/A	N/A	N/A
T-4040A (10)	N/A**	Ti-6Al-4V + 40 v% (Al_3Ti + 40v% TiB_2)	1020/304	N/A	N/A	N/A
T-4040A (11)HIP	N/A**	Ti-6Al-4V + 40 v% (Al_3Ti + 40v% TiB_2)	1020/304	N/A	N/A	N/A

* Soak temperature is approximate due to equipment failure.

** Sample has not been extruded to date, but is “in the queue.”

Table XIII: Extrusion Data for Ti-6Al-4V + 40 v% (Al_3Ti + 40 v% TiB_2) billet at 1200°C, low die ratio.

Date	6-6-1996
Alloy	T4040A
PRE-EXTRUSION HEATING CONDITIONS	
Heating Method	FURNACE
Heating Time (min)	60
Billet Temperature (°C)	1200
EXTRUSION CONDITIONS	
Extrusion Mode	DIRECT
Contained Diameter (mm)	60
Container Temperature (°C)	500
Extrude Shape	ROD
Extrusion Ratio (measured)	18:1
Ram Speed (mm/sec)	4.28
Lubrication	DAG/GLASS
Quench	AIR
EXTRUSION RESULTS	
Maximum Load (MN)	1.61
Maximum Pressure (MPa)	569
Occurred at ram displacement (mm)	30
After time (sec)	4
Steady-state Load (MN)	1.58
Steady-state Pressure (MPa)	559
Occurred at ram displacement (mm)	33
After time (sec)	5
Maximum Load (tons)	364
Total Ram Displacement (mm) - adjusted	55
Total Extrusion Time (sec)	15
Total Extruded Length (calculated)	1378
Total Test Time (sec)	48
Comment:	OK

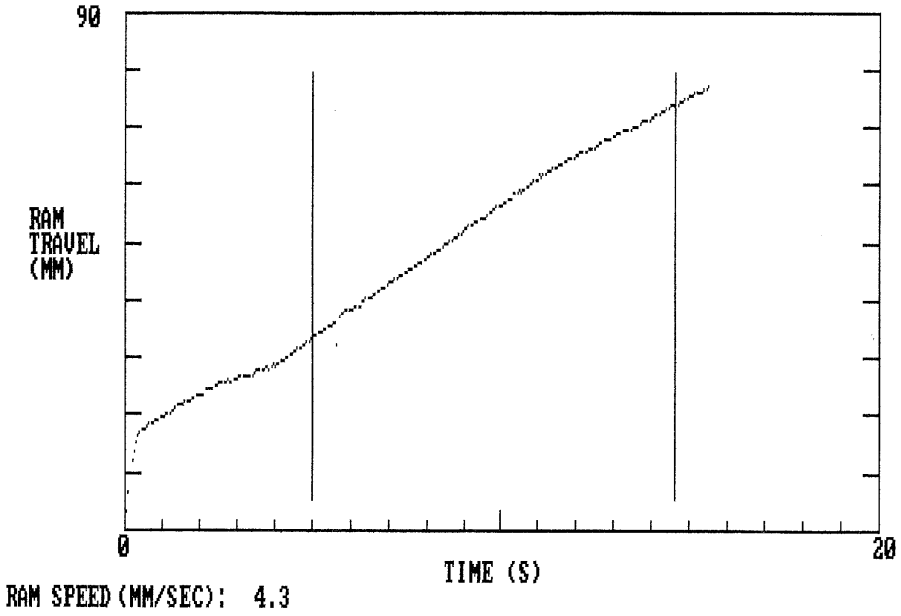

Figure 98: Ram Displacement versus Extrusion Time Chart for Ti-6Al-4V + 40 v% (Al_3Ti + 40 v% TiB_2) billet at 1200°C, low die ratio.

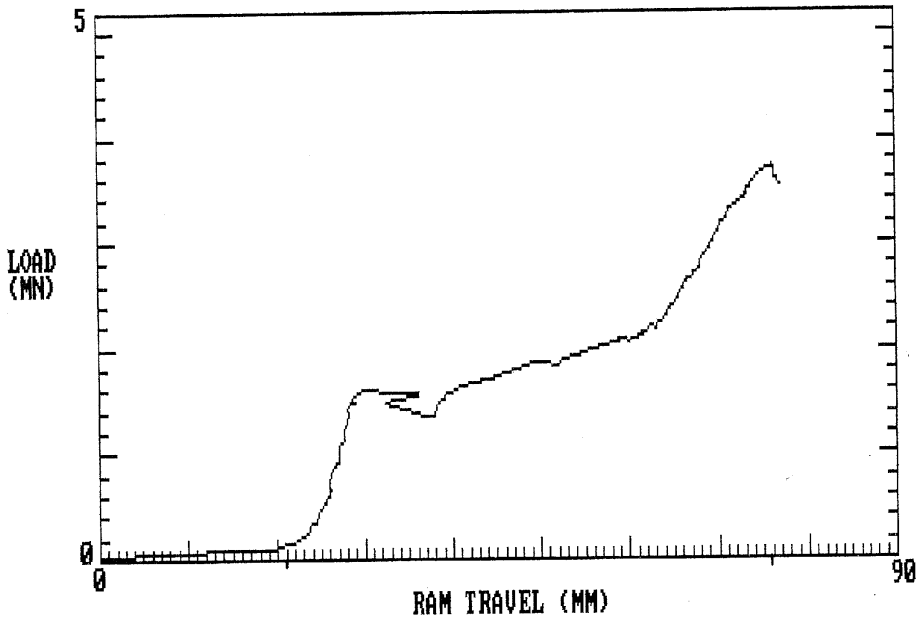

Figure 99: Extrusion Ram Load versus Ram Displacement Chart for Ti-6Al-4V + 40 v% (Al_3Ti + 40 v% TiB_2) billet at 1200°C, low die ratio.

Table XIV: Extrusion Data for Ti-6Al-4V + 40 v% (Al_3Ti + 40 v% TiB_2) billet at 1200°C, high die ratio.

Date	7-7-97
Alloy	T4040A
PRE-EXTRUSION HEATING CONDITIONS	
Heating Method	FURNACE
Heating Time (min)	60
Billet Temperature (°C)	1200
EXTRUSION CONDITIONS	
Extrusion Mode	DIRECT
Contained Diameter (mm)	60
Container Temperature (°C)	500
Extrude Shape	ROD
Extrusion Ratio (measured)	25:1
Ram Speed (mm/sec)	2.50
Lubrication	DAG/GLASS
Quench	AIR
EXTRUSION RESULTS	
Maximum Load (MN)	4.39
Maximum Pressure (MPa)	1553
Occurred at ram displacement (mm)	198
After time (sec)	23
Steady-state Load (MN)	4.38
Steady-state Pressure (MPa)	1549
Occurred at ram displacement (mm)	200
After time (sec)	25
Maximum Load (tons)	413
Total Ram Displacement (mm) – adjusted	55
Total Extrusion Time (sec)	27
Total Extrusion Length (calculated)	1175
Total Test Time (sec)	52
Comment: DID NOT FULLY EXTRUDE!!! Die ratio too high	

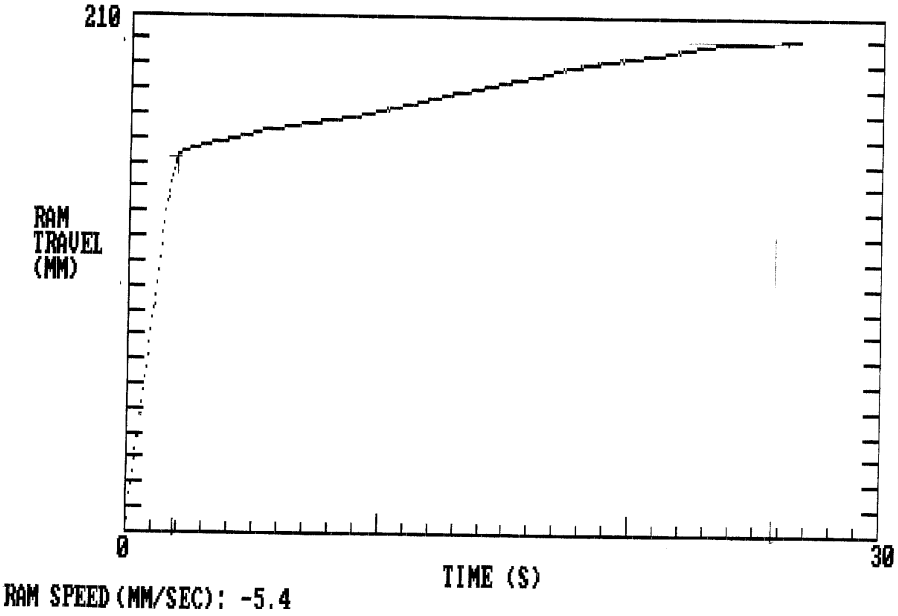

Figure 100: Ram Displacement versus Extrusion Time Chart for Ti-6Al-4V + 40 v% (Al_3Ti + 40 v% TiB_2) billet at 1200°C, high die ratio.

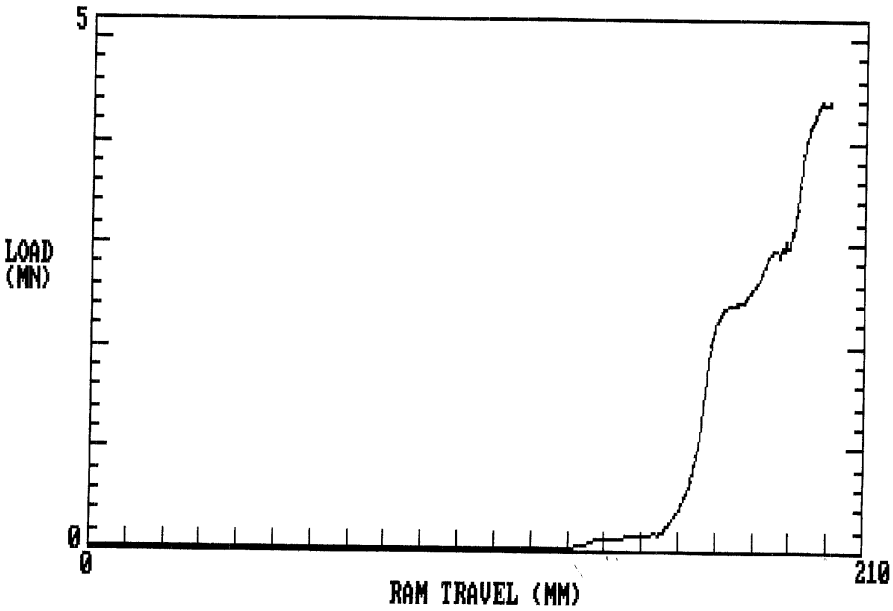

Figure 101: Extrusion Ram Load versus Ram Displacement Chart for Ti-6Al-4V + 40 v% (Al_3Ti + 40 v% TiB_2) billet at 1200°C, high die ratio.

Table XV: Extrusion Data for Ti-6Al-4V + 40 v% ($Ti_{54}Al_{46}$ + 40 v% TiB_2) billet at 1200°C, low die ratio.

Date	6-6-1996
Alloy	T4040G
PRE-EXTRUSION HEATING CONDITIONS	
Heating Method	FURNACE
Heating Time (min)	60
Billet Temperature (°C)	1200
EXTRUSION CONDITIONS	
Extrusion Mode	DIRECT
Contained Diameter (mm)	60
Container Temperature (°C)	500
Extrude Shape	ROD
Extrusion Ratio (measured)	9:1
Ram Speed (mm/sec)	4.65
Lubrication	Y/DAG/GLASS
Quench	AIR
EXTRUSION RESULTS	
Maximum Load (MN)	1.37
Maximum Pressure (MPa)	485
Occurred at ram displacement (mm)	28
After time (sec)	4
Steady-state Load (MN)	1.34
Steady-state Pressure (MPa)	474
Occurred at ram displacement (mm)	30
After time (sec)	5
Maximum Load (tons)	230
Total Ram Displacement (mm)	52
Total Extrusion Time (sec)	14
Total Extrusion Length (calculated)	720
Total Test Time (sec)	51
Comment:	OK

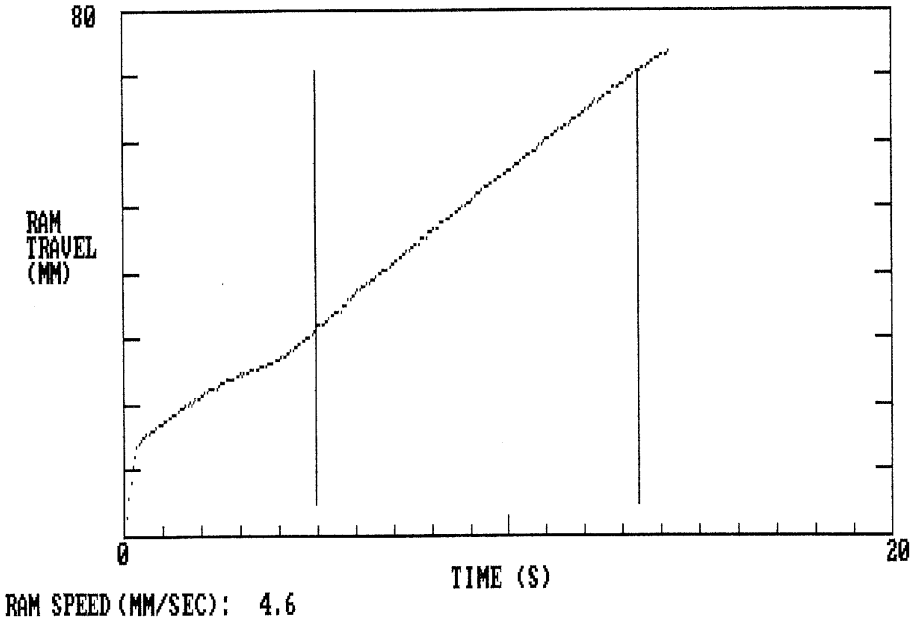

Figure 102: Ram Displacement versus Extrusion Time Chart for Ti-6Al-4V + 40 v% ($Ti_{54}Al_{46}$ + 40 v% TiB_2) billet at 1200°C, low die ratio.

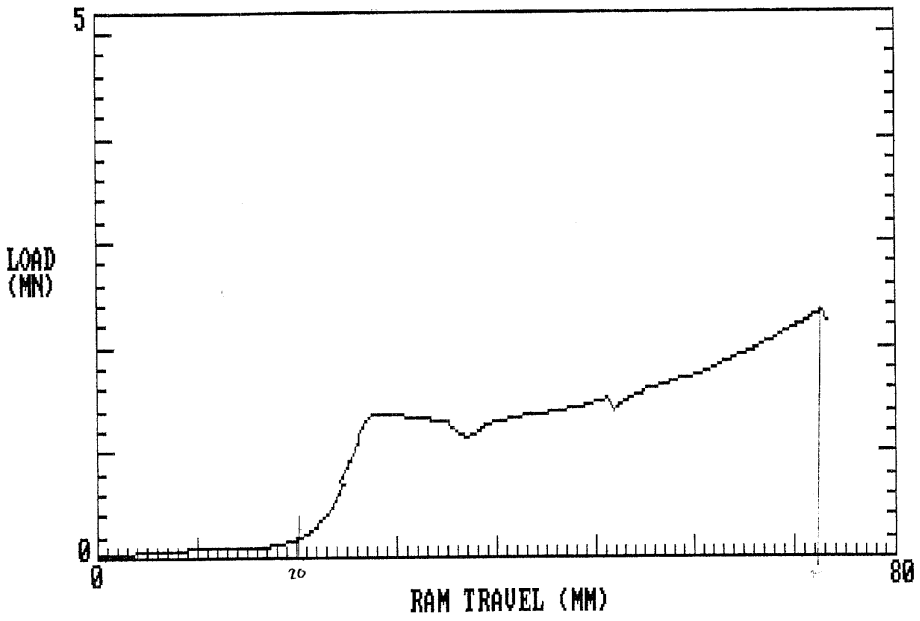

Figure 103: Extrusion Ram Load versus Ram Displacement Chart for Ti-6Al-4V + 40 v% ($Ti_{54}Al_{46}$ + 40 v% TiB_2) billet at 1200°C, low die ratio.

Table XVI: Extrusion Data for Ti-6Al-4V + 40 v% ($Ti_{54}Al_{46}$ + 40 v% TiB_2) billet at 1200°C, high die ratio.

Date	6-6-1996
Alloy	T4040G
PRE-EXTRUSION HEATING CONDITIONS	
Heating Method	FURNACE
Heating Time (min)	60
Billet Temperature (°C)	1200
EXTRUSION CONDITIONS	
Extrusion Mode	DIRECT
Contained Diameter (mm)	60
Container Temperature (°C)	500
Extrude Shape	ROD
Extrusion Ratio (measured)	25:1
Ram Speed (mm/sec)	4.28
Lubrication	DAG/GLASS
Quench	AIR
EXTRUSION RESULTS	
Maximum Load (MN)	3.98
Maximum Pressure (MPa)	1408
Occurred at ram displacement (mm)	73
After time (sec)	16
Steady-state Load (MN)	0.09
Steady-state Pressure (MPa)	32
Occurred at ram displacement (mm)	71
After time (sec)	17
Maximum Load (tons)	397
Total Ram Displacement (mm)	74
Total Extrusion Time (sec)	16
Total Extrusion Length (calculated)	1925
Total Test Time (sec)	23
Comment:	OK

Table XVII: Extrusion Data for Ti-6Al-4V + 40 v% Al_3Ti billet at 1200°C, low die ratio.

Date	8-21-97
Alloy	T4000A
PRE-EXTRUSION HEATING CONDITIONS	
Heating Method	FURNACE
Heating Time (min)	60
Billet Temperature (°C)	1200
EXTRUSION CONDITIONS	
Extrusion Mode	DIRECT
Contained Diameter (mm)	60
Container Temperature (°C)	500
Extrude Shape	ROD
Extrusion Ratio (measured)	16:1
Ram Speed (mm/sec)	2.72
Lubrication	DAG/GLASS
Quench	AIR
EXTRUSION RESULTS	
Maximum Load (MN)	2.3
Maximum Pressure (MPa)	813
Occurred at ram displacement (mm)	43
After time (sec)	10
Steady-state Load (MN)	2.28
Steady-state Pressure (MPa)	806
Occurred at ram displacement (mm)	46
After time (sec)	11
Maximum Load (tons)	337
Total Ram Displacement (mm)	63
Total Extrusion Time (sec)	26
Total Extrusion Length (calculated)	624
Total Test Time (sec)	53
Comment:	OK

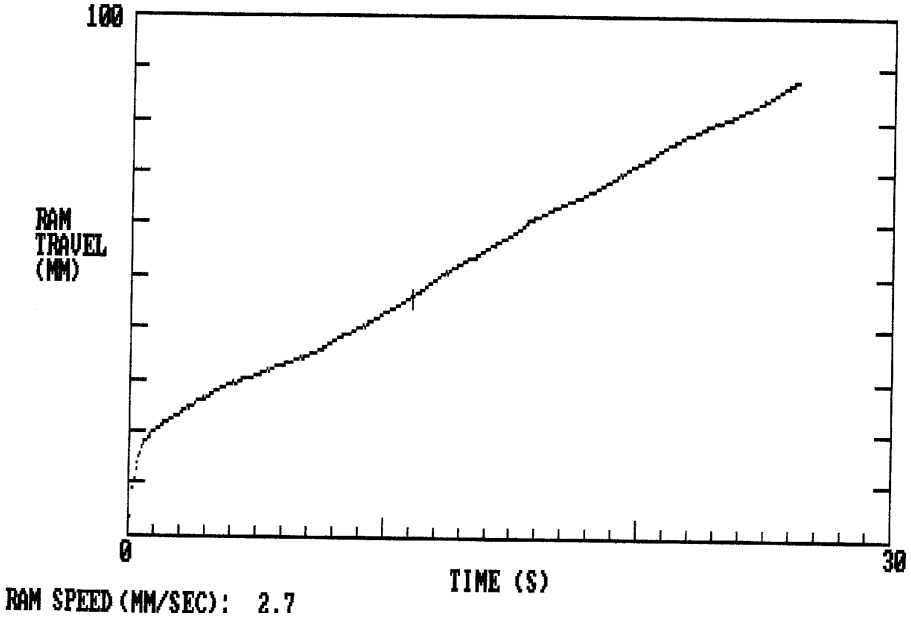

Figure 104: Ram Displacement versus Extrusion Time Chart for Ti-6Al-4V + 40 v% Al_3Ti billet at 1200°C, low die ratio.

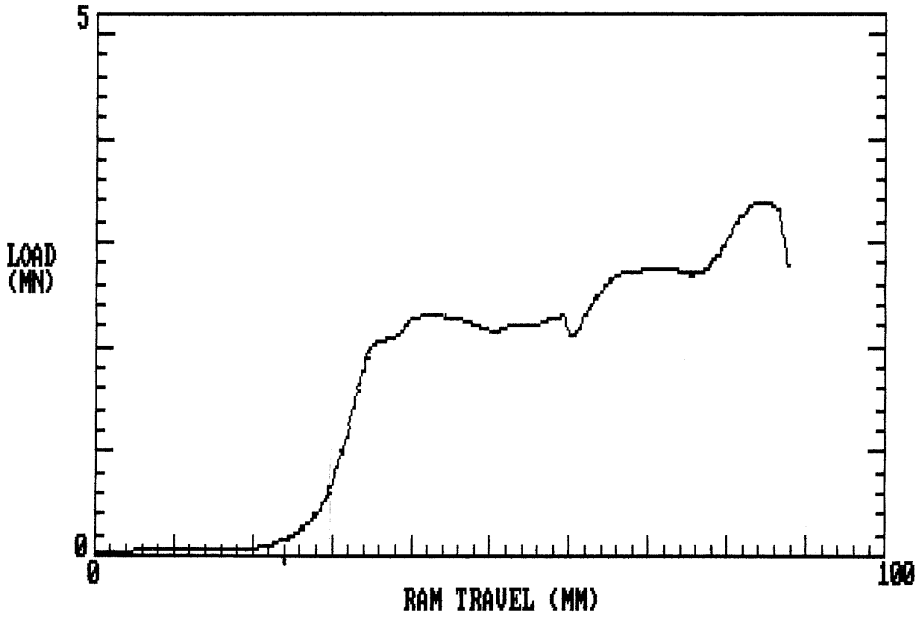

Figure 105: Extrusion Ram Load versus Ram Displacement Chart for Ti-6Al-4V + 40 v% Al_3Ti billet at 1200°C, low die ratio.

Table XVIII: Extrusion Data for Ti-6Al-4V + 40 v% (Al_3Ti + 20 v% TiB_2) billet at 1200°C, low die ratio.

Date	8-21-1997
Alloy	T4020A
PRE-EXTRUSION HEATING CONDITIONS	
Heating Method	FURNACE
Heating Time (min)	60
Billet Temperature (°C)	1200
EXTRUSION CONDITIONS	
Extrusion Mode	DIRECT
Contained Diameter (mm)	60
Container Temperature (°C)	500
Extrude Shape	ROD
Extrusion Ratio (measured)	11:1
Ram Speed (mm/sec)	2.93
Lubrication	DAG/GLASS
Quench	AIR
EXTRUSION RESULTS	
Maximum Load (MN)	1.97
Maximum Pressure (MPa)	697
Occurred at ram displacement (mm)	39
After time (sec)	10
Steady-state Load (MN)	2
Steady-state Pressure (MPa)	707
Occurred at ram displacement (mm)	42
After time (sec)	11
Maximum Load (tons)	271
Total Ram Displacement (mm)	60
Total Extrusion Time (sec)	24
Total Extrusion Length (calculated)	442
Total Test Time (sec)	47
Comment:	OK

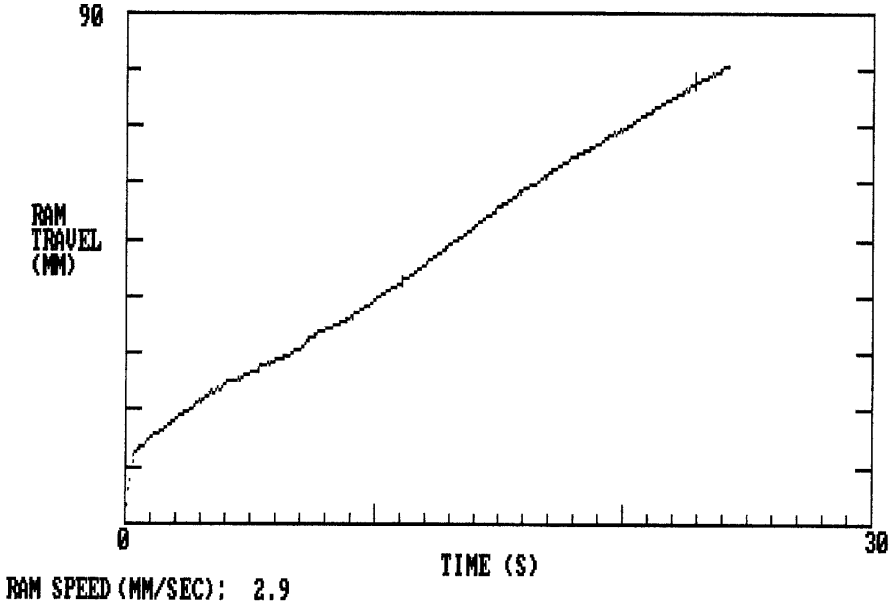

Figure 106: Ram Displacement versus Extrusion Time Chart for Ti-6Al-4V + 40 v% (Al_3Ti + 20 v% TiB_2) billet at 1200°C, low die ratio.

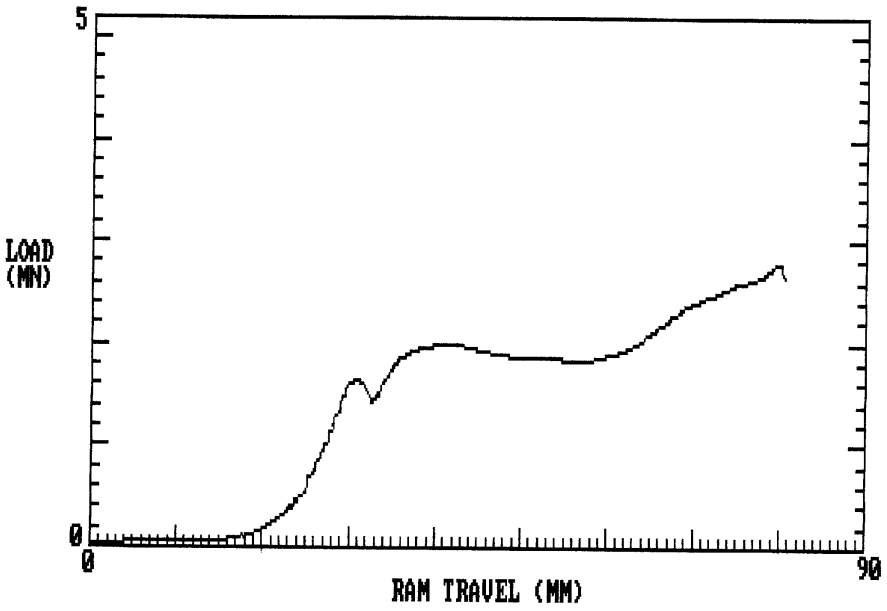

Figure 107: Extrusion Ram Load versus Ram Displacement Chart for Ti-6Al-4V + 40 v% (Al_3Ti + 20 v% TiB_2) billet at 1200°C, low die ratio.

Table XIX: Extrusion Data for Ti-6Al-4V + 20 v% (Al_3Ti + 40 v% TiB_2) billet at 1200°C, low die ratio.

Date	8-22-1997
Alloy	T2040A
PRE-EXTRUSION HEATING CONDITIONS	
Heating Method	FURNACE
Heating Time (min)	60
Billet Temperature (°C)	1200
EXTRUSION CONDITIONS	
Extrusion Mode	DIRECT
Contained Diameter (mm)	60
Container Temperature (°C)	500
Extrude Shape	ROD
Extrusion Ratio (measured)	21:1
Ram Speed (mm/sec)	3.03
Lubrication	DAG/GLASS
Quench	AIR
EXTRUSION RESULTS	
Maximum Load (MN)	1.54
Maximum Pressure (MPa)	545
Occurred at ram displacement (mm)	27
After time (sec)	6
Steady-state Load (MN)	1.46
Steady-state Pressure (MPa)	516
Occurred at ram displacement (mm)	29
After time (sec)	6
Maximum Load (tons)	259
Total Ram Displacement (mm)	59
Total Extrusion Time (sec)	22
Total Extrusion Length (calculated)	916
Total Test Time (sec)	46
Comment:	OK

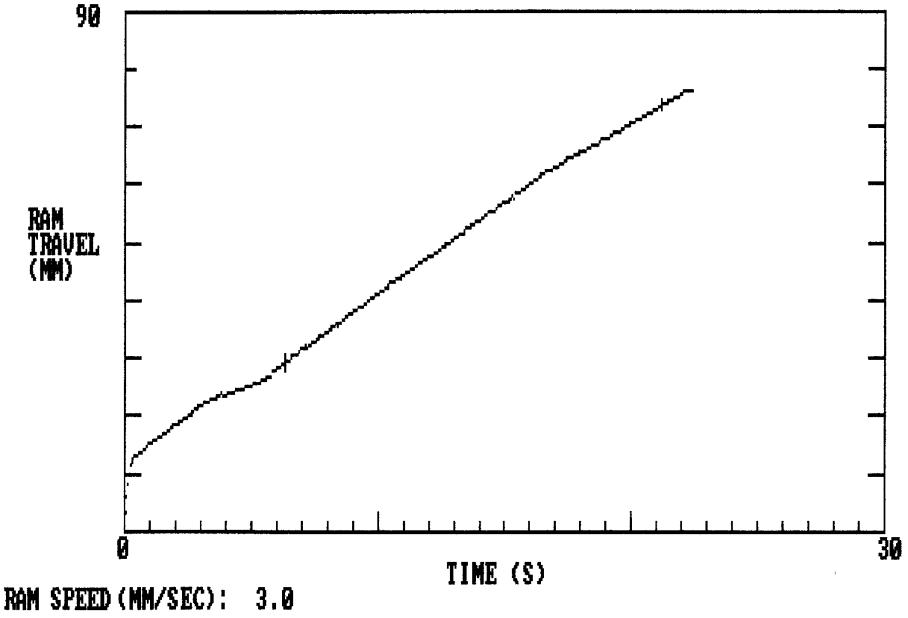

Figure 108: Ram Displacement versus Extrusion Time Chart for Ti-6Al-4V + 20 v% (Al_3Ti + 40 v% TiB_2) billet at 1200°C, low die ratio.

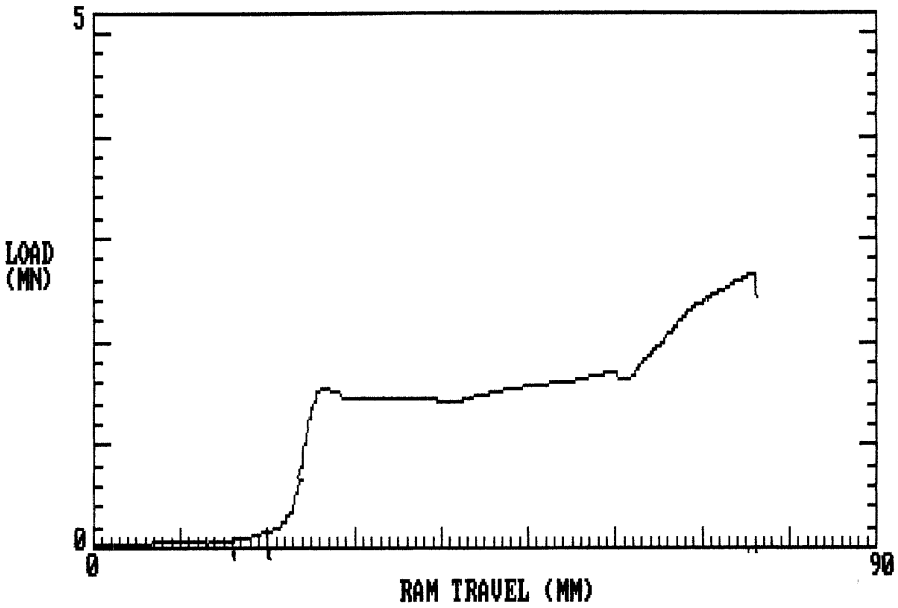

Figure 109: Extrusion Ram Load versus Ram Displacement Chart for Ti-6Al-4V + 20 v% (Al_3Ti + 40 v% TiB_2) billet at 1200°C, low die ratio.

Table XX: Extrusion Data for Ti-6Al-4V + 30 v% (Al_3Ti + 40 v% TiB_2) billet at 1200°C, low die ratio.

Date	8-22-1997
Alloy	T3040A
PRE-EXTRUSION HEATING CONDITIONS	
Heating Method	FURNACE
Heating Time (min)	60
Billet Temperature (°C)	1200
EXTRUSION CONDITIONS	
Extrusion Mode	DIRECT
Contained Diameter (mm)	60
Container Temperature (°C)	500
Extrude Shape	ROD
Extrusion Ratio (measured)	23:1
Ram Speed (mm/sec)	3.01
Lubrication	DAG/GLASS
Quench	AIR
EXTRUSION RESULTS	
Maximum Load (MN)	1.54
Maximum Pressure (MPa)	545
Occurred at ram displacement (mm)	29
After time (sec)	6
Steady-state Load (MN)	1.53
Steady-state Pressure (MPa)	541
Occurred at ram displacement (mm)	30
After time (sec)	7
Maximum Load (tons)	290
Total Ram Displacement (mm)	60
Total Extrusion Time (sec)	23
Total Extrusion Length (calculated)	968
Total Test Time (sec)	49
Comment:	OK

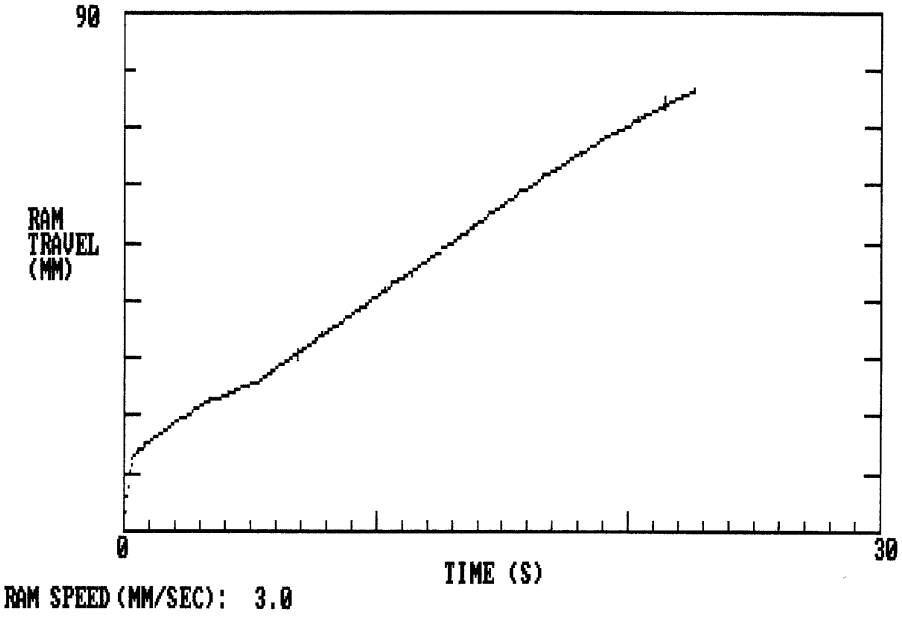

Figure 110: Ram Displacement versus Extrusion Time Chart for Ti-6Al-4V + 30 v% (Al_3Ti + 40 v% TiB_2) billet at 1200°C, low die ratio.

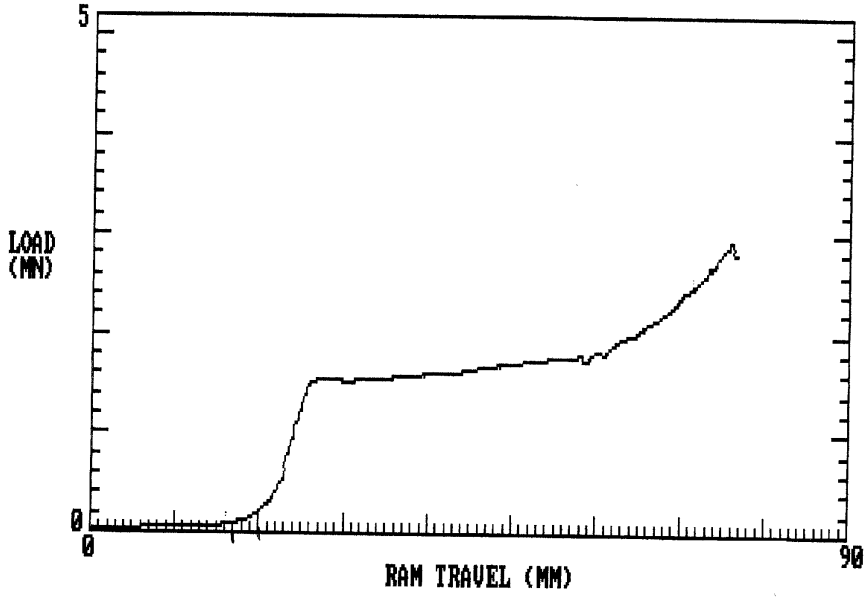

Figure 111: Extrusion Ram Load versus Ram Displacement Chart for Ti-6Al-4V + 30 v% (Al_3Ti + 40 v% TiB_2) billet at 1200°C, low die ratio.

Table XXI: Extrusion Data for Ti-6Al-4V + 30 v% (Al_3Ti + 40 v% TiB_2) billet at 1180°C, low die ratio.

Date	7-8-1997
Alloy	T3040A
PRE-EXTRUSION HEATING CONDITIONS	
Heating Method	FURNACE
Heating Time (min)	60
Billet Temperature (°C)	1200
EXTRUSION CONDITIONS	
Extrusion Mode	DIRECT
Contained Diameter (mm)	60
Container Temperature (°C)	500
Extrude Shape	ROD
Extrusion Ratio (measured)	23:1
Ram Speed (mm/sec)	2.57
Lubrication	DAG/GLASS
Quench	AIR
EXTRUSION RESULTS	
Maximum Load (MN)	2.32
Maximum Pressure (MPa)	821
Occurred at ram displacement (mm)	20
After time (sec)	9
Steady-state Load (MN)	2.26
Steady-state Pressure (MPa)	799
Occurred at ram displacement (mm)	22
After time (sec)	10
Maximum Load (tons)	321
Total Ram Displacement (mm)	53
Total Extrusion Time (sec)	25
Total Extrusion Length (calculated)	968
Total Test Time (sec)	54
Comment:	OK

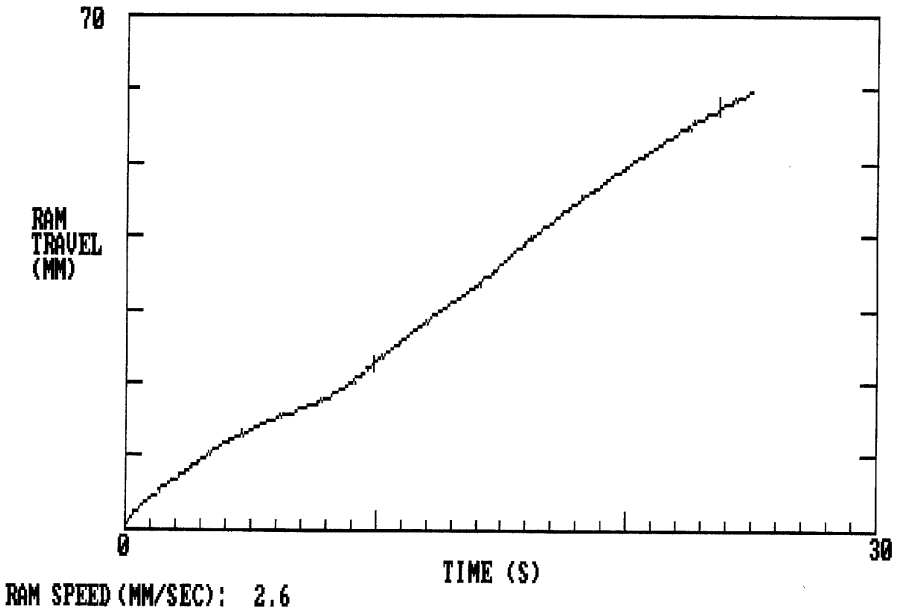

Figure 112: Ram Displacement versus Extrusion Time Chart for Ti-6Al-4V + 30 v% (Al_3Ti + 40 v% TiB_2) billet at 1180°C, low die ratio.

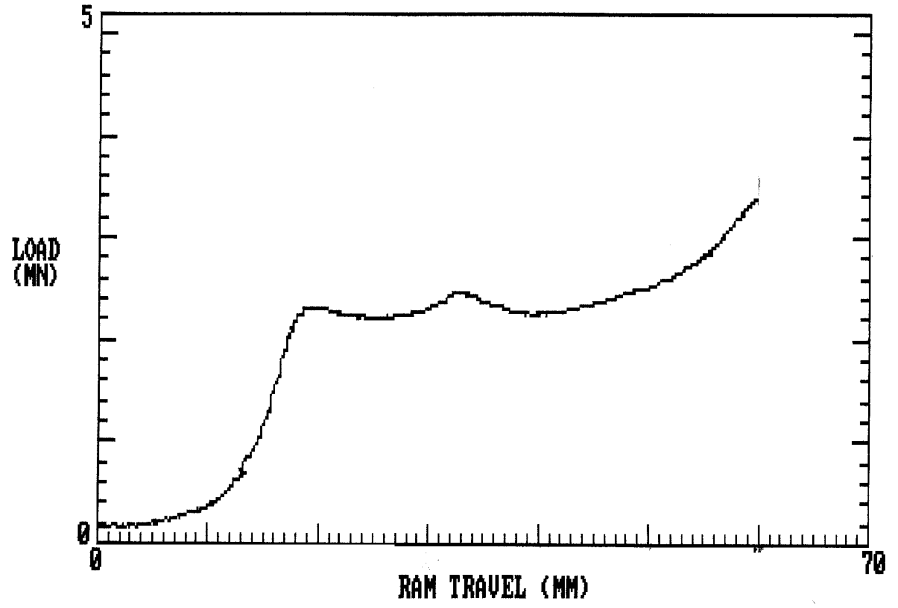

Figure 113: Extrusion Ram Load versus Ram Displacement Chart for Ti-6Al-4V + 30 v% (Al_3Ti + 40 v% TiB_2) billet at 1180°C, low die ratio.

Table XXII: Extrusion Data for Ti-6Al-4V + 30 v% (Al_3Ti + 40 v% TiB_2) (large) billet at 1180°C, low die ratio.

Date	11-18-1996
Alloy	T3040A-L
PRE-EXTRUSION HEATING CONDITIONS	
Heating Method	FURNACE
Heating Time (min)	60
Billet Temperature (°C)	1200
EXTRUSION CONDITIONS	
Extrusion Mode	DIRECT
Contained Diameter (mm)	60
Container Temperature (°C)	500
Extrude Shape	ROD
Extrusion Ratio (measured)	36:1
Ram Speed (mm/sec)	4.93
Lubrication	Y/GF
Quench	AIR
EXTRUSION RESULTS	
Maximum Load (MN)	1.54
Maximum Pressure (MPa)	545
Occurred at ram displacement (mm)	45
After time (sec)	9
Steady-state Load (MN)	1.44
Steady-state Pressure (MPa)	509
Occurred at ram displacement (mm)	50
After time (sec)	9
Maximum Load (tons)	271
Total Ram Displacement (mm)	94
Total Extrusion Time (sec)	25
Total Extrusion Length (calculated)	2016
Total Test Time (sec)	79
Comment:	OK

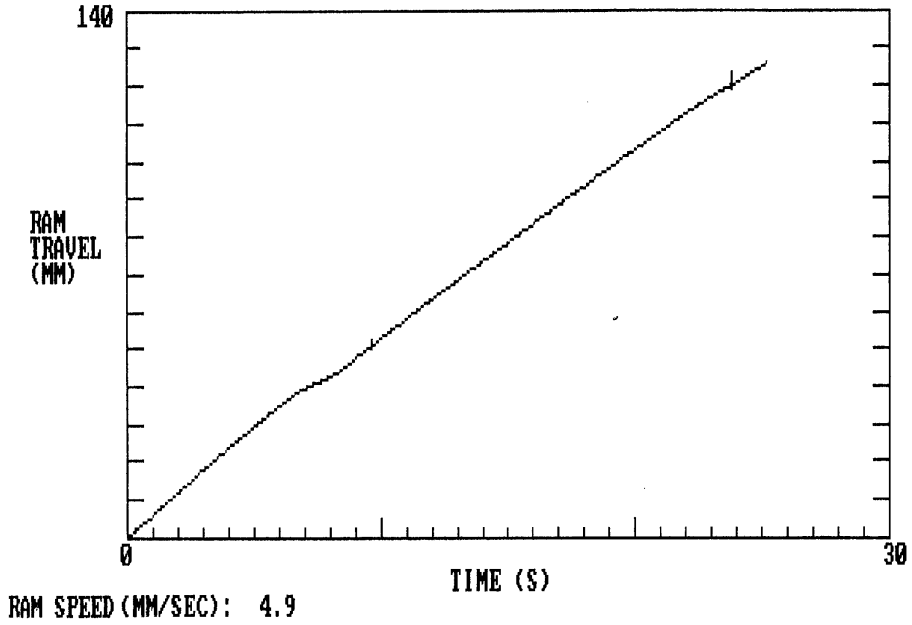

Figure 114: Ram Displacement versus Extrusion Time Chart for Ti-6Al-4V + 30 v% (Al_3Ti + 40 v% TiB_2) (large) billet at 1180°C, low die ratio.

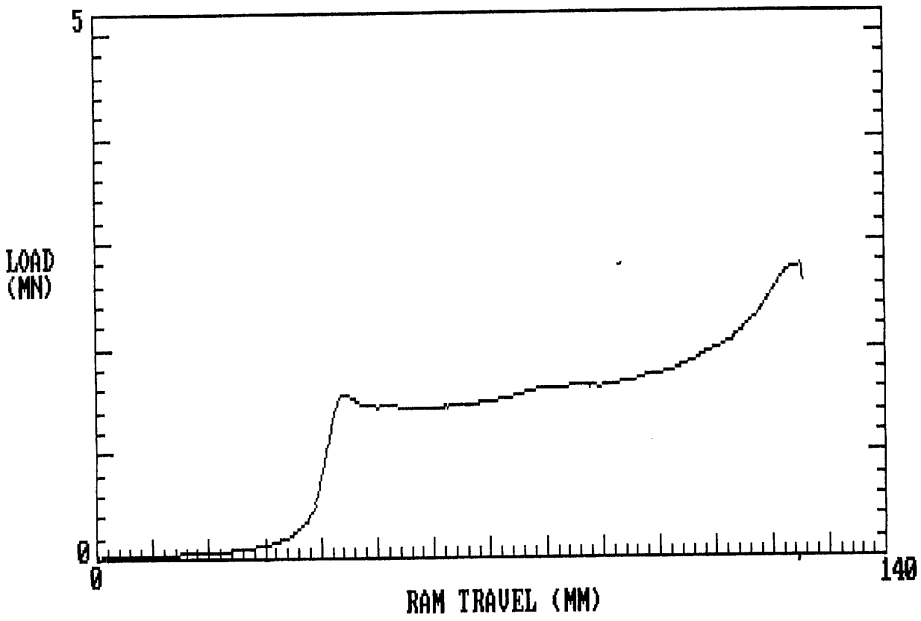

Figure 115: Extrusion Ram Load versus Ram Displacement Chart for Ti-6Al-4V + 30 v% (Al_3Ti + 40 v% TiB_2) (large) billet at 1180°C, low die ratio.

Table XXIII: Extrusion Data for Ti-6Al-4V + 30 v% (Al_3Ti + 40 v% TiB_2) (small) billet at 1180°C, low die ratio.

Date	11-25-1996
Alloy	T3040A-S
PRE-EXTRUSION HEATING CONDITIONS	
Heating Method	FURNACE
Heating Time (min)	60
Billet Temperature (°C)	1200
EXTRUSION CONDITIONS	
Extrusion Mode	DIRECT
Contained Diameter (mm)	60
Container Temperature (°C)	500
Extrude Shape	ROD
Extrusion Ratio (measured)	36:1
Ram Speed (mm/sec)	4.75
Lubrication	Y/GF
Quench	AIR
EXTRUSION RESULTS	
Maximum Load (MN)	2.13
Maximum Pressure (MPa)	753
Occurred at ram displacement (mm)	56
After time (sec)	11
Steady-state Load (MN)	2.11
Steady-state Pressure (MPa)	746
Occurred at ram displacement (mm)	61
After time (sec)	12
Maximum Load (tons)	334
Total Ram Displacement (mm)	95
Total Extrusion Time (sec)	27
Total Extrusion Length (calculated)	1980
Total Test Time (sec)	61
Comment:	OK

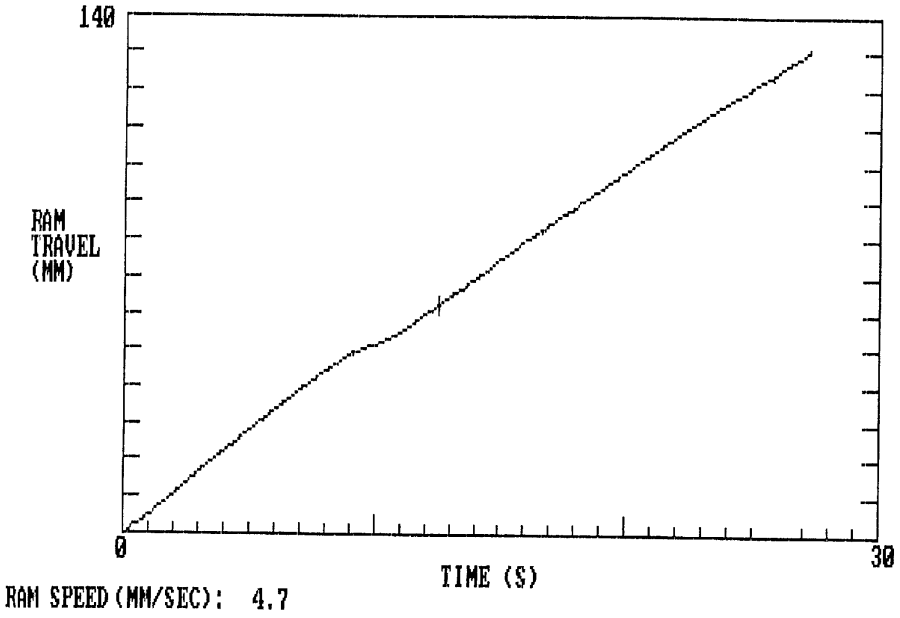

Figure 116: Ram Displacement versus Extrusion Time Chart for Ti-6Al-4V + 30 v% (Al_3Ti + 40 v% TiB_2) (small) billet at 1180°C, low die ratio.

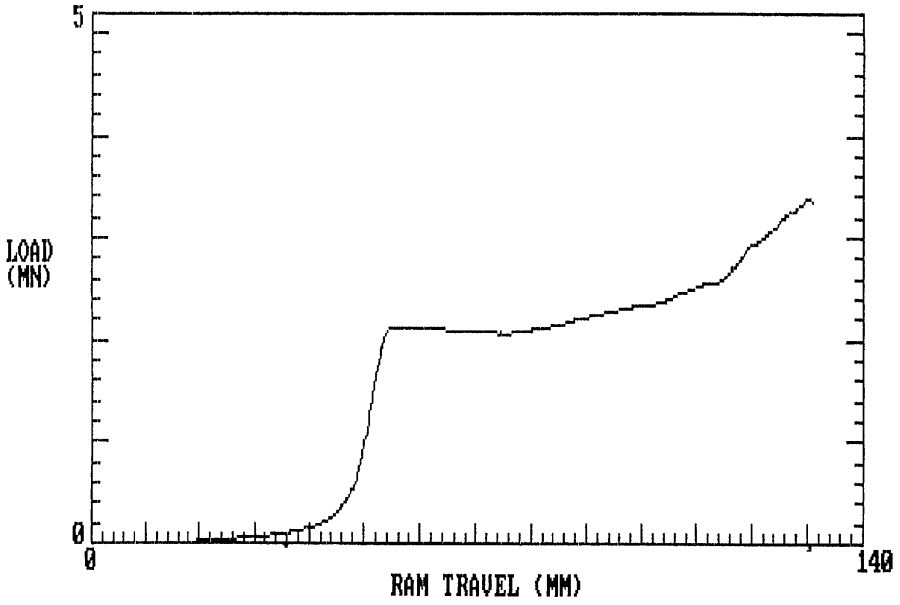

Figure 117: Extrusion Ram Load versus Ram Displacement Chart for Ti-6Al-4V + 30 v% (Al_3Ti + 40 v% TiB_2) (small) billet at 1180°C, low die ratio.

Table XXIV: Extrusion Data for Ti-6Al-4V + 40 v% (Al_3Ti + 40 v% TiB_2) billet at 1200°C, low die ratio.

Date	7-7-1997
Alloy	T4040A
PRE-EXTRUSION HEATING CONDITIONS	
Heating Method	FURNACE
Heating Time (min)	60
Billet Temperature (°C)	1200
EXTRUSION CONDITIONS	
Extrusion Mode	DIRECT
Contained Diameter (mm)	60
Container Temperature (°C)	500
Extrude Shape	ROD
Extrusion Ratio (measured)	22:1
Ram Speed (mm/sec)	2.46
Lubrication	DAG/GLASS
Quench	AIR
EXTRUSION RESULTS	
Maximum Load (MN)	2.12
Maximum Pressure (MPa)	750
Occurred at ram displacement (mm)	21
After time (sec)	9
Steady-state Load (MN)	2.12
Steady-state Pressure (MPa)	750
Occurred at ram displacement (mm)	23
After time (sec)	10
Maximum Load (tons)	348
Total Ram Displacement (mm)	51
Total Extrusion Time (sec)	26
Total Extrusion Length (calculated)	1000
Total Test Time (sec)	40
Comment:	OK

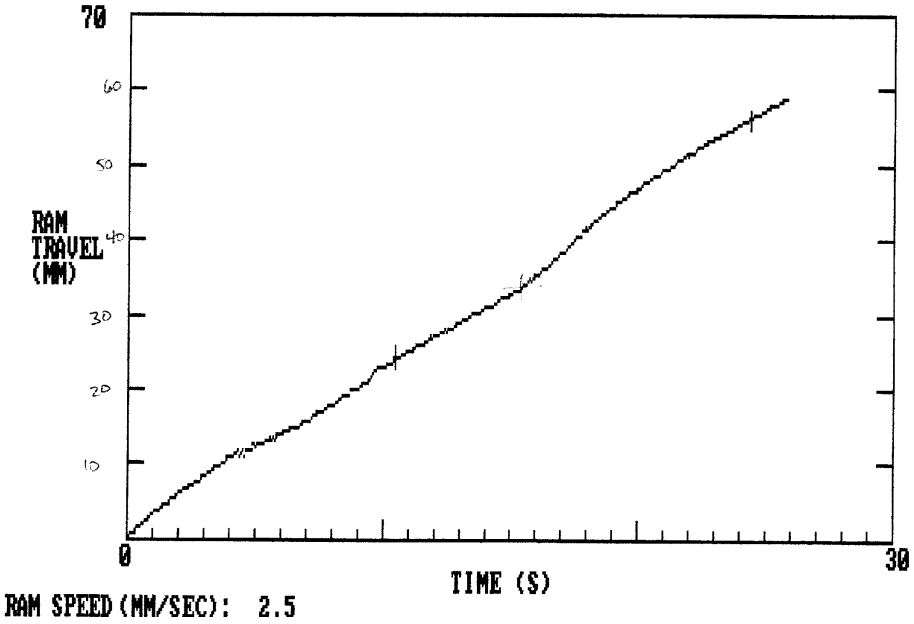

Figure 118: Ram Displacement versus Extrusion Time Chart for Ti-6Al-4V + 40 v% (Al_3Ti + 40 v% TiB_2) billet at 1200°C, low die ratio.

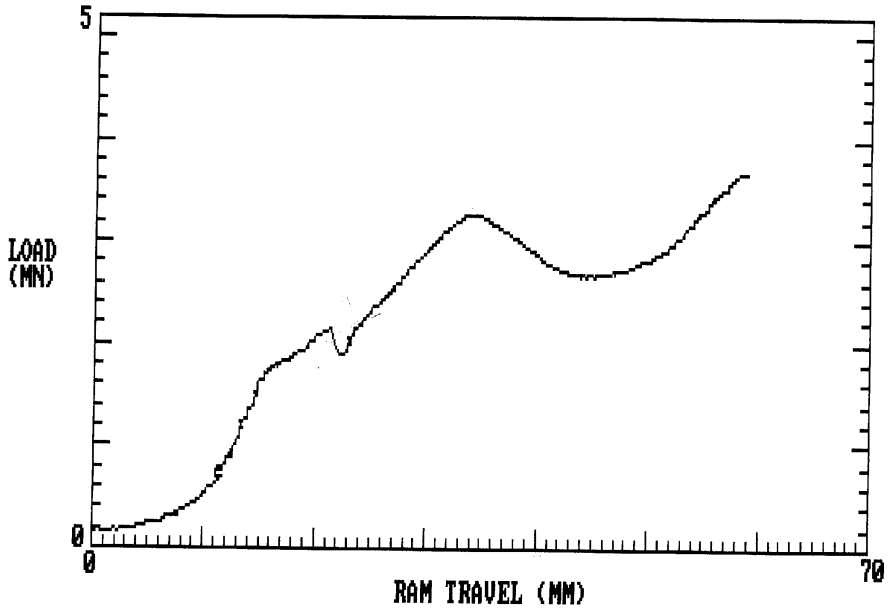

Figure 119: Extrusion Ram Load versus Ram Displacement Chart for Ti-6Al-4V + 40 v% (Al_3Ti + 40 v% TiB_2) billet at 1200°C, low die ratio.

Appendix D: Finite Element Model Input Code

Following is an example of the computer code used with ABAQUS® to produce the simulation results presented in Chapter 6. In order to change from one code to another, the remarks syntax (**) is changed to a different line in the section marked **DEFINE MATERIAL 2. In addition, the element sets (the large groups of numbers) must be changed to define the correct proportion of each. The first set of numbers, ELSET=E1, are the matrix elements, the second set, ELSET=E2, are the reinforcement particles.

```
*HEADING, UNSYMM
EXTRUSION
*RESTART,WRITE,FREQUENCY=50
*NODE
 1, 0.,0.
61, 0.,.3
2001, 0.1, 0.0
2061, 0.1, 0.3
10000,-0.1,0.0
*NGEN,NSET=AXIS
1,61,1
*NGEN,NSET=OUTSIDE
2001,2061,1
*NFILL,NSET=ALL
AXIS,OUTSIDE,20,100
*ELEMENT,TYPE=CAX4,ELSET=WORK
1,1,101,102,2
*ELGEN,ELSET=WORK
1,60,1,1,20,100,100
*ELSET,ELSET=BOT,GENERATE
1,1901,100
*ELSET,ELSET=SIDE,GENERATE
1901,1960,1
*ELSET,ELSET=CONTACT
BOT,SIDE
*ELSET,ELSET=TOP,GENERATE
60,1960,100
**
*ELSET,ELSET=E1
1, 2, 3, 4, 6, 8, 10, 11,
12, 13, 14, 15, 16, 17, 18, 19,
20, 21, 22, 23, 25, 27, 29, 30,
31, 32, 33, 34, 35, 36, 37, 38,
39, 40, 42, 44, 46, 47, 49, 51,
52, 53, 54, 56, 57, 58, 59, 60,
101, 102, 103, 105, 106, 107, 108, 110,
112, 114, 115, 116, 117, 119, 120, 121,
122, 124, 125, 126, 127, 128, 129, 130,
131, 133, 134, 136, 138, 139, 140, 141,
142, 143, 144, 145, 146, 147, 148, 149,
151, 153, 155, 156, 157, 158, 159, 160,
202, 204, 205, 206, 207, 208, 209, 210,
```

```
211, 212, 213, 214, 215, 217, 219, 221,
222, 223, 224, 225, 226, 227, 228, 229,
230, 231, 232, 233, 234, 236, 238, 240,
241, 242, 243, 244, 245, 246, 247, 248,
250, 251, 252, 253, 255, 257, 259, 260,
302, 304, 306, 307, 308, 309, 310, 311,
312, 313, 314, 316, 317, 318, 319, 321,
323, 325, 326, 327, 328, 330, 331, 332,
333, 335, 336, 337, 338, 339, 340, 341,
342, 345, 346, 347, 349, 350, 351, 352,
353, 354, 355, 356, 357, 358, 359, 360,
401, 402, 403, 404, 405, 406, 408, 410,
412, 413, 415, 416, 417, 418, 419, 420,
421, 422, 423, 425, 426, 427, 428, 430,
432, 434, 435, 436, 437, 439, 440, 441,
442, 443, 444, 445, 446, 447, 449, 451,
453, 454, 455, 456, 457, 458, 459, 460,
501, 502, 503, 504, 505, 506, 507, 508,
509, 510, 511, 513, 515, 517, 518, 519,
520, 521, 522, 523, 524, 525, 527, 528,
529, 530, 532, 534, 536, 537, 538, 539,
541, 542, 543, 544, 546, 547, 548, 549,
551, 552, 553, 554, 556, 557, 558, 560,
602, 604, 605, 606, 607, 608, 609, 610,
611, 612, 613, 614, 615, 616, 617, 619,
621, 623, 624, 625, 626, 628, 629, 630,
631, 633, 634, 635, 636, 638, 639, 640,
641, 643, 645, 647, 648, 649, 650, 651,
652, 653, 654, 655, 656, 657, 658, 660,
702, 704, 705, 707, 709, 711, 712, 713,
714, 715, 716, 717, 718, 719, 720, 721,
722, 724, 726, 728, 729, 730, 731, 732,
733, 734, 735, 736, 738, 739, 740, 741,
743, 745, 747, 748, 749, 750, 751, 752,
753, 754, 755, 756, 757, 758, 759, 760,
801, 803, 804, 805, 806, 807, 808, 809,
810, 811, 813, 815, 817, 818, 819, 820,
822, 823, 824, 825, 826, 827, 828, 829,
830, 831, 832, 834, 836, 837, 839, 840,
841, 842, 843, 844, 845, 846, 847, 849,
850, 851, 852, 854, 856, 858, 859, 860,
901, 902, 903, 905, 906, 907, 908, 909,
910, 911, 912, 913, 915, 916, 918, 920,
922, 923, 924, 925, 926, 927, 928, 929,
930, 932, 933, 934, 935, 937, 939, 941,
942, 943, 944, 945, 946, 947, 948, 949,
950, 951, 952, 953, 954, 956, 958, 960,
1001, 1002, 1003, 1005, 1007, 1009, 1010, 1011,
1012, 1014, 1015, 1016, 1017, 1018, 1019, 1020,
1021, 1022, 1024, 1026, 1028, 1029, 1030, 1031,
1032, 1033, 1034, 1035, 1036, 1037, 1038, 1039,
1041, 1042, 1043, 1045, 1047, 1048, 1049, 1050,
1051, 1052, 1053, 1054, 1055, 1056, 1057, 1060,
1101, 1102, 1103, 1104, 1105, 1107, 1109, 1111,
1112, 1113, 1114, 1115, 1116, 1117, 1118, 1119,
1120, 1121, 1122, 1123, 1124, 1126, 1128, 1129,
1131, 1133, 1135, 1136, 1137, 1138, 1140, 1141,
```

```
1142, 1143, 1144, 1145, 1146, 1147, 1148, 1150,
1152, 1154, 1155, 1156, 1157, 1158, 1159, 1160,
1201, 1202, 1203, 1204, 1205, 1206, 1207, 1208,
1209, 1211, 1212, 1213, 1214, 1216, 1218, 1220,
1221, 1222, 1223, 1225, 1226, 1227, 1228, 1229,
1230, 1231, 1232, 1233, 1235, 1237, 1239, 1240,
1241, 1242, 1243, 1244, 1245, 1246, 1247, 1248,
1249, 1250, 1252, 1254, 1255, 1258, 1259, 1260,
1301, 1303, 1305, 1306, 1307, 1308, 1309, 1310,
1311, 1312, 1313, 1315, 1316, 1317, 1318, 1320,
1322, 1324, 1325, 1326, 1327, 1328, 1329, 1330,
1331, 1332, 1333, 1334, 1335, 1336, 1337, 1339,
1341, 1342, 1344, 1346, 1348, 1349, 1350, 1351,
1352, 1353, 1354, 1355, 1356, 1357, 1358, 1359,
1401, 1403, 1405, 1407, 1408, 1410, 1411, 1412,
1413, 1414, 1415, 1416, 1417, 1418, 1419, 1420,
1422, 1423, 1424, 1425, 1427, 1428, 1429, 1431,
1432, 1433, 1434, 1436, 1437, 1438, 1439, 1440,
1442, 1443, 1444, 1446, 1448, 1450, 1451, 1452,
1453, 1454, 1455, 1456, 1457, 1458, 1459, 1460,
1501, 1502, 1503, 1504, 1505, 1506, 1507, 1509,
1510, 1511, 1512, 1514, 1516, 1518, 1519, 1520,
1521, 1523, 1524, 1525, 1526, 1527, 1528, 1529,
1530, 1531, 1533, 1535, 1537, 1538, 1539, 1540,
1541, 1542, 1543, 1544, 1545, 1546, 1547, 1548,
1549, 1550, 1552, 1554, 1555, 1557, 1559, 1560,
1601, 1602, 1604, 1605, 1606, 1607, 1608, 1609,
1610, 1611, 1612, 1614, 1616, 1618, 1619, 1620,
1621, 1622, 1623, 1624, 1625, 1626, 1628, 1629,
1630, 1631, 1633, 1634, 1635, 1636, 1638, 1640,
1641, 1642, 1643, 1644, 1645, 1647, 1648, 1649,
1650, 1651, 1652, 1653, 1654, 1655, 1657, 1659,
1701, 1702, 1703, 1705, 1707, 1708, 1710, 1712,
1713, 1714, 1715, 1716, 1717, 1718, 1719, 1720,
1721, 1722, 1723, 1725, 1727, 1729, 1730, 1731,
1732, 1733, 1734, 1735, 1736, 1737, 1739, 1740,
1741, 1742, 1744, 1746, 1748, 1749, 1750, 1751,
1752, 1753, 1754, 1755, 1756, 1758, 1759, 1760,
1801, 1802, 1803, 1804, 1805, 1806, 1808, 1810,
1812, 1813, 1814, 1815, 1817, 1818, 1819, 1820,
1821, 1822, 1823, 1824, 1825, 1827, 1829, 1831,
1832, 1834, 1835, 1836, 1837, 1838, 1839, 1840,
1841, 1842, 1844, 1845, 1846, 1847, 1849, 1851,
1853, 1854, 1855, 1856, 1857, 1858, 1859, 1860,
1901, 1902, 1903, 1904, 1905, 1906, 1907, 1909,
1910, 1911, 1912, 1913, 1914, 1916, 1918, 1919,
1921, 1923, 1924, 1925, 1926, 1927, 1928, 1929,
1930, 1931, 1932, 1933, 1934, 1936, 1938, 1940,
1941, 1942, 1943, 1944, 1945, 1946, 1947, 1948,
1950, 1951, 1952, 1953, 1955, 1957, 1959, 1960,
*ELSET,ELSET=E2
5, 7, 9, 24, 26, 28, 41, 43,
45, 48, 50, 55, 104, 109, 111, 113,
118, 123, 132, 135, 137, 150, 152, 154,
201, 203, 216, 218, 220, 235, 237, 239,
249, 254, 256, 258, 301, 303, 305, 315,
320, 322, 324, 329, 334, 343, 344, 348,
```

```
407, 409, 411, 414, 424, 429, 431, 433,
438, 448, 450, 452, 512, 514, 516, 526,
531, 533, 535, 540, 545, 550, 555, 559,
601, 603, 618, 620, 622, 627, 632, 637,
642, 644, 646, 659, 701, 703, 706, 708,
710, 723, 725, 727, 737, 742, 744, 746,
802, 812, 814, 816, 821, 833, 835, 838,
848, 853, 855, 857, 904, 914, 917, 919,
921, 931, 936, 938, 940, 955, 957, 959,
1004, 1006, 1008, 1013, 1023, 1025, 1027, 1040,
1044, 1046, 1058, 1059, 1106, 1108, 1110, 1125,
1127, 1130, 1132, 1134, 1139, 1149, 1151, 1153,
1210, 1215, 1217, 1219, 1224, 1234, 1236, 1238,
1251, 1253, 1256, 1257, 1302, 1304, 1314, 1319,
1321, 1323, 1338, 1340, 1343, 1345, 1347, 1360,
1402, 1404, 1406, 1409, 1421, 1426, 1430, 1435,
1441, 1445, 1447, 1449, 1508, 1513, 1515, 1517,
1522, 1532, 1534, 1536, 1551, 1553, 1556, 1558,
1603, 1613, 1615, 1617, 1627, 1632, 1637, 1639,
1646, 1656, 1658, 1660, 1704, 1706, 1709, 1711,
1724, 1726, 1728, 1738, 1743, 1745, 1747, 1757,
1807, 1809, 1811, 1816, 1826, 1828, 1830, 1833,
1843, 1848, 1850, 1852, 1908, 1915, 1917, 1920,
1922, 1935, 1937, 1939, 1949, 1954, 1956, 1958,
*elset,elset=elall
e1,e2
*SOLID SECTION,ELSET=E1,MATERIAL=MAT1
*MATERIAL,NAME=MAT1
**Ti-6Al-4V Matrix
*ELASTIC
1.16E10,.3
*PLASTIC
45e6,0.0
50e6,2.0
**
**DEFINE MATERIAL 2
**
*SOLID SECTION,ELSET=E2,MATERIAL=MAT2
*MATERIAL,NAME=MAT2
*ELASTIC
1.16E10,.3
*PLASTIC
**Monolithic
**45e6,0
**50e6,2.0
**4040A_Lo
**108e6,0
**120e6,2.0
**4040A_Hi
**105e6,0
**117e6,2.0
**4040G_Lo
**593e6,0
**659e6,2.0
**2040A
108e6,0
120e6,2.0
```

```
**3040A_1200
**105e6,0
**117e6,2.0
**3040A_1180
**113e6,0
**126e6,2.0
**3040A_large
**109e6,0
**122e6,2.0
**3040A_small
**110e6,0
**122e6,2.0
**********
*RIGID SURFACE, NAME=WALL, REF NODE =10000, TYPE=SEGMENTS, SMOOTH=0.2
**e=10,e=12
START,0.25,-0.53
**e = 12
**LINE,0.029,-0.53
**LINE,0.029,-0.1565
**e = 10
LINE,0.0316,-0.53
LINE,0.0316,-0.1526
**e=10,e=12
LINE,0.099999,-0.05
LINE,0.099999,0.31
LINE,0.2,0.41
*SURFACE DEFINITION, NAME=SLAVE, TRIM=YES
CONTACT
*CONTACT PAIR, INTERACTION=EXTRUDE
SLAVE, WALL
*SURFACE INTERACTION, NAME=EXTRUDE
*FRICTION
0.0
**********
*NSET,NSET=TOP,GENERATE
61,2061,100
*NSET,NSET=ALL
1,2061,1
*STEP,INC=100,AMPLITUDE=RAMP,NLGEOM
STABILIZE WORKPIECE INSIDE DIE
*STATIC
.1,10.,1e-15,10.0
*BOUNDARY
AXIS,1,1,0.0
TOP,2,2,-.000125
2061,1,1,0.0
10000,1,6,0.0
*PRINT,CONTACT=NO
*EL PRINT,FREQUENCY=0
*EL FILE, FREQUENCY=0
*NODE FILE, FREQUENCY=0
*NODE PRINT, FREQUENCY=0
*END STEP
*STEP,INC=800,AMPLITUDE=RAMP,NLGEOM
EXTRUSION
*STATIC
.1,100.,1e-15,50.0
```

```
*BOUNDARY,OP=NEW
AXIS,1,1,0.0
TOP,2,2,-.25
2061,1,1,0.0
10000,1,6,0.0
*PRINT,CONTACT=NO
*EL PRINT,FREQUENCY=0
*NODE PRINT, FREQUENCY=0
*EL FILE, FREQUENCY=0
*NODE FILE, FREQUENCY=0
*END STEP
```

Vita

Judson S. Marte was born on May 25th of 1971 outside of Philadelphia, Pennsylvania. He was raised in suburban Langhorne, PA. He attended Holy Ghost Preparatory School until he completed his high school diploma in 1989. In August of 1989 he left Langhorne to pursue the study of engineering. He joined the Materials Science and Engineering department at the Johns Hopkins University's Whiting School of Engineering. Upon successful completion of his Bachelor's degree in 1993, he moved to Blacksburg, Virginia. There he joined the Materials Science and Engineering Department at Virginia Polytechnic Institute and State University (Virginia Tech) to begin his graduate studies under the direction of Professor Stephen L. Kampe. Following the completion of his Master's degree in April of 1996, he decided to continue his exploration of metallic and intermetallic matrix composites in the pursuit of a Ph.D. These studies lead to collaborations with the Naval Research Laboratories, Oak Ridge National Laboratories, Imperial College, and MATSYS, Inc. In November of 1996 he was introduced to his future wife, Ms. Michelle Bodine, whom he intends to wed in April of 1999. Recently, he also found employment with the General Electric Corporate Research and Development Laboratories in Schenectady, New York. There he will work in the Physical Metallurgy Laboratory as a Materials Scientist specializing in thermomechanical processing.

January 8th 1998
Blacksburg, Virginia